ISSN 1580-2949
UDK 669+666+678+53 MTAEC9, 47(1)1–141(2013)

MATER. TEHNOL.	LETNIK VOLUME 47	ŠTEV. NO. 1	STR. P. 1–141	LJUBLJANA SLOVENIJA	JAN.–FEB. 2013

VSEBINA – CONTENTS

STROKOVNI ČLANKI – PROFESSIONAL ARTICLES

DOGODKI – EVENTS

Predsednik IFHTSE prof. XU Kevel izroča priznanje Fellow recognition izr. prof. dr. Vojtehu Leskovšku
The President of IFHTSE, Prof. XU Kevel, presenting the Fellow recognition to Prof. Dr. V. Leskovšek

Čestitka

Mednarodno združenje za toplotno obdelavo in inženirstvo površin podeljuje častno članstvo IFHTSE posameznikom, ki prispevajo izreden, globalno priznan in pomemben prispevek k razvoju toplotne obdelave in inženirstva površin. Izr. prof. dr. Vojteh Leskovšek je bil izvoljen za častnega člana IFHTSE na 20. kongresu, ki je bil 22. oktobra 2012 v Pekingu na Kitajskem. Priznanje temelji na njegovem dolgoročnem prispevku pri študiju toplotne obdelave in inženirstva površin z močnim poudarkom na lomni žilavosti, vakuumski toplotni obdelavi orodnih in hitroreznih jekel z uporabo kriogene tehnike, kot tudi termomehanske obdelave.

Slovenija ima spoštljivo tradicijo v proizvodnji jekel, ki dosegajo optimalne uporabne lastnosti po primerni toplotni obdelavi, od jekel za močno obremenjene dele strojev in dele motorjev za vozila do malo legiranih in hitroreznih jekel. Različna orodja, od livarskih kokil do orodij za utopno kovanje, so ključnega pomena za kvaliteto in konkurenčnost industrijskih podjetij, ki večino svoje proizvodnje prodajo v razvitih zahodnoevropskih deželah.

Po ustanovitvi prvega Laboratorija za vakuumsko toplotno obdelavo leta 1984 na Metalurškem inštitutu v Ljubljani, sedaj Inštitutu za kovinske materiale in tehno-

Congratulations

The International Federation of Heat Treatment and Surface Engineering awards the honour of Fellow of IFHTSE to individuals who have made outstanding, globally recognised and significant contributions to the development of heat treatment and surface engineering. Prof. Dr. Vojteh Leskovšek was elected as a Fellow of IFHTSE at the 20th Congress in Beijing, China on the 22nd of October 2012. The recognition is based on his long-term contribution to the study of heat treatment and surface engineering with a strong emphasis on fracture toughness, the vacuum heat treatment of tool and high-speed steels, and the use of sub-zero as well as thermochemical treatments.

Slovenia has a respected tradition in the production of steels that obtain optimal properties for use after a proper thermal treatment, from steels for heavily loaded parts of machinery and motors for parts of vehicles as well as low-alloyed and high-speed steels. Different tools, from casting moulds to forging dies, are essential for the quality and competitiveness of industrial companies marketing their products, mostly with exports to developed Western European countries.

After establishing the first laboratory for vacuum thermal treatment at the Metallurgical Institute of Ljubljana, now the Institute of Metals and Technology, in

logije, je izr. prof. dr. Leskovšek prevzel težko nalogo, da bi pokazal možnosti nove tehnologije in jo prenesel v industrijo, ki je uporabljala konvencionalne postopke in opremo za toplotno obdelavo. Z upoštevanjem možnosti razpoložljive vakuumske peči se je obrnil k proizvajalcem in uporabnikom livarskih orodij, kovaških orodij in orodij za štancanje. Po uspehu v manjših podjetjih se je tehnologija razširila tudi v večja podjetja in izvoznike, več vakuumskih naprav za toplotno obdelavo je nadomestilo konvencionalne naprave za toplotno obdelavo v večjih industrijskih podjetjih. Uspeh na področju vakuumske toplotne obdelave je bil dobra podlaga za podporo večjih industrijskih podjetij inštitutu pri nabavi naprave za tehnologijo obdelave površin v plazmi v letu 1993. Tudi uporaba te tehnologije v industrijskih podjetjih v Sloveniji je v porastu.

Poleg uvajanja in razširjanja teh dveh novih tehnologij so pomembni tudi rezultati izr. prof. dr. Leskovška na področju raziskav postopkov toplotne obdelave. Opazen dosežek je bilo uvajanje metode za določanje lomne žilavosti trdih in krhkih jekel, posebno še hitroreznih in močno legiranih orodnih jekel. Rotacijska simetrija vzorcev omogoča, da se izognemo nenatančnosti, povezani z nesimetrično hitrostjo ohlajanja vzorcev, in izračun kritične velikosti napake, ki vpliva na zdržljivost industrijskih orodij. Pomemben uspeh je tudi razvoj enačbe, ki povezuje lomno žilavost hitroreznih in ledeburitnih jekel s trdoto po Rockwellu, vsebnostjo zaostalega avstenita, z deležem in razdaljo med karbidi, kot tudi z modulom elastičnosti. Številni članki s citiranjem, uporabnost in znanstveni dosežki so razširili ime izr. prof. dr. Vojteha Leskovška v skupnostih za toplotno obdelavo in orodna jekla ter podprli njegovo izvolitev za častnega člana IFHTSE. Njegov uspeh je dober zgled za mlade, da s trdim delom lahko tudi znanstvenik iz majhne države doseže mednaroden ugled in priznanje.

Priznanje in izvolitev izr. prof. dr. Vojteha Leskovška za častnega člana IFHTSE odlikuje tudi Inštitut za kovinske materiale in tehnologije, Ljubljana.

Iskrene čestitke izr. prof. dr. Vojtehu Leskovšku v imenu kolegov in sodelavcev inštituta ter industrijskih podjetij.

prof. dr. Franc Vodopivec

1984, Prof. Dr. Leskovšek took over the difficult task of demonstrating the possibilities of the new technology and its expansion in industrial companies using conventional processes and equipment for thermal treatment. Considering the possibilities of the available vacuum furnaces, he turned to producers and users of casting moulds, forging and stamping dies. Thanks to successes in smaller companies, the technology expanded to larger companies and exporters and several vacuum-treatment facilities substituted conventional heat treatment in larger industrial companies. The success in vacuum heat treatment was a good reference for the support of several industrial companies for the institute to acquire the equipment for plasma surface treatment technology in 1993. The use of this technology in industrial companies in Slovenia is also expanding.

Besides the introduction and expansion of two new technologies of remarkable importance are the results of Prof. Dr. Leskovšek in the field of the research of heat-treatment processes. A notable achievement was the introduction of a method for determining the fracture toughness of hard and brittle steels, especially high-speed and high-alloyed tool steels. The rotational symmetry of the specimens makes it possible to avoid inaccuracies related to the uneven cooling rate of specimens and the calculation of a critical defect size that affects the useful life of industrial tools. Another remarkable success is the development of an equation that relates the fracture toughness of high-speed and ledeburitic tool steels to Rockwell hardness, the content of residual austenite, the fraction of carbide particles and spacing as well as the modulus of elasticity. A number of articles with the quoted and other original applied and scientific findings have spread the name of Prof. Dr. Vojteh Leskovšek in the heat-treatment and tool-steels communities and supported his election to Fellow of IFHTSE. His success is a good example for youth, that with hard and properly focused work, scientists from small countries can also acquire an international reputation and recognition.

The recognition and election of Prof. Dr. Vojteh Leskovšek as Fellow of IFHTSE also honours the Institute of Metals and Technology, Ljubljana, Slovenia.

We would like to offer our sincere congratulation to Prof. Dr. Vojteh Leskovšek on behalf of his colleagues and collaborators from the institute and industrial companies.

Prof. Dr. Franc Vodopivec

UDK 577.11:577.115
Review article/Pregledni članek

ISSN 1580-2949
MTAEC9, 47(1)5(2013)

POLYHYDROXYALKANOATES: BIODEGRADABLE POLYMERS AND PLASTICS FROM RENEWABLE RESOURCES

POLIHIDROKSIALKANOATI: BIORAZGRADLJIVI POLIMERI IN PLASTIKE IZ OBNOVLJIVIH VIROV

Martin Koller[1,2], Anna Salerno[1], Alexander Muhr[1], Angelika Reiterer[1], Gerhart Braunegg[2]

[1]Graz University of Technology, Institute of Biotechnology and Biochemical Engineering, Petersgasse 12, 8010 Graz, Austria
[2]ARENA – Association for resource efficient and sustainable technologies, Inffeldgasse 23, 8010 Graz, Austria
martin.koller@tugraz.at

Prejem rokopisa – received: 2012-07-24; sprejem za objavo – accepted for publication: 2012-08-28

Polyhydroxyalkanoates (PHAs) attract considerable attention as sustainable "green plastics" with a real potential to replace their petrol-based competitors in some applications in the not-too-distant future. To reach this goal PHAs must be able to compete with the established petrol-based plastics in both technical and economic terms. The current PHA production is based on prized substrates of high nutritional value such as sucrose, starch or vegetable oils. An alternative, carbon-rich industrial waste can be used as a suitable feedstock. This would contribute to making PHAs economically competitive and would avoid the conflict with human nutrition or animal feeding.
Consequently, the decision about the location of the PHA-production facilities depends on the preferable in-house availability of such waste streams. The issue of competitive, large-scale PHA production in Europe was the topic of the ANIMPOL and the WHEYPOL projects. Both intended to develop novel processes for the transformation of abundant, locally available, renewable wastes. In the ANIMPOL case, waste lipids from slaughterhouses are converted to glycerol and a mixture of saturated and unsaturated fatty acid esters (FAEs), better known as biodiesel. The production of saturated FAEs is 50 000 t per year in Europe, decreasing the biodiesel performance as an engine fuel. However, within the project it was demonstrated that they can be efficiently metabolized to PHAs. In the WHEYPOL project attention was focused on 1.4×10^8 t per year of whey from dairies. This waste is of limited use and causes environmental concern. However, lactose, the main carbohydrate found in whey, can be used as a substrate in the WHEYPOL bioprocesses. These strategies demonstrate the feasibility of making "green plastics" competitive by integrating their manufacturing directly into the existing production lines, where the convertible waste streams accrue.

Keywords: animal waste, biodiesel, biopolymers, lipids, polyhydroxyalkanoates, whey

Polihidroksialkanoati (PHA) vzbujajo posebno pozornost kot trajnostna "zelena plastika" z realno možnostjo, da nadomestijo svoje tekmece, ki temeljijo na nafti, za določene namene uporabe v bližnji prihodnosti. Za dosego tega cilja morajo biti PHA sposobni tekmovati tako po tehničnih kot po ekonomskih vidikih z uveljavljenimi plastikami na osnovi nafte. Sedanja proizvodnja PHA temelji na dragih podlagah z veliko hranilno vrednostjo, kot so saharoza, škrob ali rastlinska olja. Kot alternativna surovina se lahko uporabi z ogljikom bogate industrijske odpadke. To bi prispevalo k bolj ekonomični izdelavi PHA in bi preprečilo konflikt s prehrano ljudi in krmo živali.
Posledično je odločitev o lokaciji izdelave PHA odvisna od razpoložljivosti in virov takih odpadkov. Vprašanje konkurenčne proizvodnje PHA v velikih količinah v Evropi je bila tema projektov ANIMPOL in WHEYPOL. Oba sta imela namen razviti nove postopke predelave obilnih in lokalno razpoložljivih obnovljivih odpadkov. V primeru ANIMPOL-a so bili odpadni lipidi iz klavnic pretvorjeni v glicerol in mešanico estrov (FAE) nasičenih in nenasičenih maščobnih kislin, bolj poznani kot biodizel. Proizvodnja nasičene FAE v Evropi je 50 000 t na leto in zmanjšuje zmogljivost biodizla kot pogonskega goriva. Projekt je pokazal, da jih lahko pretvorimo v PHA. Pri projektu WHEYPOL je bila pozornost usmerjena na $1{,}4 \times 10^8$ t na leto sirotke iz mlekarn. Ta odpadek ima omejeno uporabo in povzroča okoljske skrbi. Vendar pa se laktoza, glavni ogljikovodik v sirotki, lahko uporabi kot osnova pri WHEYPOL-bioprocesih. Te strategije kažejo, da je mogoča proizvodnja konkurenčne "zelene plastike" z vključitvijo njihove izdelave neposredno v proizvodne linije, kjer se vredni odpadki pojavljajo.

Ključne besede: živalski odpadki, biodizel, biopolimeri, lipidi, polihidroksialkanoati, sirotka

1 INTRODUCTION

1.1 "Green plastics" today

Currently, we are experiencing a remarkably dynamic biopolymer market with an impressive increase in the volume and range of the products: in 2010, the market value reached a magnitude of 10^{10} US dollars with an obvious upward trend. Only from 2008 to 2015, the global production of biopolymers is estimated to increase from 180 kt to 1710 kt (Plastic Additives and Compounding 2008). This positive development is unfortunately associated with an emergence of various plastics that are labeled with the stylish attribute "green plastic" by the manufactures, but display properties that do not match the strict definitions by which they could be classified as *biobased*, *biodegradable*, *compostable* or *biocompatible*. On the other hand, polyhydroxyalkanoates (PHAs) are natural, thermoplastic, aliphatic biopolyesters that fully comply with these requirements.[1] Among all bio-based plastics, they are unique by being entirely produced and degraded by living cells.[2] The spectrum of their potential applications ranges from simple packaging to high-quality materials for niche uses.

1.2 General aspects of PHAs

PHAs are synthesized and stored as intracellular granules by a wide range of prokaryotic genera using various renewable feedstocks. Predominately, the conversion of hexoses, pentoses, starch, sucrose, lactose, maltose, lipids, alcohols, or methane is reported in literature.[3–5] **Figure 1** provides a scanning transmission electron microscopy (STEM) picture of *Cupriavidus-necator* cells cultivated on carbohydrates in a continuous process. PHA inclusions are well visible as bright, refractive granules amounting to the mass fraction 52 % of the cell mass.

Principally, a high intracellular energy charge, characterized by an elevated pool of acetyl-CoA, NAD(P)H, ATP and others, promotes a PHA formation. Such conditions result from a sufficient availability of an external carbon source and a restricted supply of the growth-essential substrates such as nitrogen, phosphate, dissolved oxygen, or certain micro-components.[3,6,7] PHAs carry out important biological tasks, mainly acting as intracellular-energy and carbon reserves that can be re-utilized under the conditions of carbon starvation.[8] They are crucial for the regulation of the intracellular energy flow, routing the carbon compounds to the metabolic pathways and acting as protective factors against the environmental pressures like osmotic shock, UV irradiation, desiccation, heat and oxidative stress.[9]

1.3 Material properties and downstream processing

PHAs are polyesters consisting mainly of enantiomerically pure *R*-configured 3-hydroxyalkanoate (3HA) monomers; the general chemical structure is shown in **Figure 2**.

Depending on the microbial production strain, the nutrient supply and the process parameters during a biosynthesis, PHA-polymer chains contain 100 to 100 000 3HA units. Among all known PHAs, the homopolyester of *R*-3-hydroxybutyrate (3HB)-poly ([*R*]-3-hydroxybutyrate) (PHB) is most intensely studied and understood. Unfortunately, PHB exhibits a rather high crystallinity that hampers its processability. The low difference between the decomposition temperature (around 270 °C) and the high melting point (around 180 °C) provides a "window of processability" that is too narrow for many processing techniques, e.g., a melt extrusion or blowing of plastic films. This can be overcome by interrupting the crystalline PHB matrix with an incorporation of additional PHA building blocks, mainly 3-hydroxyvalerate (3HV) or an achiral building block of 4-hydroxybutyrate (4HB). The resulting co-polyesters display enhanced material properties in a broader range of applications. The exact material properties are strongly dependent on the monomer composition of co-polyesters. This composition can be triggered during a PHA biosynthesis by feeding the precursor substrates to obtain the desired building blocks. For example, 3HV building blocks are produced by many PHA-accumulating strains supplying odd-numbered fatty acids as precursors that lead to 3HV in the synthesized PHAs.[8]

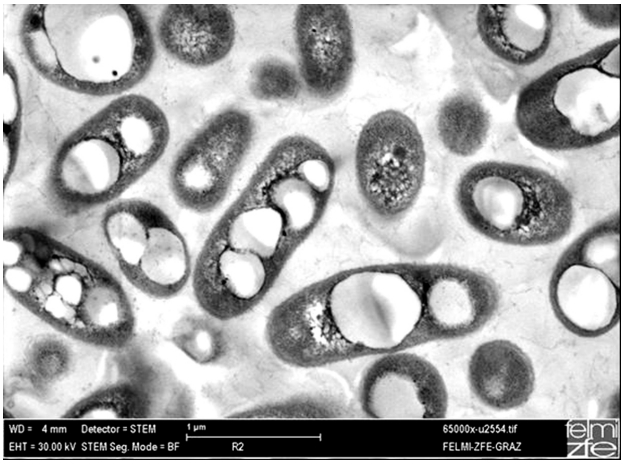

Figure 1: STEM picture of *Cupriavidus-necator* cells harboring PHA biopolymers (magnification 65.000x)
Slika 1: STEM-posnetek celic *Cupriavidus necator*, ki zadržujejo PHA-biopolimere (povečava 65000-kratna)

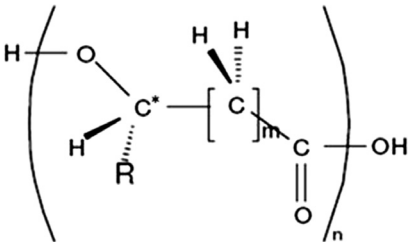

Figure 2: General chemical structure of PHAs. The asterisk (*) indicates the chiral center, *n*: number of building blocks in the polyester chain (for natural PHAs: *n* = 100 to 10000), *m*: number of carbon atoms in the monomer backbone; in the case of 3HAs, *m* = 1, R: side chain of the building blocks; in the case of 3HB, R = -CH_3.
Slika 2: Splošna kemijska struktura PHA. Zvezdica (*) označuje kiralni center, *n*: število gradnikov v poliestrski verigi (pri naravni PHA: *n* = 100 do 10000), *m*: število ogljikovih atomov v monomerni hrbtenici; v primeru 3HAs, *m* = 1, R: stranska veriga gradnikov; v primeru 3HB, R = -CH_3.

After a production of the PHA-rich cells, efficient downstream processing is needed. This includes separating the biomass from the liquid phase, a PHA recovery from the biomass, and product refining. A PHA recovery from the cells may include a solvent or a supercritical fluid extraction, a chemical or enzymatic digestion of the cell wall, using high cell fragility of special microbial species, or a mechanical cell disruption.[10] The choice of the best method mainly depends on the required product purity that will satisfy the envisaged application. The recovered biopolyesters can be processed with the conventional equipment well established in the polymer industry. This technological path leads to proper biodegradable and biobased substitutes for a variety of "classical" petrol-based plastics such as thermoplastics, elastomers, and even latex rubbers.[11–14]

2 CHALLENGES IN THE PRODUCTION OF PHAs AND THE ATTEMPTS TO OVERCOME THEM

2.1 Global PHA production

Despite the enormous efforts during the last decades dedicated to the improvements in the PHA production, characterization and processing on the laboratory and pilot scale, their ultimate market penetration has not yet taken off. However, serious activities undertaken in the past by ICI-Marlborough (UK), Chemie Linz (Austria), and, more recently, by Monsanto, Metabolix (both USA), PHBISA (Brazil), Tepha (USA) and Tianan or Shandong (PR China) constitute laudable exceptions. Due to an obvious gap between the often highly enthusiastic public announcements made by the manufacturers citing their capacities, and the actual PHA production, it is challenging to collect reliable data on the quantities of PHAs that are currently produced on the (semi)industrial scale. Realistically, it can be estimated that today PHAs cover about 5 % of the world's biolastic market, and less than 0.05 % of the overall global plastic production.

2.2 Economics of the PHA production: decisive factors

The major part, up to a half, of the entire PHA production costs is attributed to the cost of carbon substrates. On the one hand, from the ethical point of view, the explosive nutritional situation of the mankind in many global regions strongly discourages the utilization of various renewable feedstocks that can be used for food, for the production of chemicals, plastics or fuels; starch or edible oils are the prime examples. On the other hand, there are a number of diverse industrial carbon-rich wastes that do not interfere with the nutrition chain, and, at the same time, cause disposal problems and costs. Their utilization as carbon substrates for the microbial processes is a viable strategy for overcoming this ethical conflict and can be considered as the most promising approach in making PHAs economically competitive. Waste renewable resources like lignocellulosics, carbohydrates, waste lipids or alcohols, are mainly produced in agriculture and connected industrial branches.[8,12,15,16]

In addition to introducing the substrates, costs have to be reduced by optimizing the downstream processing required for the PHA recovery after a cell harvest. As intracellular products, PHAs have to be separated from the surrounding non-PHA cell mass (NPCM, also known as the residual biomass) that mainly consists of proteins, lipids, nucleic acids and polysaccharides. Here, a high usage of hazardous solvents and enormous energy demand still constitute the state-of-the-art, somewhat contradicting the patterns of sustainability and economic feasibility.[3,17]

Apart from the selection of raw materials and the improvements in downstream processing, enhanced productivity reached through the design of an optimal engineering set-up is indispensable for the final breakthrough of PHAs on the market. Batch and fed-batch discontinuous fermentation modes are currently most commonly used techniques for the microbial PHA production.[18–20] In contrast, the continuous production mode is a well-known tool for achieving high productivities, lower production costs and a constant product quality in biotechnological processes. Therefore, an increasing research is focusing on investigating and assessing the potential of continuous PHA-production processes.[21–23] Recently, based on the kinetic considerations regarding biomass growth and PHA accumulation, the continuous production of PHB in a five-stage bioreactor cascade (5-CSTR) was investigated.[23] This 5-CSTR acts as a device-related engineering substitute for a tubular bioreactor that is theoretically the best match for the process-engineering requirements for an efficient PHA production from a kinetic point of view. As the main results, the authors report on a high PHB productivity of 1.85 g/(L h), and a constant and superior product quality concerning the mechanical properties and molecular masses.[23]

3 CURRENT ROUTES IN PHA RESEARCH

Current research in the field of PHAs focuses on several key topics. The application of growth additives that shorten the time for the production of a catalytically active biomass is a pre-requisite for enhancing the entire volumetric productivity of the process. Inexpensive growth additives can be found in agriculture, e.g., proteinaceous materials or side streams from the cultivation of green grass land, and were already tested successfully on the laboratory scale.[24]

Efforts in the field of genetic engineering mainly intend to increase the volumetric PHA productivity and achieve higher molar masses of the biopolymers. This can be accomplished with a knock-out of enzymes responsible for the intracellular PHA degradation. In addition, metabolic bottle necks that can limit a fast and complete substrate conversion can be overcome by genetic modifications. Enhancement of the microbial oxygen uptake may be improved by inserting the genes encoding catalase or peroxidases.[25]

In the field of downstream processing, together with lower energy consumption, environmentally safe and efficient solvents are investigated in order to enhance the recovery of PHAs from the cells. This goes in parallel with an examination of the novel biological lysis methods and enhanced strategies for a mechanical cell disruption. For an efficient polymer recovery, an increase in both the intracellular polymer content as well as the PHA granule size is beneficial. These factors are determined during the PHA biosynthesis.[26] In addition, the remaining NPCM has to be converted in a sustainable, value-adding way. Currently, the research in this direction is devoted to the anaerobic digestion of NPCM in

biogas plants, its application in agriculture as a "green fertilizer", or to the chemical or enzymatic digestion of NPCM into a nutrient-rich cocktail to be used for subsequent microbial cultivations. Downstream processing can also be facilitated by genetic modification; boosted nuclease excretion after a cell disruption results in decreased amounts of nucleic acids in the medium, leading to a lower viscosity that facilitates the separation of the PHA granules from the surrounding liquid phase.

The technological drawbacks of the bio-production itself can be handled by an application of the robust, microbial production strains that remain genetically stable for a long time under continuous cultivation conditions. At the same time, they should resist the contamination with the microbial competitors that, by endangering the whole production set-ups, represent a high risk.[8] Using extremophilic species, like the halophilic archaeon *Haloferax mediterranei,* minimizes the normally indispensable, energy-demanding sterilization precautions for the PHA production set-ups.[27,28]

In future, continuous PHA production should not only aim to increase the volumetric productivity, but also to open the door for tailor-made material properties by fine-tuning the polyester composition. This can be accomplished with the formation of block-copolymers, where a sequential arrangement of softer and harder polymer segments can result in well-adjusted novel polymeric materials. Here, a multistage bioreactor cascade for the PHA production is presented with potentially adequate process engineering equipment.[23]

During the last decades, the preparation of nanocomposites and composites involving natural fibers has become one of the key segments in the biopolymer science. To enhance material properties, PHAs can be processed together with a variety of compatible matters, resulting in the creation of novel materials. For this purpose, polymeric materials like poly(vinyl alcohol), poly(lactic acid), poly(ε-caprolactone), synthetic analogues of PHAs (e.g., atactic PHB), inorganic (e.g., clays or calcium carbonate) and organic (bagasse, wheat flour, fruit peels, fruit fibers, saw dust and straw) fillers of agricultural origin were already tested.[29,30] Nanocomposites have a potential to improve special polymer properties, such as gas permeability and thermal and mechanical characteristics. Here, only rather small amounts of a filler (mainly modified clay) are needed to improve the material performance.[29] Natural-fiber composites often display excellent mechanical properties, and decrease the density of the final product. In most cases, the fibers from agricultural residues are used as fillers; their application additionally enhances the biodegradability and reduces the production cost of the final product.[30]

4 CASE STUDY 1: FROM SURPLUS WHEY TO PHA BIOPOLYESTERS

Whey is a surplus product in the cheese industry. Casein precipitates from milk enzymatically or by acidification. This transformation results in curd cheese (mainly caseins) and full-fat whey that undergoes a degreasing and concentration procedure. From the resulting whey concentrate, whey retentate (protein fraction) is removed; the remaining whey permeate (carbohydrate fraction) contains about 80 % of the lactose originally included in the milk.

In 2008, 1.6×10^8 t of whey were produced according to the estimates from OECD and FAO. The production has increased continually in the past and this trend is expected to continue in the future. The highest quantities of whey are available in the northern hemisphere with roughly 4×10^7 t in the USA, 2.2×10^5 t in Canada, and 5×10^7 t in the EU-25.[31]

Due to its quantities, whey is not only an excess raw material, but it also causes disposal problems because of its high biochemical oxygen demand.[18,32] It accrues in the volumes almost equal to the processed milk, which means that the processing of one million liters of milk into cheese, almost one million liters of whey has to be treated. This exemplary quantity contains up to 50 t of lactose as the main carbon ingredient in whey. Just in the northern Italy, where a number of large dairies are located, about 1 million liters of whey have to be disposed off daily. This is often accomplished with a direct release of untreated whey into the aquatic environments.

Hence, it was reasonable to design an integral process for the PHA production from the surplus whey including the following steps:[24]

- Set-up of the optimized upstream technology for the feedstock whey
- Set-up of the optimized PHA-formation conditions with the selected microbial strains using the whey lactose as a carbon source
- Set-up of the biotechnological strategy for triggering the polymer composition as a tool for fine-tuning PHA properties
- Optimization of the downstream strategy for a PHA recovery
- Detailed product characterization
- Economic and ecological appraisal of the entire process and its steps
- Evaluation of the applications of the products

It is obvious that the discussed points can only be achieved, if there are intense interactions between the experts in different scientific fields: microbiology (a search for the ideal microbial production strain), biotechnology (the fermentation technology as the core part), chemical engineering (tailor-made downstream processing, design of industrial plant), polymer science (an on-going characterization of the products), and life-cycle assessment (LCA).

Within the FP5 Growth Program of the EU, the WHEYPOL project realized these ideas between 2001 and 2004. The demanded interactions between different research areas were put into practice with the formation

of a network consisting of seven scientific groups and three industrial partners each specialized in a certain field needed for the process development.

In a study that was accomplished within the WHEY-POL project, Koller and colleagues[27] compare the potential of three prokaryotic wild-type strains for the utilization of whey as carbon feedstock for the PHA production. In this work the archaeon *Haloferax mediterranei* and the eubacterial strains *Pseudomonas hydrogenovora* and *Hydrogenophaga pseudoflava* were investigated in bioreactors on the laboratory scale.

Among these organisms, *Haloferax mediterranei* turned out to be the most promising candidate for an eventual industrial-scale PHA production using whey. This is due to the strain's high robustness and stability; the risk of microbial contamination during the cultivation is restricted to the absolute minimum, thus a lot of energy can be saved with lower sterility demands. Additionally, the strain produces a P(3HB-*co*-8 %-3HV) co-polyester directly from the 3HV-unrelated carbon-source whey, avoiding the costs for odd-numbered acids as the 3HV-related precursors.[33] The strain grew well on hydrolyzed whey permeate with the maximum specific growth rate μ_{max} of 0.11 1/h. PHAs were accumulated at the maximum specific production rate of 0.08 g/(g h). The conversion yield for whey sugar to PHA amounted to 0.33 g/g. After a further optimization of the production conditions, the productivity of this strain on hydrolyzed whey permeate was increased to 0.09 g/(L h) (the specific rate of 0.15 g/(g h); 16.8 g/L of biomass containing 73 % of PHAs were finally obtained. By co-feeding the precursors for 3HV and 4HB production (pentanoic acid and γ-butyrolactone, respectively), together with whey permeate as the main carbon source, a high value P-(3HB-*co*-21.8 %-3HV-*co*-5.1 %-4HB) terpolyester was completed by *Haloferax mediterranei*. A detailed characterization of thermal properties and molecular-mass distribution of the materials was accomplished; the results for polymer characterization indicate that the materials might be of special interest for application in the medical field. The partial conversion of whey sugars to 3HV units and the excellent polymer characteristics (low melting temperature, high molecular masses within a narrow distribution), together with a simple recovery of PHAs from the cells, make the strain especially interesting. The estimated production price amounted to € 2.82 per kg of PHAs. For a further process improvement, the recycling of the highly saline side streams should be tested and optimized.[27,28]

P. hydrogenovora features the disadvantages of low final polymer contents, low productivity and product yields due to a redirection of the carbon flux towards unwanted by-products such as various organic acids. Using this organism, the final PHB homopolyester content amounted to the mass fraction 12 % (qp: 2.9 mg/(g h)). By co-feeding the 3HV-releated precursor pentanoate, the strain accumulated 12 % of poly-3(HB-*co*-21%-HV) (qp: 2.0 mg/(g h)).[28,34]

The research showed that *H. pseudoflava* produces PHAs of a rather good quality (high molar masses of M_w = 859 MDa and low polydispersities of 3.3) from whey at acceptable specific production rates and yields, but is not competitive with *H. mediterranei* in terms of strain stability and robustness. In detail, using this strain, 40 % of poly-3(HB-*co*-5 %-HV) in the cells with an addition of pentanoic acid (qp: 12.5 mg/(g h)) was obtained. Without the pentanoic acid, the strain accumulated 30 % of the homopolyester PHB in the cells (qp: 16.0 mg/(g h)).[28]

5 CASE STUDY 2: SLAUGHTERING WASTE FOR THE PHA PRODUCTION

Animal lipids from slaughtering and animal-processing industries in Europe amount to more than 500000 t per year. It is estimated that using this waste stream for biodiesel production through transesterification results in 50000 t of saturated biodiesel (SFAE) fraction. SFAE causes problems in fuel mixtures due to its precipitation at a low temperature, which may result in filter plugging. Using SFAE as a carbon feed stock, 35000 t of PHAs can theoretically be produced annually (a yield of 0.7 g of PHAs per g of SFAE). Considering the entire amount of biodiesel that is currently produced in the EU-25 (about 22 Mt), approximately 2 Mt of glycerol phase (CGP) are available as the major by-product of the conversion of lipids to biodiesel. This is in considerable excess over the quantities of the glycerol needed for its various classical applications. If applied in the production of microbial PHA-accumulating biomass, one can expect more than 0.4 g of biomass or PHAs per gram of glycerol. Regarding the entire quantity of glycerol from the animal-lipid transesterification, one can estimate that more than 20000 t of PHA-rich biomass can be produced annually. These amounts are shown in **Figure 3**.

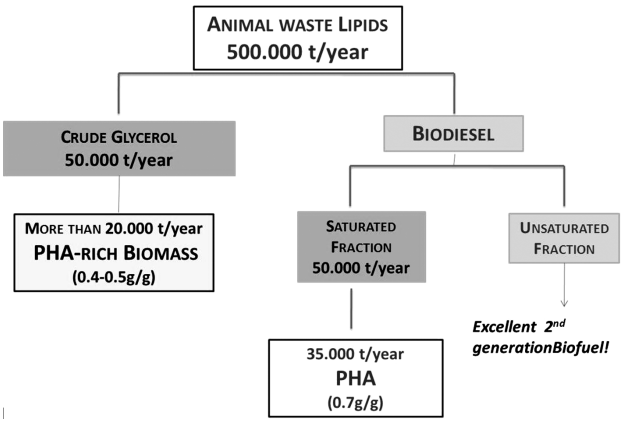

Figure 3: Amounts of available animal-waste lipids, and the potential PHA production

Slika 3: Količina razpoložljivih živalskih lipidov in mogoča proizvodnja PHA iz njih

In 2010, the project "Biotechnological conversion of carbon-containing wastes for eco-efficient production of high-added value products", acronym ANIMPOL, was launched and funded through the FP7 of the EU.

Within this project, a sound industrial process for the conversion of lipid-rich animal waste from the meat processing industry into biodiesel is being developed using innovative methods. Saturated biodiesel fractions have a negative effect on biodiesel fuel properties, are separated and, subsequently, used as feedstock for the biotechnological production of PHAs. The remaining unsaturated biodiesel fraction performs as an excellent 2nd generation biofuel. The significance of the project is obvious considering the high quantities of animal-derived waste in Europe. The project brings together partners managing waste resources from slaughter-houses, the rendering industry, biodiesel production, as well as the polymer-processing industry.

Experimentally, the most promising results for the PHA production from the animal-waste-derived SFAE are obtained by using *Cupriavidus necator*, a well-known wild-type strain from the Burkholderiaceae family. Fast microbial growth, satisfying cell densities, and high volumetric productivities of PHA homo- and co-poly-esters, together with promising material characteristics, were obtained.

Figure 4 illustrates the fermentation pattern of the laboratory bioreactor-scale production of PHB with *C. necator* using SFAE as the main carbon source. This fermentation was accomplished by using SFAE as the sole carbon source for both the biomass growth and the PHA accumulation in the fed-batch cultivation mode (a repeated supply of SFAE according to its conversion by the cells). The maximum of 28.0 g/L of PHAs was obtained, corresponding to the PHA share in a cell's dry mass that is 80.3 %. The specific growth rate of the

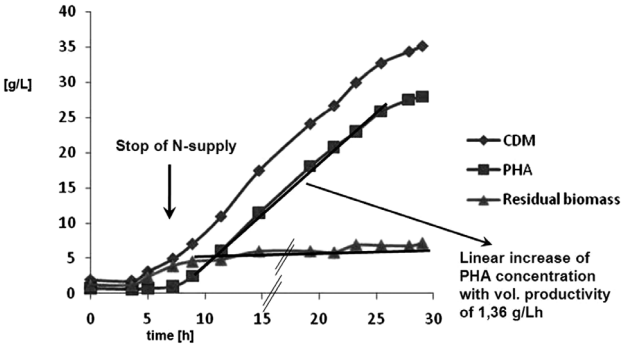

Figure 4: Fermentation pattern for the poly-(3HB-*co*-0.84 %-3HV) production with *C. nector* on SFAE. The arrow at t = 7 h indicates the limitation of the nitrogen supply. Parallel lines at the time axis and the time curve for residual biomass indicate the end of the microbial growth after the nitrogen depletion, provoking the redirection of the intracellular carbon flow towards the PHA accumulation.

Slika 4: Model fermentacije za poli-(3HB-*co*-0,84 %-3HV) proizvodnjo s *C. nector* na SFAE. Puščica pri t = 7 h kaže omejitev dobave dušika. Vzporedne linije na časovni krivulji za preostalo biomaso kažejo na konec mikrobne rasti po izčrpanju dušika, kar spodbudi preusmeritev toka medceličnega ogljika proti kopičenju PHA.

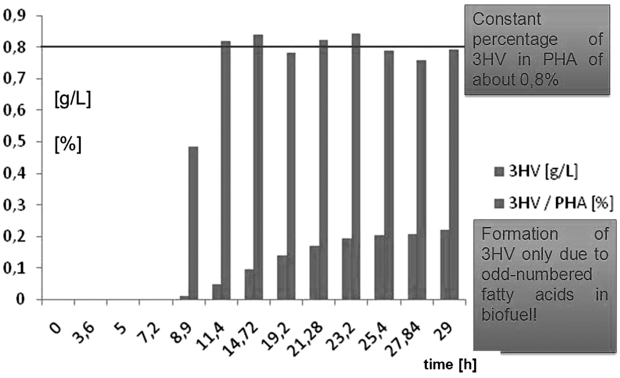

Figure 5: Poly-(3HB-*co*-0.84 %-3HV) production with *C. nector* on SFAE: composition of the polyester (small bars) and 3HV concentration (high bars) during the process

Slika 5: Proizvodnja poly-(3HB-*co*-0,84 %-3HV) s *C. nector* na SFAE: sestava poliestra (mali stolpci) in koncentracija 3HV (veliki stolpci) med postopkom

production strain amounted to 0.17 L/h. Especially the yield of the biomass production from SFAE of more than 0.6 g of CDM per g of SFAE is exceptionally high if compared to the well-known PHA substrates like sugars, where the theoretical yield does not exceed 0.48 g/g. This is due to the metabolic background of fatty acid catabolism of the cells. Considering the early stage of the process development, the high volumetric PHA productivity of 0.94 g/(L h) for the entire process can also be considered very promising if compared to the available data for the industrial PHA production from expensive substrates. Taking into account only the phase of the predominant PHA accumulation after nitrogen limitation, volumetric productivity was as high as 1.36 g/(L h). Regarding the specific volumetric productivity during nitrogen-limited conditions, the value of 0.19 g/(g h) was calculated. This is significantly higher than the values reported before for the utilization of whey lactose. During this phase, residual biomass (NPCM) concentration remained constant at about 7 g/L (see **Figure 4**). In addition, the produced PHA was a poly-(3HB-*co*-0.84 %-3HV) copolyester; here, odd-numbered fatty acids in SFAE acted as 3HV-related precursor substrates. The composition of the polyester during the fermentation and the concentration of 3HV in the fermentation broth are illustrated in **Figure 5**. It is well visible that, due to the identical composition of the added SFAE during the entire process, the share of 3HV in PHA (about 0.8 %) is constant during the phase of nitrogen limitation.

6 CONCLUSIONS

The study presents strategies for upgrading industrial wastes like surplus whey and residues from the slaughtering and biodiesel industries to feedstocks for biopolymer production. This approach can be regarded as a promising route for making the entire PHA-biopolymer-production process economically competitive. The selection of the discussed raw materials

is especially important to provide European industry with an advantage, on the one hand, to handle tremendous waste streams through a value-added conversion, and, on the other hand, to break new ground in developing and commercializing bio-polymeric materials.

Uniting the potential enhancements of each process step, one can make substantial progress towards an environmentally benign and cost-efficient technology. The development of efficient biopolymer-production processes needs a close cooperation between the experts from industry and different scientific fields; hence, a multidisciplinary approach is required. Decision makers from companies, chemical engineers, microbiologists, enzymologists, polymer scientists, genetic engineers, and the experts involved in LCA and the Cleaner Production studies have to join their respective expertise. Such an approach has a potential to close the existing gaps between the success achieved on the laboratory scale that, in most cases, affects only singular aspects of the biopolymer production, and the final success of competitive bio-plastics on the market.

Regardless of the selected microbial production strain, the facilities for the PHA production from whey and animal-derived waste should be integrated into the existing process lines of large dairies or biodiesel companies, where the raw material actually accrues. This can be considered as a viable strategy for minimizing the production costs by taking profit through the synergistic effects.

Due to the environmental considerations and expected shortage of fossil reserves, the increasing global demand for bio-plastics in the future is generally undisputed. Available data about the laboratory-scale developments shows a significant progress in combining the environmental benefit of the future-oriented bio-polyesters with the economic viability of their production. This development will hopefully facilitate the decisions of responsible policy-makers from various renewable waste-generating industries and from the polymer industry to break new ground in a sustainable production. If successfully implemented, these seminal biopolymers will be decoupled from the manufacturing, where biopolyester and biofuel syntheses compete with human nutrition, frequently lacking consideration of environmental requirements and acceptable human working conditions.

Acknowledgement

The authors gratefully acknowledge the support of the European Commission in the projects *WHEYPOL* (GRD2-2000-30385) and *ANIMPOL* (Contract No: 245084). Furthermore, the authors are thankful for the STEM picture of *C. necator* provided by Dr. Elisabeth Ingolić, FELMI-ZFE Graz.

7 REFERENCES

[1] A. Kržan, S. Hemjinda, S. Miertus, A. Corti, E. Chiellini, Standardization and certification in the area of environmentally degradable plastics, Polymer Degradation and Stability, 91 (**2006**), 2819–2833

[2] M. Koller, A. Salerno, A. Reiterer, H. Malli, K. Malli, K. H. Kettl, M. Narodoslawsky, H. Schnitzer, E. Chiellini, G. Braunegg, Sugarcane as feedstock for biomediated polymer production, In: J. F. Goncalves (ed.), Sugarcane: Production, Cultivation and Uses, 1st ed., Nova Science Publishers, Inc., 2012

[3] M. Koller, A. Salerno, M. Miranda de Sousa Dias, A. Reiterer, G. Braunegg, Modern biotechnological polymer synthesis: a review, Food Technology and Biotechnology, 48 (**2010**) 3, 255–269

[4] K. Sudesh, T. Iwata, Sustainability of biobased and biodegradable plastics, Clean, 36 (**2008**) 5–6, 433–442

[5] M. Titz, K. H. Kettl, K. Shahzad, M. Koller, H. Schnitzer, M. Narodoslawsky, Process optimization for efficient biomediated PHA production from animal-based waste streams, Clean Technologies and Environmental Policy, 14 (**2012**), 495–503

[6] Y. B. Kim, R. W. Lenz, Polyesters from microorganisms, Advances in Biochemical Engineering/Biotechnology, 71 (**2001**), 51–79

[7] J. Helm, K. D. Wendlandt, M. Jechorek, U. Stottmeister, Potassium deficiency results in accumulation of ultra-high molecular weight poly-beta-hydroxybutyrate in a methane-utilizing mixed culture, Journal of Applied Microbiology, 105 (**2008**) 4, 1054–61

[8] G. Braunegg, G. Lefebvre, K. F. Genser, Polyhydroxyalkanoates, biopolyesters from renewable resources: physiological and engineering aspects, Journal of Biotechnology, 65 (**1998**) 2–3, 127–161

[9] M. Koller, I. Gasser, F. Schmid, G. Berg, Linking ecology with economy: insights into polyhydroxyalkanoate-producing microorganisms, Engineering in Life Sciences, 11 (**2011**) 3, 222–237

[10] N. Jacquel, C. W. Lo, Y. H. Wei, H. S. Wu, S. S. Wang, Isolation and purification of bacterial Poly(3-Hydroxyalkanoates), Biochemical Engineering Journal, 39 (**2008**) 1, 15–27

[11] C. S. K. Reddy, R. Ghai, K. V. C. Rashmi, Polyhydroxyalkanoates: an overview, Bioresource Technology, 87 (**2003**), 137–146

[12] S. Khanna, A. K. Srivastava, Recent advances in microbial Polyhydroxyalkanoates, Process Biochemistry, 40 (**2005**), 607–619

[13] Q. Ren, A. Grubelnik, M. Hoerler, K. Ruth, R. Hartmann, H. Felber, M. Zinn, Bacterial poly(hydroxyalkanoates) as a source of chiral hydroxyalkanoic acids, Biomacromolecules, 6 (**2005**), 2290–2298

[14] C. Q. A. Chen, Microbial polyhydroxyalkanoates (PHA) based bio- and materials industry, Chemical Society Review, 38 (**2009**), 2434–2446

[15] D. K. Y. Solaiman, R. D. Ashby, T. A. Foglia, W. N. Marmer, Conversion of agricultural feedstock and co-products into poly(hydroxyalkanoates), Applied Microbiology and Biotechnology, 71 (**2006**) 6, 783–789

[16] M. S. Khardenavis, S. N. Kumar, T. Mudliar, Biotechnological conversion of agro-industrial wastewaters into biodegradable plastic, poly-ß-hydroxybutyrate, Bioresource Technology, 98 (**2007**), 3579–3584

[17] B. Kunasundari, K. Sudesh, Isolation and recovery of microbial polyhydroxyalkanoates, eXPRESS Polymer Letters, 5 (**2011**) 7, 620–634

[18] H. O. Kim, Y. J. Wee, J. N. Kim, J. S. Yun, H. W. Ryu, Production of lactic acid from cheese whey by batch and repeated batch cultures of *Lactobacillus* sp. RKY2, Applied Biochemestry and Biotechnology, 129 (**1995**), 694–704

[19] W. S. Ahn, S. J. Park, S. Y. Lee, Production of Poly(3-Hydroxybutyrate) by Fed-Batch Culture of Recombinant Escherichia coli with a Highly Concentrated Whey Solution, Applied Environmental Microbiology, 66 (**2000**) 8, 3624–3627

[20] R. V. Nonato, P. E. Mantelatto, C. E. V. Rossell, Integrated production of biodegradable plastic, sugar and ethanol, Applied Microbiology and Biotechnology, 57 (**2001**), 1–5

[21] M. Zinn, H. U. Weilenmann, R. Hany, M. Schmid, T. Egli, Tailored synthesis of poly([R]-3-hydroxybutyrate-co-3-hydroxyvalerate) (PHB/HV) in *Ralstonia eutropha* DSM 428, Acta Biotechnology, 23 (**2003**), 309–316

[22] Z. Sun, J. A. Ramsay, M. Guay, B. A. Ramsay, Fermentation process development for the production of medium-chain-length poly-3-hydroxyalkanoates, Applied Microbiology and Biotechnology, 75 (**2007**), 475–485

[23] A. Atlic, M. Koller, D. Scherzer, C. Kutschera, E. Grillo Fernandes, P. Horvat, E. Chiellini, G. Braunegg, Continuous production of Poly([(R]-3-hydroxybutyrate) by *Cupriavidus necator* in a multistage bioreactor cascade, Applied Microbiology and Biotechnology, 91 (**2011**), 295–304

[24] M. Koller, R. Bona, G. Braunegg, C. Hermann, P. Horvat, M. Kroutil, J. Martinz, J. Neto, P. Varila, L. Pereira, Production of polyhydroxyalkanoates from agricultural waste and surplus materials, Biomacromolecules, 6 (**2005**), 561–565

[25] S. P. Ouyang, Q. Liu, L. Fang, G. Q. Chen, Construction of pha-operon-defined knockout mutants of *Pseudomonas putida* KT2442 and their applications in Poly(hydroxyalkanoate) production, Macromolecular Bioscience, 7 (**2007**) 2, 227–233

[26] G. Q. Chen, Plastics completely synthesized by bacteria: Polyhydroxyalkanoates, in: Plastics from Bacteria, Natural Functions and Applications, Microbiology Monographs, 14 (**2010**), 17–38

[27] M. Koller, P. J. Hesse, R. Bona, C. Kutschera, A. Atlic, G. Braunegg, Biosynthesis of high quality polyhydroxyalkanoate co- and terpolyesters for potential medical application by the Archaeon *Haloferax mediterranei*, Macromolecular Symposia, 253 (**2007**), 33–39

[28] M. Koller, P. J. Hesse, R. Bona, C. Kutschera, A. Atlic, G. Braunegg, Various Archae- and Eubacterial Strains as Potential Polyhydroxyalkanoate Producers from Whey Lactose, Macromolecular Bioscience, 7 (**2007**), 218–226

[29] E. Chiellini, P. Cinelli, F. Chiellini, S. H. Imam, Environmentally degradable bio-based polymeric blends and composites, Macromolecular Biosciences, 4 (**2004**) 3, 218–231

[30] M. Pietrini, L. Roes, M. K. Patel, E. Chiellini, Comparative life cycle studies on Poly(3-hydroxyalkanoate)-based composites as potential replacement for conventional petrochemical plastics, Biomacromolecules, 8 (**2007**), 2210–2218

[31] P. M. R. Guimarães, J. A. Teixeira, L. Domingues, Fermentation of lactose to bio-ethanol by yeasts as part of integrated solutions for the valorisation of cheese whey, Biotechnology Advances, 28 (**2010**), 375–384

[32] M. Viñas, L. Borzacconi, J. Martínez, Anaerobic treatment of yeast manufacturing wastewater in UASB reactors, Environmental Technology, 15 (**1994**), 79–85

[33] E. Žagar, A. Kržan, Distribution Dependence on Molar Mass in Microbial Poly(3-hydroxybutyrate-co-3-hydroxyvalerate) copolyesters, Acta Chimica Slovenica, 56 (**2009**) 2, 386–391

[34] M. Koller, R. Bona, E. Chiellini, E. Grillo Fernandes, P. Horvat, C. Kutschera, P. J. Hesse, G. Braunegg, Polyhydroxyalkanoate production from whey by *Pseudomonas hydrogenovora*, Bioresource Technology, 99 (**2008**), 4854–4863

UDK 669.715:620.28
Review article/Pregledni članek

ISSN 1580-2949
MTAEC9, 47(1)13(2013)

CHALLENGES AND ADVANTAGES OF RECYCLING WROUGHT ALUMINIUM ALLOYS FROM LOWER GRADES OF METALLURGICALLY CLEAN SCRAP

RECIKLIRANJE GNETNIH ALUMINIJEVIH ZLITIN IZ NIZKOCENOVNIH VRST METALURŠKO ČISTEGA ODPADNEGA ALUMINIJA

Varužan Kevorkijan

Impol R&R, d. o. o., Partizanska 38, 2310 Slovenska Bistrica, Slovenia
varuzan.kevorkijan@impol.si

Prejem rokopisa – received: 2012-09-05; sprejem za objavo – accepted for publication: 2012-09-25

In the recycling of wrought aluminium alloys from lower grades of scrap (metallurgically clean but highly contaminated with non-metallic impurities) the following two tasks were identified as the most demanding: (i) achieving the required final chemical composition of an alloy with a minimal addition of primary aluminium and alloying elements; and (ii) keeping the level of impurities (inclusions, hydrogen, trace elements and alkali metals) in the molten metal below the critical level. Because of the lack of chemically based refining processes for reducing the concentration of alloying and trace elements in the molten aluminium, once the concentrations of these constituents in the melt exceed the corresponding concentration limits, the only practical solution for their reduction would be an appropriate dilution with primary metal. To avoid such a costly correction, carefully predicting and ensuring the chemical composition of the batch in the pre-melting stage of casting should be applied. Fortunately, some of the impurities, like hydrogen and alkali metals, as well as various (mostly exogeneous) inclusions, could be successfully reduced by employing existing refining procedures.

In this work, (i) the state-of-the-art technologies, including some emerging technical topics such as the evolution of wrought alloys toward scrap-intensive compositions, monitoring of the content of organics in the incoming scrap and the quality of molten metal achieved by different smelting and refining technologies, and (ii) the relevant economic advantages of the recycling of wrought aluminium alloys from the lower grades of scrap are reported. By analyzing the market prices of various grades of scrap and the total cost of their recycling, the cost of aluminium ingots made from recycled aluminium was modelled as a function of aluminium and the alloying-element content in the incoming scrap. Furthermore, scrap mixtures for producing aluminium wrought alloys of standard quality from lower grades of scrap and with a significant new added value were illustrated.

Keywords: wrought aluminium alloys, recycling, low grades of aluminium scrap, quality of recycled metal, economic benefits

Pridobivanje recikliranega aluminija standardne kakovosti iz nizkocenovnih virov bo v prihodnje odločilno vplivalo na konkurenčnost in uspešnost evropske aluminijske industrije. Pri recikliranju gnetnih aluminijevih zlitin iz nizkocenovnih vrst odpadnega aluminija (metalurško čistih, vendar onesnaženih z nekovinskimi nečistočami) sta posebej zahtevni naslednji dve tehnološki nalogi: (i) zagotavljanje želene kemijske sestave aluminijeve zlitine ob minimalnem dodatku primarnega aluminija in legirnih elementov in (ii) ohranjanje nivoja nečistoč (vključkov, vodika, elementov v sledovih in alkalijskih kovin) v talini v mejah dovoljenega. Ker koncentracijo legirnih elementov in elementov v sledovih v talini tehnološko ni mogoče spreminjati s kemijskimi postopki rafinacije, je, brž ko njihova koncentracija preseže dovoljeno mejo, edina rešitev redčenje z dodatkom primarnega aluminija. Tovrstnemu dragemu načinu zagotavljanja predpisane kemijske sestave taline se lahko izognemo le z doseganjem želene kemijske sestave pred taljenjem, tj. na stopnji načrtovanja vhodne zmesi. Preostale nečistoče, kot so npr. vodik in alkalijske kovine ter nekateri vključki (predvsem primarni), lahko uspešno obvladujemo že s sedanjimi postopki rafinacije taline, ki jih tu opisujemo.

V tem delu tudi opisujemo (i) sodobne tehnološke postopke načrtovanja recikliranju prijaznih sestav gnetnih aluminijevih zlitin s povečanim deležem odpadnega aluminija, spremljanja koncentracije organskih nečistoč v vhodnem odpadnem aluminiju ter določanja kakovosti taline, pridobljene z različnimi postopki taljenja in rafinacije, in ugotavljamo (ii) ekonomske prednosti proizvodnje gnetnih aluminijevih zlitin z recikliranjem metalurško čistega odpadnega aluminija nižjega cenovnega razreda. Izhajajoč iz sestave in cen različnih vrst odpadnega aluminija ter stroškov njihovega recikliranja nam je uspelo razviti funkcionalni model, ki določa ekonomičnost proizvodnje ingotov iz recikliranega aluminija na osnovi vsebnosti aluminija in legirnih elementov v vhodnem materialu. Model smo aplicirali na različne vrste nizkocenovnega odpadnega aluminija in pokazali, da proizvodnja gnetnih zlitin standardne kakovosti iz tovrstnih virov zagotavlja najvišjo mogočo dodano vrednost.

Ključne besede: gnetne aluminijeve zlitine, recikliranje, nizkocenovne vrste odpadnega aluminija, kakovost recikliranih zlitin, ekonomske prednosti

1 INTRODUCTION

In recent years recycling of low-grade scrap has become an increasingly important issue of the metal supply for both casting and wrought alloys. Looking to the future, the production of recycled aluminium of standard quality from the cheapest sources will play an increasingly significant role in the growth of the European aluminium industry. Despite the economic slowdown, the consumption of primary aluminium in the EU is expected to increase (to 8 Mt by 2012), while the European production of primary aluminium is expected to decrease (gradually down to 2.86 Mt by 2012). The gap between the expected production of primary aluminium and its consumption (of about 5.24 Mt) will be covered by the imports and recycling inside the EU.

At the same time, the continuous increase in the relative proportion of recycled- vs. primary-aluminium sources will be driven by the pressure to improve business results and striving for individual profit maximisation. Additional very important benefits of recycling aluminium from low-grade scrap are: (i) spreading the risk of a potential shortage of raw materials by diversifying the supply sources of aluminium away from exclusively primary metal and clean scrap suppliers; and (ii) an improvement in the logistics – ensuring an appropriate and cost-effective supply from different scrap sources. Other advantages of recycling low grades of aluminium scrap are the additional energy savings and a higher compositional flexibility in combination with clean grades of scrap and dross.

For several decades, a kind of belief existed in the aluminium industry that the standard quality of wrought alloys could be achieved only by combining sufficient amounts of primary aluminium, internal scrap and only clean, well-sorted external scrap. Consequently, ingots made from primary aluminium, internal scrap and clean industrial, or external, old scrap (a single wrought alloy with the mass fraction less than 2 % of non-metallic impurities) were obligatory in the mass production of wrought alloys as the only source of the new and recycled aluminium capable of assuring the standard quality of end products.

Scrap for the production of wrought alloys should be sorted with a strict control of the concentration of alloying elements in order to achieve the prescribed compositional tolerances[1–12]. An additional problem is caused by a very limited ability of wrought alloys to tolerate the elements not normally present in their composition. In other words, well-defined wrought scrap of a proper composition can be effectively remelted into a wrought alloy of the same composition, but it is very demanding to achieve a new wrought composition with direct reuse, without an addition of the primary metal and alloying elements. An addition of primary aluminium is necessary to dilute impurities (the elements not normally present in a wrought alloy) to an acceptable level, while the alloying elements are added, if necessary, for the correction of their concentration. Thus, most of the external scrap inside the EU (above 60 %) is preferably applied in the production of casting alloys and only the remainder is dedicated to remelting.

Although non-metallic impurities can also significantly influence the quality of the molten metal, it is not obligatory that the scrap for wrought alloys should be clean, without any organic and other non-metallic impurities, if these could be effectively removed before or during the recycling procedure. Some of the advanced melting furnaces, such as various rotary or multi-chamber units, allow direct melting of highly contaminated scrap (e.g., painted and lacquered scrap) with the thermal de-coating and the consequent recycling.

Moreover, in the internal technical documentation for the production of wrought alloys, more or less empirical compositions were often established, resulting in the production mixtures with the prescribed amounts of primary aluminium, internal, industrial external and old external scrap. However, it is important to note that such empirical compositions are usually adapted to the common availability of various raw materials and in many cases these are ***below the real potential of a possible replacement*** of primary aluminium with scrap without influencing the standard quality of the final products. The problem is that in many cases these empirical compositions are also approved by the customers, becoming, in that way, a contractual obligation of a producer of the alloys.

On the other hand, it is well known that for aluminium alloys (especially wrought alloys) a practical "compositional-tolerance limit" exists and a fairly complete knowledge of these tolerance limits for all the elements is needed, especially in the recycling operations where unexpected and unusual impurities can creep in inadvertently, and even normal impurities may tend to accumulate and build up to a disastrous degree. In most cases, the influence of these tolerance limits for various elements and various combinations of the elements on the properties (and particularly on the selected properties) of wrought alloys is not well investigated. Because of that, customers often require ***more narrow compositional tolerances*** than necessary, creating unnecessary losses for themselves and the casting house. Customers lose an important part of the competitiveness of their products in downstream business activities by paying more for non-optimal tolerance limits and, at the same time, a casting house loses the added value by producing alloys from more expensive inputs.

As an example, the average new added value created by producing wrought alloys from external contaminated scrap is about 7 % of LME. For the aluminium dross in the form of pressed skulls the new added value is significantly higher and can reach approximately one third of LME (considering pressed skulls as internal scrap).

2 DIFFICULTIES IN RECYCLING THE EXISTING WROUGHT ALUMINIUM ALLOYS

As already mentioned, the main difficulty in the production of wrought aluminium alloys from scrap is to achieve the proper chemical composition of a melt with a minimum addition of primary aluminium and alloying elements. Technically, the problem is in the missing technology (an economically acceptable, chemically based refining process) for reducing the concentration of the critical allying elements, such as copper, iron, manganese, silicon and zinc, in a melt batch produced from various sorts of scrap. Once the concentration of these critical elements in a melt is above the concentration

limit for a particular wrought alloy, the only practical solution would be their dilution by primary metal. Another technical solution is to avoid an incorrect melt composition by carefully predicting and assuring the chemical composition of the batch in a pre-melting stage of casting. In principle, there is also the third solution: to convince the customers to accept the so-called "recycling-friendly wrought alloys" – in other words, the alloys with broad compositional-tolerance limits and, consequently, to some extent, a different quality-to-cost ratio. This could be an important future trend in developing new wrought alloys, working hand in hand with customers in the implementation of their requirements for scrap-friendly compositions[1–4], but for the existing alloys and existing customer demands such an approach has definitely quite a limited potential and it is also too risky.

In most of the current plants, the predominant mode of recycling – a more accurate scrap blending or a very strict melt dilution – is decided on the basis of the margin between recycled metal and primary aluminium. However, it is important to note that this margin – the difference between the price of primary aluminium (which is determined globally) and the price of recycled metal (which is calculated locally) – is affected by internal and external circumstances. Among internal factors the most important are: (i) permanent and stable sources of new and old scrap, concentrated sufficiently in one area to justify the cost of collecting; (ii) a scrap-collecting and sorting infrastructure including devices for removing impurities and delivery to a recycling plan; (iii) a method of recycling that is economically competitive with the production of primary aluminium and (iv), a market willing to accept the composition and the quality of wrought alloys made from scrap.

More expensive, clean and sorted scrap (mainly new or industrial scrap) contains a minimum concentration of critical elements, while in the old scrap of a lower cost it becomes more critical.[13] In typical municipal old scrap, which is a cost-effective source of aluminium, the minimal concentration of critical elements (silicon, iron, copper, manganese, zinc, magnesium) is typically too high for direct remelting into wrought compositions without a dilution by primary aluminium (**Table 1**).

Table 1: Typical concentrations of the main alloying elements in the municipal old scrap[13]
Tabela 1: Običajne koncentracije najpogostejših legirnih elementov v komunalnem odpadnem aluminiju[13]

Element	Concentration (%)
Fe	0.60–1.00
Si	0.30–9.00
Cu	0.25–4.00
Mn	0.60–1.50
Zn	0.25–3.00
Mg	0.20–2.00
Cr	0.05–0.30
Ni	0.04–0.30
Pb	0.02–0.25
Sn	0.02–0.30
Bi	0.02–0.30
Ti	0.05–0.25

On the other hand, in the new scrap resulting from collecting and/or treating the metal that forms during the production of aluminium products before these are sold to the final users, the right alloy composition is assured in advance; however, the cost of such scrap is significantly higher and its availability is usually limited to closed production loops.

3 ECONOMICS OF RECYCLING CONTAMINATED WROUGHT ALUMINIUM SCRAP

The economics of recycling wrought aluminium alloys from scrap is specific and differs from the economics of recycling cast alloys, since cast alloys have higher compositional-tolerance limits for impurities and can absorb a wider variety of scrap. During the production of cast alloys from scraps of various compositions, refiners are able to add alloying elements and remove certain unwanted elements after the melting process. Cast alloys tend to have higher alloy content than wrought alloys and because of that they are difficult to recycle into anything other than cast alloys, since the removal of most alloying elements from the molten aluminium would be impractical. On the other hand, wrought scrap cannot be used for the production of new wrought alloys unless separated by alloys or alloy groups and/or diluted with an addition of primary metal.

In this regard, a possible way of improving the recycling of wrought aluminium alloys is the use of new and old scrap with higher amounts of organic impurities. Most aluminium scrap mixtures currently used for the production of wrought aluminium alloys from low-grade scrap have an organic-impurity content in the mass fraction lower than 8 %. The most common organic impurities are oils, polymers such as polyester and epoxy, rubber, lacquers, paints, etc. In some heavily contaminated aluminium scrap, the organic-impurity level exceeds 18–20 %, while in the clean industrial scrap the non-aluminium impurity level is usually less than 2 %. The main reasons to start using contaminated instead of clean scrap for the production of wrought aluminium alloys are the improved added value (a net-profit surplus achieved per weight unit of aluminium or aluminium alloys of the standard quality recycled from the low-quality aluminium scrap) and better logistics (scrap sourcing, availability on the market and improved supply flexibility). The key advantage is the fact that the cost of contaminated scrap is significantly lower than the cost of clean scrap of the same pre-sorting quality (e.g., a single alloy or a single-series grade), in that way providing an opportunity for producing aluminium wrought alloys of the standard quality and with

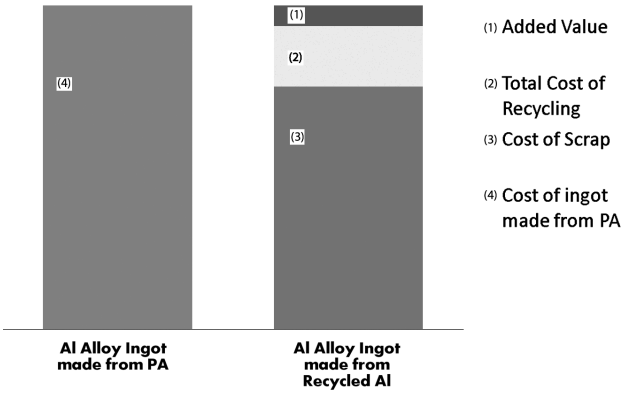

Figure 1: Structure of the cost of Al ingots made from recycled aluminium
Slika 1: Struktura cene Al-ingotov, izdelanih iz recikliranega aluminija

improved competitiveness. The prerequisite for this lies in an appropriate performance of the entire recycling process, from the scrap sourcing and purchasing strategy to the complete recovery of all the by-products, in order to achieve the standard quality of the recycled aluminium and the proper economy. In practice, irrespective of the fact that the recycling of contaminated scrap is more demanding and costly than the remelting of clean scrap, the total cost per weight unit of recycled aluminium or aluminium alloy of the standard quality produced from contaminated scrap is lower than the cost of remelted aluminium or an Al-alloy counterpart produced from clean scrap that is nowadays much in demand for the production of wrought alloys, **Figures 1** and **2**.

As a rule, clean scrap (e.g., the scrap with a minimum of 98 % of Al) represents a costly raw material for the production of wrought alloys. Its market price is close to the one theoretically expected, calculated according to the aluminium content and the cost of recovery. Therefore, the usage of clean scrap in the production of wrought alloys provides only limited possibilities for creating a new added value or, in other words, for lowering of the cost of the input. Typically, the market prices for clean scrap of a single wrought alloy vary slightly below or above the price of the counterpart ingots, depending on their market availability[14,15] (**Table 2**).

On the contrary, the market price of contaminated scrap (the scrap with, e.g., 80 % of Al and 20 % of non-metallic, mostly organic impurities) ranges significantly (10–25 %) below the theoretically expected price based on the aluminium content and the cost of recovery[14,15] (**Table 2**).

Thus, taking into account the cost of recycling and all the related costs, the total cost of producing recycled aluminium alloy fabricated from clean scrap is usually close to the cost of melting the same alloy from primary aluminium (including the cost of the appropriate alloying elements). In contrast to that, by using less-clean scrap (the scrap contaminated with organic impurities) and applying the proper recycling technology, a higher net

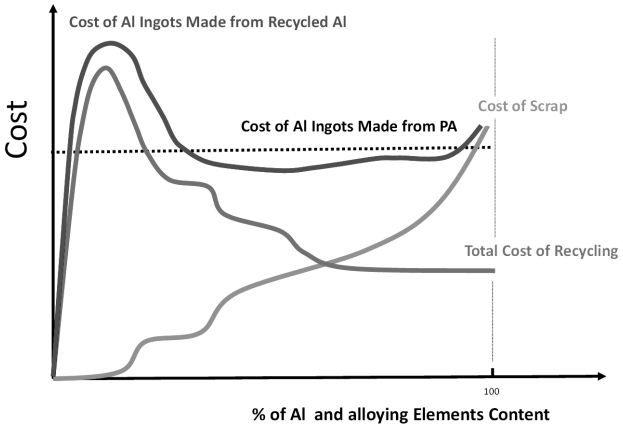

Figure 2: Cost of aluminium ingots made from recycled aluminium as a function of aluminium and alloying-element content in the incoming scrap
Slika 2: Spreminjanje cene aluminijevih ingotov, izdelanih iz recikliranega aluminija, v odvisnosti od vsebnosti aluminija in legirnih elementov v vhodnem odpadnem aluminiju

Table 2: Composition and average price* of selected scrap types[14,15]
Tabela 2: Struktura in povprečna cena* izbranih vrst odpadnega aluminija[14,15]

Scrap description	Aluminium content (%)	Oxides (%)	Foreign material (%)	Average price (% LME)
One single wrought alloy	97.2	1.0	1.8	95–99
Two or more wrought alloys of the same series	97.2	0.8	2.0	80–85
Used beverage cans	94	0.8	5.2	55–60
End of profiles with a thermal bridge (one single wrought alloy)	78	3.8	18.2	55–70
Turnings, one single alloy	95.3	3.7	1.0	80–85
Mixed turnings, two or more alloys	84.0	3.3	12.8	75–80
Packaging (coated)	71.5	3.8	24.7	55–65
Packaging (de-coated)	86.1	12.9	1.0	92–95
Dross (one single wrought alloy)	55.7	44.3	-	15–45

*The reported values are only indicative
*Predstavljene vrednosti cen so le informativnega značaja

added value (typically between 5 % and 10 %) can be achieved.

It is important to note that a significant part of the new added value is gained by successful buying of less clean grades of scrap. Hence, it is necessary to understand ***the local*** new and old scrap markets and organize cost-effective buying from the nearest scrap suppliers or though collecting new scrap.

The second part of the new added value is achieved in the process of scrap separation, where the optimum level and method (e.g., hand sorting or automatic screening) of separation should be selected following the compromise between the degree of compositional separation and the cost of achieving it, also taking into consideration that a lower level of compositional separation leads, during the final melting, to a higher consumption of primary aluminium for diluting impurities. Of all the sorting technologies, hand sorting remains the most common method of recovering aluminium. Because a load of mixed scrap (even new, industrial one) often includes a limited number of alloys, hand sorting often makes it possible to produce single-alloy scrap products. Even if this is not possible, hand sorting can help meet specifications for the other scrap grades by removing impurities. A dealer's experience and knowledge of his suppliers is often useful in hand sorting, because the appearance of a piece of new scrap – the shape of punching, the type of a scrapped part – will be sufficient to identify the alloy.

Finally, the remaining part of the new added value depends on the competitiveness of the selected remelting technology, which should be able to provide the highest metal yield, the standard quality of the molten metal and an operation in accordance with the standard environmental regulations.

4 MELTING TECHNOLOGIES FOR CONTAMINATED SCRAP

Generally, regarding the level of organic impurities, two scrap-melting approaches are practiced: with or without melting additives[16]. Without melting additives it is possible to melt clean scrap, preferably containing less than 2–3 % of organic impurities and contaminated scrap (with less than about 10 % of organic impurities) by applying twin or multi-chamber melting furnaces. The scrap with a higher amount of organic impurities should be melted with an addition of melting additives (usually a NaCl and KCl salt mixture) in a drum rotary furnace with a fixed axis, which is the universal furnace for melting all kinds of highly contaminated scrap, including aluminium dross and pressed skulls. However, a more advanced and economic way of recycling aluminium from dross and pressed skulls is with a tilting rotary furnace, in which recycling can be performed with a significantly lower amount of added salts. In addition, tilting rotary furnaces are often used in recycling cast alloys, while only a limited numbers of such devices have been installed until now for the recycling of wrought alloys. It is important to note that salts provide the best quality of a molten metal. The salt mixture covers the aluminium to prevent further oxidation, strips away the oxide layer from the molten metal, promotes the coalescence of metallic droplets and dissolves or suspends other impurities attached to the metal. Therefore, the use of salt is imperative for achieving the maximum quality of recycled aluminium, especially when highly contaminated scrap and scrap with a large specific surface area are melted.

However, salts are costly additives in the production and result in a significant amount of the salt cake by-product, whose processing introduces an extra cost of salt recovery and the deposition of the non-metallic residue on commercial or industrial landfills. The melting strategy for recycling wrought alloys from scrap contaminated with organic impurities depends on several factors, among which the maximum level of organic impurities in the batches prepared for melting is one of the most important. For melting contaminated scrap salt free, various possibilities exist. The most advanced and integrated device for direct melting of contaminated scrap without melting additives is the multi-chamber furnace with a tower. The alternative is to melt contaminated scrap in a twin-chamber furnace. However, in this case the organic impurities should be reduced in advance to some acceptable level. Salt-free remelting devices (e.g., three-chamber melting furnace, twin-chamber furnace with a tower, etc.) are suitable for contaminated scrap having less than 10 % of the total organic impurities. This could be achieved mechanically by shredding or by thermal de-coating. The practical alternative is lowering the amount of organic impurities by mixing the contaminated scrap with a sufficient amount of clean scrap.

In any case, the melting technology chosen will determine the allowed level of organic impurities in the scrap, as well as the eventual necessity for melting additives. Currently, there is no single universal melting device flexible enough for all the grades of scrap (regarding the content of organic and non-metallic impurities, as well as the scrap specific surface area), operating without melting additives. For example, the double-pass rotary drum furnace is the only furnace that is suitable for all kinds of scrap. However, it operates with the highest salt factor. On the other hand, salt-free devices are limited by the amount of organic impurities, which can also reduce productivity. The same problem exists in rotary furnaces, where the highest productivity is achieved with a well controlled amount of organic impurities.

5 EVOLUTION OF WROUGHT ALLOYS TOWARD SCRAP INTENSIVE COMPOSITIONS

First of all, it is important to note that customers do not buy a wrought alloy composition but wrought properties. This fact, which is crucial in a negotiation about the ***optimum*** wrought-alloy composition, should be well recognized by both parties involved in an order negotiation – not only by customers, but also by producers of wrought alloys, and vice-versa.

Unfortunately, in the existing, standardized wrought aluminium alloys the tolerance limits for all the constituents of the alloys were well defined before scrap recycling became the key issue in the added-value engineering along the aluminium production chain. Thus, when ordering these traditional alloys, customers are more or less obliged to request the standard composition and properties.

The common limitation of the existing wrought alloys is that they are not compositionally tolerant enough to be produced by direct mixing and melting of scrap batches without sorting the mixed scraps to the desired level. Therefore, traditional wrought aluminium alloys offer only limited opportunities for a direct reuse of the recycled wrought alloy scrap without tight compositional corrections (the so-called "sweetening") by primary metal and alloying elements.

In the current wrought alloys the real operational dilemma of how well to sort[17] depends on the extent of primary aluminium, which is to be substituted by a recycled grade without influencing the quality of the wrought alloy. It is absolutely clear that the amount of primary aluminium, which can be effectively replaced in a particular wrought alloy by a recycled metal, depends on the level of compositional separation of the scrap. In other words, more precisely compositionally separated scrap has a higher potential for replacing primary aluminium without affecting the quality of the final alloy. Theoretically, by repurposing the completely sorted scrap (one single wrought alloy), a zero consumption of primary aluminium can be achieved in the production of wrought alloys. However, in order to avoid the economic inefficiencies occurring when such high-value scrap is repurposed into compositionally more tolerant wrought alloys, it is always necessary, in practice, to measure the net economic benefits of such a replacement, taking into consideration the cost of separation and the market value of the selected wrought alloy.

On the other hand, compositionally less-separated scrap grades with the alloys inside the same series, two wrought alloys of different series or even a mixture of various wrought alloys, will require, during the melting, an additional consumption of primary aluminium for diluting the impurities influencing the final economic benefit of such a substitution.

In any case, it is important to note that the "de facto" role of primary aluminium is the dilution of the impurity level (not sufficiently reduced through compositional separation of scrap) and not the provision of a sometimes mystic, necessary amount of "virgin metal", which is, according to some opinions, obligatory for achieving the standard quality of wrought alloys.

Finally, the question of economy arises again. By applying the state-of-the-art scrap-separation technology, from a technical point of view, it is possible to achieve compositionally well separated grades of scrap suitable for direct melting to the appropriate wrought alloys. The problem is that this is still not economically reasonable due to the high cost of scrap separation to a level of impurities acceptable for the ***existing*** wrought alloys. For that very reason, the technique of creating a new added value through scrap recycling should lead toward a formulation of new, recycling-friendly wrought alloys if, finally, this would be acceptable for the end product customers.

There are several fundamental questions to be answered concerning future developments of new wrought alloys designed to provide wider compositional tolerances of the existing or other alloying elements and, hence, better opportunities for scrap consumption. The most important one is whether these new alloys can possibly be composed without a critical loss of application properties or, in other words, still provide the valuable and desired combination of wrought properties for customers. Significant efforts, scientifically, technologically and financially, will be necessary for achieving this goal and implementing it in the industrial usage. Another important question concerns a possible long-term reduction in the number of wrought aluminium alloys by establishing a limited number of universal wrought compositions, making the refining of alloys easier. Although a unification of wrought compositions was proposed several times in the past, the actual development is progressing toward a further diversity of the alloys and highly tuned properties.

Irrespective of whether a new generation of recycling-friendly wrought alloys will be developed or the existing ones unified, it is important to note that newly tailored wrought alloys will require a fulfilment of the following two, hardly compatible, demands: (i) compositions with relatively broad specification limits on the major alloying elements and more tolerant limits on impurities; (ii) no significant restrictions on performance characteristics for final applications. A complete development and implementation of such alloys is, obviously, not an easy metallurgical task and will remain, most probably, the challenge for future decades.

6 DETERMINING THE CONTENT OF ORGANICS IN ALUMINIUM SCRAP

The suitability of aluminium scrap with organics as an appropriate source of aluminium in terms of value and quality for the production of wrought aluminium alloys

of the standard quality depends on its metallurgical composition and content of organic and other impurities (humidity, non-metals such as oxides, non-oxides, etc.)[1]. The metallurgical composition of incoming scrap, influenced by the mix of the included alloys, is routinely determined in recycling plants by standard optical emission spectroscopy. However, a similarly fast and cost-effective method of analysing the amount of organics and other impurities in the representative samples of incoming scrap is still under development[2,3].

In recycling plants specialising in recycling of low grades of aluminium scrap, timely and accurate information about the amount of organics and other impurities in the incoming scrap is an absolute prerequisite in achieving a higher net added value. The goal is, considering the amount of organics and other impurities, to recycle each grade of scrap with the optimum recycling procedure from both the economic and the metallurgical aspects.

From an economic point of view, the content of organics and other impurities (of non-aluminium phases) defines the cost of scrap and it is thus absolutely indispensable information in commercial issues related to scrap buying, as well as the added-value engineering of the entire process of recycling[1].

From the metallurgical aspect, the amount of organics and other impurities determines the key technological parameters of recycling and the process of refining the molten metal for achieving the standard quality of end products. Firstly, the amount of organics determines the exothermic/endothermic behaviour of the incoming scrap and the volume of gaseous products liberated during the early stages of recycling. In addition, the concentration of organics and other impurities favours the formation of inclusions, influencing the quality of the molten metal[4].

Aluminium scrap, especially the grades with organics, represents a highly exothermic input (e.g., scrap with approximately 6 % of organic impurities is exothermic enough for self-melting). During the melting of such an input, a huge amount of energy and gaseous products are generated simultaneously, influencing the productivity, the cost of recycling, as well as the quality of the molten aluminium obtained – in particular its suitability for the production of wrought aluminium alloys for highly demanding end products.

Inclusions appearing as various solid particles in molten aluminium or aluminium alloy can be classified into two main groups: (i) indigenous or *in-situ* inclusions, and (ii) exogenous inclusions. The growth of indigenous inclusions is caused by chemical reactions taking place in the melt due to the existing chemical composition and the applied processing parameters (temperature, time, atmosphere, etc.). In contrast with that, exogenous inclusions already exist as a separate phase in the system before the melting and are introduced to the melt by raw materials, alloying elements, additives, refractory materials and the furnace atmosphere[4].

Exogenous inclusions can be effectively removed by filtering. On the other hand, the presence of indigenous inclusions may be prevented effectively only by mastering the overall reactivity in the system – by selecting and maintaining the proper chemical composition of the melt and the processing parameters.

Regarding the overall reactivity in a system, it is particularly important to note that the level of impurities, and the resultant chemical reactivity in remelted aluminium scrap with organics (painted scrap), is quite different from that in primary metal or remelted clean scrap. The organic component of paint can be volatilized during decoating and pyrolysis, but paint often contains inorganic compounds (fillers and pigments) that do not respond to thermal processing or become converted to oxides or other (usually binary) compounds, remaining on the surface of pyrolyzed scrap as exogenous inclusions. Many of these exogenous inclusions may also react with molten aluminium and/or alloying elements dissolved in the melt, creating indigenous as well as new exogenous inclusions.

Note that fillers and pigments can react either with molten aluminium or/and in parallel with some of the alloying elements dissolved in the melt. Hence, in real scrap mixtures of a very complex chemical impurity composition originating from organics, it is very important to take into account all the thermodynamically possible chemical reactions enabling the formation of inclusions. The aim of such a consideration is a careful prescription of the tolerance limits for all the recycled alloy constituents (incoming scrap), including impurities originating from organics.

Due to an enormous growth of the secondary aluminium industry, the development of an industrial method of determining the amount of organics and other impurities in incoming scrap has become a highly important issue. This is particularly the case in recycling plants and casting houses where low grades of scrap are also used for the production of wrought aluminium alloys. Thus, the purpose of this paper is to present an industrial method of determining the amount of organics and other impurities in representative samples of incoming scrap.

6.1 Batch and continuous procedures of a TG analysis

Industrial TG/DTA analyses can be run either as a batch or a continuous process, **Figures 3** and **4**.

The batch TG/DTA device is schematically presented in **Figure 5**.

A significantly higher productivity of a scrap analysis can be achieved with the TG/DTA unit presented in **Figure 6**, which operates continuously.

The accuracy of measuring the humidity and the organics content in the batch method (in an inert

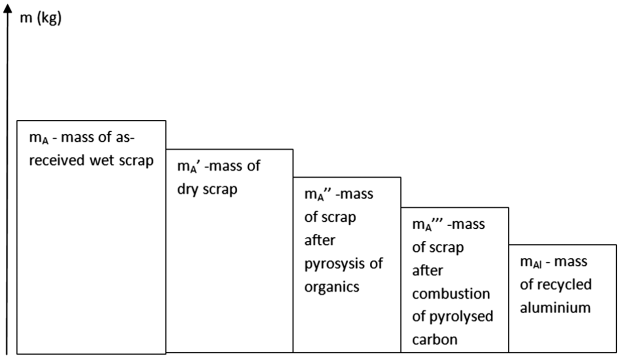

Figure 3: Histogram of mass changes of a representative scrap sample during TG/DTA performed in the batch mode
Slika 3: Histogram spreminjanja mase reprezentativnega vzorca odpadnega aluminija pri šaržni TG/DTA-analizi

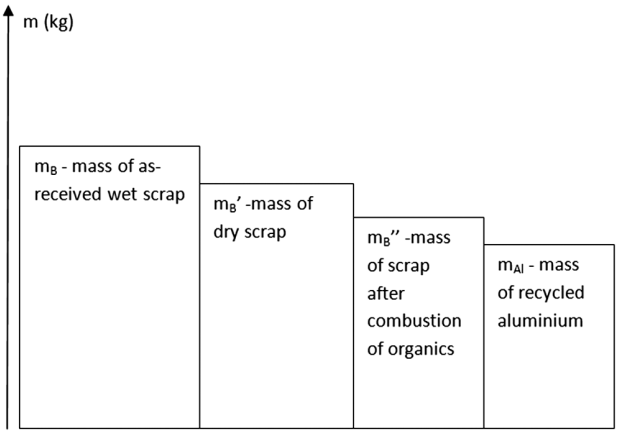

Figure 4: Histogram of mass changes of a representative scrap sample during TG/DTA performed in the continuous mode
Slika 4: Histogram spreminjanja mase reprezentativnega vzorca odpadnega aluminija med zvezno TG/DTA-analizo

atmosphere) depends on the sensitivity of the balance employed. In our case this was ±50 g, corresponding to the maximum relative error of about 1 %. The lowest relative error was obtained in the samples with minimum

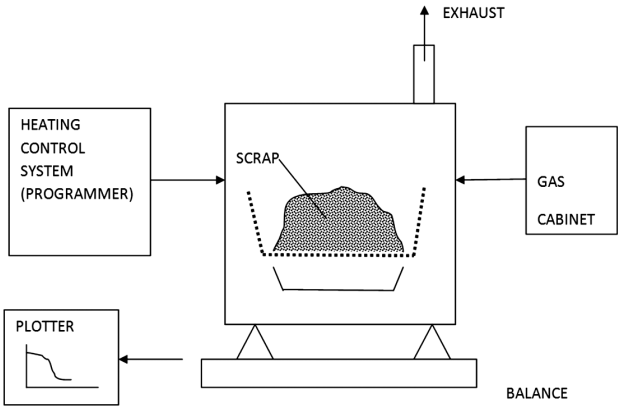

Figure 5: Industrial TG/DTA device operating in the batch mode
Slika 5: Shema industrijske opreme za šaržni postopek TG/DTA-analize

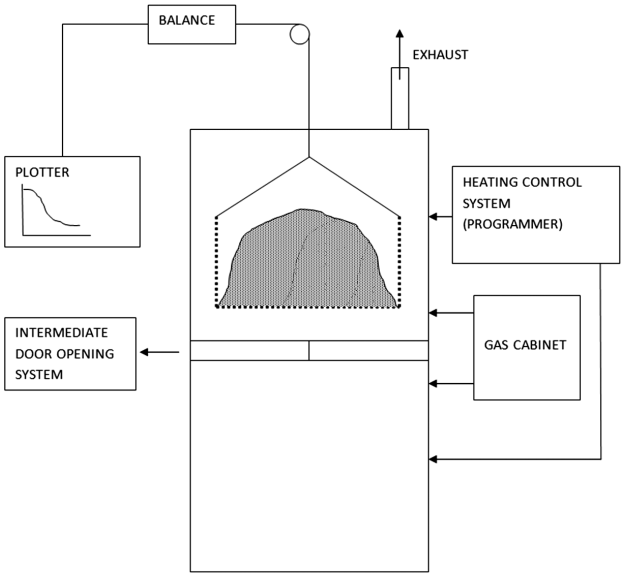

Figure 6: Industrial TG/DTA device capable of operating in both continuous and batch modes
Slika 6: Shema industrijske opreme za TG/DTA-analizo odpadnega aluminija, ki omogoča merjenje po šaržnem ali zveznem postopku

Table 3: Comparison of experimental results of the TG/DTA analysis for aluminium scrap obtained in the batch and continuous modes
Tabela 3: Primerjava eksperimentalnih rezultatov TG/DTA-analize odpadnega aluminija, pridobljenih pri šaržnem in zveznem načinu merjenja

Scrap lot 1	Sample A, batch mode	Sample B, continuous mode
Humidity (%)	0.7 ± 0.02	0.8 ± 0.02
Content of organics (%)	15.6 ± 0.4	14.1 ± 0.4
Content of non-organics including aluminium (%)	84.6 ± 2	85.8 ± 2
Recycled aluminium* (%)	73.6 ± 2	74.7 ± 2

* The estimated recycling efficiency was 0.88

weight losses (the minimum content of organics). For example, the relative error of measuring the organic content in a sample with an initial mass of 50 kg and

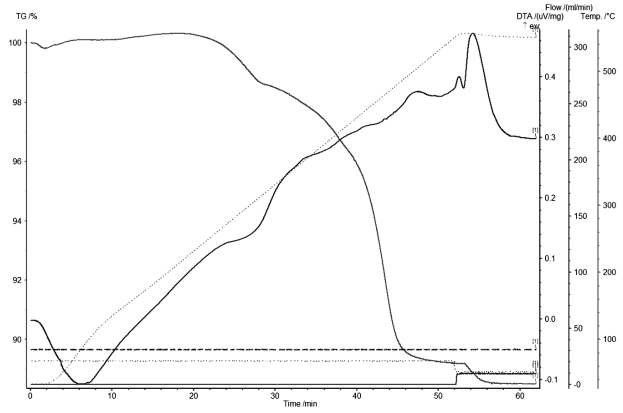

Figure 7: TG/DTA curve obtained in the batch-process mode
Slika 7: TG/DTA-krivulja pri šaržnem postopku merjenja

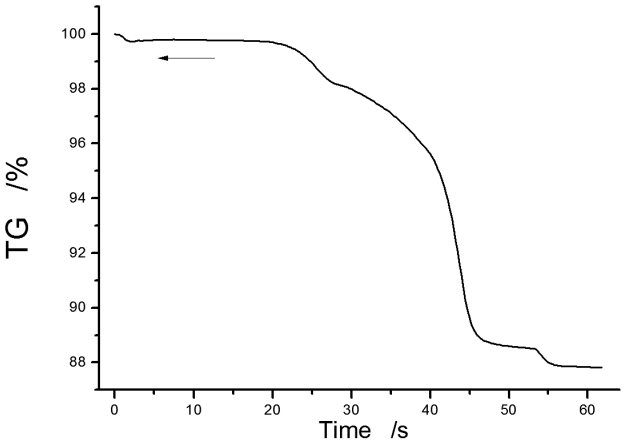

Figure 8: Example of a TG curve generated in the continuous mode
Slika 8: Primer TG-krivulje, pridobljene pri zveznem postopku merjenja

approximately 10 kg of organics was about 0.25 %, while in a sample of the same initial mass but having 80 % of organics, the relative error of measurement was 1 %. However, in both cases the relative error of measurement is within the demands of industrial users.

The accuracy of measuring humidity and organics content with the continuous method (in an oxidizing atmosphere of argon with 1 % of oxygen) in the same way depends on the sensitivity of the balance applied and, in addition, on the time and temperature of the thermal degradation of organics, and is usually lower than in the batch mode. The most important prerequisite in achieving the highest accuracy of measurement in the continuous mode, similar to that achieved in the batch mode, is an efficient minimization of oxidation of aluminium during the thermal degradation of organics in the scrap sample. Due to the fact that the molar mass of aluminium oxide is almost twice as high as the molar mass of the stoichiometrically equivalent amount of aluminium, any oxidation of aluminium during the TG/DTA measurement is detected as an increase in the mass of the remaining scrap sample and, correspondingly, interpreted as a lower content of organics.

Two basic approaches are practiced for minimizing aluminium oxidation during the TG/DTA measurement performed in the continuous mode: (i) prolonged exposure of the scrap sample at a lower temperature (480 °C to 520 °C), or rapid heating of the scrap at a temperature just below the melting point (560 °C to 620 °C). The right combination of the temperature and the time strongly depends on the scrap morphology (a thick or thin gauge), the kind of organics (soluble oil, mineral oil, paint, plastic or lacquer) and the percentage of the organic phase. On that account, for each particular lot of incoming scrap, in which the organics content is to be analysed by an industrial TG/DTA measurement made in the continuous mode, the proper time and temperature of a complete organics removal with a minimum aluminium oxidation should be defined in advance. The best way of selecting the proper temperature and time is based on the results (humidity, content of organics, content of non-organics including aluminium) obtained on a representative sample in the batch mode as the reference values. Accordingly, the parameters of the continuous mode (temperature and time) should be selected to reproduce the results at the same accuracy level as determined in the batch mode.

It is important to note that the industrial TG/DTA device developed for working in the continuous mode (**Figure 5**) can quite easily also operate in the batch mode. This can be done by heating the sample in the bottom chamber starting at room temperature in an atmosphere of pure argon. The decisive advantage of such an industrial TG/DTA device is in its ability to operate in both modes. Thus, the optimisation of the processing parameters (temperature and time) for operating in the continuous mode with the same level of accuracy as in the batch mode gained a reference counterpart and become an end-user-friendly and routine operation, easily applicable to a wide spectrum of incoming aluminium scraps. Following this methodology, the batch measurement should be completed first, irrespective of the scrap morphology, the kind of organics and the percentage of organic phase, thus providing the complete reference values of a scrap analysis. After that, in the second step, the main processing parameters (temperature and time) of the continuous mode should be tuned in order to assure, at the same accuracy level, comparable results for a scrap analysis.

A comparison of the experimental results (**Figures 7** and **8**) obtained with the TG/DTA analysis performed in the batch and continuous mode (**Table 3**) clearly confirms that the parameters of the continuous mode applied in this work (temperature: 560 °C, holding time: 60 s) were correctly selected, resulting in comparable values of humidity, content of organics and content of non-organics including aluminium.

7 QUALITY OF THE MOLTEN METAL

The quality of the molten metal is one of the critical issues, particularly if low-grade scrap becomes the

Table 4: Common impurities in primary and recycled molten aluminium[18]
Tabela 4: Najpogostejše nečistoče v talini na osnovi primarnega in sekundarnega aluminija[18]

Impurity	Concentration in primary aluminium melt	Concentration in recycled aluminium melt
Hydrogen	0.1–0.3 µg/g	0.4–0.6 µg/g
Inclusions (PoDFA scale)	>1 mm^2/kg (Al_4C_3)	0.5–5.0 mm^2/kg (Al_2O_3, MgO, $MgAl_2O_4$, Al_4C_3, TiB_2)
Sodium	30–150 µg/g	<10 µg/g
Calcium	2–5 µg/g	5–40 µg/g
Lithium	0–20 µg/g	<1 µg/g

dominant raw material for the production of wrought alloys of the standard quality.

As already discussed, various scrap-melting technologies influence the quality of the resulting metal through the concentration of the most common impurities in the molten aluminium, such as hydrogen, reactive metals and inclusions.

Throughout almost the whole of the 20th century, the aluminium produced by remelting scrap was treated by customers as less valuable than primary aluminium produced by electrolysis, mostly due to the concerns over the purity of the recycled metal compared to that of primary aluminium[18,19] (**Table 4**). However, the development of the refining technology (in-line degassing and filtration) and analytical methods for measuring the impurity levels in the past 20 years eliminated this ***stigma*** completely, providing the same quality of the ***refined*** molten aluminium, irrespective of its fabrication pre-history.

8 CHALLENGES FOR THE FUTURE

The most important reasons for the increasing demands for lower-grade scrap consumption in wrought-alloy production are in seeking individual profit maximisation, a shortage of clean scrap and both a shortage and the high price of primary aluminium.

The increased consumption of lower grades of scrap (contaminated external scrap) in the production of wrought aluminium alloys makes the achieving of the standard quality of the end products more challenging. Thus, scrap pre-sorting from alloy to alloy, or at least in a series of alloys, proper mixing of various scraps to provide the required chemical composition of the raw material before melting with a minimum consumption of ingots and alloying elements, advanced melting technology for achieving a high yield and the required environmental standards, as well as refining and filtration to assure the standard quality of the alloy, are increasingly necessary.

The development of new alloys with the required properties (e.g., tensile properties, workability, heat treatment, deformation, etc.) could be achievable with more flexible compositional limits. It would be necessary to develop such recycling-friendly wrought compositions and demonstrate to customers the ability to tailor end properties and the economic benefits created by high contents of scrap.

The following advancements in technology will be necessary to achieve the production of any wrought alloys from scrap without ecological problems:

- Develop and design melting furnaces that minimize the melt loss (oxidation and dross formation during remelting) and consumption of melting additives, improve cost effectiveness and productivity, increase safety and reduce emissions.
- Develop a low-cost process for metal purification to enable the production of primary alloys from recycled scrap, including the methods to remove specific impurities such as Mg, Fe, Pb, Li, Si, and Ti.
- Develop new, scrap-tolerant wrought alloys that better match scrap to the specifications for an increased utilization.

However, it is important to note that until now, there have been no effective methods for fulfilling the above requirements technically and economically. Most of the investigations (e.g., metal purification) are still at the stage of fundamental or early applied research, with their progress being uncertain and not foreseeable. Hence, the earliest eventual implementation at the industrial level might be expected in the coming decades.

9 CONCLUSION

Because of high costs and shortages of raw materials (primary aluminium and clean scrap), the main challenge for the producers of wrought aluminium alloys and semis are: (i) running the production with alternative, cost-effective sources of aluminium; and (ii) with the sources of metal that are more easily available.

According to the general estimation that between 3–10 % of LME is the average amount of the new added value achieved by remelting contaminated scrap, the consumption of low-grade scrap, which is already frequently practised by the producers of cast alloys, is also being increasingly introduced by remelters.

However, in contrast to mixed scrap for refiners, scrap batches for remelting should be compositionally well correlated with the chemical composition of the wrought alloy to be produced (preferably consisting of one alloy) and clean enough (not oxidized or contaminated with non-metallic impurities). Traditionally, remelters were defined as the producers of wrought alloys, mainly from clean and sorted wrought-alloy scrap and also distinguished from refiners by a lack of refining capability.

Recent developments in the remelting technology and inside the global recycling industry – together with the actual global economic crisis – started to change this traditional framework toward a new mentality of remelters. Following the opportunities for creating a new added value in their niche business, remelters reconciled the production of wrought alloys from less clean, the so-called ***metallurgically*** clean scrap, which can be contaminated even with high amounts of various non-metallic (e.g., organic) impurities. In addition, they became familiar with achieving the proper composition of scrap batches before loading the scrap into the furnace (through the refining of scrap), avoiding the more expensive dilution of impurities by primary aluminium during the melting. To this end, several ***pre-melting operations*** (scrap sorting and separation, as well as the in-house-scrap batch compositional blending) were integrated into the production chain, together with some ***post-melting operations***, such as the traditional molten-metal refining.

With all these changes contributing essentially to the creation of a new added value, a new mentality of remelters closer to the refining-production practice was established inside the EU, increasing the importance of contaminated scrap as a long-term source of aluminium for wrought alloys. Actually, remelters well understood that the most significant part of the new added value is created through proper scrap buying and sorting, while only the remainder is gained by advanced remelting. Thus, a kind of "scrap refining" practice must be introduced to keep different aluminium alloys separated at some appropriate level, considering both the metallurgical and economic point of view. The key issue is to achieve the right alloy composition of a scrap mixture before melting and not at the end of melting by diluting the impurity content to the required level. The only way to achieve this is by being fully acquainted with the scrap quality through an excellent knowledge of the scrap market, the individual scrap suppliers and an internal knowledge of scrap sampling.

10 REFERENCES

[1] D. G. Altenpohl, P. Paschen, Aluminium, 77 (**2001**) 1–2, 8

[2] S. K. Das, Materials Science Forum, 519–512 (**2006**), 1239

[3] S. K. Das, In Light Metals 2006, Ed. T. J. Galloway, TMS-AIME, Warrendale, PA 2006, 911

[4] S. K. Das, In Aluminium Recycling and Processing for Energy Conservation and Sustainability, Ed. J. A. S. Green, ASM International 2007, 147

[5] R. Hirve, Metalworld, 8 (**2009**) 3, 32

[6] R. E. Sanders, Jr., JOM, 53 (**2001**) 2, 21

[7] J. B. Hess, Metal. Mater. Trans. A, 14 (**1993**), 323

[8] D. G. Altenpohl, Aluminium: Technology, Applications and Environment, 6th ed., TMS-AIME, Warrendale, PA 1998, 15

[9] G. Rombach, In Light Metalas 2002, Ed. W. Schneider, TMS-AIME, Warrendale, PA 2002, 1011

[10] M. E. Schlesinger, Aluminum Recycling, CRC Press, Broken Sound Parkway, NW 2007, 9

[11] M. E. Schlesinger, Aluminum Recycling, CRC Press, Broken Sound Parkway, NW 2007, 171

[12] Aluminium Association, International Ally Designation and Chemical Composition Limits for Wrought Aluminium and Wrought Aluminium Alloys, Aluminium Association, Arlington, VA 2009

[13] M. E. Schlesinger, Aluminum Recycling, CRC Press, Broken Sound Parkway, NW 2007, 101

[14] U. M. J. Boin, M. Bertram, JOM, 57 (**2005**) 8, 26

[15] A&L, The aluminium figures, Edimet (www.edimet.com)

[16] Ch. Schmitz, Handbook of Aluminium Recycling, Vulkan-Verlag, Essen, Germany 2006, 74

[17] P. Li, S. Guldberg, H. O. Riddervold, R. Kirchain, In EPD Congress 2005, Ed. M. E. Schlesinger, TMS, Warrendale 2005, 1159

[18] M. E. Schlesinger, Aluminum Recycling, CRC Press, Broken Sound Parkway, NW 2007, 171

[19] M. E. Schlesinger, Aluminum Recycling, CRC Press, Broken Sound Parkway, NW 2007, 172

UDK 678.7:621.793
Original scientific article/Izvirni znanstveni članek

ISSN 1580-2949
MTAEC9, 47(1)25(2013)

GRAPHITE-FLAKE CARBON-BLACK-REINFORCED POLYSTYRENE-MATRIX COMPOSITE FILMS DEPOSITED ON GLASS-FIBER WOVEN FABRICS AS PLANE HEATERS

KOMPOZIT POLISTIRENA, OJAČAN Z GRAFITNIMI LUSKAMI IN SAJAMI, NANESEN NA TKANINO IZ STEKLENIH VLAKEN ZA PLOŠČATE GRELNIKE

Mustafa Erol[1,2,3], Erdal Çelik[1,2]

[1]Dokuz Eylul University, Department of Metallurgical and Materials Engineering, Buca, 35160 Izmir, Turkey
[2]Dokuz Eylul University, Center for Production and Applications of Electronic Materials (EMUM), Buca, 35160 Izmir, Turkey
[3]Dokuz Eylul University, Graduate School of Natural and Applied Sciences, Buca, 35160 Izmir, Turkey
m.erol@deu.edu.tr

Prejem rokopisa – received: 2012-05-07; sprejem za objavo – accepted for publication: 2012-07-04

Graphite-flake carbon-black/polystyrene composite films as plane heaters are promising materials since they are smarter than the traditional heating elements. In the present study, we are concerned mainly with the production, characterization and industrial application of graphite-flake carbon-black-reinforced polystyrene-matrix composite films deposited on glass-fiber woven fabrics as plane heaters. Within this scope, graphite flakes and carbon-black powders were dispersed in polystyrene gel and deposited on glass-fiber woven fabrics with different weight ratios. Subsequently, the films were dried at 60 °C for 30 min in the air. Structural and surface properties of the produced films were characterized with XRD and SEM, respectively. Electrical and heating properties were determined with a hand-made experimental setup containing a multimeter and a thermocouple. It was found that uniform and partially ordered films depending on the weight ratio and percolation threshold were obtained as plane heaters. Planar heating of up to 60 °C was observed with a 24-V DC power supply.

Keywords: plane heater, composite, graphite flake, carbon black, conductive polymer

Kompozitne plasti polistirena z grafitnimi luskami – sajami so obetajoči materiali za ploščate grelnike, ker so „pametnejši" od tradicionalnih grelnih elementov. V tej študiji obravnavamo proizvodnjo, karakterizacijo in industrijsko aplikacijo kompozitne tanke plasti polistirena, ojačanega z grafitnimi luskami – sajami, nanesenega na tkanino iz steklenih vlaken, za ploščate grelnike. S tem namenom so bile v tej študiji grafitne luske in saje razpršene v polistirenskem gelu, nanesene v različnem masnem razmerju na tkanino iz steklenih vlaken. Nato so bile tanke plasti sušene pri 60 °C 30 min na zraku. Strukturne in površinske lastnosti nastalih tankih plasti so bile ocenjene z XRD in SEM. Električne in grelne lastnosti so bile določene z ročno izdelano sestavo, ki vsebuje multimeter in termoelement. Ugotovljeno je bilo, da je pri ploščatih grelnikih enakomerna in delno urejena plast odvisna od razmerja mas in deleža pronicanja. Pri uporabi enosmerne napetosti 24 V je bilo opaženo segrevanje ploščatih grelcev do 60 °C.

Ključne besede: ploščati grelnik, kompozit, grafitne luske, saje, prevoden polimer

1 INTRODUCTION

Polymers with their specific nature are known as good insulators for electronic applications. Developments of the polymers, together with the new researches, have focused on desired conductivities and a wide range of application for decades. The conductivity of polymers can be obtained in two ways: (a) by producing a polymer that is intrinsically conductive or can be made so by doping and (b) by loading an electrically insulating matrix with conductive fillers[1]. The fillers, which involve conductivity, are generally based on metallic materials such as Ni, Cu, Ag, Al and Fe[2–4] as well as carbon derivates such as carbon black, carbon fiber, graphite and carbon nanotube[5–8].

Natural graphite is mostly used in refractories, steelmaking (as a heating element/electrode), expanded graphite, brake linings, foundry facings and lubricants. The heating property of graphite is a significant issue for electric-arc furnaces in the steel industry. As heating has been an important process for humankind for ages, the above issue has also been present since the discovery of fire up until today's modern heating technologies. With respect to heating, fires, stoves, heat exchangers, air conditioners, furnaces, irons, floor heaters, etc. are the products that fulfill this requirement. These heating systems generally use fossil fuels (wood, petroleum, natural gas, etc), as well as solar energy and electricity. Due to the physical nature of heated air, it flows from bottom to top in a heated place. Taking this into account, efficient systems for heating, like floor heaters, can be selected. There are many detailed researches on floor heating in several reports[9–12]. In addition, due to their conductive properties, graphite and carbon-black powders were incorporated into its structure to provide for the resistivity of the final composite structure. Nevertheless, to the best of our knowledge, no experimental work has been reported in the literature on the self-heating properties of polymer-graphite and carbon-black

composites and their application as plane heaters using composite films.

The fabrication of uniform graphite-flake carbon-black/polystyrene composite films is impossible by using conventional methods such as melting and heating because of several difficulties. To circumvent this problem, as explained in ref.[1], a similar gelation technology was employed to dissolve polystyrene pellets in a quickly evaporating solvent. Graphite-flake and carbon-black powders were dispersed in a polystyrene-chloroform gel matrix with different concentrations. The obtained gel containing these powders was deposited on glass-fiber woven fabrics to obtain the intended plane heaters. Then the structure, the surface morphology, as well as electrical and heating properties of the deposited composite films were investigated.

2 EXPERIMENTAL DETAILS

Graphite flakes (Tupras), carbon black (Selen Chemistry), polystyrene pellets (Tupras Petkim) and chloroform (Aldrich) were commercially provided to produce a new-generation heating element. Polystyrene pellets were dissolved in chloroform using an ultrasonic bath for 60 min and subsequently a viscous gel was obtained prior to depositing the composite films. Graphite-flake and carbon-black powders were basically added to obtain the gel as schematically illustrated in **Figure 1**. After these processes, graphite-flake carbon-black-reinforced polystyrene-matrix mixtures were prepared for the plane-heating composite element. The strategy for determining the composite samples was based on a composite including the total powder weight against the polystyrene weight with a ratio of 0.6 that is referred to as X. Here the coefficient of X as 1, 2 and 4 means that the ratios are 0.6, 1.2 and 2.4, respectively. Beside this, the weight ratio of carbon black/graphite flake was determined as C/G = 0.62 for the composites including 1X, 2X and 4X. In order to determine individual effects of the powders on the properties, the composites containing just carbon black and just graphite were prepared as 1XC and 1XG, respectively. The details and definitions of the above mixture specifications were noted in **Table 1**.

Table 1: Mixture specifications and content data
Tabela 1: Pregled mešanic in podatki o vsebnosti

Precursor	4X*	2X*	1X*	1XG*	1XC*
Polystyrene (g)	1	1	1	1	1
Chloroform (ml)	8	8	8	8	8
Carbon black (g)	0.92	0.46	0.23	0.6	0
Graphite (g)	1.48	0.74	0.37	0	0.6

*X indicates a composite having the mass ratio C/G = 0.62
Coefficients of X indicate (C + G)/P

As the substrate choice is an important parameter for any film-deposition technique, glass-fiber, woven fabric substrates with a planar density of 100 g/m^2 were chosen because of their flexibility and high-temperature service abilities. The produced mixtures were spray painted on these substrates using an air-compressor-based mechanism. After that deposited films were dried to remove the solvent at 60 °C for 30 min on a hot plate for three times.

X-ray diffraction (XRD, Rigaku D/MAX-2200/PC) patterns of the coatings were determined to identify the phase structure using a diffractometer with CuK_α irradiation. The surface properties of the films were examined with the help of scanning electron microscopy (SEM, JEOL JSM 6060).

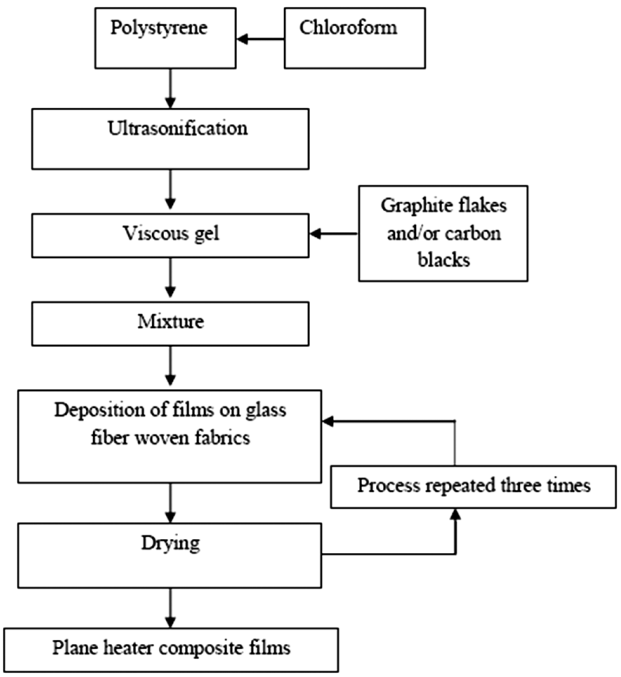

Figure 1: Schematic illustration of the process
Slika 1: Shematski prikaz procesa

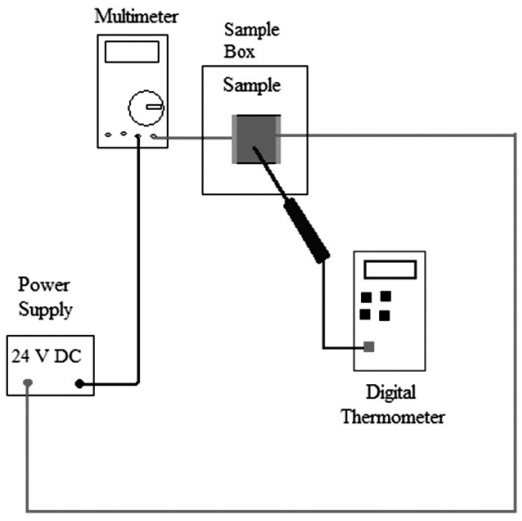

Figure 2: Experimental setup for determining electrical and heating properties of composite films
Slika 2: Eksperimentalni sestav za določanje električnih in grelnih lastnosti kompozitnih tankih plasti

Electrical and heating properties of the composite coatings were determined using the basic experimental setup as illustrated in **Figure 2**. This basic setup consisted of a digital thermometer, a 24-V direct-current (DC) power supply and a multimeter (used as an ampermeter in this circuit). Square specimens with the dimensions of 30 mm × 30 mm were cut and electrodes were painted on two edges with a silver paste as depicted with the orange color in **Figure 2**. The specimens were fixed to the circuit using copper jaws. The circuit current and the time versus the temperature data were noted from this set up. The resistances of the film were basically calculated using Ohm's law.

3 RESULTS AND DISCUSSION

The XRD patterns of the produced composite films on the glass-fiber woven fabrics are demonstrated in **Figure 3** in order to prove that their structure consists of both graphite flakes and carbon-black powder. As seen from the XRD patterns, the main peaks of graphite and carbon were determined at the diffraction angle of 26.6°. With respect to increasing the total powder amount, higher proportional-intensity data was recorded retaining the mixture contents listed in **Table 1**. In addition, crystalline-like polystyrene structure was clearly found in this data. This pattern proves that polystyrene, graphite flakes and carbon-black powder are physically mixed in the composite structure as no structural or chemical change was observed. As expected, another observation of the XRD results showed a highly amorphous band of specimen 1XG and a highly crystalline structure of 1XG.

Microstructural properties of the composite films observed via SEM are shown in **Figure 4**. As can be seen from the micrographs, an efficient composite coating was prepared for the heating elements. It should be noted that the round areas were considered to be the bubbles left after the evaporation of the solvent due to an increase in the pore number and size against the relative solvent amount. It is also important to note here that the other areas on the micrographs were found to be polystyrene matrices encapsulating powder agglomerations.

The electrical behavior of the films was determined with the experimental setup (**Figure 2** for details) and the measured current data was used to calculate the resistance values according to the basic Ohm's law. The measured and calculated electrical properties are listed in **Table 2**. In the light of electrical measurements, the samples 1X, 1XG and 1XC were found to be highly insulating according to the resistance values. This is because the above particle/composite weight ratio of 0.6 is found to be lower than the intended structure. Percolation threshold is an important phenomenon, as reported in the research by S. Isaji et al.[1]; however, there is no study of a polystyrene matrix filled with both graphite

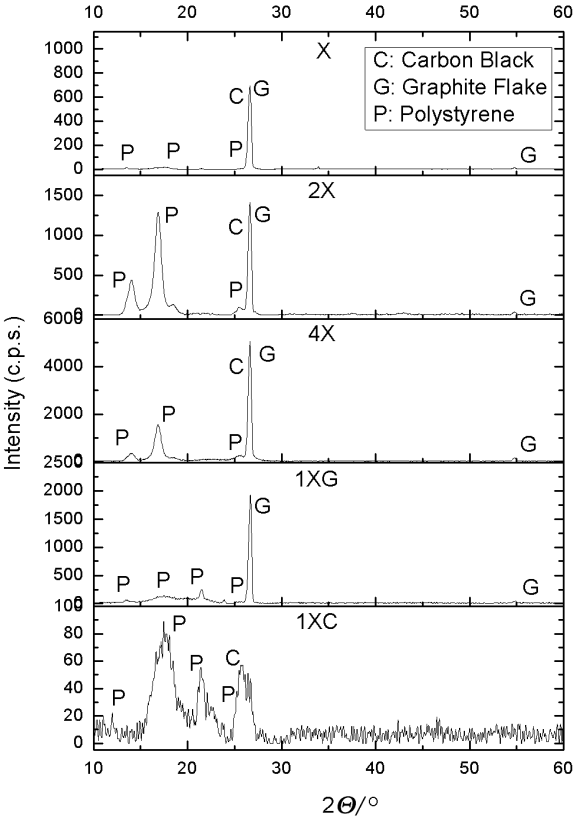

Figure 3: XRD patterns of the composite films on glass-fiber woven fabrics

Slika 3: Rentgenski posnetki kompozitnih tankih plasti na tkanini iz steklenih vlaken

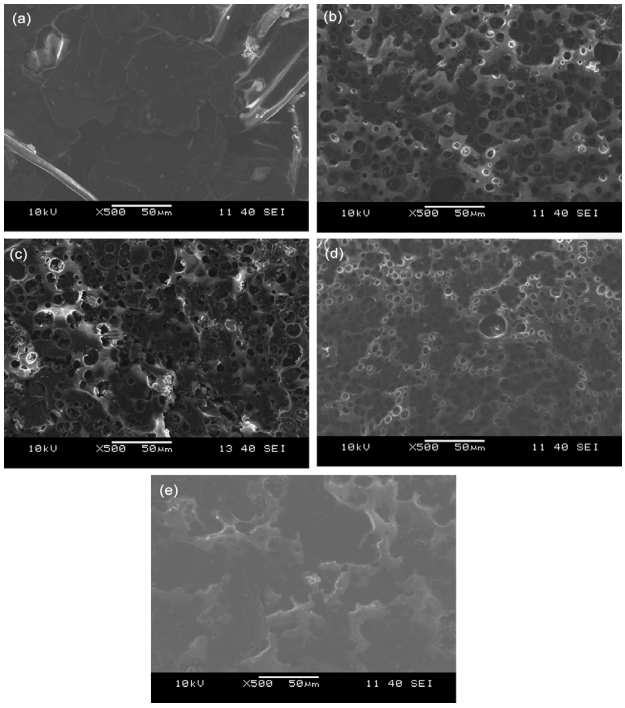

Figure 4: SEM micrographs of the composite films on glass-fiber woven fabrics including: a) 4X, b) 2X, c) X, d) 1XC, e) 1XG

Slika 4: SEM-posnetki kompozitne tanke plasti na tkanini iz steklenih vlaken: a) 4X, b) 2X, c) X, d) 1XC, e) 1XG

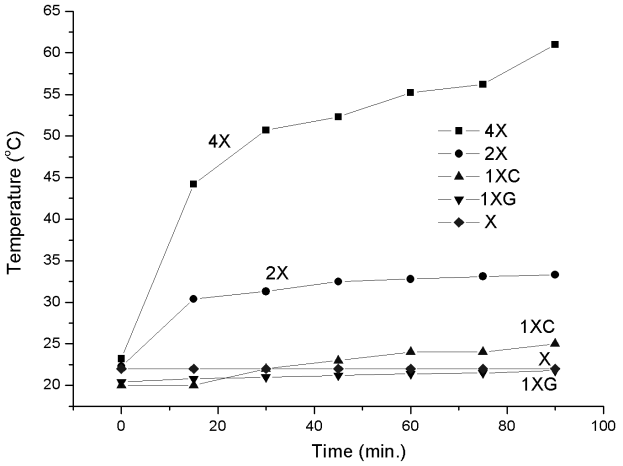

Figure 5: Time versus the obtained temperature results for the heating-element samples
Slika 5: Odvisnost časa in dosežene temperature pri ogrevanju vzorcev grelnih elementov

and carbon. In this study, the ratio of the powders loaded by us can be regarded as lower than the percolation threshold for the above samples. In this way, heating was obtained from these samples, as noted in **Figure 5**, which clarifies the variation of temperature with time and sample type. According to **Figure 5**, the samples such as 4X and 2X were determined to be good candidates for a plane heating that can reach the temperatures of 65 °C and 35 °C in 90 min, respectively.

Table 2: Electrical properties of the samples
Tabela 2: Električne lastnosti vzorcev

Sample code	DC voltage (V)	Current (mA)	Resistance (kW)
4X	24	9.611	2.49
2X	24	19.04	1.26
1X	24	0.25	96
1XC	24	0.02	1200
1XG	24	0.01	2400

It is interesting that the samples evaluated in this study were employed with a power supply unit of 24-V DC. As a result, the plane-heater coatings with large surfaces are applicable with 110-AC and 220-AC city voltages, as listed in **Table 2**. It also needs to be pointed out that this heating system does not emit any harmful gaseous or liquid impurities unlike the heating systems consuming fossil fuels. In addition, an easy layout and application efficiency make the system a good candidate heating device.

4 CONCLUSIONS

Graphite-flake carbon-black-reinforced polystyrene-matrix composite films were successfully deposited on glass-fiber woven substrates as plane heaters. Structural and microstructural results indicate a good compatibility between the powders and the matrix without any chemical interaction among them and a good surface quality with a partial orientation of the reinforcement powders. Samples 4X and 2X were found to be good candidate materials for plane-heating systems or devices. The composite films are believed to be the new-generation heating elements due to being cost-effective, environmentally friendly and energy friendly. For these reasons, the composite films will start a new era in the heating sectors.

Acknowledgement

This study was financially supported by Ayçe Mühendislik Co. and the Turkish Ministry of Science, Industry and Technology with the project code 00360-STZ-2009-1.

5 REFERENCES

[1] S. Isaji, Y. Bin, M. Matsuo, Electrical conductivity and self-temperature-control heating properties of carbon nanotubes filled polyethylene films, Polymer, 50 (**2009**), 1046–1053
[2] D. Bloor, K. Donnelly, P. J. Hands, P. Laughlin, D. Lussey, A metal-polymer composite with unusual properties, J. Phys. D: Appl. Phys., 38 (**2005**), 2851–2860
[3] P. V. Notingher, D. Panaitescu, H. Paven, M. Chipara, Some characteristics of conductive polymer composites containing stainless steel fibers, Journal of Optoelectronics and Advanced Materials, 6 (**2004**), 1081–1084
[4] T. Yamamoto, E. Kubota, A. Taniguchi, S. Dev, K. Tanaka, K. Osakada, Electrically conductive metal sulfide polymer composites prepared by using organosols of metal sulfides, Chem. Mater., 4 (**1992**), 570–576
[5] S. Geethaa, K. Kannan, S. Kumarb, S. Meenakshia, M. T. Vijayana, D. C. Trivedia, Synergetic effect of conducting polymer composites reinforced E-glass fabric for the control of electromagnetic radiations, Composites Science and Technology, 70 (**2010**), 1017–1022
[6] A. Russameeden, J. Pumchusak, Preparation of fiber-reinforced electrically conducting polypropylene composites by wet-lay process for use as bipolar plate in a proton exchange membrane fuel cell, Journal of Metals, Materials and Minerals, 18 (**2008**), 121–124
[7] A. B. Kaiser, Y. W. Park, Current-voltage characteristics of conducting polymers and carbon nanotubes, Synthetic Metals, 152 (**2005**), 181–184
[8] K. R. Reddy, B. C. Sin, K. S. Ryu, J. C. Kim, H. Chung, Y. Lee, Conducting polymer functionalized multi-walled carbon nanotubes with noble metal nanoparticles: Synthesis, morphological characteristics and electrical properties, Synthetic Metals, 159 (**2009**), 595–603
[9] B. Chen, J. J. Liu, Y. Y. Sun, Study on thermal performance analysis method of direct-gain solar dwellings with floor heating, Proceedings of ISES World Congress, 3 (**2009**), 804–808
[10] R. Zeng, X. Wang, W. Xiao, Y. Zhang, Q. Zhang, H. Di, Thermal performance of phase change material energy storage floor for active solar water-heating system, Front. Energy Power Eng. China, 4 (**2010**) 2, 185–191
[11] Z. P. Song, R. Z. Wang, X. Q. Zhai, An experimental and simulation study on performance of solar-powered floor heating system, Proceedings of ISES World Congress 2007, 5 (**2009**), 2224–2228
[12] Z. G. Lin, S. Y. Zhang, X. Z. Fu, Y. Wang, Investigation of floor heating with thermal storage, Journal of Central South University of Technology, 13 (**2006**), 399–403

UDK 519.61/.64:662.62
Izvirni znanstveni članek/Original scientific article

ISSN 1580-2949
MTAEC9, 47(1)29(2013)

POSTOPKI PRIPRAVE ZA PROIZVODNJO TRDNIH GORIV IZ NENEVARNIH ODPADKOV

THE PROCESSES OF PREPARATION FOR THE PRODUCTION OF SOLID FUELS FROM NON-HAZARDOUS WASTE

Janez Ekart[1], Niko Samec[1], Filip Kokalj[1], Brigita Polanec[2]

[1]Univerza v Mariboru, Fakulteta za strojništvo, Smetanova 17, 2000 Maribor, Slovenija
[2]MD Inženiring, d. o. o., Loška ulica 8, 2000 Maribor, Slovenija
janez.ekart@gmail.com

Prejem rokopisa – received: 2012-05-07; sprejem za objavo – accepted for publication: 2012-09-18

Namen raziskovalnega dela v predstavljenem članku je bil z matematičnim modelom poiskati rešitev za pripravo trdnih goriv iz nenevarnih odpadkov, ki se lahko predelajo v trdno gorivo v skladu z veljavno nacionalno zakonodajo. Nenevarni odpadki so definirani z DIREKTIVO 2008/98/ES Evropskega parlamenta in Evropskega sveta (19. 11. 2008) – Priloga III[1]. Z uporabo matematičnega modela in njegovim orodjem občutljivosti, vezanim na posamezne lastnosti vhodnih odpadnih materialov, smo iz razpoložljivih odpadnih materialov z znanimi parametri njihovega organskega in anorganskega dela poiskali rešitev za njihovo najbolj optimalno izrabo. Iz razpoložljivih odpadnih materialov smo v maksimalnem masnem deležu pripravili zahtevano trdno gorivo z vsemi potrebnimi kakovostnimi lastnostmi z najvišjim mogočim kakovostnim razredom in iz preostanka razpoložljivih masnih tokov ostanek trdnega goriva slabše kakovosti, ki ga pa še vedno lahko plasiramo na trgu z možnostjo sosežiga v cementarnah ali sežigalnicah odpadkov. Pri ugotavljanju kakovosti nenevarnih odpadkov in trdnega goriva je bilo pomembno njihovo pravilno vzorčenje, ki se je izražalo v stopnji homogenizacije vzorcev, ki imajo vsak zase svoje kemijske, fizikalne in energijske lastnosti. Analiza kovinskega dela nenevarnih odpadkov je bila pomembna zaradi podatkov o pričakovanih emisijskih vrednostih v dimnih plinih, letečem pepelu, pepelu in žlindri, ki nastane pri sosežigu trdnega goriva v kurilni napravi. Analiza nekovinskega dela nenevarnih odpadkov je bila pomembna z vidika energijske vrednosti trdnega goriva in tehnoloških ter okoljskih posledic. Rezultati raziskovalnega dela so pokazali, da je mogoče iz razpoložljivih nenevarnih odpadkov doseči sorazmerno majhen masni delež visokokakovostnega trdnega goriva iz odpadkov glede na celotno razpoložljivo maso odpadkov, ki je sedaj v Sloveniji.

Ključne besede: nenevarni odpadki, trdno gorivo, kurilna vrednost, matematični model, razred trdnega goriva

The purpose of the research work in the presented article was to find a solution, by means of a mathematic model, to the problem of how to prepare solid fuels from non-hazardous waste that can be processed into solid fuels according to the national law in force. Non-hazardous waste is defined by the DIRECTIVE 2008/98/ES of the European Parliament and the Council (19.11.2008) – Annex III.[1] With the application of a mathematical model and its sensitivity tool, depending on the individual characteristics of the input waste material, the optimal utilization of different waste streams at disposal based on organic and inorganic parameters for the most optimal solution for exploitation was calculated. From the waste material at disposal the desired solid fuel was made in the maximum mass amount with all the necessary qualitative characteristics with the highest quality class and from the rest of the available mass stream solid fuel of lower quality that can still be placed on the market for incineration at cement kilns or incinerators was made. When defining the quality of non-hazardous waste and solid fuel one of the most important tasks of the research was to sample the waste and the fuel correctly, which was reflected in the degree of sample homogenization to find out the chemical, physical and energy characteristics. The analysis of the metal part of the non-hazardous waste was important because of the data about the expected air-emission values of the flue gas, the fly ash, the ash and the slag that occurs when incinerating solid fuel in the heating system. The analysis of the non-metal part of the non-hazardous waste was important from the view of the calorific value of the solid fuel and of the technological and environmental impact. The results of the research showed that it is possible to achieve from the non-hazardous waste at disposal a relatively small mass fraction of high-quality solid fuel from waste according to the whole amount of mass available in Slovenia at present.

Keywords: non-hazardous waste, solid fuels, calorific value, mathematical model, classification of solid fuels

1 UVOD

Za zmanjšanje obremenitev odlagališč in povečevanje izkoriščanja potenciala odpadkov so na področju ravnanja z odpadnimi materiali nujne druge rešitve v primerjavi z uveljavljenimi v naši državi. Ker imajo vsi organski odpadni materiali neko kurilno vrednost, je smiselna tudi rešitev z energijsko izrabo tistih odpadnih materialov, ki niso primerni za snovno izrabo. Trdna goriva iz odpadnih materialov imajo višjo stopnjo energijske izrabe odpadkov v primerjavi s klasičnimi sežigalnicami odpadkov, saj temeljijo na izrabi alternativnih energijskih virov in ne na odstranjevanju odpadkov, kot to velja za klasične sežigalnice.

Težišče raziskovalnega dela sta uporabljena metoda laboratorijskih analiz razpoložljivih odpadnih materialov in matematični model mešanja teh odpadnih materialov s ciljem proizvodnje trdnih goriv z želenimi lastnostmi. Dodatna laboratorijska analiza trdnega goriva in analiza emisijskih vrednosti pri sežigu trdnega goriva je zadostna osnova, da v nadaljnjem raziskovalnem delu poiščemo odmike od pričakovanih rezultatov in temu primerno z analizo občutljivosti matematičnega modela izvršimo korekcijo deležev odpadnih materialov v trdnem gorivu.

2 EKSPERIMENTALNI DEL

Za določitev fizikalnih in kemijskih lastnosti trdnega goriva imamo na razpolago laboratorijske analize razpoložljivih frakcij nenevarnih odpadkov, in sicer:

- vsebnost vlage,
- vsebnost pepela,
- *GCV* – zgorevalna toplota (MJ/kg),
- masni delež Cl (%),
- vsebnost Hg (mg/MJ),
- vsebnost Cd (mg/kg),
- masni delež S (%).

Pogoj za pridobivanje laboratorijskih rezultatov za frakcije razpoložljivih odpadkov in trdnega goriva sta bila njihovo predhodno vzorčenje in homogenizacija. Vzorčenje in homogenizacija vzorcev sta potekala v skladu s tehničnimi specifikacijami in standardi: EN 14899:2005,[2] SIST EN 15442:2011,[3] SIST EN 15443: 2011[4] in SIST-TS CEN/TS 15413:2007.[5] Za homogenizacijo vzorcev frakcij odpadkov in trdnega goriva sta bila uporabljena:

- rezalni mlin Retsch SM 2000 za večstopenjsko mletje 0,8 cm, 0,4 cm ter 0,2 cm in
- centrifugalni mlin Retsch ZM 200 za homogenizacijo vzorcev.

Določevanje vlage je potekalo v skladu s standardom SIST EN 15414-3:2011,[6] uporabljena je bila žarilna komora Nabertherm GmbH.

Določevanje zgorevalne toplote (zgornje kurilne vrednosti) je potekalo s kalorimetrom IKA Werke C5000 in z uporabo adiabatnega delovnega procesa z validirano metodo po DIN 51900, kar je v skladu s standardom SIST EN 15400:2011.[7]

Preostale uporabljene metode:

- Hg (mg/kg) v suhi snovi – ISO 5666:1999, pogl. 5, modif.[8]
- Cd (mg/kg) v suhi snovi – SIST EN ISO 17294-2: 2005[9]
- S (%) – izlužek – ASTM D 4239 (metoda C):1997[10]
- Cl (%) – metoda titracije s titratorjem Metrohm TITRANDO 809 po SIST EN 15408:2011[11]

2.1 Uporaba matematičnega modela

Pri izdelavi in uporabi matematičnega modela smo izhajali iz variante, s katero bi iz razpoložljivih frakcij odpadkov pridobili trdno gorivo z maksimalno mogočo kakovostjo in ostanek trdnega goriva s slabšo kakovostjo.

Na osnovi predpisanih meril za določitev kakovostnega razreda goriva so bili upoštevani naslednji osnovni parametri: *GCV*, Cl, Hg, Cd in S.

Celotna masa odpadkov za predelavo v trdno gorivo je izražena z enačbo:

$$m_I = \sum_{i=1}^{n} m_i \quad n \in N \tag{1}$$

m_I – skupna masa vseh frakcij odpadkov, ki so na razpolago (kg)

m_i – masa *i*-te frakcije odpadkov (kg)

Podatki za maso posamezne frakcije so bili pridobljeni z evidenčnimi listi, ki so pri prevzemu odpadkov obvezni.

Ker je bilo na razpolago več frakcij odpadkov, je bilo pri sestavi trdnega goriva treba upoštevati njihove lastnosti in deleže. Deleži frakcij odpadkov so bili izraženi z enačbo:

$$d_i = m_i/m_I \quad n \in N \tag{2}$$

d_i – masni delež posamezne frakcije odpadkov

m_i – masa *i*-te frakcije odpadkov

m_I – skupna masa odpadkov

V imenovalcu je bila celotna masa vseh razpoložljivih frakcij odpadkov.

Posamezen parameter v trdnem gorivu je bil izračunan po enačbi:

$$G_{I(j)} = \frac{\sum_{i=1}^{n} G_{I(j)} \cdot m_I}{m_I} \quad n \in N \tag{3}$$

j – parameter (*GCV*, Cl, Cd, Hg, S)

$G_{I(j)}$ – vrednost *j*-tega parametra skupnega goriva iz odpadkov

$G_{i(j)}$ – vrednost računanega parametra *i*-te frakcije odpadkov po *j*-tem parametru

m_i – masa *i*-te frakcije odpadkov

m_I – skupna masa odpadkov

V Sloveniji imamo kakovost trdnega goriva opredeljeno z Uredbo,[12] ki definira kakovostne razrede trdnega goriva v Prilogi 3 (**tabela 1**).

Z matematičnim modelom so bili izračunani relativni deleži posameznih frakcij odpadkov, ki so nam bili na razpolago, z upoštevanjem njihovih posameznih parametrov v odvisnosti od referenčnega parametra, katerega razred za trdno gorivo je določil prevzemnik.

Relativne vrednosti parametrov posamezne frakcije odpadkov so bile izračunane po enačbi:

Tabela 1: Podatki osnovnih frakcij odpadkov
Table 1: Data of the basic waste fractions

Frakcije odpadkov	Masa, *m*/t	*GCV*/(MJ/kg)	*w*(Cl)/%	*ρ*(Cd)/(mg/kg)	*σ*(Hg)/(mg/MJ)	*w*(S)/%
Lahka frakcija MKO	120	15,9	0,48	1,8	0,22	0,02
Odpadki iz industrije (Gorenje)	50	21,7	0,55	2	0,32	0,12
Ostanek po razvrščanju embalaže	30	14,2	0,84	1,6	0,10	0,02

$$p_{i(j)} = \frac{G_{i(j)}}{G_{(j)\,\mathrm{ref.}}} \quad (4)$$

$p_{i(j)}$ – relativna vrednost *i*-te frakcije po *j*-tem parametru
$G_{i(j)}$ – vrednost računanega parametra *j i*-te frakcije
$G_{(j)ref.}$ – želena vrednost parametra *j*

Tako so bile izračunane relativne vrednosti posameznih parametrov v odnosu na želene (referenčne) parametre za vse frakcije odpadkov.

Da bi lahko določili vrednosti optimalnih lastnosti trdnega goriva, smo uporabili izločitvena merila za vsak parameter in za vsako frakcijo odpadkov posebej (*if* relativna vrednost *j*-tega parametra ≥1, zapiši 1, drugače pa 0). Z upoštevanjem izločitvenih meril po posameznih parametrih *j* je bila za optimalne lastnosti trdnega goriva določena nova skupna masa osnovnih frakcij odpadkov, ki je bila izračunana po enačbi:

$$m_{v(j)} = m_I \sum_{i=1}^{n} (d \cdot p_{i(j)}) \quad n \in N \quad (5)$$

$m_{V(j)}$ – nova masa po izločitvi

Za primešanje posameznih frakcij odpadkov smo določili variacijski razmik (*VR*) med lastnostmi optimalnega trdnega goriva in trdnega goriva po zahtevah prevzemnika:

$$VR = \left| G_{\mathrm{opt.}} - G_{(j)\,\mathrm{ref.}} \right| \quad (6)$$

$G_{\mathrm{opt.}}$ – vrednost *j*-tega parametra optimalnega trdnega goriva
$G_{(j)\mathrm{ref.}}$ – vrednost *j*-tega parametra trdnega goriva, ki ustreza zahtevam prevzemnika

Parameter primešanja G_j določimo z variacijskim razmikom in maso po izločitvi. Če je parameter G_j enak 0, je primešanje dodatne frakcije dovoljeno, sicer ne. Za izračun teoretično mogoče mase frakcije odpadkov za primešanje smo uporabili enačbo:

$$m_{\mathrm{dom}(j)} = \frac{VR \cdot m_{V(j)}}{G_{(j)\,\mathrm{ref.}} - G_{i(j)}} \quad (7)$$

$m_{\mathrm{dom}(j)}$ – teoretična mogoča masa primešanja za parameter *j*

Za primešanje smo pri izračunu po matematičnem modelu upoštevali, da lastnosti enega izmed osnovnih frakcij odpadkov ustrezajo lastnostim referenčnega trdnega goriva, kot ga zahteva prevzemnik. Zato smo določili, da tej frakciji odpadkov primešamo razpoložljivi preostali osnovni frakciji odpadkov s ciljem, da iz obstoječe osnovne mase odpadkov zagotovimo maksimalno mogočo maso trdnega goriva, ki bo ustrezalo referenčnim vrednostim. Glede na lastnosti frakcij odpadkov smo določili prioritetni red primešanja. Kot prvi prioritetni red primešanja smo uporabili frakcijo odpadkov, ki je v največjem deležu posameznih parametrov $j_{1,5}$ bila najbližje parametrom referenčnega trdnega goriva (kot ga zahteva prevzemnik). Ker smo imeli tri dodatne frakcije odpadkov in pet parametrov, ki smo jih analizirali v posamezni frakciji odpadkov za primešanje, smo uvedli matriko za primešanje s tremi stolpci in petimi vrsticami. Pri tem je prvi stolpec pomenil frakcijo odpadkov V1, drugi stolpec frakcijo odpadkov V2 in tretji stolpec frakcijo odpadkov V3. Vrstice so pomenile posamezne parametre $j_{1,5}$. Merilo za formiranje matrike:

– prva vrstica, prvi stolpec matrike (1,1) : if V1 = $\mathrm{razred}_{\mathrm{ref.}}$ – vpiši 1, drugače vpiši 0

Za prvi prioritetni red primešanja smo dobili matriko:

$$\begin{matrix} 0 & 1 & 0 \\ 0 & 1 & 0 \\ 0 & 1 & 0 \\ 0 & 1 & 0 \\ 0 & 1 & 0 \end{matrix}$$

Rezultat matrike pove, da smo v prvem prioritetnem redu primešanja uporabili frakcijo odpadkov V2. Po enakem postopku smo dobili matriko drugega in tretjega prioritetnega reda primešanja. Po določitvi prioritetnih redov primešanja frakcij odpadkov smo določili količino (maso) primešanja frakcije odpadkov na podlagi meril posameznih parametrov $j_{1,5}$ in enačbe:

$$m_{(j)P_1} = m_{\mathrm{dej.}} \cdot P_{n(jxi)} \quad (8)$$

$m_{(j)P_1}$ – masa domešavanja frakcije odpadkov prve prioritete po *j*-tem parametru
$m_{\mathrm{dej.}}$ – dejanska masa primešanja vseh frakcij odpadkov
$P_{n(jxi)}$ – pripadajoči prioritetni red mešanja

Za izračun vrednosti skupne mase smo uporabili enačbo (primer parameter *GCV*):

$$m_{jS_n} = m_{(j)P_1} + m_{V(j)} \quad (9)$$

m_{jS_n} – skupna masa *n*-tega materiala po *j*-tem parametru
$m_{(j)P_1}$ – masa primešanja prvega prioritetnega reda po *j*-tem parametru

Po enakem sistemu smo izračunali količine primešanja za druge parametre frakcije odpadkov V1 in nato količine primešanja v drugem in tretjem prioritetnem razredu.

Končno maso primešanja za optimalno trdno gorivo smo izračunali po enačbi:

$$m_{\mathrm{TAG}} = m_{\mathrm{ref.}} + \sum_{i=1}^{n} m_{p_i} \quad (10)$$

m_{TAG} – masa končnega goriva želenega razreda
$m_{\mathrm{ref.}}$ – masa vzorca trdnega goriva, ki izpolnjuje pogoje želenega razreda
m_{pi} – vsota mas primešanih frakcij odpadkov k vzorcu trdnega goriva, ki izpolnjuje pogoje želenega razreda

Po primešanju frakcij odpadkov v prvem, drugem in tretjem prioritetnem redu primešanja smo dobili trdno gorivo, ki je izpolnjevalo pogoje želenega razreda v celotni masi $_{\mathrm{TAG}}$ in ostanek trdnega goriva slabšega kakovostnega razreda, ki bi ga lahko hkrati sežigali v cementarnah ali sežigalnicah odpadkov.

Slika 1 prikazuje diagram poteka priprave referenčnega trdnega goriva in ostanka trdnega goriva. Na

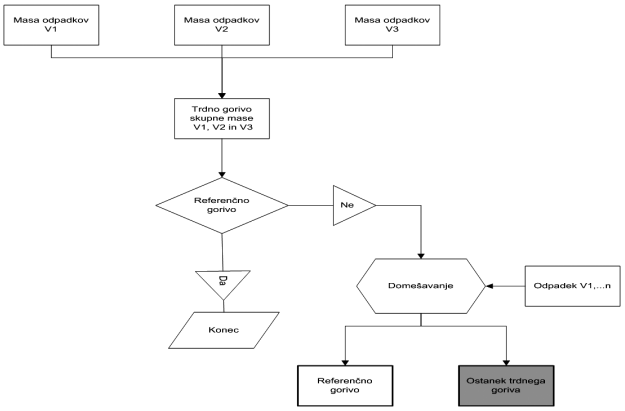

Slika 1: Procesni diagram priprave referenčnega trdnega goriva in ostanka trdnega goriva
Figure 1: Flow chart of the preparation of the reference solid fuel and its residues

sliki 2 je prikazan model osnovnega masnega toka frakcij odpadkov in primešanja ločenih frakcij z uporabo matematičnega modela, s čimer dosežemo produkt trdnega goriva po zahtevah prevzemnika in ostanek trdnega goriva slabše kakovosti.

Ker smo imeli na razpolago tri dodatne frakcije odpadkov, smo k ostanku trdnega goriva primešali ločene frakcije odpadkov po naslednji enačbi:

$$m_{\text{ost.}} = m_0 + \sum_{i=1}^{n} m_{p_i} \quad n \in N \tag{11}$$

$m_{\text{ost.}}$ – masa ostanka goriva po primešanju ločenih frakcij odpadkov
m_0 – masa ostanka goriva pred primešanjem
m_{pi} – vsota mas primešanih frakcij odpadkov k ostanku trdnega goriva

3 REZULTATI

Na razpolago smo imeli 200 t osnovnih frakcij odpadkov in 50 t ločenih frakcij za primešanje. V količini 200 t odpadkov so bili taki s parametri, določenimi na podlagi njihovega vzorčenja in laboratorijskih analiz (**tabela 1**). Podatke o ločenih frakcijah za primešanje prikazuje **tabela 2**.

Z uporabo celotne osnovne mase frakcij odpadkov in njihovih lastnosti, ki jih prikazuje **tabela 1**, smo z uporabo enačbe (3) izračunali parametre trdnega goriva (**tabela 3**).

V skladu s Prilogo 3 Uredbe[12] smo pridobljeno gorivo zaradi kurilne vrednosti uvrstili v razred 3. Drugi parametri so ustrezali trdnemu gorivu razreda 2, nekateri celo razredu 1.

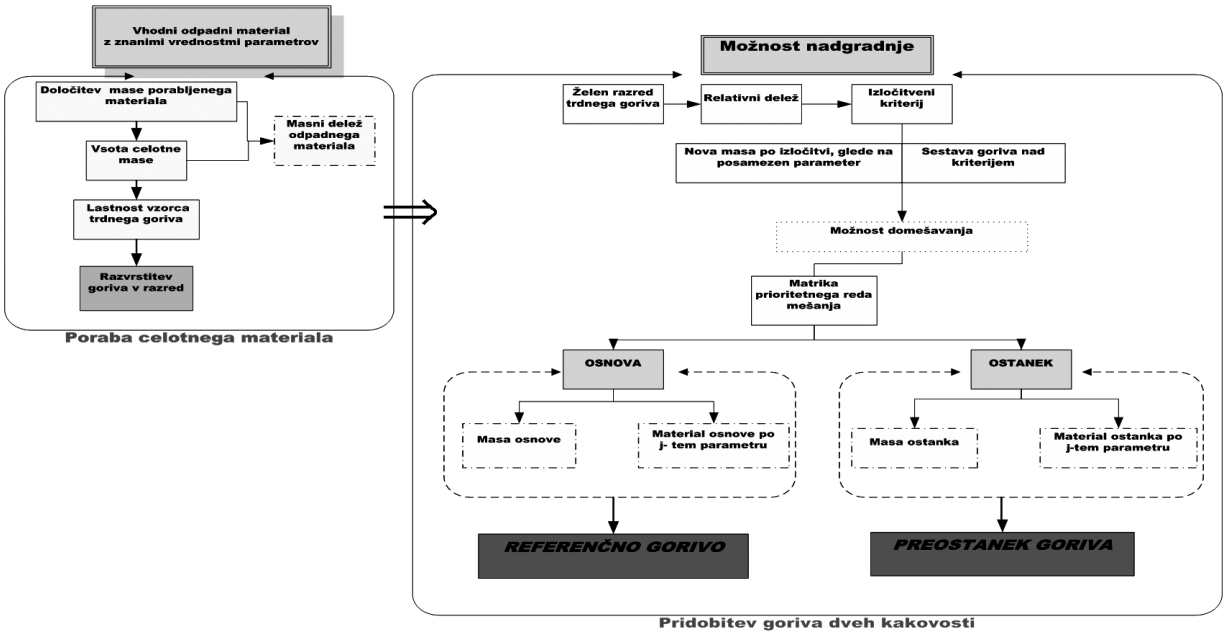

Slika 2: Model osnovnega masnega toka in domešavanja ločenih frakcij odpadkov z uporabo matematičnega modela
Figure 2: Model of the basic mass stream and co-mixing of the separated waste fractions with the use of the mathematical model

Tabela 2: Ločene frakcije odpadkov za domešavanje
Table 2: Separated waste fractions for co-mixing

Frakcije odpadkov	Masa, *m*/t	*GCV*/(MJ/kg)	*w*(Cl)/%	*ρ*(Cd)/(mg/kg)	*σ*(Hg)/(mg/MJ)	*w*(S)/% [4]
Tekstil	20	30,5	0,23	2	0,10	0,01
Odpadni les	20	7,4	0,19	2	0,32	0,12
Rumene vreče	10	20,9	0,7	2	0,10	0,01

Potencialni prevzemnik je zahteval trdno gorivo razreda 2, kar je za doseganje višje kurilne vrednosti goriva pomenilo potrebo po primešanju k osnovnemu trdnemu gorivu razreda 3. Za pripravo trdnega goriva razreda 2 smo z izločitvenimi merili z uporabo enačbe (5) izračunali maso trdnih goriv iz osnovnih frakcij odpadkov, pri čemer smo dobili trdno gorivo kakovosti, ki jo prikazuje **tabela 4**.

Sicer smo že z uporabo izločitvenih meril pri osnovni masi frakcij odpadkov teoretično dosegli dve kakovosti trdnega goriva, od katerih je eno ustrezalo razredu 2 kot našemu referenčnemu gorivu. S primešanjem frakcije odpadkov iz osnovnega masnega toka k referenčnemu gorivu smo želeli povečati maso referenčnega goriva. Z uporabo enačb od (6) do (10) smo s primešanjem z uporabo osnovnih frakcij odpadkov dosegli povečanje mase referenčnega goriva razreda 2 in zmanjšali maso ostanka trdnega goriva, pri kateri se je zmanjšala vrednost *GCV* in je zato bil uvrščen v razred 4.

Rezultati primešanja v obsegu osnovnega masnega toka frakcij odpadkov so prikazani v **tabeli 5**.

S primešanjem dodatne ločene frakcije odpadkov V4 – tekstil k ostanku trdnega goriva iz osnovne mase frakcij odpadkov po enačbi (11) smo v prvem koraku izboljšali kakovost ostanka trdnega goriva iz osnovne mase frakcij odpadkov, tako da je ostanek trdnega goriva iz razreda 4 prešel v razred 3. S primešanjem vseh dodatnih ločenih frakcij odpadkov k ostanku trdnega goriva iz osnovnega masnega toka frakcij odpadkov smo dobili trdno gorivo razreda 4, vendar z bistveno višjim *GCV*, kot ga je imel ostanek iz osnovnega masnega toka frakcij odpadkov. Vsi drugi parametri so ustrezali razredu 1 oziroma razredu 2.

Rezultate primešanja ločenih frakcij odpadkov k ostanku trdnega goriva iz osnovnega masnega toka prikazuje **tabela 6**.

4 DISKUSIJA

Fizikalno-matematična izhodišča niso upoštevala vseh procesov, ki potekajo pri predelavi med proizvodnjo, kot so na primer mletje in izločevanje anorganskih materialov, temveč smo obravnavali samo vhod in izhod procesa. Matematični model omogoča izračun parametrov trdnega goriva s poljubnim številom frakcij odpadkov, vendar je z vidika tehnološke rešitve doziranja frakcij odpadkov primerno računati z istočasnim doziranjem do maksimalno treh frakcij odpadkov. Za določevanje lastnosti goriva je bil upoštevan zakon o ohranitvi mase, zato so bili za vsak masni tok frakcije odpadkov pomembni vsi parametri.

Ker je proizvodnja goriva zasnovana na mehanski obdelavi, so se lastnosti trdnega goriva izražale samo v velikosti delcev in homogenizaciji. Izločene kovine niso pomenile pomembnega deleža in v matematičnem modelu v masnem toku niso bile upoštevane. Na podlagi analitičnih podatkov laboratorijskih analiz se je njihovo izločanje v procesu kazalo v povečanju vrednosti *GCV* trdnega goriva.

Strokovna literatura za posamezne parametre trdnih goriv obravnava problematiko trdnih goriv parcialno, ne obravnava pa meril, kako doseči konfekcionirano trdno gorivo na podlagi izbire odpadnih materialov, ki imajo vsak zase določene kemijske, fizikalne in energijske lastnosti. V strokovnih člankih, ki obravnavajo področje trdnih goriv, področja uporabe matematičnega modela za izračun kemijskih in fizikalnih lastnosti trdnih goriv ni bilo mogoče najti. Sicer so v strokovni literaturi[13] navedene ugotovitve o tem, da je osnova postopka ocenjevanja lastnosti celotno stanje materialov. Uporaba čiste mehanske separacijske tehnike zagotavlja, da se zmes z vidika materialov vhodnih odpadkov ne preoblikuje in da razpoložljive separacijske tehnike ne puščajo materialov v sistemu. Z uporabo zakona o ohranitvi mas in energije je stanje na vhodu enako stanju vsote izhodnih masnih tokov. Velja enačba:

$$X_{i\text{nput}}\,(\text{S}) = M_{\text{input}} \times C_{\,i\text{nput}}\,(\text{S}) = \sum_{i=1}^{k} MP_i \cdot CP_i(s) \quad (12)$$

pri čemer je:

X – obremenitev

k – število izhodov

C – koncentracija

M – referenčna masa funkcionalne enote (kilogram ostanka na tono vstopnega materiala)

P_1 – indikator izhod 1

P_i – indikator izhod i

S – substanca elementa

S preizkusi je bilo ugotovljeno, da so kemijski elementi, kot so klor, kadmij in svinec, v odpadkih pogosto koncentrirani. Tudi z optimirano tehniko ločevanja je možnost za njihovo zmanjšanje omejena zaradi razdelitve koncentracije teh elementov v različnih komponentah masnega toka odpadkov. V nasprotju s Cd in Pb je prispevek cinka v odpadkih bolj enakomerno porazdeljen. Podatki o koncentracijah nevarnih snovi v odpadkih in njihova porazdelitev v gospodinjskih odpadkih (mešani komunalni odpadki) ter rezultati ločevanja z uporabo različnih tehnik ločevanja kažejo, da so mehanske operacije ločevanja zadostne za izločanje odpadkov, ki vsebujejo nevarne snovi.

Ugotovljeno je, da delež plastike iz mešanih komunalnih odpadkov narašča z ločevanjem le-teh v bobnastem situ od 26,3 % na 57,8 %. Prav tako vsebnost vlage v mešanih komunalnih odpadkih pade s tem načinom ločevanja od 50 % na 40 %, kar je z vidika priprave trdnega goriva pomemben podatek. Vendar pa je vpliv predhodno sortiranih trdnih odpadkov na objekte za pridobivanje energije v različnih državah še vedno negotov zaradi inherentne kompleksnosti sestave trdnih odpadkov.[14]

Študija uporabe RDF je ugotovila, da njegova uporaba v cementnih pečeh namesto premoga ali koksa ponuja okoljske prednosti pri zmanjšanju toplogrednih

Tabela 3: Parametri trdnega goriva z uporabo celotne mase osnovnih frakcij odpadkov
Table 3: Parameters for the solid fuel produced with the total mass of the basic waste fractions

Parameter	Vrednost	Razred
Masa, *m*/kg	200000	
GVC/(MJ/kg)	17,095	3
w(Cl)/%	0,5515	2
σ(Hg)/(mg/MJ)	0,013044861	1
ρ(Cd)/(mg/kg)	1,82	2
w(S)/%	0,045	1

Tabela 4: Trdno gorivo iz osnovnih frakcij odpadkov z uporabo izločitvenih meril
Table 4: Solid fuel produced from basic fraction using the eliminating criteria

Trdno gorivo		Razred 2		Razred 3	
Parameter	Enota	Vrednost	Razred	Vrednost	Razred
masa, *m*	kg	50000		150000	
GVC	MJ/kg	21,7	2	15,56	3
w(Cl)	%	0,550	2	0,552	2
σ(Hg)	mg/MJ	0,0147	1	0,01248	1
ρ(Cd)	mg/kg	2,0	2	1,76	2
w(S)	%	0,12	1	0,02	1

Tabela 5: Trdno gorivo z domešavanjem v obsegu osnovnega masnega toka
Table 5: Solid fuel produced with co-mixing from the basic mass stream

Trdno gorivo		Razred 2		Razred 4	
Parameter	Enota	Vrednost	Razred	Vrednost	Razred
masa, *m*	kg	70731,7		129268,3	
GVC	MJ/kg	24,279	2	13,164	4
w(Cl)	%	0,456	2	0,6036	3
σ(Hg)	mg/MJ	0,0114	1	0,0139	1
ρ(Cd)	mg/kg	2,0	2	1,7215	2
w(S)	%	0,0878	1	0,0216	1

Tabela 6: Trdno gorivo z domešavanjem dodatnih ločenih frakcij odpadkov
Table 6: Solid fuel produced with co-mixing from the additional separated waste fractions

Trdno gorivo		Domešavanje V4		Domešavanje V4, V5 in V6	
Parameter	Enota	Vrednost	Razred	Vrednost	Razred
masa, *m*	kg	149268		179268	
GVC	MJ/kg	15,487	3	14,887	4
w(Cl)	%	0,5535	2	0,521	2
σ(Hg)	mg/MJ	0,0126	1	0,016	1
ρ(Cd)	mg/kg	1,7588	2	1,799	2
w(S)	%	0,02	1	0,049	1

plinov, medtem ko nastanek polutantov v plinastem agregatnem stanju ni pomemben dejavnik.[15] Zanimiva je tudi primerjava med mešanimi komunalnimi odpadki in RDF za primer energijske izrabe na območju Castilla y Leona (Španija). Tako je bila ugotovljena vsebnost vlage v organskem delu mešanih komunalnih odpadkov 58,33 % in v RDF 42,26 %, pri analizi vsebnosti vlage v papirju in kartonu mešanih komunalnih odpadkov pa je ugotovljeno 55,59 % vlage, v RDF pa samo 16,72 %. Posledično temu je bila tudi *GCV* v dostavljenem stanju mešanih komunalnih odpadkov 10,16 kJ/kg, v RDF pa 18,28 kJ/kg.[16]

Proizvajalci trdnih goriv lahko matematični model uporabljajo samo ob izpolnjevanju pogojev za zagotavljanje kakovosti trdnega goriva iz odpadkov v skladu s standardom SIST EN15358:2011 Trdna alternativna goriva – Sistemi vodenja kakovosti,[17] ki vključujejo stalno kontrolo odpadkov na vhodu in produkta trdnega goriva na izhodu z njihovim vzorčenjem ter izvedbo laboratorijskih analiz.

Raziskovalno delo, ki je predstavljeno v tem članku, daje možnost nadaljnje raziskave trdnih goriv predvsem na osnovi ugotovljenih emisij snovi v zrak pri zgorevanju trdnega goriva. Z uporabo teoretičnih preračunov emisij je mogoče izvesti primerjave z eksperimentalno določenimi vrednostmi emisij snovi v dimnih plinih pri zgorevanju trdnega goriva iz odpadkov. Za celovito bilanco transformacije škodljivih snovi pa so bile opravljene tudi analize pepela in žlindre, ki sta ostala po zgorevanju. To omogoča postavljanje matematičnega modela, ki bo napovedoval vpliv zgorevanja posameznega goriva na okolje že na osnovi temeljite analize vzorca trdnega goriva.

Zahvala

Avtorji smo hvaležni Javni agenciji za tehnološki razvoj Republike Slovenije in Evropski uniji oziroma Evropskemu skladu za regionalni razvoj za sofinanciranje tega razvojno investicijskega projekta (RIP 09) z naslovom "Obnovljivi viri energije iz odpadkov – postopki predelave odpadkov v trdno gorivo in njegova energijska izraba s sežigom in uplinjanjem".

Acknowledgement

The authors gratefully acknowledge the Public Agency for Technology of the Republic of Slovenia and the European Union; the European Fund for Regional Development for co-funding this research investment project in the framework RIP 09 with the title "Renewable energy from waste – the processes of waste processing into solid fuel and its energy recovery with combustion and gasification".

5 LITERATURA

[1] DIREKTIVA 2008/98/ES Evropskega parlamenta in Evropskega sveta (19. 11. 2008) – Priloga III
[2] EN 14899:2005; Karakterizacija odpadkov-vzorčenje odpadkov – Okvirno navodilo za pripravo in uporabo načrta vzorčenja
[3] SIST EN 15442:2011; Trdno alternativno gorivo – Metode vzorčenja
[4] SIST EN 15443:2011; Trdno alternativno gorivo – Metode za pripravo laboratorijskega vzorca
[5] SIST TS CEN/TS 15413:2007; Trdno alternativno gorivo – Metode za pripravo testnega vzorca iz laboratorijskega vzorca

[6] SIST EN 15414-3:2011; Trdno alternativno gorivo – Določevanje vsebnosti vlage z metodo sušenja v sušilni komori – 3. del: Vlaga v preizkusnem vzorcu

[7] SIST EN 15400:2011; Trdno alternativno gorivo – Določevanje kurilne vrednosti

[8] ISO 5666:1999, pogl. 5, modif.; metoda za določevanje živega srebra (standard, korigiran z ISO 12846:2012)

[9] SIST EN ISO 17294-2:2005; Določevanje težkih kovin z uporabo induktivno sklopljene plazme z masnim selektivnim detektorjem (ICP-MS)

[10] ASTM D 4239 (metoda C):1997; standardna testna metoda za določevanje vsebnosti žvepla v zgorevalni komori z visokotemperaturnim režimom

[11] SIST EN 15408:2011; Trdna alternativna goriva – Metode za določevanje žvepla (S), klora (Cl), fluora (F) in broma (Br)

[12] Uredba o predelavi nenevarnih odpadkov v trdno gorivo, Ur. l. RS št. 57/2008

[13] V. S. Rotter, T. Kost, J. Winkler, B. Bilitewski, Material flow analysis of RDF Production processes, Waste management, (**2004**), 1005–1021

[14] N. B. Chang, Y. H. Chang, W. C. Chen, Evaluation of heat value and its prediction for refuse-derived fuel, The Science of the Total Environment, (**1997**), 139–148

[15] G. Genon, E. Brizio, Perspectives and limits for cement kilns as a destination for RDF, Waste management, (**2008**), 2375–2385

[16] C. Montejo, C. Costa, P. Ramos, M. C. Marquez, Analysis and comparison of municipal solid waste and reject fraction as fuels for inceneration plants, Applied Thermal Engineering, (**2011**), 2135–2140

[17] SIST EN15358:2011 Trdna alternativna goriva – Sistemi vodenja kakovosti

UDK 621.785.5:620.178
Original scientific article/Izvirni znanstveni članek

ISSN 1580-2949
MTAEC9, 47(1)37(2013)

PROBLEMS ASSOCIATED WITH A ROBOT LASER CELL USED FOR HARDENING

PROBLEMATIKA ROBOTSKEGA LASERSKEGA KALJENJA

Matej Babič[1], Matjaž Milfelner[2], Igor Belič[3], Peter Kokol[4]

[1]Emo-Orodjarna, d. o. o., Bežigrajska cesta 10, 3000 Celje, Slovenia
[2]Tic-Lens, d. o. o., Bežigrajska cesta 10, 3000 Celje, Slovenia
[3]Institute of Metals and Technology, Lepi pot 11, 1000 Ljubljana, Slovenia
[4]University of Maribor, Faculty of Health Sciences, Žitna ulica 15, 2000 Maribor, Slovenia
babicster@gmail.com

Prejem rokopisa – received: 2012-05-29; sprejem za objavo – accepted for publication: 2012-07-30

Laser hardening is a surface-hardening process. It is used exclusively on ferrous materials suitable for hardening, including steel and cast iron with a carbon content of more than 0.2 %. This article describes robot laser hardening, the results of previous work, research and experience with robot laser hardening. The second part of the paper describes the problems associated with robot laser hardening at different angles. We wanted to find the impact of the angles on the hardness of the material. Therefore, we directed the laser beam at different angles, including perpendicular, in the process of hardening. We made test patterns of a standard label on the materials of DIN standard 1.2379.

Keywords: hardening, robot, laser, parameters

Lasersko kaljenje je proces površinskega utrjevanja. Uporablja se izključno za železne materiale, ki so primerni za kaljenje in vsebujejo več kot 0,2 % ogljika. V članku opisujemo robotsko lasersko kaljenje, navajamo rezultate dosedanjega dela in raziskav ter izkušnje z laserskim kaljenjem. Drugi del opisuje problematiko robotskega laserskega kaljenja pri različnih kotih. Želeli smo ugotoviti, kako kot laserskega žarka vpliva na trdoto materiala. Kot laserskega žarka smo spreminjali glede na smer potovanja, kakor tudi pravokotno na smer potovanja laserskega žarka. Naredili smo vzorce standardne oznake po DIN standardu 1.2379.

Ključne besede: kaljenje, robot, laser, parametri

1 INTRODUCTION

Laser hardening[1–5] is a metal-surface treatment process that complements the conventional flame- and induction-hardening processes. A high-power laser[6–10] beam is used to heat the metal surface rapidly and selectively to produce hardened case depths of up to 1.5 mm with hardness values of up to 65 HRc. This has a hard martensitic microstructure providing improved properties, such as wear resistance and increased strength. To harden the workpiece, the laser beam usually warms the outer layer to just under the melting temperature (about 900 °C to 1400 °C). Once the desired temperature is reached, the laser beam starts moving. As the laser beam moves, it continuously warms the surface in the processing direction.[11,12] The high temperature causes the iron atoms to change their position within the metal lattice (austenization). As soon as the laser beam moves away, the hot layer is very rapidly cooled by the surrounding material in a process known as self-hardening. This rapid cooling prevents the metal lattice from returning to its original structure and producing martensite. The laser beam hardens the outer layer or case of the workpiece. The hardening depth of the outer layer is typically from 0.1 mm to 1.5 mm. However, on some materials, it may be 2.5 mm or more. A greater hardening depth requires a larger volume of the surrounding material to ensure that the heat dissipates quickly and the hardening zone cools fast enough. Relatively low power densities are needed for hardening. At the same time, the hardening process involves the treatment of extensive areas of the surface. That is why the laser beam is shaped so that it irradiates an area that is as large as possible. This irradiated area is usually rectangular. Scanning optics are also used in hardening. They are used to move a laser beam with a round focus back and forth very rapidly, creating a line on the work piece with a power density that is virtually uniform. This method makes it possible to produce hardened tracks up to 60 mm wide.

2 EXPERIMENTAL METHOD AND MATERIALS PREPARATION

A robot laser cell can be used to provide the heat necessary for a treatment process. The absorbed radiation from the laser of the laser cell heats up the surface layer to a temperature where austenite can form. In this work we research how the parameter of angle impacts on the hardness of the material. We used a RV60-40 robot laser cell from Reis Robotics, which is a leading technology company for robotics and system integration. The articulated-arm robot series is the most important robot kinematics for industrial use. As 6-axes universal robots with high path speeds and large work envelopes the RV-robots are especially suited for the

tough demands of path-related tasks. The design based on FEM and CAD stands out due to its excellent static and dynamic behaviour. Their robotic automation solutions are used by all major application fields, such as solar energy, foundry, welding and hardening. The Reis Robotics group comprises three German subsidiaries and eight international subsidiaries as well as representative agencies in many countries. The laser beams have a rectangular shape. We used 5 mm × 13 mm optics, which means that with this optic we hardened a width of approximately 13 mm. Robot lasers work continuously with wavelength of 700–1000 nm. The maximum power of a robot laser cell is 3000 W. However, we hardened specimens with a 2000 W output power. The specimen was material of DIN standard 1.2379. We hardened the material at 2 mm/s using 1100 °C. There are different and interesting problems regarding the robot laser hardening of metals. The problem can be represented geometrically, as seen in **Figures 1** to **3**.

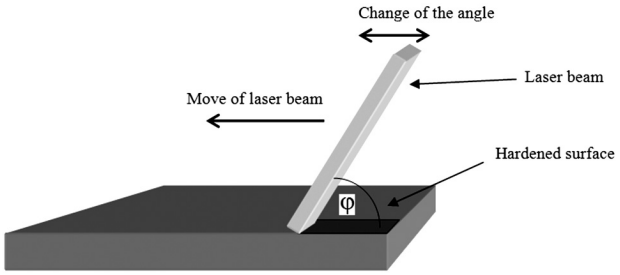

Figure 1: Problem 1 of the robot laser hardening: the variation of the incidence angle $\varphi \in (0°, 90°)$ between the right-hand side of laser beam and the material surface

Slika 1: 1. Primer laserskega kaljenja: spreminjanje vpadnega kota $\varphi \in (0°, 90°)$ med desno stranjo laserskega žarka in površino materiala

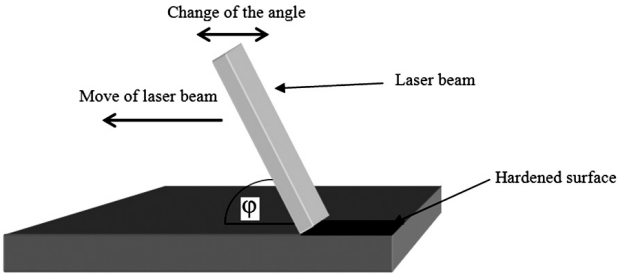

Figure 2: Problem 2 of the robot laser hardening: the variation of the incidence angle $\varphi \in (0°, 90°)$ between the left-hand side of laser beam and the material surface

Slika 2: Drugi primer laserskega kaljenja: spreminjanje vpadnega kota $\varphi \in (0°, 90°)$ med levo stranjo laserskega žarka in površino materiala

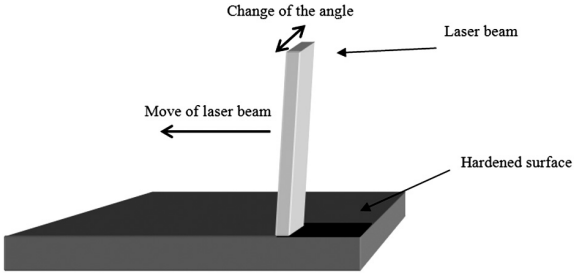

Figure 3: Problem 3 of robot laser hardening: the lateral incidence angle of the laser beam on the material surface and the beam movement direction

Slika 3: Tretji primer laserskega kaljenja: spreminjanje lateralnega vpadnega kota laserskega žarka glede na površino materiala in smer gibanja žarka

Similar problems arise in the following situation. We harden materials at an incidence angle of $\varphi \neq 90°$. **Figure 3** shows the situation where we changed the angles in different directions. We see that the upper part of the beam has a longer travel time than the lower part of the beam. This means that the lower part of the hardened piece is better than the upper. The workpiece will not be evenly hardened and the final result of the laser hardening will not be good.

To analyse the results we used the method of intelligent system, i.e., a neural network. Neural networks are model-less approximators; they are capable of performing an approximation – modelling operations regardless of any relational knowledge of the nature of the modelled problem. This relational knowledge is typically represented by a set of equations describing the observed variables and constants used to describe the system's dependencies. A common use of neural networks is multi-dimensional function modelling[13,14], i.e., the re-creation of the system's behaviour on the basis of a set of known discrete points representing the various states of the system. We used feedforward neural networks with supervised training algorithms.

3 RESULTS

We are interested in the hardness of the robot laser-hardened material as we change the incidence angle of the laser beam on the substrate material. We have two options. Firstly, we can change the angle with regard to the direction of the laser beam. Here, we also have we two options. In this situation we have conducted tests for angles of $\varphi \in \{15°, 30°, 45°, 60°, 75°, 90°\}$ between the right-hand side of the laser beam and the material surface (**Figure 1**). However, we have conducted tests for angles of $\varphi \in \{15°, 30°, 45°, 60°, 75°, 90°\}$ between the left-hand side of laser beam and the material surface (**Figure 2**). This means that we made six tests for each option. In these two options the width of the hardening is unchanged. Second, we can change the angle with regard to the perpendicular direction of the laser beam. We have conducted tests for angles of $\varphi \in \{15°, 30°, 45°, 60°, 75°, 90°\}$. In these options we have different widths of hardening, because we change the angle with regard to the perpendicular direction of the laser beam. The results are presented in **Figure 9**. We varied the amounts of power supplied to the laser beam when we made tests on the tool steel 1.2379. In all the tables we present the hardness before hardening, after hardening and the average hardness after hardening.

3.1 Variation of the incidence angle with regard to the direction of the laser beam

Again, we have two options (**Figures 1** and **2**). First, we change the angle with regard to the direction of the laser beam (the problem is presented in **Figure 1**). The results of the measurements are shown in **Table 1**.

Table 1: Relationship between the angles and the hardness
Tabela 1: Povezava med kotom φ in trdoto

φ/°	Hardness after hardening (HRc)	Average hardness after hardening (HRc)	Hardness before hardening (HRc)
15	62, 63, 62, 56	61.5	9
30	59, 59, 59, 63, 62	60.4	9
45	61, 61, 61 ,60, 61	60.8	9
60	61, 62, 61, 50, 56	58	9
75	61, 62, 61, 50, 61	59	9
90	61, 61, 61, 48, 62	58.6	9

All the data from **Table 1** we analysed with the neural network. **Figure 4** shows the relationship between the incidence angle and the hardness.

Second, we changed the angle with regard to the direction of the laser beam (the problem is presented in **Figure 2**). The results of the measurements are shown in **Table 2**.

Table 2: Relationship between the angles and the hardness
Tabela 2: Povezava med kotom φ in trdoto

φ/°	Hardness after hardening (HRc)	Average hardness after hardening (HRc)	Hardness before hardening (HRc)
15	61, 69, 52, 57, 56	55	9
30	54, 57, 58, 56, 56	56.2	9
45	51, 56, 56, 49, 54	53.2	9
60	52, 55, 54, 54 ,56	54.2	9
75	50, 55, 56, 23, 43	45.4	9
90	58, 59, 57, 60, 59	58.6	9

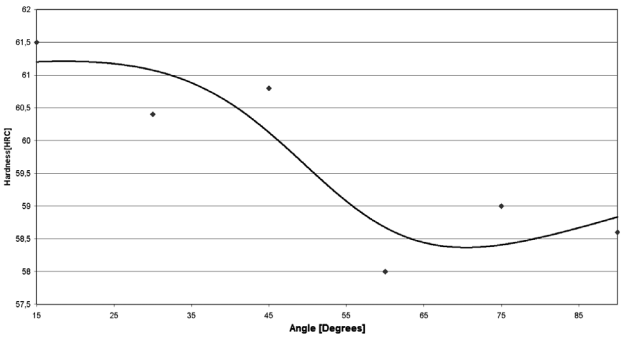

Figure 4: Relationship between the angles and the hardness. The modelling of the relationship was obtained using the four-layer neural network (from **Table 1**).
Slika 4: Razmerje med vpadnimi koti in trdoto. Modeliranje razmerja je bilo narejeno s štiri-nivojskim nevronskim sistemom (podatki so v **tabeli 1**).

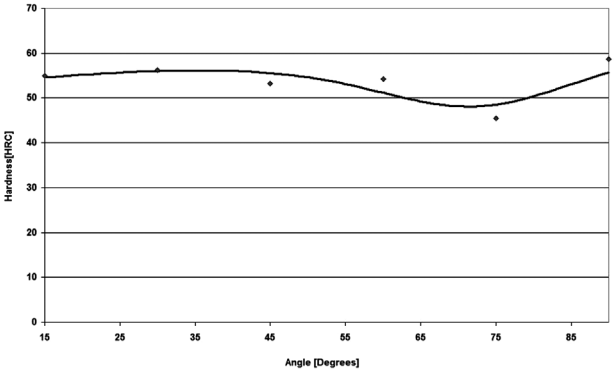

Figure 5: Relationship between the angles and the hardness. The modelling of the relationship was obtained using the four-layer neural network (from **Table 2**).
Slika 5: Razmerje med vpadnimi koti in trdoto. Modeliranje razmerja je bilo narejeno s štiri-nivojskim nevronskim sistemom (podatki so v **tabeli 2**).

All the data from **Table 2** we analysed with the neural network. **Figure 5** shows the relationship between the incidence angles and the hardness.

3.2 Variation of the incidence angle with regard to the perpendicular direction of the laser beam

In this case we changed the angle with regards to the perpendicular direction of the laser beam (**Figure 3**). We chose the same angles of $\varphi \in \{15°, 30°, 45°, 60°, 75°,$

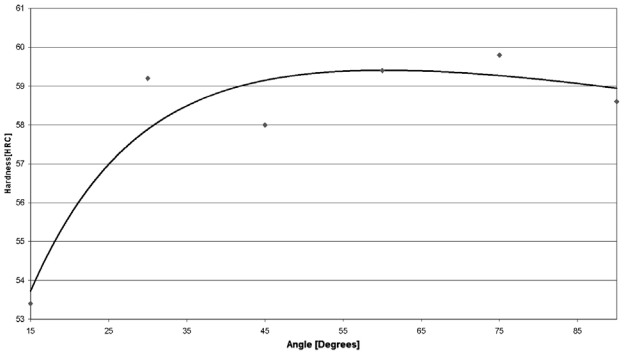

Figure 6: Relationship between the angles and the hardness. The modelling of the relationship was obtained using the four-layer neural network (from **Table 3**).
Slika 6: Razmerje med vpadnimi koti in trdoto. Modeliranje razmerja je bilo narejeno s štiri-nivojskim nevronskim sistemom (podatki so v **tabeli 3**).

Table 3: Relationship between the angles and the hardness
Tabela 3: Povezava med kotom φ in trdoto

φ/°	Hardness after hardening (HRc)	Average hardness after hardening (HRc)	Hardness before hardening (HRc)
15	49, 48, 49, 61, 60	53.4	9
30	56, 57, 57, 63, 63	59.2	9
45	54, 56, 55, 64, 61	58	9
60	56, 57, 58, 63, 63	59.4	9
75	57, 57, 59, 63, 63	59.8	9
90	57, 60, 58, 58, 60	58.6	9

90°}. There is no need to consider two options since those options are symmetrical.

All the data from **Table 3** we analysed with the neural network. **Figure 6** shows the relationship between the incidence angles and the hardness.

4 DISCUSSION

By using angular functions we can calculate the width of the hardening at a certain angle. Here, the following information is already known: the width of the optics (d) and the angle (φ) under which the hardening is conducted. The hardening width is calculated. The width of the beam optics represents one side of a right-angle triangle, the angle (φ) of hardening is the right-angle triangle's opposite side, which was marked with the width of the optics (d). The beam hardening of the workpiece is the hypotenuse of the right-angle triangle, denoted by x. After delivery the sinus is

$$\sin \varphi = d/x \ , \ d \in \{5, 8, 13, 16, 23, 28\} \text{ mm}, \quad \varphi \in (0°, 180°) \qquad (1)$$

By changing the angle φ of the longitudinal hardening of the workpiece, we can achieve different degrees of hardness in the materials (section 3.1). By changing the angle φ with regard to the transverse hardening and the different sizes of optics, we can achieve a different width of hardening at a given time. **Figure 7** shows that the maximum power is used when the laser beam falls below the minimum angle in our study, i.e., 15°. In this position we achieve the area of hardening, but for that we require more time and power. An imprecisely measured width due to the hardening occurs as a small deviation from the calculated width of the hardening with equation (1). However, the measurement results are fairly accurate. We are interested in conditions that return better results. In our case the most favourable solution to the problem is the hardness of the material.

Figure 8 shows the relationship between the hardness and the angle of hardening. In this graph we can see a comparison of the three different types of robot laser hardening by changing the angle of the laser beam.

Figure 9 presents the relationship between the width and the angle of hardening with regards to the perpendicular direction of the laser beam. We can see that by increasing the angle, the width of the hardening decreases, which we can prove with equation (1).

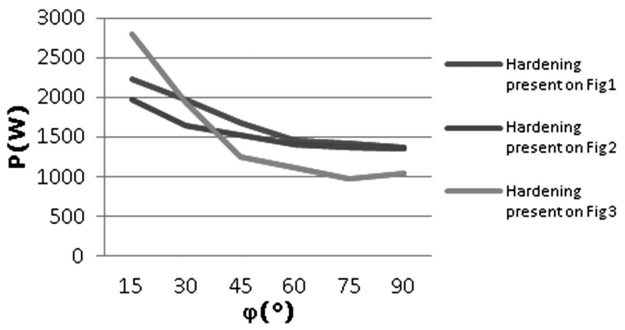

Figure 7: Relationship between the power and the angles of hardening
Slika 7: Razmerje med močjo in kotom, pod katerim kalimo

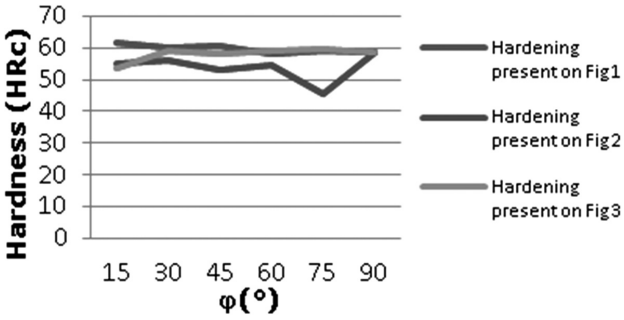

Figure 8: Relationship between the hardness and of the angle of hardening
Slika 8: Razmerje med trdoto in kotom, pod katerim kalimo

We analysed the graph with two different methods. First, we used linear regression. Second, we used the modelling of the relationship that was obtained by the four-layer neural network. For **Figures 4, 5** and **6** we calculated the correlation coefficient, which represents the size of the linear connection of the hardness and the fractal dimension. The correlation coefficient R for graph 1 is –0.8324, for graph 3, –0.88263 and for graph 5, 0.65799. We can see that the correlation coefficients are not similar. Because the correlation coefficients are not 0, the variable hardness and the angles of hardening are correlated. Smaller values of the angles tend to be linked to the hardness values, which tell us that there is a negative correlation coefficient. This is presented in **Figures 4** and **6**. But in **Figure 5** we have a different situation – a positive correlation coefficient. The purpose of this work has been to study how the angles of the robot laser cell impact on the hardness of the specimens. The presented problem could be solved in order to modify the laser beam's intensity across the width. This means that the first laser beam is divided into several parts. Then each part of the laser beam is divided into the

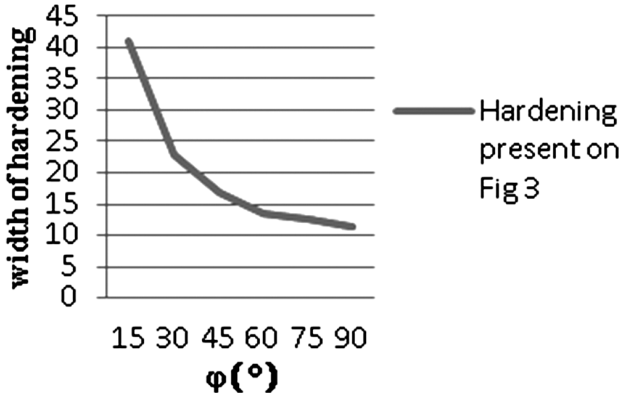

Figure 9: Relationship between the width and the angle of hardening with regards to the perpendicular direction of the laser beam
Slika 9: Razmerje med širino kaljenja in kotom kaljenja glede na pravokotno smer kaljenja laserskega žarka

specified strength. The part of the laser beam that made the longest journey gave most of the power to that part of the beam, and the part that had the shortest path to the device, gave the smallest amount of laser beam intensity.

5 CONCLUSION AND FUTURE WORK

Robot laser hardening is very useful in the automotive (e.g., machine parts for transmission shafts, axles, running surface, torsion springs, gears), military and aerospace industries. The process has several advantages over conventional induction hardening. However, even in the robot laser-hardening process there are problems, as described in this paper. Thus, we still have enough unsolved problems in robot laser hardening. Robot laser cells have several parameters that affect the final result of the hardening. These laser parameters are the power, the energy density, the focal distance, the energy density at the focus, the focal position, the temperature and the speed of germination. In the future we want to explore how different angles of the laser beam in the hardening process affect the hardened patterns in:

- dual robot laser-beam hardening (laser beam is divided into two parts),
- pixel robot laser hardening,
- robot laser hardening with changes to the velocity and the temperature of the laser beam.

6 REFERENCES

[1] G. E. Totten, Steel Heat Treatment Handbook, 2nd ed., CRC Press, 2006

[2] J. Grum, P. Žerovnik, R. Šturm, Measurement and Analysis of Residual Stresses after Laser Hardening and Laser Surface Melt Hardening on Flat Specimens, Proceedings of the Conference “Quenching ’96", Ohio, Cleveland, 1996

[3] H. W. Bergmann, Current Status of Laser Surface Melting of Cast Iron, Surface Engineering, 1 (**1985**) 2, 137–156

[4] W. W. Daley, Laser processing and analysis of material. Chapter 1: Laser and Laser radiation, Plenum Press, New York 1983, 158–162

[5] V. G. Gregson, Chapter 4: Laser and heat treatment. In Laser Materials Procesing, M. Bass, Ed.; Materials Procesing Theory and Practices, North-Holland Publishing Company, Amsterdam 1983, 201–234

[6] J. Grum, R. Šturm, Calculation of Temperature Cycles Heating and Quenching Rates During Laser Melt – Hardening of Cast Iron. In: LAJL Sarton, HB Zeedijk eds., Proc. Of the 5th European Conf. On Advanced Materials and Processes and Applications, Materials, Functionality&Desing, vol. 3. Surface Engineering and Functional materials. Maastricht, NL 1997, 3/155 – 3/159

[7] S. L. Engel, Surface hardening – basics of laser heat treating. In: E. A. Metzbower, ed., Source Book on Applications of the Laser in Metalworking, American Society for Metals, Metals Park, Ohio 1981, 149–171

[8] A. Tizian, L. Giordano, E. Ramous, Laser surface treatment by rapid solidification. In Laser in Materials Processing. E. A. Metzbower, Ed.; Conference Proceedings; American Society for Metals: Metals Park, Ohio, 1983, 108–115

[9] J. Meijer, M. Seegers, PH Vroegop, GJW Wes. Line hardening by Low-Power CO_2 Laser. In: C. Albright, ed. Laser Welding, machining and Materials Processing. Proceedings of the International Conference on Applications of Laser and Electro-Optics "ICALEO’85" San Francisco, 1985, Berlin: Springer-Verlag, Laser Institute of America, 1986, 229–238

[10] J. Grum, R. Šturm, Properties of Laser Surface Melt Hardening on Cast Iron, Conference on Laser Treatment of Materials ECLAT ’96, Stuttgart, Germany, 501–508

[11] J. Grum, R. Šturm, P. Žerovnik, Residual Stresses of Overlapping Laser Melt Hardening of Gray and Nodular Iron, Fourth European Conference on Residual Stresses, Cluny en Bourgogne, Francija, 1996, 144–146

[12] S. Mordike, H. B. Pruel, H. Szengel, Laser Oberflächenbehandlungeine Productionsreifes Verfahren für vielfältige Anwendungen, Nove tehnologije toplinske obrade metala, Međunarodno savetovanje, Zagreb, Croatia, 1990, 1–12

[13] D. Tikk, L. T. Kóczy, T. D. Gedeon, A survey on universal approximation and its limits in soft

[14] M. ElHafnawi, M. Mysara, Recurrent Neural Networks and Soft Computing, Intech, Rijeka, 2012

UDK 621.7:621.7.019
Original scientific article/Izvirni znanstveni članek

ISSN 1580-2949
MTAEC9, 47(1)43(2013)

A BURNISHING PROCESS BASED ON THE OPTIMAL DEPTH OF WORKPIECE PENETRATION

POSTOPEK GLADILNEGA VALJANJA NA OSNOVI OPTIMALNE GLOBINE PRODIRANJA V OBDELOVANEC

Djordje Vukelic[1], Dragomir Miljanic[2], Sasa Randjelovic[3], Igor Budak[1], Dragan Dzunic[3], Milan Eric[3], Marko Pantic[3]

[1]University of Novi Sad, Faculty of Technical Sciences, Department for Production Engineering, Trg Dositeja Obradovica 6, 21000 Novi Sad, Serbia
[2]Metalik DOO, Trebješka 6/26, 81400 Niksic, Montenegro
[3]University of Kragujevac, Faculty of Engineering, Department for Production Engineering, Sestre Janjic 6, 34000 Kragujevac, Serbia
vukelic@uns.ac.rs

Prejem rokopisa – received: 2012-06-26; sprejem za objavo – accepted for publication: 2012-08-27

This paper deals with the problem of defining the trajectory of a stiff burnishing tool that would be optimal from the point of view of surface quality. The basic goal of this work is to gain an insight into the very process from the microscopic aspect, with the primary focus on material flow and roughness variations. Based on theoretical considerations, we planned an experiment with the aim to verify the initial hypotheses about the analysis of roughness change and a determination of the optimal depth of the workpiece penetration. Through matching and the superposition of surface profiles formed at various contact pressures, i.e., various burnishing forces and various penetration depths of the burnishing ball into the profile roughness, the phenomenon of roughness change was explained. Theoretical assumptions related to a determination of the optimum tool trajectory have largely been confirmed from the point of view of surface quality. The balls within the stiff tool system, which follow a predetermined depth of penetration into the roughness profile, very likely provide optimum surface quality, regardless of the initial machining. Based on experimental results, it is highly possible that the depth of the penetration of tool (burnishing ball) should equal the roughness profile height of the previously machined surface. The analysis of results obtained by the measurement of the surface roughness and the super-positioning of the profiles obtained by burnishing with various burnishing forces, significantly contributed to the explanation of the roughness peaks' deformation phenomenon. The proposed burnishing method could be of special importance in the burnishing of roughly machined surfaces, where R_p reaches high values. Investigations presented in this paper open a number of new directions, such as the testing of a stiff tool system with various workpiece materials and burnishing regimes, with different surface roughnesses as the result of the initial machining. We believe that the proposed model can significantly improve our present knowledge of the burnishing process.

Keywords: burnishing, surface quality, stiff tool system, profile peaks, profile valleys

Članek obravnava problem določanja optimalne trajektorije togega gladilnega orodja glede na kvaliteto površine. Osnovni cilj tega dela je vpogled v postopek obdelave na mikroskopskem nivoju, osredinjen na tečenje materiala in spreminjanje hrapavosti površine. Na osnovi teoretičnega raziskovanja so avtorji pripravili preizkus za potrditev začetne hipoteze o spremembi hrapavosti in določanju optimalne globine prodiranja v obdelovanec. Z usklajevanjem in predpostavljanjem profila površine, ki nastane pri različnih pritiskih, to je z različnimi silami pri gladilnem valjanju in za različne globine prodiranja gladilnih kroglic na profil hrapavosti, je bil pojasnjen pojav spreminjanja hrapavosti. Teoretične predpostavke za določanje optimalne poti orodja so bile potrjene s stališča kvalitete površine. Kroglice v togem orodju, ki sledijo vnaprej določenemu prodiranju v profil hrapavosti, zelo verjetno zagotavljajo optimalno kvaliteto površine, ne glede na predhodno obdelavo površine. Na osnovi eksperimentalnih rezultatov je najbolj verjetno, da naj bi bila globina prodiranja orodja (gladilne kroglice) enaka višini profila hrapavosti predhodno obdelane površine. Analiza rezultatov, dobljenih z meritvami hrapavosti površine, dobljene pri gladilnem valjanju z različnimi silami gladilnega valjanja, je pomembno prispevala k razjasnitvi pojava hrapavosti. Predlagana metoda glajenja je lahko pomembna pri gladilnem valjanju grobo obdelanih površin, kjer R_p dosega velike vrednosti. Raziskave, predstavljene v tem prispevku, odpirajo številne nove smeri, kot so preizkušanje sistemov togih orodij z različnimi materiali obdelovancev in režimi gladilnega valjanja pri različnih hrapavostih iz predhodne obdelave. Avtorji menijo, da predlagani model lahko pomembno prispeva k sedanjemu poznanju postopkov glajenja površin.

Ključne besede: gladilno valjanje, kvaliteta površine, sistem togega orodja, profil vrhov, profil dolin

1 INTRODUCTION

In manufacturing industry, surface roughness plays a vital role in product performance. Regardless of whether a product is shaped with or without chip removal, there are a number of factors that influence workpiece surface roughness, such as workpiece characteristics (physical and mechanical properties, chemical composition, micro-geometry, macro-geometry, etc.), machining equipment (stiffness, kinematics, sensitivity to heat transfers, etc.), tool (material, shape, surface quality, rigidity, wear, etc.), cooling and lubricating agent (chemical composition, viscosity, method of application, etc.), as well as the characteristics of the machining or forming process (strain, strain rates, stress distribution inside a workpiece, heat generation, etc.).[1–3] In addition to numerous machining processes (milling, grinding, polishing, honing, lapping) which contribute to a lower surface roughness,[4] there is also the burnishing process.

Ball/roller burnishing is a cold-finishing process without chip removal that plastically forms the surface layer of a workpiece. The purpose of this finishing process is not to achieve a dimensional accuracy but a surface quality with appropriate roughness,[5–10] micro-

hardness,[11–13] wear and corrosion resistance,[14–16] fatigue- and tensile strength.[14,15,17] Furthermore, residual tensile surface stresses, which are the result of previous machining (turning, milling, etc.), are transformed by burnishing into compressive stress, thus improving several mechanical properties.[17–20] The penetration depth of compressive stresses as well as the thickness of hardened surface layer depend on the workpiece material and the applied loads. Compressive stresses decrease from the workpiece surface to the interior, while the penetration depth can reach up to 1 mm, depending on the workpiece material and the loads. Such a treatment achieves a smooth surface with a hard layer on the workpiece surface, which is the result of the deformation strengthening caused by intensive plastic deformation of the surface layer. It also diminishes the surface defects (as the result of surface plastic deformation) and modifies the surface microstructure.[21–23] Among the advantages of ball/roller burnishing are flexibility, cost-effectiveness and the possibility to use simple machining equipment.

In burnishing, the working part of the tool (hard ball or roller) is rolled over workpiece surface. As the result of rolling over the surface, high contact (Hertz) pressures occur, which overstep the yield stress, leading to plastic forming of the surface layer. Roughness peaks are deformed, and through plastic flow we begin to fill the roughness valleys between them, evening out the texture of the surface roughness.

Burnishing can be used on workpieces of various materials, such as the bronze,[24] aluminum[5,17,18,25–27] and various steels.[7,9,10,16,20–23] Brinksmeier et al.[21] showed that the burnishing of workpieces with a large content of unstable austenite can lead to a deformation-induced martensitic transformation. This proved that it is possible to include martensitic transformation in a mechanical surface treatment without introducing additional thermal processes. Besides using burnishing on various material workpieces, this process can also be applied on workpieces of various geometries, which makes it practical for treating outer and inner cylindrical surfaces as well as small- and large-area flat surfaces.

The tools that are used in this process feature a ball or a roller as the working element whose design should provide smooth rolling over the workpiece surface, without sliding and the occurrence of adhesive bonding during work. There are various design solutions that provide the free rolling of the working element, using backing-up balls[17,24] or roller bearings, as is the case in this work. The force with which the ball presses against the workpiece surface is most often regulated by calibrated springs,[24–27] although different solutions also exist, featuring pressurized fluid,[21–23,28] flexible tool holders,[29] etc. In addition, there are tool carriers that are specially designed for application on large-area flat surfaces, which reduce the processing time while being able to accommodate several simple burnishing tools.[17,30]

Numerous researchers have studied this process, investigating the influence of ball/roller material and dimensions, workpiece material, tool geometry, and process parameters, i.e., the burnishing speed, feed, pressure force, and number of passes. There are a number of papers that investigate the optimization of process parameters.[10,12,18,19,24–26] However, achieving an optimum set of burnishing parameters for a specific workpiece material requires a large number of experiments. In order to limit that number, Response Surface Methodology (RSM)[17] and the Taguchi method[24] are employed. For this reason it is very important to develop an appropriate mathematical model that predicts the surface-quality parameters with the required accuracy.[17,30,31]

Furthermore, there are a number of papers that compare burnishing to alternative processes that provide similar output results.[9,14,32–34] Also, some authors have investigated the surface quality achieved by burnishing, considering previous machining. For example, Bouzid et al.[35] have established that the best burnishing results are achieved with grinding as the initial machining. There are some authors who used finite-element analyses (FEA) to model the burnishing process, achieving satisfactory results.[34,36]

The papers analyzed in this section allow us to conclude that the burnishing force is the most influential parameter regarding surface roughness, hardness, thickness of the hardened layer, as well as the likelihood of surface damage (layer peeling) during processing. Gharby et al.[30] have investigated the burnishing of AISI 1010 steel plates and established a limit of 400 N burnishing force, stating that above this limit the workpiece surface layers begin to peel off. The same author[17] conducted experiments on 1050A aluminium and established an optimal burnishing force of 115 N, pointing out that a combination of large burnishing forces and large feeds deteriorates the surface roughness. Most of the investigations dealing with this subject varied the burnishing force within the range 0–400 N. In this paper we focused on the influence of the burnishing force on the surface roughness, while the force was varied within the range 0–450 N.

The optimal forces are determined for specific workpiece material types and their characteristics. From the reviewed literature it can be concluded that the burnishing force is used as an optimization parameter. However, considering the very burnishing process (surface strengthening and surface quality), it is better to consider the magnitude of the contact pressure between the burnishing ball and the workpiece surface as an optimization parameter. A numerical determination of the magnitude and the distribution of contact pressures requires data on the ball/roller radius, the radius of workpiece surface curvature (in the case that the burnishing is performed on a lathe, it is the billet radius, otherwise, for flat surfaces, an infinite radius of curvature is assumed), and the data on the module of elasticity and the Poisson

coefficient for the workpiece and the ball/roller material. However, most often the available literature on the subject of burnishing does not provide these data. Bearing in mind that the profiles of the machined surfaces are inherently stochastic, it is extremely difficult to determine the values of the contact pressures with the required certainty. All this considered, most investigators of burnishing process choose to consider the burnishing force as the parameter of influence, rather than the more relevant contact pressure.

Considering the large number of material types in industrial applications and the wide range of their properties, the broader application of the burnishing process would require an extensive database with the optimal contact pressures for all types of materials. This is especially true if one considers that the optimal contact pressure is not only related to the workpiece material characteristics but also to the process parameters (feed, number of passes, initial surface quality, etc.).

For that reason, the focus of this investigation is placed on establishing the depth to which the stiff burnishing tool penetrates the roughness valleys, i.e., the optimal value for this depth which, considering the force magnitude and other process parameters, provides near-optimal surface quality.

The available references mostly agree on ranking the influential parameters (burnishing force, feed, number of passes and other factors) based on their relative impact on the surface quality. However, an optimal surface roughness can be achieved at various levels of burnishing forces. Therefore, optimal burnishing forces depend on the workpiece material properties and the ball/roller diameter, the burnishing parameters and the initial surface quality. It is worth noting that the investigations published so far have not looked into the phenomenon of roughness peaks, which leaves space for an investigation into the changes that take place in the surface roughness during the burnishing.

The initial hypothesis in this investigation supposes that it is possible to define a near-optimal penetration depth of the burnishing tool into the workpiece roughness profile, which would result in a near-optimal surface quality, depending on the magnitude of the burnishing force and other burnishing parameters.

Within this investigation, experiments were conducted with the aim to verify the initial hypotheses pertaining to an analysis of the surface topography changes and a determination of the near-optimal tool trajectory. By monitoring the changes that take place in the roughness profiles at various depths of tool penetration into the roughness valleys, an optimal penetration depth was determined that corresponds to the minimal surface roughness (R_a). In these experiments a specially designed stiff tool system was employed. It should be noted that the phenomenon of workpiece surface strengthening was not within the scope of this investigation. As previously discussed, this study is dealing primarily with the problem of workpiece surface quality in burnishing, and also looks into the problem of optimizing the surface quality as a function of tool (ball) penetration depth into the workpiece surface roughness profile. Finally, experimental investigations were performed on a tempered steel.

2 THEORETICAL CONSIDERATIONS

In this section theoretical considerations of the burnishing process are presented as the rolling of a ball over the roughness peaks on the previously machined workpiece (**Figure 1**). The burnishing is performed with a tool system of high stiffness, consisting of a ball with a defined radius R, mounted on a carrier that provides free rolling.

During the burnishing process the burnishing ball is also exposed to lateral forces. The theoretical model proposed in this paper does not consider these forces for the following reasons:

- The rolling resistance of the ball during relative motion over the workpiece surface represents the lateral force. This force can be neglected, considering the 0.001 order of magnitude of the rolling resistance coefficient, as well as the relatively high ratio between the normal (vertical) load and the rolling resistance.
- The remaining lateral forces can also be neglected if one considers the exclusively large ratios between the ball radius and the maximum surface profile peak height, which is often the case in ball burnishing. In such conditions the angle between the lines drawn from the ball centre, connecting the two points of ball/profile contact, is very small, which means that the vertical load on the burnishing ball is predominant, as illustrated in **Figure 2**.

The considered model pertains to static loads, neglecting the dynamic force component. This is justified in cases when burnishing is performed at relatively low

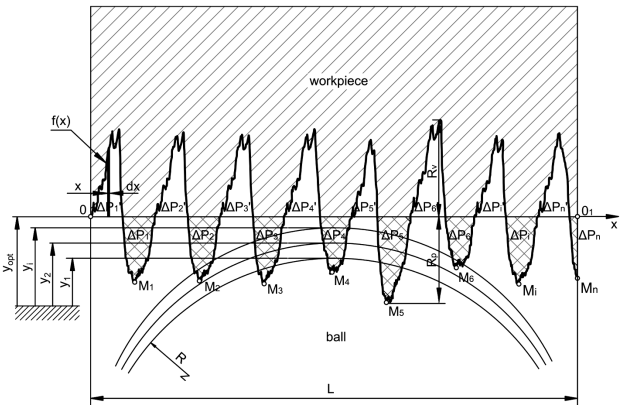

Figure 1: Theoretical analysis of the burnishing process based on a stiff tool system

Slika 1: Teoretična analiza postopka gladilnega valjanja, zasnovanega na sistemu togega orodja

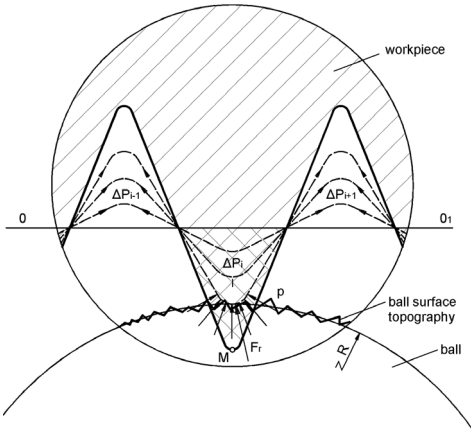

Figure 2: The contact zone during ball burnishing and the supposed directions of material flow
Slika 2: Kontaktno področje med procesom gladilnega valjanja in predvidena smer toka materiala

speeds, which is the case in this experimental investigation. The authors maintain that, given the discussed restrictions, the developed model can prove useful in clarifying the phenomenon of workpiece surface profile variations at various penetration depths of a stiff tool system.

Depending on the ball radius, the roughness pitch and the roughness form, the contact between the ball and the workpiece is established over one or more roughness peaks (neighbourhood of points M_1, M_2, ... M_n). In the course of the ball's penetration into the roughness profile, over the planes parallel to OO_1 axis, the area of the contact surface between the ball and the roughness peaks increases. For a predefined tool displacement, y_i, (tool movement into roughness profile, from a reference point) there follows: $F(y_1) \geq F(y_2) \geq ... \geq F(y_i)$, where $F(y_i)$ is the force corresponding to the y_i coordinate.

If the goal is to achieve the maximum surface quality, it is essential to establish the depth, y_{opt}, which represents the optimal tool penetration into the roughness profile.

One of the possible models of material flow in the contact zone during burnishing is presented in **Figure 2**. Due to the high contact pressures that exceed the yield stress, roughness peaks begin to flow and gradually fill the valleys. It is well known that surface strengthening should be the most pronounced in the layers closer to the profile peaks. In other words, the intensity of the surface strengthening drops towards the profile valleys. This results in the fewer hard material layers being suppressed towards the profile valleys by the layers of greater hardness.

As the tool penetration depth, y, increases, the roughness valleys are filled. We supposed in this work that the tool penetration depth y should be determined based on the recorded surface roughness profile prior to burnishing, according to:

$$y \approx R_p \tag{1}$$

where: R_p is the maximum height of the surface roughness profile before burnishing. The resulting equality is:

$$\sum_{i=1}^{i=n} \Delta P_i \cong \sum_{i=1}^{I=n} \Delta P_i' \tag{2}$$

where ΔP_i is the surface area of i-th peak relative to the mean profile line, $\Delta P_i'$ is the surface area of i-th valley relative to mean profile line, that is:

$$\int_0^L f(x)\mathrm{d}x\Big|_{f(x)<0} \cong \int_0^L f(x)\mathrm{d}x\Big|_{f(x)>0} \tag{3}$$

Evidently, the roughness profile curve of the previously machined surface (prior to burnishing) does not have an analytical function, $f(x)$. However, based on the numerical data obtained by modern devices for surface-roughness measurements it is possible to check whether the condition of approximate equality between the surface areas of the profile peaks and the valleys processed by burnishing. This should require dedicated software, which is one of the goals for future investigation. The assumptions made in this work claim that the optimal surface quality in burnishing of previously machined surfaces is achieved for a tool penetration depth that equals the maximum peak height, R_p, which roughly conforms with the condition of equality between the surface areas of the roughness peaks and valleys. These assumptions are based on the following facts:

- The material which flows along the surface roughness peaks should be allowed some space to deposit (**Figure 2**). The condition of equality between the surface areas of the peaks and valleys theoretically allows a simultaneous decrease of the roughness peaks, R_p, and the roughness valleys, R_v.
- When the tool (ball) is displaced for y_{opt} relative to some reference location into the roughness profile, the material will flow from the peaks, filling the valleys and leaving the profile without additional peaks.
- Presumably, the flow of material in the surface peaks predominantly occurs through the widening and narrowing of peak profiles. This claim is supported by assumption that, due to the large ratio of the ball radius (R) and the relatively small feeds used in the initial machining, the resulting contact force that compresses the profile peaks probably assumes a direction normal to the mean profile line (**Figure 2**). Thus, regardless of the stochastic nature of the initial surface roughness profile, it is realistic to expect that the proposed burnishing method, based on a stiff tool system, will yield a better surface quality compared to the burnishing tools that operate with a constant force (provided by spring mechanisms). Due to variations in the material resistance, such tools oscillate considerably, which represents the source of the additional roughness and profile waviness.

To confirm the theoretical assumptions, **Figure 3** presents the results of preliminary investigations that

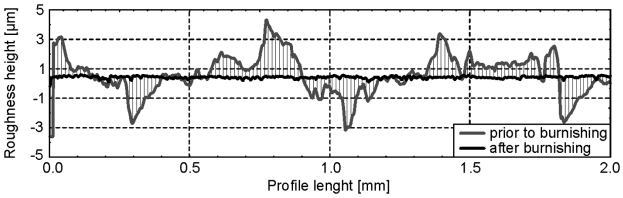

Figure 3: Superimposed recordings of the surface profiles
Slika 3: Prekrivanje meritev hrapavosti površine

involved a stiff tool system with the ball penetration depth limited to the maximum peak height. The same scale was used to represent the superimposed surface roughness profiles before and after the completion of the burnishing process. The finished surface of very small roughness, R_a = 0.061 µm (**Figure 3**), was obtained with a 5 µm penetration depth, which approximately corresponds to a maximum profile peak height, R_p = 4.3 µm, of the same surface prior to burnishing.

3 EXPERIMENTAL INVESTIGATION

The experimental investigation included burnishing of the cylindrical surface. The burnishing was performed on a specimen (billet) of tempered steel, 36CrNiMo4, hardness 42 HRC. The specimen dimensions were d = 50 mm and L = 400 mm. The burnishing was performed on a universal lathe (**Figure 4**) with a specially designed

Figure 4: Photograph of burnishing tool in operation
Slika 4: Posnetek orodja med gladilnim valjanjem

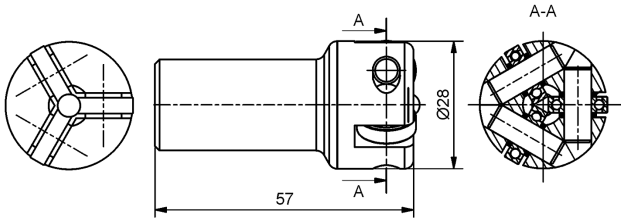

Figure 5: Technical drawing of burnishing tool system
Slika 5: Tehnična risba orodja

stiff tool system, a technical drawing of which is shown in **Figure 5**. The system was designed with three roller bearings that support the burnishing ball at the areas defined by the neighbourhoods of three points, ensuring that the ball rolls in a plane. The burnishing ball featured a 7 mm diameter and was made of steel, A 295 52100 (USA/ASTM). The ball hardness was 65 HRC, while its surface roughness was equal to R_a = 0.02 µm.

Considering the burnishing ball, it should be noted that, due to the limited load capacity of the small roller bearings (**Figure 5**), the maximum allowed force on the ball is limited to F = 600 N. Thus, it is important to emphasize that it was not possible to perform burnishing with penetration depths above the maximum peak height on the previously machined surface.

The burnishing was performed in a single pass, with a feed rate f = 0.05 mm/r and the number of revolutions n = 45 r/min. A small number of revolutions was selected in order to eliminate the negative thermal and dynamic effects. Considering the initial hypotheses and the goal of this investigation, the tendency was towards avoiding intensive heating of the burnishing ball, as well as any significant vibrations of the tool system and the workpiece. All this allowed a deeper insight into the very process, as well as a more realistic comparison between the proposed theoretical model and the experimental results. Loads were applied using a cross slide on a universal lathe. Mounted on the lathe was a dynamometer, Kistler 9265A, which supported the tool system. The level of loading was determined by this dynamometer prior to the initiation of the burnishing process. Also, during the burnishing process, the Kistler 9265A dynamometer was used for continuous monitoring of the burnishing force used in the process. Both workpiece sections were previously lathed to different surface roughness and subsequently burnished with six different burnishing forces. Upon completion of the burnishing process, a Talisurf 6 was used to measure the burnished surface roughness parameters (R_a and R_p). Measurements were taken in both sections (initial machining 1, and initial machining 2), along the contour lines on the workpiece, in three radial directions oriented at 120° relative to the axis of the workpiece. **Figure 6** shows a

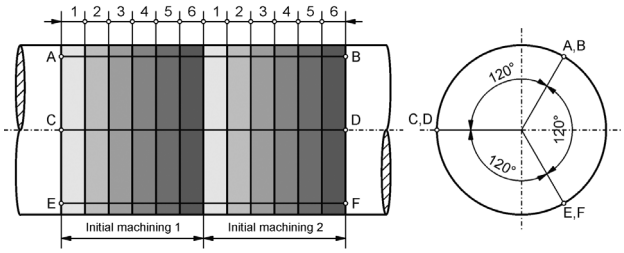

Figure 6: Schematic drawing of the fields in which the burnishing forces were measured, and the locations of the contour lines along which the roughness measurements were taken
Slika 6: Shematičen prikaz polj, na katerih so bile izmerjene sile med gladilnim valjanjem, in položaj linij, vzdolž katerih je bila izmerjena hrapavost

drawing with the marked sections used to measure the burnishing forces, showing the locations of the contour lines along which the roughness measurements were taken. The referential length for taking the roughness measurements equalled 3 × 0.8 = 2.4 mm. Burnishing was performed on two previously machined surfaces with different roughness (initial machining 1, and initial machining 2 – **Figure 6**). The first initial machining was performed with the following parameters: feed rate f = 0.5 mm/r, depth of cut d = 1 mm, and number of revolution n = 710 r/min. The second initial machining was performed with f = 0.1 mm/r, while the rest of parameters were identical to the first initial machining.

Thus, the values of y represent the real ball-penetration depths into the roughness profile. These values were measured after the completion of the burnishing process, which eliminated the errors due to the elastic deformations of the workpiece, tool system, and support.

We believe that measurements of the maximum peak heights along the three profile lines helped mitigate the negative influence of technological errors (deviation from circularity during the workpiece rotation and the workpiece elasticity). This influence is manifested through a more or less pronounced dispersion of the burnishing force within particular sections. It is not only a logical assumption, but was actually observed in the experiment, that each variation in the burnishing force within a burnishing section, resulted in a roughness

4 RESULTS

The experimental results encompass the data on the burnishing forces that were used in the process as well as the data on the roughness parameters of the burnished surfaces.

Table 1 presents the mean values of the burnishing force, the standard deviations, the minimum and maximum burnishing forces generated during the process, and the surface-roughness parameters (arithmetic mean surface roughness, R_a, maximum peak height, R_p, and maximum valley height, R_v). Based on the maximum peak height on the profile of the previously machined surfaces, $R_{p(init)}$, as well as the maximum peak height, $R_{p(F)}$, measured upon completion of the burnishing process in a particular section and along a particular contour line, the ball penetration depths were calculated according to:

$$y = R_{p(init)} - R_{p(F)} \quad (4)$$

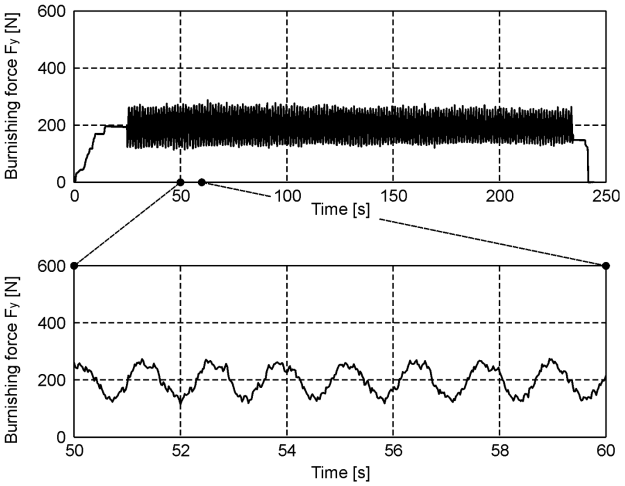

Figure 7: Typical recording of the burnishing force signal
Slika 7: Značilen zapis signala sile pri gladilnem valjanju

Table 1: Results of the experimental investigation
Tabela 1: Rezultati preizkusov

Forces and roughness parameters			Initial machining 1						Initial machining 2					
			R_a [μm]		R_p [μm]		R_v [μm]		R_a [μm]		R_p [μm]		R_v [μm]	
			7.3 ÷ 7.53		15 ÷ 16		–13 ÷ –14		4.5 ÷ 5.4		14 ÷ 17		–16 ÷ –19	
			Number of measurement – force variation –						Number of measurement – force variation –					
			1	2	3	4	5	6	1	2	3	4	5	6
Forces and dispersion of forces		F_{ysr} [N]	47.98	67.41	32.30	55.53	213.28	320.70	81.75	166.08	194.86	322.37	305.21	444.28
		σ_{Fn} [N]	25.21	36.32	26.05	40.51	103.20	103.46	34.71	52.74	39.88	47.98	38.31	56.77
		F_{ymin} [N]	8.14	16.74	0	3.16	74.32	125.57	21.31	83.00	113.49	216.88	220.71	318.03
		F_{ymax} [N]	111.68	169.94	103.88	169.23	432.60	577.61	182.97	289.21	287.77	428.39	389.76	569.26
Profile line on workpiece	AB	R_a [μm]	6.6	6.9	6.6	6.9	4.1	1.04	0.84	1.33	1.05	0.49	0.85	0.774
		R_p [μm]	13	15	13	15	9	1.9	3.6	3.5	2.5	1.3	2	2.27
		y [μm]	3	1	3	1	7	14.1	13.7	13.8	14.8	16	15.3	15.03
	CD	R_a [μm]	5.7	5.06	3.69	4.31	0.57	0.84	1.82	0.627	0.51	0.41	0.5	0.52
		R_p [μm]	12	8.8	7.8	8.6	1.3	1.8	5	2.02	1.4	1.5	1.2	1.3
		y [μm]	4	7.2	8.2	7.4	14.7	14.2	12	14.89	15.6	15.5	15.8	15.7
	EF	R_a [μm]	6.59	6.85	6.1	6.35	2.75	1.2	1.89	0.88	0.76	0.54	1.01	0.55
		R_p [μm]	13.1	14.3	12.3	12.6	4.3	2.3	6.1	2.4	2.4	1.5	2	2.8
		y [μm]	1.9	0.7	2.7	2.4	10.7	12.7	7.9	11.6	11.6	12.5	12	11.2

deviation (see the measurement results for R_p, along profile lines AB, CD, and EF – **Table 1**).

A typical example of a burnishing-force signal recording is shown in **Figure 7**. In the burnishing force signal pattern one clearly distinguishes near-periodic variations within a single revolution. Namely, the force variations repeat every 1.33 s, which approximately corresponds to n = 45 r/min. This indicates that variations in the burnishing-force magnitude, and, consequently, variations in the surface quality, occur due to errors in the number of workpiece revolutions degrees of its elastic deformations in particular sections, which inevitably leads to variations in the contact pressure between the tool and the workpiece surface. Since the experiment was performed with an extremely stiff tool system, minor errors in the circularity of rotation and small deviations in the workpiece elastic deformations were sufficient to generate a significant dispersion of the burnishing force.

Through the processing of measurement signals acquired with the Talisurf 6 profilometer, the profiles of treated surfaces were superimposed for a visual analysis of the changes in the surface roughness due to a varied burnishing force. **Figures 8** and **9** show the superimposed profiles generated by applying different burnishing forces on two surfaces previously machined to various surface-roughness values. These diagrams (**Figures 8** and **9**) pertain to the first initial machining, with the surface roughness ranging within the R_a = 7.3–7.53 μm interval. From the diagrams in **Figures 8** and **9** we can see that the increase of the burnishing force gradually leads to a significant reduction of the surface roughness.

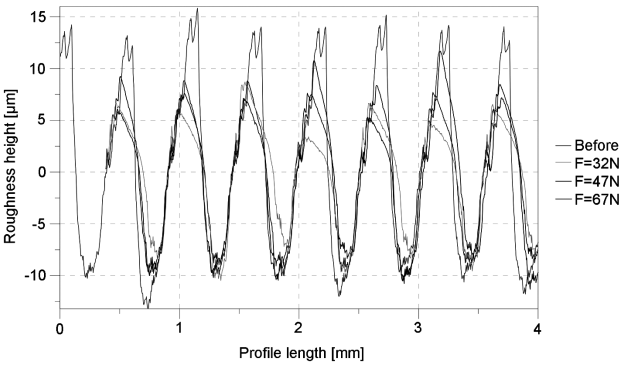

Figure 8: Superimposed profiles generated by burnishing after the first initial machining, with F = 32 N, F = 47 N and F = 67 N

Slika 8: Prekrivanje profilov, dobljenih pri glajenju s silo F = 32 N, F = 47 N in F = 67 N, na predhodno obdelani površini

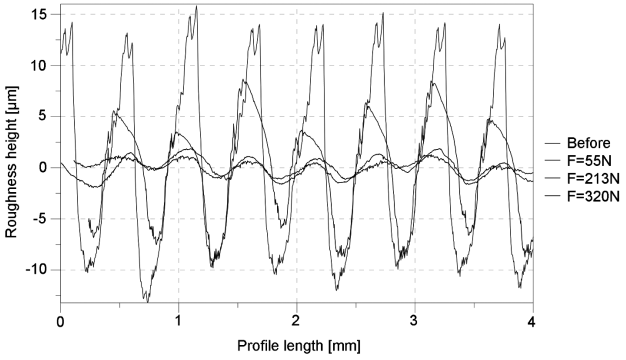

Figure 9: Superimposed profiles generated by burnishing after the first initial machining, with F = 55 N, F = 213 N and F = 320 N

Slika 9: Prekrivanje profilov, dobljenih pri glajenju s silo F = 55 N, F = 213 N in F = 320 N, na predhodno obdelani površini

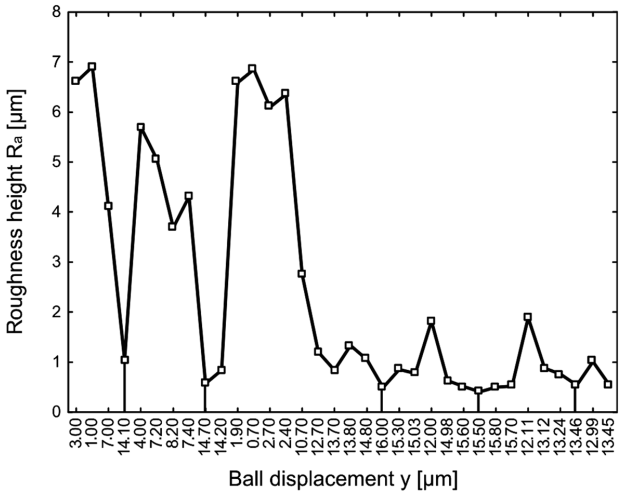

Figure 10: Dependence of the surface roughness R_a, on the depth of the ball penetration into the roughness profile

Slika 10: Odvisnost hrapavosti površine R_a od globine prodiranja kroglic v profil hrapavosti

It is interesting to note that for both initial machinings, the ball penetration depths that are close to the maximum peak height of the previously machined surface correspond to lowest R_a values (**Table 1**).

Based on the data from **Table 1** the diagram in **Figure 10** shows, for both initial machinings, the dependence between the roughness, R_a, and y, which represents the ball penetration depth. For both initial machinings, the diagram shows an obvious trend of the surface roughness (R_a) variations as a function of the ball penetration depth. Evidently, for both initial machinings, the surface roughness drops sharply until it reaches the maximum peak height of the previously machined surface roughness profiles, i.e., $y = R_p$ = 14–17 μm. After that point, the surface roughness decreases very slightly.

5 DISCUSSION

Numerous authors have focused their investigations on defining the optimal burnishing force. As previously discussed, the widespread and efficient application of burnishing should require an extensive database containing optimal values for the burnishing forces that are a function of a number of parameters (workpiece material, burnishing feed, number of passes, and quality of surface prior to burnishing). In this work the focus is placed on defining the appropriate penetration depth of a stiff burnishing tool system, i.e., the depth that will

provide an optimal surface roughness, regardless of the force magnitude and the other parameters of the burnishing process. Discussed were the basic theoretical considerations according to which the rolling of a ball within a stiff tool system, and the penetration into the roughness profile up to the predefined depth, are very likely to provide near-minimal surface roughness, where equalities (1) and (3) apply.

The basic assumptions in this paper were largely confirmed by the results of the experimental investigation. The diagram in **Figure 10** clearly indicates that the displacement of the burnishing ball into the roughness profile, *y*, which is close to the maximum peak height of the previously machined surface-roughness profiles, provides the lowest surface roughness, R_a. For the first initial machining (**Table 1**) the maximum peak height is in the range R_p = 15–16 μm. From the diagram in **Figure 10** it is evident that y = 14.7 μm (measured along the profile line CD – **Table 1**), which corresponds to R_p = 15–16 μm in the case of first initial machining, results in the near-minimal surface roughness, R_a = 0.57 μm (see **Figure 10** and **Table 1**).

Considering the second initial machining (**Table 1**), the maximum peak height is in the range R_p = 14–17 μm. The diagram shown in **Figure 10** clearly indicates that y = 15.5 μm (measured along the profile line CD – **Table 1**), which corresponds to the maximum peak height, R_p = 14–17 μm, results in a near-minimal surface roughness, R_a = 0.41 μm. It should be noted that in the case of the second initial machining (**Table 1**) on the profile lines AB and CD there are a number of y values that are approximately equal to R_p = 14–17 μm, and which correspond to a near-minimal surface roughness, as shown in **Figure 10**. Based on the previous discussion, and the diagram in **Figure 10**, it is logical to suppose that the optimum ball-penetration depth equals the maximum peak height, R_p, of the previously machined surface. This claim is also supported by the trend of the change of surface roughness R_a depending on the ball-penetration depth (**Figure 10**). Based on the diagram shown in **Figure 10** it is obvious that, for both initial machinings, the surface roughness, R_a, drops significantly until the ball-penetration depth reaches the maximum peak height achieved with the previous machining. After that, the decrease of R_a is significantly milder. With the first initial machining (higher surface roughness) the percentage change of the surface roughness, R_a, is significantly higher. Thus, regardless of the surface quality obtained with the previous machining, the values of y that are close to the maximum peak height, result in the lowest values of surface roughness. This fact can be valuable when applying burnishing on surfaces with a rough previous machining.

Therefore, a high surface quality can be achieved with a tool displacement that corresponds to the maximum peak height, R_p, of the previously machined workpiece surface. It is evident that the material flowing from the profile peaks should be allowed allocation space (**Figure 2**). Besides, the condition of equality of the cross-section surface areas of the roughness peaks and valleys theoretically allows the simultaneous decrease of the peak, R_p, and the valley height, R_v. The material which flows from the profile peaks fills up the valleys leaving the profile without additional peaks. The theoretical claim that material flow from the peaks mostly manifests as their widening, is convincingly illustrated by the experimental results (**Figures 8** and **9**). Experimental investigations were conducted on a universal lathe and it was not possible to precisely define the depth of the ball penetration into the roughness profile. In other words, the limited accuracy of the lathe slide ways, the presence of clearances and the system compliance prevented the burnishing ball from moving exactly along the direction defined by the theoretical considerations. For that reason, we determined the required displacement in an indirect way, monitoring the variation of the forces during burnishing. Thus, the forces were periodically increased in order to achieve a penetration depth that approximately equals the maximum peak height of the previously machined surface, R_p. The diagrams in **Figures 8** and **9** clearly show a gradual decrease of the roughness over the 32–320 N force interval. One of the basic goals was to visually identify the oscillation of the profile curve of the burnished surface, around the line that divides the profile of the previously machined surface into two, approximately equal, surface areas of peaks and valleys (**Figure 9**).

6 CONCLUSIONS

Theoretical assumptions pertaining to defining an optimal tool trajectory that results in the best surface quality were largely confirmed in this experiment. A ball rolling within a high-stiffness tool system, according to a predefined penetration depth, provides a near-optimal condition, i.e., minimal surface roughness, regardless of the quality of the initial machining. Based on the experimental results, the ball should penetrate the surface roughness profile up to a depth that approximately equals the maximum peak height achieved by the initial machining. The results of this study allow the assumption that ball-penetration depths beyond R_p do not significantly contribute to the surface quality, primarily because the displaced material should create new, probably higher profile peaks. According to the results of the measurement, regardless of the surface quality on a previously machined surface, the value of y that is close to the maximum peak height results in the lowest R_a. This could be especially valuable when burnishing relatively rough surfaces.

An analysis of the surface-roughness measurement results and the super positioning of the profiles generated using various burnishing forces and tool displacements, largely explained the phenomenon of the roughness

peaks' deformation. Having this and the theoretical considerations in mind, we can conclude that the defined penetration depth, $y \approx R_p$, satisfies the condition of approximate equality of surface areas defined by the roughness profile peaks and valleys. The proposed burnishing methodology could be especially valuable when dealing with roughly machined surfaces with significant R_p.

The research reported in this paper opens up a number of new, interesting directions for research, such as the testing of a stiff tool system with various workpiece materials, different burnishing regimes, and various surface roughnesses as a result of the initial machining. We believe that the proposed model casts new light on the burnishing process. It opens up new directions of research involving stiff tool systems and penetration depths that yield a near-minimal surface roughness, regardless of the workpiece material, the burnishing parameters, and the initial surface roughness. Future work should involve an investigation of surfaces that drastically differ from the aspect of the surface roughness achieved by previous machining. They should be penetrated by a burnishing ball beyond the maximum profile peak height. In this way it would be possible to verify the results obtained in this study as well as open up new directions for research on the burnishing process.

7 REFERENCES

[1] L. Gusel, R. Rudolf, B. Kosec, Metalurgija, 48 (**2009**) 2, 103–107

[2] B. Karpe, B. Kosec, T. Kolenko, M. Bizjak, Metalurgija, 50 (**2011**) 1, 13–16

[3] H. Tozan, Teh. Vjesn., 18 (**2011**) 2, 187–191

[4] M. Kurt, S. Hartomacyoglu, B. Mutlu, U. Koklu, Mater. Tehnol., 46 (**2012**) 3, 205–213

[5] M. H. El-Axir, O. M. Othman, A. M. Abodiena, J. Mater. Process. Technol., 202 (**2008**) 1–3, 435–442

[6] M. H. El-Axir, Int. J. Mach. Tools. Manuf., 40 (**2000**) 11, 1603–1617

[7] H. Hamadache, L. Laouar, N. E. Zeghib, K. Chaoui, J. Mater. Process. Technol., 180 (**2006**) 1–3, 130–136

[8] M. H. El-Axir, A. A. Ibrahim, J. Mater. Process. Technol., 167 (**2005**) 1, 47–53

[9] S. Fang-Jung, H. Chih-Cheng, J. Mater. Process. Technol., 205 (**2008**) 1–3, 249–258

[10] L. Liviu, N. V. Sorin, M. Ioan, Precis. Eng., 29 (**2005**) 2, 253–256

[11] M. H. El-Axir, O. M. Othman, A. M. Abodiena, J. Mater. Process. Technol., 196 (**2008**) 1–3, 120–128

[12] M. H. El-Axir, M. M. El-Khabeery, J. Mater. Process. Technol., 132 (**2003**) 1–3, 82–89

[13] M. M. El-Khabeery, M. H. El-Axir, Int. J. Mach. Tools Manuf., 41 (**2001**) 12, 1705–1719

[14] A. M. Hassan, A. M. S. Momani, Int. J. Mach. Tools Manuf., 40 (**2000**) 12, 1775–1786

[15] A. M. Hassan, A. S. Al-Bsharat, J. Mater. Process. Technol., 59 (**1996**) 3, 250–256

[16] K. Palka, A. Weronski, K. Zaleski, J. Achiev. Mater. Manuf. Eng., 16 (**2006**) 1–2, 57–62

[17] F. Gharbi, S. Sghaier, H. Hamdi, T. Benameur, Int. J. Adv. Manuf. Technol., 60 (**2012**) 1–4, 87–99

[18] X. Yu, L. Wang, Int. J. Mach. Tools. Manuf., 39 (**1999**) 3, 459–469

[19] H. Y. Luo, J. Y. Liu, L. J. Wang, Q. P. Zhong, Proc. Inst. Mech. Eng. Part B-J. Eng. Manuf., 220 (**2006**) 6, 893–904

[20] W. Bouzid, O. Tsoumarev, K. Sai, Int. J. Adv. Manuf. Technol., 24 (**2004**) 1–2, 120–125

[21] E. Brinksmeier, M. Garbrecht, D. Meyer, J. Dong, Prod. Eng. Res. Devel., 2 (**2008**) 2, 109–116

[22] E. Brinksmeier, M. Garbrecht, D. Meyer, CIRP Ann-Manuf. Technol., 57 (**2008**) 1, 541–544

[23] D. Meyera, E. Brinksmeier, F. Hoffmann, Proc. Eng., 19 (**2011**), 258–263

[24] T. A. El-Taweel, M. H. El-Axir, Int. J. Adv. Manuf. Technol., 41 (**2009**) 3–4, 301–310

[25] A. Sagbas, F. Kahraman, Mater. Tehnol., 43 (**2009**) 5, 271–274

[26] U. Esme, Mater. Tehnol., 44 (**2010**) 3, 129–135

[27] M. Nemat, A. C. Lyons, Int J. Adv. Manuf. Technol., 16 (**2000**) 7, 469–473

[28] L. N. Lopez de Lacalle, A. Lamikiz, J. A. Sanchez, J. L. Arana, Int. J. Adv. Manuf. Technol., 32 (**2007**) 9–10, 958–968

[29] Y. C. Lin, S. W. Wang, H. Y. Lai, Int J. Adv. Manuf. Technol., 23 (**2004**) 9–10, 666–671

[30] F. Gharbi, S. Sghaier, K. J. Al-Fadhalah, T. Benameur, J. Mater. Eng. Perform., 20 (**2011**) 6, 903–910

[31] A. Bougharriou, W. Bouzid Sai, K. Sai, Int. J. Adv. Manuf. Technol., 51 (**2010**) 1–4, 205–215

[32] S. Fang-Jung, A. C. Chao-Chang, L. Wen-Tu, Int. J. Adv. Manuf. Technol., 28 (**2006**) 1–2, 61–66

[33] A. Akkurt, Met. Sci. Heat Treat., 53 (**2011**) 3–4, 145–150

[34] A. Akkurt, J. Mater. Eng. Perform., 20 (**2011**) 6, 960–968

[35] W. Bouzid Sai, J. L. Lebrun, J. Mater. Eng. Perform., 12 (**2003**) 1, 37–40

[36] W. Bouzid Sai, K. Sai, Int. J. Adv. Manuf. Technol., 25 (**2005**) 5–6, 460–465

UDK 519.61/.64:621.77
Original scientific article/Izvirni znanstveni članek

ISSN 1580-2949
MTAEC9, 47(1)53(2013)

CALCULATION OF THE LUBRICANT LAYER FOR A COARSE SURFACE OF A BAND AND ROLLS

IZRAČUN SLOJA MAZIVA NA GROBI POVRŠINI TRAKU IN VALJEV

Dušan Ćurčija[1], Franc Vodopivec[2], Ilija Mamuzić[1]

[1]Croatian Metallurgical Society, Berislavićeva 6, 10000 Zagreb, Croatia
[2]Institute of Metals and Technology, Lepi pot 11, 1000 Ljubljana, Slovenia
mamuzic@simet.hr

Prejem rokopisa – received: 2012-07-03; sprejem za objavo – accepted for publication: 2012-09-26

The effect of the average roughness of a lubricated band caused by dressing processes is analysed by applying the Reynolds differential equation for lubrication with the incorporated average roughness and evolution in the Fourier series to the third member. The analysis has shown that the average roughness has two effects on the lubricant-layer thickness in the entering section of the deformation zone. For a small surface roughness, the nominal lubricant-layer thickness decreases slowly (if the process is treated as occurring on a smooth surface) and the thickness grows again with an increase in the roughness. The basis for the analysis was the numerical Monte-Carlo method and the developed approximate analytical solution was in acceptable agreement with the numerical method.

Keywords: surface roughness, lubricant-layer thickness, Reynolds equation, Monte-Carlo method, Fourier series

Analiziran je vpliv povprečne hrapavosti mazanega traku pri procesih dresiranja. Podlaga analize je Reynoldsova diferencialna enačba za mazanje z vključeno povprečno hrapavostjo in obravnavo s Fourierovo vrsto do tretjega člena. Analiza je pokazala, da ima povprečna hrapavost dva učinka na debelino plasti maziva v vhodnem preseku področja deformacije. Pri majhni začetni hrapavosti se nominalna debelina plasti maziva počasi zmanjšuje (če se proces obravnava, kot da poteka na gladki površini) in znova raste, če se povečuje hrapavost. Podlaga za analizo je bila numerična metoda Monte Carlo, razvita pa je bila tudi približna analitična rešitev, ki se zadovoljivo ujema z numerično.

Ključne besede: hrapavost površine, debelina plasti maziva, Reynoldsova enačba, metoda Monte Carlo, Fourierova vrsta

1 INTRODUCTION

This technology is strongly associated with the quality of technological lubricants as it:

- diminishes the contact friction,
- removes the heat, cools the tool and diminishes the wear,
- diminishes the deformation resistance and the deformation work,
- diminishes the sticking to the tool and keeps the surface of the product clean.

The basic groups examined in this work[1–3] are:

- liquid emulsions,
- fats and compounds,
- consistent lubricants,
- transparent/glass lubricants,
- powder lubricants and
- metallic lubricants.

Technological lubricants must meet a series of requirements, beginning with a high lubricity – the ability to form a flat, firm layer separating the contact surfaces – then there are thermal consistency and stability that prevent the damaging effect of the product corrosion, the properties not posing any health and environmental risks, etc.

The liquid emulsions, whose compounds are mixtures of vegetable and mineral oils, are especially used in the cold rolling of 0.3–0.4 mm thick sheets and strips.

In the cold rolling of sheets and strips, the dressing process is also used with an application of liquid lubricants to reduce undulation.

2 MATHEMATICAL MODELLING

Mathematical modelling is a requirement of today's metallurgy[4,5] and it is also used in the field of plastic deformation of metals. For an analysis of smooth surfaces[6,7] the following equation is used:

$$\frac{\mathrm{d}p}{\mathrm{d}x}=\frac{6\mu(v_0+v_\mathrm{R})}{\varepsilon^2(x)}-\frac{12\mu Q}{\varepsilon^2(x)} \tag{1}$$

$$Q(x)=\int_0^{\varepsilon(x)}u\mathrm{d}y=\frac{1}{12\mu}\frac{\mathrm{d}p}{\mathrm{d}x}\varepsilon^3(x)+\left(\frac{v_0+v_\mathrm{R}}{2}\right)\varepsilon(x) \tag{2}$$

The geometry of the lubricant contact[8] and the length of the lubricant wedge are described with the relations (3), (4) and (5):

$$\varepsilon(x)=\varepsilon_0+R\left[\cos\alpha-\sqrt{1-\left(\sin\alpha-\frac{x}{R}\right)^2}\right] \tag{3}$$

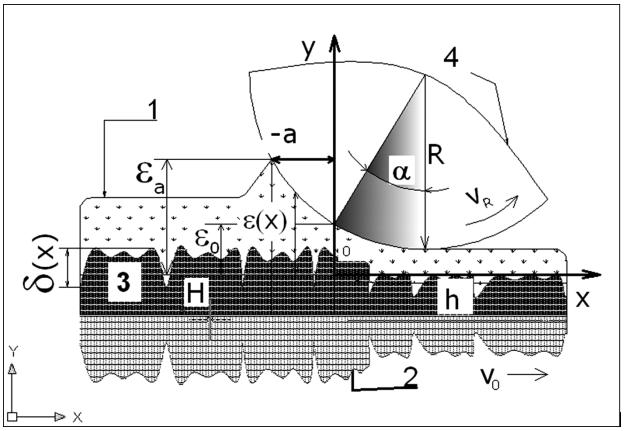

Figure 1: Model of the tribomechanical system; 1- lubricant layer $\varepsilon(x)$ – nominal thickness for smooth surfaces, 2- band – in dressing processes the adhering angle α is low, 3- average band roughness $\delta(x)$ – casual sheet roughness, 4- roll defined by surface smoothness. In **Table 1** the roughness is R_z = 8 μm.

Slika 1: Model tribomehanskega sistema; 1- plast maziva $\varepsilon(x)$ – nominalna debelina za gladke površine, 2- trak – pri procesu dresiranja pri majhnem kotu stika α, 3- povprečma hrapavost traku $\delta(x)$ – slučajna hrapavost traku, 4- valj z definirano gladkostjo površine. V **Tabeli 1** je njegova hrapavost R_z = 8 μm.

$$a = R\left[\sqrt{1-\left(\cos\alpha-\frac{\varepsilon_a}{R}+\frac{\varepsilon_0}{R}\right)^2}-\sin\alpha\right] \tag{4}$$

$$\varepsilon(x) = \varepsilon_0 - \alpha x + \frac{x^2}{2R} - \frac{\alpha x^3}{2R^2} + \frac{x^4}{8R^3} \tag{5}$$

For the average sheet roughness[9], the mathematical relation in accordance with **Figure 1** is:

$$\left\langle \frac{\mathrm{d}p}{\mathrm{d}x_0} \right\rangle = 6\mu(v_0+v_R)\left[\left\langle \frac{1}{\varepsilon^2(x_0)}\right\rangle - \frac{\left\langle \frac{1}{\varepsilon_0^2}\right\rangle}{\left\langle \frac{1}{\varepsilon_0^3}\right\rangle}\left\langle \frac{1}{\varepsilon^3(x_0)}\right\rangle\right] \tag{6}$$

$$\left\langle \varepsilon(x_0)\right\rangle = \varepsilon(x)+\delta(x) \tag{7}$$

Reflexion of sheet roughness is added, as ε_0, to the lubricant wedge (4). The calculation is possible only with numerical mathematical methods and, in the program MATHEMATICA, the numerical method Monte Carlo was used. In the theoretical calculations regarding the model of the average roughness, the following function developed to the third term of Fourier series was applied:

$$\delta(x) = \frac{4}{\pi}\left(\sin x + \frac{1}{3}\sin 3x + \frac{1}{5}\sin 5x\right)R_z \tag{8}$$

3 RESULTS AND DISCUSSION

In **Table 1** the standard values of geometrical, rheological and kinematic characteristics of the processes of theoretical investigations are given according to the Russian-Ukrainian[10,11] authors.

Table 1: Standard lubricant characteristics for theoretical calculations
Tabela 1: Standardne značilnosti maziva za teoretične izračune

Parameter	Value	Unit
γ- piezo coefficient of viscosity	2.18E-7	Pa^{-1}
p_0- rolling pressure	20E6	Pa
v_R- circumferential roll speed	10	m/s
v_0- sheet speed	6	m/s
R- roll radius	0.35 (0.25)	m
μ_0- lubricant dynamic viscosity $\mu = \mu_0 \exp(\gamma * p_0)$ Barussa equation	0.024–0.048	Pa s
α- gripping angle	0–0.02	rad
ε_a- lubricant thickness on sheet	0.001–0.00001	m
A- technological parameter	1965512 (3934525)	m^{-1}
$A = (1-\exp(-\gamma * p_0)/6\mu_0\gamma(v_0+v_R))$		
$R_z \approx 6\delta$	R_z = 1–10	μm

The parameters in **Table 1** are of two groups:
1- lubricant rheological characteristics (μ_0, γ)
2- geometrical characteristics of the technological process (R, α, R_z)
3- kinematics (v_0, v_R)

Table 2: Lubricant-layer exit results (μm)
Tabela 2: Izhodni rezultati za plast maziva (μm)

	0	1	2	3	4	5	6	7
0	10.102	10.095	10.087	10.075	10.059	10.039	9.92	9.207
1	10.003	9.996	9.988	9.976	9.959	9.934	9.819	9.099
2	9.941	9.935	9.926	9.914	9.898	9.872	9.757	9.031
3	9.92	9.914	9.905	9.893	9.876	9.851	9.735	9.008
4	9.94	9.933	9.925	9.913	9.896	9.87	9.755	9.03
5	9.998	9.991	9.983	9.971	9.954	9.929	9.814	9.093
6	10.09	10.083	10.075	10.063	10.046	10.021	9.907	9.193
7	10.21	10.204	10.195	10.184	10.167	10.143	10.03	9.322
8	10.354	10.348	10.339	10.328	10.312	10.287	10.175	9.475
9	10.517	10.51	10.502	10.491	10.474	10.45	10.339	9.645
10	10.693	10.686	10.678	10.667	10.651	10.627	10.517	9.828
11								
12								

4- compounds (A, roughness space angle)

The solutions of differential equation (6) are partially given in **Table 2**.

The examined roughness is classified[12,13] in 10 vertical classes and the band profile roughness in 32 horizontal classes.

In principle, with a decreasing band-lubricant thickness (ε_a in **Figure 1**) the lubricant thickness in the entering section of the metal deformation zone is also decreased (ε_0). As shown in[14], the lubricant wedge has the ideal geometry and can give economic savings of the lubricant in the metalworking technology.

The numerical integration of equation (6) was checked with the approximate[15–17] analytical solutions possible in the case of practical interest, which is found in equations (9), (10a)–(10e) and (11). Equation (9) is the simplest analytical solution that does not consider the thickness of the band lubricant layer, $\varepsilon_a >> \varepsilon_0$. With a clear complexity, equation (11) corrects this deficiency:

$$315AR^3\alpha^7 - 168R^2\alpha^4 - 1824\delta^2 = 0$$
$$\varepsilon_0 = 0.5R\alpha^2 \ldots A = \frac{1-exp(-\gamma p_0)}{6\mu\gamma(v_0+v_R)} \quad (9)$$

$$W_1 = A - \left[\frac{4}{3\alpha^3 R} - 4\frac{R^2}{3\left[R\sqrt{1-\left(\cos\alpha - \frac{\varepsilon_a}{R}+\frac{\varepsilon_0}{R}\right)^2} - R(\sin\alpha-\alpha)\right]^3}\right] \quad (10a)$$

$$-W_2 = 3\delta^2\left[\frac{16}{7\alpha^7 R^3} - 16\frac{R^4}{3\left[R\sqrt{1-\left(\cos\alpha - \frac{\varepsilon_a}{R}+\frac{\varepsilon_0}{R}\right)^2} - R(\sin\alpha-\alpha)\right]^7}\right] \quad (10b)$$

$$W_3 = \frac{\varepsilon_0^3 + 3\varepsilon_0\delta^2}{\varepsilon_0^2 + 6\delta^2} \quad (10c)$$

$$W_4 = \frac{8}{5\alpha^5 R^2} - 8\frac{R^3}{5\left[R\sqrt{1-\left(\cos\alpha - \frac{\varepsilon_a}{R}+\frac{\varepsilon_0}{R}\right)^2} - R(\sin\alpha-\alpha)\right]^5} \quad (10d)$$

$$-W_5 = 32\frac{R^5}{5\left[R\sqrt{1-\left(\cos\alpha - \frac{\varepsilon_a}{R}+\frac{\varepsilon_0}{R}\right)^2} - R(\sin\alpha-\alpha)\right]^9} \quad (10e)$$

$$W_1 + W_2 + W_3 * (W_4 + W_5) = 0 \quad (11)$$

In **Table 3** approximate numerical and analytical solutions are compared. The approximate numerical solutions can be compared with numerical integration only for the entering roughness profile, thus, at the entering section of the deformation zone with $x = 0$.

It is clear from **Table 3** that the simple analytical form of equation (9) with numerous approximations describes well the lubricant layer for the case of a lubricant excess on the sheet and the rolls.

Table 3: Comparison of approximate analytical and numerical Monte-Carlo solutions for one point of the graph crossing from **Figure 2**

Tabela 3: Primerjava približnih analitičnih in numeričnih rešitev Monte Carlo za eno točko prereza grafa na **sliki 2**

Case conditions	Approximate analytical solutions, eq. (11) and (9)	Monte-Carlo method, eq. (6)
$x = 0$ (initial roughness profile) $R_z = 1$ μm $R_z \approx 6\,\delta$ $\alpha = 0.00918759$ rad $A = 1965512$ m^{-1} $R = 0.35$ m	$\varepsilon_a = 0.001$ m $\varepsilon_0 = 14.721$ μm (11) $\varepsilon_0 = 14.771$ μm (9) $\varepsilon_a = 0.0001$ m $\varepsilon_0 = 13.834$ μm (11)	$\varepsilon_a = 0.001$ m $\varepsilon_0 = 14.772$ μm $\varepsilon_a = 0.0001$ m $\varepsilon_0 = 13.761$ μm
$x = 0$ (initial roughness profile) $R_z = 10$ μm $R_z \approx 6\,\delta$ $\alpha = 0.0092867$ rad $A = 1965512$ m^{-1} $R = 0.35$ m	$\varepsilon_a = 0.001$ m $\varepsilon_0 = 15.024$ μm (11) $\varepsilon_0 = 15.092$ μm (9) $\varepsilon_a = 0.0001$ m $\varepsilon_0 = 13.511$ μm (11)	$\varepsilon_a = 0.001$ m $\varepsilon_0 = 15.077$ μm $\varepsilon_a = 0.0001$ m $\varepsilon_0 = 13.429$ μm
$x = 0$ (initial roughness profile) $R_z = 10$ μm $R_z \approx 6\,\delta$ $\alpha = 0.00840867$ rad $A = 3934525$ m^{-1} $R = 0.25$ m	$\varepsilon_a = 0.001$ m $\varepsilon_0 = 8.776$ μm (11) $\varepsilon_0 = 8.838$ μm (9) $\varepsilon_a = 0.0001$ m $\varepsilon_0 = 8.464$ μm (11)	$\varepsilon_a = 0.001$ m $\varepsilon_0 = 8.755$ μm $\varepsilon_a = 0.0001$ m $\varepsilon_0 = 8.429$ μm

Table 4: Effect of the two-sided roughness of the sheet and rolls, congruous for ε_0

Tabela 4: Vpliv dvostranske hrapavosti traku in valjev, kongruenten za ε_0

$x = 0$ (initial roughness profile) $R_z = 10$ μm, average roughness, horizontal (transversal) $R_z = 8$ μm, longitudinal roll roughness $R_z \approx 6\,\delta$ (GOST 2789-73) $\alpha = 0.00840867$ rad $A = 3934525$ m^{-1} $R = 0.25$ m	Monte-Carlo method $\varepsilon_a = 0.0001$ m $\varepsilon_0 = 9.299$ μm $\varepsilon_0 = 8.429$ μm	
	One-sided roughness of the sheet $\varepsilon_a = 0.0001$ m $\varepsilon_0 = 8.429$ μm	Two-sided roughness of the sheet and roll $\varepsilon_a = 0.0001$ m $\varepsilon_0 = 8.919$ μm
	$R_z \to 0$ $\varepsilon_a = 0.0001$ m $\varepsilon_0 = 7.877$ μm	

The longitudinal band profile on abscissa in shown in 66 classes and on ordinate in 11 classes for roughness (0–10 μm). It is useful to calculate the lubricant thickness ε_0 in the range of 8.5–12.5 μm in the area of I-I. Q, K and W designations connect the specific areas of the network diagram with the contour plot (an aircraft picture of the network diagram).

B and C are the left and right sides of the band roughness defined as a sine evolution function in the Fourier series: B in the range of (π–2π) rad and C in (0–π) rad.

Line P in **Figure 2** represents the nominal lubricant-layer thickness on side C, thus, by having the thickness for $R_z \approx 6$ μm, an equivalent to the lubricant-layer thickness on a smooth surface is obtained. Side B does not have this property.

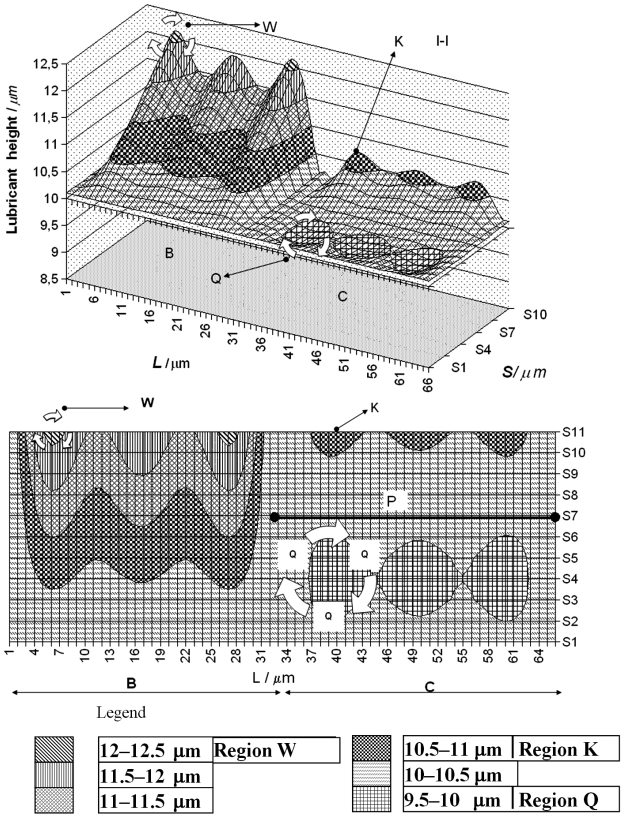

Figure 2: Effect of the average sheet roughness and smooth rolls on ε_0
Slika 2: Vpliv povprečne hrapavosti traku in gladkih valjev na ε_0

In **Figure 3** both sides of the roll longitudinal roughness C from **Figure 2** are shown. The average roughness conserves the same properties as in **Figure 2**. The longitudinal roughness profile in the range of classes 33 to 66 gives a more stable hydrodynamic lubrication, while for classes 1 to 33 the hydrodynamic lubrication is already seriously impaired by the low roughness of the band and rolls. The lubricant layer decreases rapidly and spreads to fractal areas. A stable lubrication can be achieved on small band segments and around class 4 of the longitudinal sheet profile and around classes 10 and 30. The complex shapes of the lubrication space are probably determined by the band and roll roughness in the entering section of the deformation zone that determines a different lubrication layer than in the case of smooth-sheet and roll surfaces.

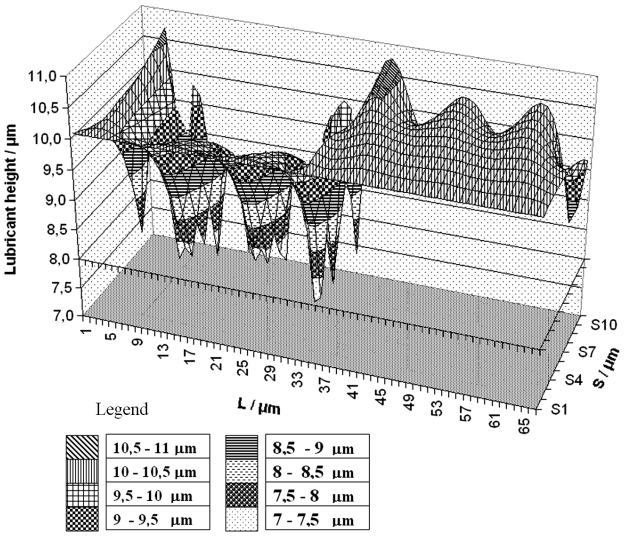

Figure 3: Effect of the average sheet roughness and longitudinal roll roughness on ε_0 (**Table 4**)
Slika 3: Vpliv povprečne hrapavosti traku in longitudinalne hrapavosti valjev na ε_0 (**tabela 4**)

4 CONCLUSIONS

Based on the results of theoretical analyses of the effect of the band roughness on the lubrication dressing processes, the following conclusions are proposed:

- The average band roughness has a critical value when it starts to affect positively the lubricant layer with its increase in comparison with a smooth surface. Up to line P in **Figure 2**, the lubricant layer has a tendency to increase and to decrease the formation of sunk baskets in area *Q*. The theoretical explanation for this is that the surface roughness determines the shape of the lubricant layer for every value of R_z. This is the range of a stable lubrication.
- If congruous roll roughness is added to the average band roughness, forming a longitudinal roll roughness with the positive side in the range of $(0–\pi)$, the thickness of the lubricant layer in the entering section of the band deformation zone will increase its longitudinal profile from class 33 to 66 (**Figure 3** and **Table 4**) and will approach the boundary lubrication.
- The developed approximate analytical solutions agree with the numerical integration of equation (6) and ensure a reliable approach to the analysis.
- If the technological process was performed with a nominal lubricant-layer thickness marked with line P in **Figure 2** the best roll rhythm would be obtained without significant fluctuations of the lubricant thickness, especially in the case of the boundary-lubrication proximity. This includes the control of the roll roughness.

5 SYMBOLS AND FIGURES

Symbol	Unit	Comment
ε_0	m, (μm)	Lubricant thickness in the entering section of the deformation zone (**Figure 1**)
$\varepsilon(x)$	m	Lubricant thickness in the range of $[-a : 0]$, **Figure 1**, equations (3) and (5)
ε_a	m	Lubricant thickness ahead of the entering section of the deformation zone
a	m	Length of the lubricant wedge (**Figure 1**), equation (4)
α	rad	Band dressing angle
v_R	m/s	Circumferential roll speed

v_T	m/s	Mandrel speed
R	m	Roll radius
R_z	m	Roughness of the band surface, equation (8)
δ^2		Dispersion roughness of the sheet and rolls according to equation (9)
δ_x		Casual lubricant thickness depending on the band roughness (and rolls)
< >		Operative mathematical expectation
x, y		Descartes coordinates
$Q(x)$	–	Volume use of lubricant (on the band perimeter)
μ_0	Pa s	Lubricant dynamic viscosity by the rolling pressure
μ	Pa s	Lubricant dynamic viscosity by the air pressure
u	m/s	Lubricant rate on the abscissa
γ	m^2/N	Piezo coefficient of lubricant viscosity
p	Pa	Rolling pressure
Q	m^2/s	Use of lubricant on the mandrel perimeter – a one-dimensional model
dp/dx	Pa/m	Pressure gradient in the lubricant layer, equation (1)
sin α	rad	Marking the trigonometric function for the griping alpha angle
H	m	Enter band thickness
h	m	Exit band thickness
A	m^{-1}	Technological parameter: $A = [1- \exp(-\gamma p)] / [6\mu_0\gamma(v_R + v_0)]$
exp, π	2.718	Base of natural logarithm (3.141)
[14]	1–1	Reference
1 µm	10^{-6} m	Micrometre
S	µm	Band- and roll-roughness classes
L	µm	Longitudinal holding-band profile
Q, K, W		Markers for **Figure 2**

6 REFERENCES

[1] I. Mamuzić, V. M. Drujan, Teorija, Materijali, Tehnologija čeličnih cijevi, Hrvatsko Metalurško Društvo, Zagreb 1996, 428–435

[2] D. Ćurčija, Mater. Tehnol., 37 (**2003**) 5, 237–254

[3] D. Ćurčija, I. Mamuzić, F. Vodopivec, Metalurgija, 45 (**2006**) 3, 250 (Summary)

[4] A. I. Gubin, B. B. Veselovskiy, D. Ćurčija, A. A. Kochubey, Mathematical simulation and choice of optimum thermal models of continuous events, Metalurgija, 47 (**2008**) 3, 255 (Summary)

[5] Iu. V. Brazaluk, O. O. Kochubey, D. Ćurčija, M. V. Polyakov, D. V. Yevdokymov, On a mathematical model of particle in liquid metal, Metalurgija, 47 (**2008**) 3, 256 (Summary)

[6] D. Ćurčija, I. Mamuzić, Mater. Tehnol., 43 (**2009**) 1, 23–30

[7] D. Ćurčija, I. Mamuzić, Goriva i maziva, 48 (**2009**) 1, 3–28

[8] D. Ćurčija, I. Mamuzić, Mater. Tehnol., 42 (**2008**) 2, 59–63

[9] D. Ćurčija, I. Mamuzić, Metalurgija, 44 (**2005**) 4, 295–300

[10] O. P. Maksimenko, N. P. Podberezniij, Izvestija Černaja metallurgija, 73 (**2003**) 10, 12–16

[11] O. P. Maksimenko, A. A. Semenča, Sučasni problemi metalurgii, 8 (**2005**), 99–103

[12] O. P. Maksimenko, O. E. Lejko, Sučasni problemi metalurgii, 8 (**2005**), 93–99

[13] P. I. Klimenko, Sučasni problemi metalurgii, 8 (**2005**), 44–49

[14] S. M. Ionov, V. I. Kantorovič, S. A. Šepovalov, A. N. Krjukov, Sučasni problemi metalurgii, 8 (**2005**), 224–228

[15] D. M. Me, S. P. Liu, J. F. Zheng, Met. Form. Technol., 20 (**2002**) 5, 29–32

[16] Y. T. Keun, B. H. Lee, R. H. Wagner, J. Mater. Process. Technol., 130 (**2002**), 60–63

[17] D. Ćurčija, I. Mamuzić, Goriva i maziva, 46 (**2007**) 1, 23–44

UDK 537.622:621.318.1
Original scientific article/Izvirni znanstveni članek

ISSN 1580-2949
MTAEC9, 47(1)59(2013)

STRUCTURAL AND MAGNETIC PROPERTIES OF CERIUM-DOPED YTTRIUM-IRON GARNET THIN FILMS PREPARED ON DIFFERENT SUBSTRATES USING THE SOL-GEL PROCESS

STRUKTURNE IN MAGNETNE LASTNOSTI S CERIJEM DOPIRANE ITRIJ-ŽELEZOVE GARNETNE TANKE PLASTI, IZDELANE S SOL-GEL POSTOPKOM NA RAZLIČNIH PODLAGAH

Yavuz Öztürk[1], Mustafa Erol[2], Erdal Çelik[2,3], Ömer Mermer[1,3], Gökalp Kahraman[1], Ibrahim Avgın[1]

[1]Ege University, Dept. of Electrical and Electronics Engineering, Bornova, 35100 Izmir, Turkey
[2]Dokuz Eylul University, Dept. of Metallurgical and Materials Engineering, Buca, 35160 Izmir, Turkey
[3]Dokuz Eylul University, Center for Production and Applications of Electronic Materials (EMUM), Buca, 35160 Izmir, Turkey
yavuzoz@hotmail.com

Prejem rokopisa – received: 2012-07-13; sprejem za objavo – accepted for publication: 2012-08-27

The cerium-substituted yttrium-iron garnet (Ce-YIG) $Ce_xY_{3-x}Fe_5O_{12}$ is considered as a promising material for applications in high-performance magnetic and magneto-optic devices. In this work cerium-substituted yttrium-iron garnet films were produced on fused silica and Si(100) substrates using the sol-gel technique from solutions with the yttrium/cerium molar ratio 2.8/0.2. A heat treatment was applied to those as-deposited garnet films at temperatures ranging from 800 °C to 1000 °C for 2 h in air. The as-deposited garnet films were characterized by X-ray diffraction (XRD) and scanning electron microscopy (SEM) to investigate their structural properties. A vibrating-sample magnetometer was used at room temperature to characterize the magnetic properties of the as-deposited garnet thin films.

Keywords: sol-gel, yttrium-iron garnet, magnetic properties

S cerijem nadomeščen itrij-železov garnet (Ce-YIG, $Ce_xY_{3-x}Fe_5O_{12}$) je obetajoč material za uporabo v visoko zmogljivih magnetnih in magnetnooptičnih napravah. V tem delu je bila izdelana s cerijem nadomeščena itrij-železova garnetna tanka plast na kremenovem steklu in podlagi Si(100) z uporabo sol-gel tehnike iz raztopine z molskim razmerjem itrij/cerij 2,8/0,2. Nanesena garnetna plast je bila 2 h toplotno obdelana na zraku v temperaturnem območju od 800 °C do 1000 °C. Te plasti so bile karakterizirane z rentgensko difrakcijo (XRD), njihove strukturne značilnosti pa so bile pregledane z vrstičnim elektronskim mikroskopom (SEM). Vibracijski magnetometer je bil uporabljen pri sobni temperaturi za ovrednotenje magnetnih lastnosti nanesenih tankih garnetnih plasti.

Ključne besede: sol-gel, itrij-železo garnet, magnetne lastnosti

1 INTRODUCTION

Pure YIG films and their substituted derivatives have been researched for decades because of their wide range of applications in the microwave, communication and magnetic detection areas[1–3]. For instance, YIG is known to be one of the important ferrites in 1–2 GHz microwave applications owing to its small FMR line width[4]. However, the integration of garnets into semiconductor electronics is not straightforward as this process requires the garnet materials to be in nano/micro-sized dimensions. The magnetic and magneto-optical properties of YIG thin films will be affected by some parameters, namely, the type of the substituted material, the synthesis methods, the substrate and the structure/microstructure of YIG films[5–9].

YIG is the most representative and well-known compound among the rare-earth iron garnets. The definite composition and the presence of only trivalent metal ions make YIG particularly suitable for magnetic studies. There are eight formula units, $Y_3Fe_2(FeO_4)_3$, in a unit cell with a lattice constant $a = (1.2376 \pm 0.0004)$ nm. Some magnetic properties, such as magnetization, remanence, coercivity, Faraday rotation depend critically on the structure and the microstructure of the materials. Also, it is well known that deviations from stoichiometry have a strong influence on the magnetic properties of ferrites. There are three sub-lattices: tetrahedral (d), octahedral (a) and dodecahedral (c) in YIG and they are surrounded by four, six and eight oxygen ions, respectively. Among the five iron ions, which represent a formula unit, three are in 16 octahedral sites and two are in 24 tetrahedral sites[10]. A magnetic moment of 4.64×10^{-24} J/T per formula unit results from anti-ferromagnetic super-exchange interaction between the Fe^{3+} ions in these two different sites through the intervening O^{2-} ions. This corresponds to the moment of the one Fe^{3+} ion that is present at a tetrahedral site in numbers greater than the Fe^{3+} ions at an octahedral site. YIGs are also of scientific importance because of the wide variety of magnetic properties that we can obtain when substituting Y by rare-earth metals or substituting Fe by other trivalent cations.

A variety of techniques have been applied to obtain YIG thin films, such as radio-frequency (RF) sputtering, liquid-phase epitaxial (LPE) growth and pulsed-laser deposition (PLD). Most of these methods are generally vacuum type and expensive. Aside from vacuum-type expensive techniques, different wet chemical methods have been used to obtain the YIG structure, such as sol-gel, co-precipitation, micro-emulsion synthesis, citrate gel routes, hydrothermal synthesis, etc.[4–8]. In related researches, production processes usually focused on obtaining powder and bulk materials instead of producing thin films. Powder or bulk ceramic production techniques require high annealing temperatures and long processing duration, as mentioned in ref[11]. Materials that were used as components of electronic, magneto-optic or magnetic devices are all physically based on the movement of ions, the interaction of light and the change of the orientation in the structure. These structural properties change negatively with increasing material thickness or volume. In this way, producing thin films instead of thick films (coatings) or bulk materials will provide low annealing temperatures and a controlled structure. To the best of our knowledge, there are few studies on obtaining YIG thin films with chemical methods[4–8,12]. Unlike obtaining powder, producing thin films can be achieved at relatively low temperatures, like 700–1000 °C using the sol-gel method as a wet chemical route[8]. Nevertheless, it has been proved that the sol-gel process offers considerable advantages, such as better mixing of the starting materials and excellent chemical homogeneity in the final product. Moreover, the molecular level mixing and the tendency of partially hydrolyzed species to form extended networks facilitate the structure evolution, thereby lowering the crystallization temperature[13,14].

In this study, $Ce_xY_{3-x}Fe_5O_{12}$ thin films were successfully deposited from solution with a Y/Ce molar ratio of 2.8/0.2 on Si(100) and fused silica substrates through the sol-gel method from solutions that were synthesized with ethylhexanoate and 2,4-pentanedionate based precursors.

2 EXPERIMENTAL DETAILS

The precursor materials Fe 2,4-pentanedionate (0.1766 mg), Yttrium 2-Ethylhexanoate (0.1452 mg) and Ce 2-Ethylehexonate (0.01140 mg), were dissolved in methanol and glacial acetic acid (GAA) in order to form a 0.23-M solution with the chemical composition Ce : Y : Fe = 0.2 : 2.8 : 5. Three different solutions (A, B and C) with different methanol and GAA ratios were prepared as listed in **Table 1**. **Table 1** also shows the pH values of the solutions. In this study, GAA acts as a chelating agent to involve a homogenous solution. A higher GAA concentration leads to a poor interaction with the substrate and a lower GAA concentration leads to poorly dissolved precursors in a manner of the macro view. As a result, solution B was determined to be appropriate for deposition on substrates, since it has good wetting and chelating properties. The prepared optimal solutions were dip-coated on the fused silica and Si(100) substrates at room temperature in air. The gel films were dried at 300 °C for 10 min, and consequently heat treated in the range 800–1000 °C for 2 h in air in an electrical furnace. After this procedure, the specimens were cooled down from the annealing temperatures.

Table 1: Solvent – Chelating agent contents and pH values of the solutions A, B and C
Tabela 1: Vsebnost in pH vrednost raztopin topilo – kelat, A, B in C

Solution	Methanol (ml)	GAA (ml)	pH
A	2	1.5	3.6
B	2.5	1	3.05
C	3	0.5	2.5

X-ray diffraction (XRD, Rigaku D/MAX-2200/PC) patterns of the films were determined to identify the phase structure. The surface properties and topographies of the films were examined using scanning electron microscopy (SEM, JEOL JSM 6060) with attached energy-dispersive spectroscopy (EDS). The magnetic properties of samples were determined with a vibrating-sample magnetometer (VSM, Lakeshore 736, 7400) at room temperature.

3 RESULTS AND DISCUSSION

XRD patterns of selected samples on Si(100) and fused silica substrates are depicted in **Figures 1** and **2** respectively. All the produced films contain cubic Ce-substituted YIG films. As reported in the literature[15–17], cubic YIG formation with other impurity phases such as Y_2O_3, $FeYO_3$ and Fe_2O_3 was generally observed at temperatures between 700 °C and 1100 °C. In the present research, neither Y_2O_3 nor $FeYO_3$ phase formations were observed in the YIG film on either

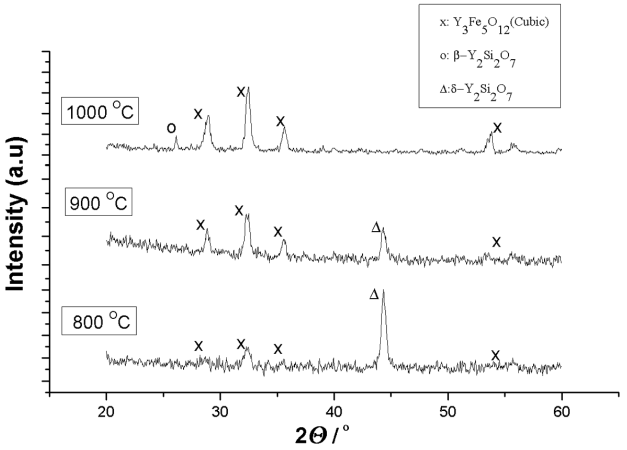

Figure 1: XRD patterns of Ce-YIG films coated on Si(100), annealed between 800 °C and 1000 °C for 2 h in air
Slika 1: XRD-posnetki Ce-YIG plasti na Si(100), žarjeni med 800 °C in 1000 °C, 2 h na zraku

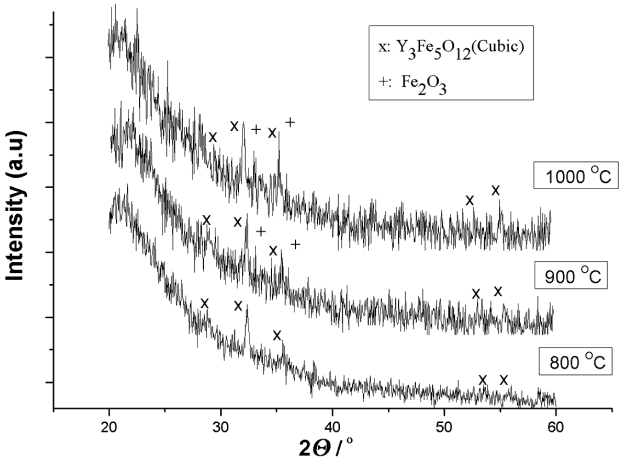

Figure 2: XRD patterns of Ce-YIG films coated on fused silica, annealed between 800 °C and 1000 °C for 2 h in air

Slika 2: XRD-posnetki Ce-YIG plasti na taljenem kremenu, žarjene med 800 °C in 1000 °C, 2 h na zraku

Si(100) or fused silica substrates. However, even though the Fe_2O_3 phase was found in the films on fused silica, it was not determined in the films on Si(100). At the same time, two different crystal structured yttrium silicate phases that transform from δ-$Y_2Si_2O_7$ to β-$Y_2Si_2O_7$ at 1000 °C were found. The formation of these silicate phases was considered to be substrate-film interactions. This formation and the increased annealing temperature affect the crystallization behaviour of the garnet in a positive way.

It is well known that the activation energy for nucleation is reduced by good lattice matching across the interface. As mentioned ref.[18] the nucleation mechanism depends on the substrates and denser nucleation was observed with an increasing lattice match. When the XRD results of the films on both substrates were compared, the Si substrates that were oriented exhibited better crystallization features than the amorphous fused silica. The different crystallization behavior observed for two substrates can be explained by the formation of silicate phases and differences in the nucleation mechanism. Furthermore, fused silica has a high resistance to chemicals, which reduces both interactions with the solution and silicate phase formation.

Sol-gel deposition is a wet chemical route in which the film quality is affected by various parameters such as substrate interaction, pH, humidity, and temperature. In order to tailor the magnetic and magneto-optical properties, film quality and homogeneity must be taken into consideration, as reported in refs[19,20]. The microstructural properties of Ce-YIG films were denoted in **Figure 3**. As can be seen from these micrographs, we have successfully obtained a coating of garnet structure with minor cracks. **Figure 3a** provides a general view of the structure of the films. In addition, some micro-size cracks structure can be seen on the magnified image, which is the result of the substrate film interaction, as shown in **Figure 3b**. The optimum thicknesses of the films were found to be around 300 nm using a profilometer. As far as magnetic properties are concerned, the magnetic hysteresis loop (M-H) of the Ce-YIG films on different substrates annealed at different temperatures was recorded with the VSM at room temperature. **Figures 4** and **5** diagrammatically clarifies the M-H loop of the Ce-YIG layers grown on the Si substrate annealed at

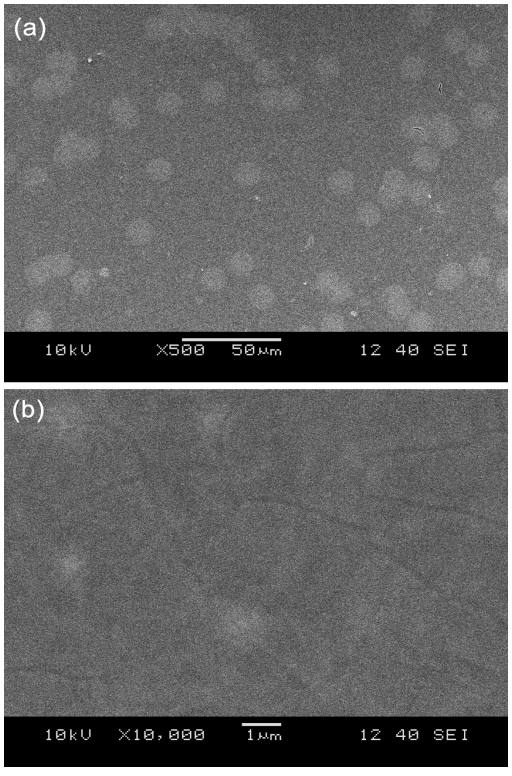

Figure 3: XRD SEM micrographs of Ce-YIG on Si(100) prepared at 1000 °C

Slika 3: XRD SEM-posnetka Ce-YIG na Si(100), pripravljenem pri 1000 °C

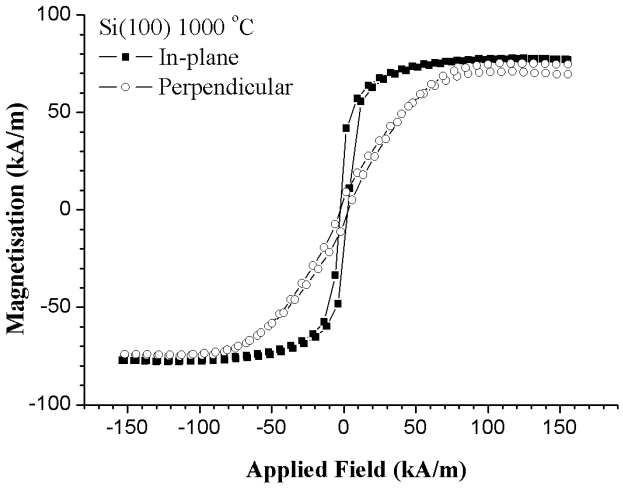

Figure 4: Magnetic hysteresis loops of Ce-YIG on Si(100) substrate annealed at 1000 °C

Slika 4: Magnetna histerezna zanka Ce-YIG na podlagi Si(100), žarjeno pri 1000 °C

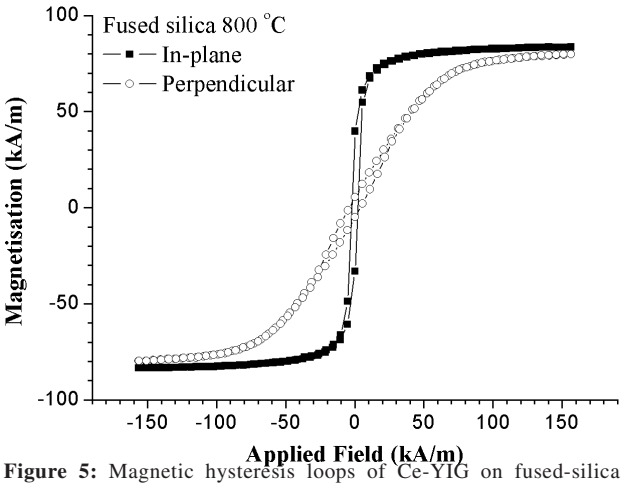

Figure 5: Magnetic hysteresis loops of Ce-YIG on fused-silica substrate annealed at 800 °C

Slika 5: Magnetna histerezna zanka Ce-YIG na taljenem kremenu, žarjeno pri 800 °C

1000 °C and 800 °C, respectively. The applied magnetic field (H_{ex}) is both in plane and perpendicular with respect to the Si wafer. Different annealing temperatures were also applied on the Ce-YIG film on Si and their M-H loops were also measured, but are not shown in the figure. All the parameters related to the magnetic properties of these films were summarized in **Table 2**. These results indicate that strong magnetic anisotropy has been detected for different annealing temperatures of the Ce-YIG films. As the annealing temperature increases, the coercivity values of the film decreases for a field perpendicular to the Si wafer but this does not change significantly for the in-plane field. The saturation magnetization values increase strongly as the annealing temperature increases. This shows that an increase of the annealing temperature changes the substrate–film interaction[21] and also increases the Ce-YIG phase with respect to the $Y_2Si_2O_7$ phases.

In order to compare the effect of different substrates on the magnetic properties, the Ce-YIG film was coated on fused silica. Again, all the films were annealed at the same temperature as that of the Ce-YIG on the Si substrate. **Figure 5** shows the M-H loop of Ce-YIG on fused silica annealed at 800 °C. The magnetic properties of these films for different annealing temperatures were also summarized in **Table 3**. As is evident from **Table 3**, increasing the annealing temperature does not change significantly the coercivity values for a field perpendicular to wafer; however, it decreases them for an in-plane field. For fused-silica substrates the saturation magnetization values decrease strongly when the annealing temperature increases. In this case decreasing the saturation magnetization is mainly due to the formation of the Fe_2O_3 phase in the films, as shown by the XRD pattern in **Figure 2**. This was also confirmed in our previous study[12].

A different range of magnetization values as compared to the bulk in garnet thin films have commonly been observed[21–23]. Lower values of the magnetization explained by parasitic phases in the structure or poorly crystallized and magnetically disordered grain-boundary materials[24]. A strong in-plane magnetic anisotropy was observed for the Ce-YIG films grown on both substrates, indicating that the substrate–film interaction has an important role in the formation of the crystalline structure as well as the magnetic properties. Because of the in-plane anisotropy, these kinds of films are useful for applications of planar waveguides and magnetic biasing.

4 CONCLUSIONS

Ce-substituted YIG thin films were synthesized on fused silica and Si(100) substrates with solutions prepared from Ce, Y, and Fe-based precursors. The microstructural (SEM) results indicate good surface quality with micro cracks. Also, two different crystallization

Table 2: Magnetic properties of Ce-YIG films on Si substrate at different annealing temperatures

Tabela 2: Magnetne lastnosti plasti Ce-YIG na Si-podlagi pri različnih temperaturah žarjenja

Substrate	Annealing temp. (°C)	Saturation Magnetization (kA/m)	Perpendicular		In-plane	
			Remanence (kA/m)	Coercivity (kA/m)	Remanence (kA/m)	Coercivity (kA/m)
Si(100)	800	33	4	4.856	11	2.070
Si(100)	900	51	4	3.185	15	2.070
Si(100)	1000	78	7	2.866	22	2.468

Table 3: Magnetic properties of Ce-YIG films on fused-silica substrate at different annealing temperatures

Tabela 3: Magnetne lastnosti plasti Ce-YIG na kremenovem steklu pri različnih temperaturah žarjenja

Substrate	Annealing temp. (°C)	Saturation Magnetization (kA/m)	Perpendicular		In-plane	
			Remanence (kA/m)	Coercivity (kA/m)	Remanence (kA/m)	Coercivity (kA/m)
Fused silica	800	83	7	4.299	41	2.229
Fused silica	900	49	6	4.936	28	2.627
Fused silica	1000	39	5	4.459	23	2.946

dynamics were observed for the two substrates. The YIG phase was obtained at 800 °C with the highest magnetization value (83 kA/m) in all the samples deposited on the fused-silica substrates. The Fe_2O_3 phase was obtained at higher annealing temperatures. For the Si(100) a strong substrate-layer interaction was observed, which causes yttrium silicate phases. Higher annealing temperatures led to a substrate-film interaction with higher crystallization and increased magnetization. All the films show strong in-plane anisotropy that would be suitable for waveguide- or magnetic-biasing-based devices.

Acknowledgement

This work was financially supported by the Scientific and Technological Research Council of Turkey (TUBITAK, project number 106T651).

5 REFERENCES

[1] S. Higuchi, Y. Furukawa, S. Takekawa, O. Kamada, K. Kitamura, K. Uyeda, Sens. Actuators A, 105 (**2003**), 293

[2] T. Shintaku, T. Uno, Jpn. J. Appl. Phys., 35 (**1996**), 4689

[3] K. Matsumoto, S. Sasaki, Y. Yamanobe, K. Yamaguchi, T. Fujii, Y. Asahara, J. Appl. Phys., 70 (**1991**), 1624

[4] V. G. Harris, A. Geiler, Y. Chen, S. D. Yoon, M. Wu, A. Yang, Z. Chen, P. He, P. V. Parimi, X. Zuo, C. E. Patton, M. Abe, O. Acher, C. Vittoria, J. Magn. Magn. Mater, 321 (**2009**), 2035

[5] P. Vaqueiro, M. P. Crosnier-Lopez, M. A. Lopez-Quintela, J. Solid State Chem., 126 (**1996**), 161

[6] X. Z. Guo, B. G. Ravi, P. S. Devi, J. C. Hanson, J. Margolies, R. J. Gambino, J. B. Parise, S. Sampath, J. Magn. Magn. Mater., 295 (**2005**), 145

[7] M. Inoue, T. Nishikawa, H. Otsu, H. Kominami, T. Inui, J. Am. Ceram. Soc., 80 (**1997**), 2157

[8] C. S. Kuroda, T. Taniyama, Y. Kitamoto, Y. Yamazaki, J. Magn. Magn. Mater., 241 (**2002**), 201

[9] K. Matsumoto, S. Yamamoto, Y. Yamanobe, A. Ueno, K. Yamaguchi, T. Fujii, Jpn. J. Appl. Phys., 30 (**1991**), 1696

[10] S. Geller, M. A. Gilleo, Acta Cryst, 10 (**1957**), 239

[11] Z. Abbas, M. Ramadan Al-habashi, K. Khalid, M. Maarof, Eur. J. Sci. Res., 36 (**2009**), 154

[12] Y. Ozturk, I. Avgın, M. Erol, E. Çelik, Advances in Nanoscale Magnetism, Springer Proceedings in Physics, 122 (**2009**), 113

[13] H. Xu, H. Yang, J. Mater. Sci.: Mater Electron, 19 (**2008**), 589

[14] H. Bahadur, A. K. Srivastava, R. K. Sharma, S. Chandra, Nanoscale Res. Lett., 2 (**2007**), 469

[15] X. Zhou, W. Cheng, F. Lin, X. Ma, W. Shi, Appl. Surf. Sci., 253 (**2006**), 2108

[16] Z. Wei, G. Cuijing, J. Rongjin, F. Caixiang, Z. Yanwei, Mater. Chem. Phys., 125 (**2011**), 646

[17] H. G. Beh, R. Irmawati, Y. Noorhana, K. P. Lim, IJET, 2 (**2009**), 261

[18] M. B. Park, N. H. Cho, J. Magn. Magn. Mater, 231 (**2001**), 253

[19] M. Xiangyang, S. Jian, S. Zhang, D. Que, J. Mater. Sci. Lett., 17 (**1998**), 1635

[20] M. Xiangyang, Z. Shouye, L. Fengzhen, Q. Duanlin, J. Mater. Sci. Mater. Electron, 9 (**1998**), 347

[21] K. H. Shin, M. Mizoguchi, M. Inoue, J. Magn., 12 (**2007**), 129

[22] A. C. Rastogi, V. N. Moothy, Mater. Sci. Eng. B, 95 (**2002**), 131–136

[23] N. Kumar, D. S. Misra, N. Venkataramani, S. Prasad, R. Krishnan, J. Magn. Magn. Mater., 276 (**2004**), 899

[24] E. Popova, N. Keller, F. Gendron, M. Guyot, M. C. Brianso, Y. Domond, M. Tessier, J. Appl. Phys., 90 (**2001**), 1422

UDK 669.715:544.225
Original scientific article/Izvirni znanstveni članek

ISSN 1580-2949
MTAEC9, 47(1)65(2013)

STRUCTURAL STABILITY AND ELECTRONIC PROPERTIES OF $AlCu_3$, $AlCu_2Zr$ AND $AlZr_3$

STABILNOST STRUKTURE IN ELEKTRONSKE LASTNOSTI $AlCu_3$, $AlCu_2Zr$ IN $AlZr_3$

Rong Cheng, Xiao-Yu Wu

Shenzhen Key Laboratory of Advanced Manufacturing Technology for Mold & Die, College of Mechatronics and Control Engineering, Shenzhen University, Shenzhen 518060, P. R. China
songxp12345@yeah.net

Prejem rokopisa – received: 2012-07-23; sprejem za objavo – accepted for publication: 2012-08-28

First-principles calculations were performed to study the alloying stability and electronic structure of the Al-based intermetallic compounds $AlCu_3$, $AlCu_2Zr$ and $AlZr_3$. The results show that the lattice parameters obtained after the full relaxation of the crystalline cells are consistent with the experimental data, and these intermetallics have a strong alloying ability and structural stability due to their negative formation energies and their cohesive energies. A further analysis revealed that the single-crystal elastic constants at zero-pressure satisfy the requirements for the mechanical stability of cubic crystals. The calculations on Poisson's ratio show that $AlCu_3$ is much more anisotropic than the other two intermetallics. In addition, calculations on the densities of states indicate that the valence bonds of these intermetallics are attributed to the valence electrons of Cu 3d states for the $AlCu_3$, Cu 3d and Zr 4d states for $AlCu_2Zr$, and Al 3s, Zr 5s and 4d states for $AlZr_3$, respectively. In particular, the electronic structure of the $AlZr_3$ shows the strongest hybridization.

Keywords: $AlCu_3$, $AlCu_2Zr$, first-principles, electronic structure

Narejeni so bili prvi načelni izračuni stabilnosti legiranja in elektronske strukture aluminijevih intermetalnih zlitin ($AlCu_3$, $AlCu_2Zr$ in $AlZr_3$). Rezultati kažejo, da se mrežni parametri po polni relaksaciji kristalnih celic ujemajo z eksperimentalnimi podatki in da imajo te intermetalne zlitine veliko sposobnost legiranja ter stabilno strukturo zaradi negativne tvorbene energije in kohezivnih energij. Nadaljnje analize so pokazale, da elastična konstanta monokristala pri ničelnem tlaku ustreza zahtevam mehanske stabilnosti kubičnega kristala. Izračun Poissonovega količnika pokaže, da je $AlCu_3$ bolj anizotropen kot drugi dve intermetalni zlitini. Dodatno izračun gostote stanj pokaže, da so valenčne vezi teh treh intermetalnih zlitin vezane na valenčne elektrone Cu 3d-stanja za $AlCu_3$, Cu 3d in Zr 4d-stanja za $AlCu_2Zr$, ter Al 3s, Zr 5s in 4d-stanja za $AlZr_3$, posebno elektronska struktura $AlZr_3$ pa kaže najmočnejšo hibridizacijo.

Ključne besede: $AlCu_3$, $AlCu_2Zr$, načelen izračun, elektronska struktura

1 INTRODUCTION

Intermetallics involving aluminum and transition metals (TMs) are known to have a high resistance to oxidation and corrosion, elevated-temperature strength, relatively low density, and high melting points, which make them desirable candidates for high-temperature structural applications[1,2]. In particular, zirconium can effectively enhance the mechanical strength of the alloys when copper and zinc elements exist in aluminum and Al-based alloys[3]. Adding Zr to the Al-Mg alloys can effectively remove or reduce hydrogen, grain refinement, pinholes, porosity and hot cracking tendency, and so improve the mechanical properties[4]. Many investigations have focused on the constituent binary systems, such as Al-Cu, Al-Zr, and Cu-Zr [5–10]; however, there has been a lack of systematic theoretical and experimental investigations for binary and ternary systems, especially for ternary alloy systems.

In recent years, first-principles calculations based on the density-functional theory have become an important tool for the accurate study of the crystalline and electronic structures and mechanical properties of solids[11]. In the present study, we report on a systematic investigation of the structural, elastic and electronic properties of Al-based alloys ($AlCu_3$, $AlZr_3$ and $AlCu_2Zr$) using first-principles calculations, and the results are discussed in comparison with the available experimental data and other theoretical results.

2 COMPUTATIONAL METHOD

All the calculations were performed using the Vienna ab-initio Simulation Package (VASP)[12,13] based on the density-functional theory (DFT)[14]. The exchange and correlation energy was treated within the generalized gradient approximation of Perdew–Wang 91 version (GGA-PW91)[15]. The interaction between the valence electrons and the ions was described by using potentials generated with Blöchl's projector augmented wave (PAW) method[16]. The PAW potential used for Al treats the 3s, 3p states as valence states, and the other electron-ion interaction was described by the 3d, 4s valence states for Cu, 5s, 4d, 5p valence states for Zr. A plane-wave energy cut-off was set at 450 eV for the $AlCu_3$ and $AlCu_2Zr$, and at 350 eV for the $AlZr_3$. Brillouin Zone integrations were performed using the Monkhorst-Pack[17] k-point meshes, e.g., the k-point meshes for $AlCu_3$,

$AlCu_2Zr$ and $AlZr_3$ were 15×15×15, 9×9×9 and 13×13×13 for optimizing the geometry and calculating the elastic constants, and 25×25×25, 19×19×19and 23×23×23 for calculations of the density of states (DOS) at the equilibrium volume, respectively. Optimizations of the structural parameters (atomic positions and the lattice constants) for each system were performed using the conjugate gradient method, and the coordinates of the internal atoms were allowed to relax until the total forces on each ion were less than 0.01 eV/(10^{-1} nm). The total energy and density of states (DOS) calculations were performed with the linear tetrahedron method using Blöchl corrections[18]. In order to avoid wrap-around errors, all the calculations were performed using the "accurate" setting within VASP.

3 RESULTS AND DISCUSSION

3.1 Equilibrium properties

The $AlCu_3$ and $AlZr_3$ alloys have the simple cubic Cu_3Au ($L1_2$ type, space group Pm-3m) structure[19,20]. The $AlCu_2Zr$ alloy is a partially ordered Cu_2MnAl-type fcc structure with the Fm-3m space group[21]. Firstly, these crystal structures were optimized with a relaxation of the cell shape and the atomic positions. The equilibrium volume V_0, bulk modulus B_0 and the pressure derivation of the bulk modulus B'_0 of the $AlCu_3$, $AlCu_2Zr$ and $AlZr_3$ were determined by fitting the total energy calculated at different lattice-constant values to a Birch-Murnaghan equation of state[22]. The results of the first-principles calculations are listed in **Table 1**. From **Table 1** it is clear that the results of our calculations compare very favorably with the experimental data. This shows that the used parameters are reasonable.

It is known that the stability of a crystal structure is correlated to its cohesive energy[23], which is often defined as the work that is needed when the crystal is decomposed into single atoms. Hence, the lower the cohesive energy is, the more stable the crystal structure is[23]. In the present study, the cohesive energies (E_{coh}) of the $AlCu_3$, $AlCu_2Zr$ and $AlZr_3$ crystal cells can be calculated by:

$$E_{coh}^{ABC} = \frac{(E_{tot} - N_A E_{atom}^A - N_B E_{atom}^B - N_C E_{atom}^C)}{N_A + N_B + N_C} \quad (1)$$

where E_{tot} is the total energy of the compound at the equilibrium lattice constant, and E_{atom}^A, E_{atom}^B, E_{atom}^C are the energies of the isolated atoms A, B and C in the freedom states. N_A, N_B and N_C refer to the numbers of A, B and C atoms in each unit cell. The energies of the isolated Al, Cu and Zr atoms are –0.276 eV, –0.254 eV and –2.054 eV, respectively. The cohesive energies (E_{coh}) per atom of all the crystal or primitive cells are calculated from Eq. (1), and the results of the calculations are listed in **Table 2**. From the calculated values we find that the cohesive energy of $AlZr_3$ is 2.237 eV and 1.413 eV per atom lower than that of $AlCu_3$ and $AlCu_2Zr$, respectively. Therefore, of the three phases, the $AlZr_3$ phase has the highest structural stability, followed by $AlCu_2Zr$ and finally the $AlCu_3$. This means that for the $AlZr_3$, $AlCu_2Zr$, and $AlCu_3$ alloys the structural stability is higher with increasing amounts of Zr in the crystal.

Table 2: Total energy E_{tot}, cohesive energy E_{coh} and formation energy ΔH of $AlCu_3$, $AlCu_2Zr$ and $AlZr_3$

Tabela 2: Celotna energija E_{tot}, kohezivna energija E_{coh} in tvorbena energija ΔH za $AlCu_3$, $AlCu_2Zr$ in $AlZr_3$

Compound	E_{tot} /eV per atom	E_{coh} /eV per atom	ΔH/eV per atom
$AlCu_3$	–3.897	–3.637	–0.177
$AlCu_2Zr$	–5.261	–4.551	–0.359
$AlZr_3$	–7.574	–5.964	–0.307

In order to compare the alloying abilities of the present compounds, we calculate the formation energy ΔH, which can be given by:

$$\Delta H_{ABC} = \frac{(E_{tot} - N_A E_{solid}^A - N_B E_{solid}^B - N_C E_{solid}^C)}{N_A + N_B + N_C} \quad (2)$$

where E_{solid}^A, E_{solid}^B, E_{solid}^C are the energies per atom of the pure constituents A, B and C in the solid states, respectively. And the other variables are as defined for Eq. (1). If the formation energy is negative, the formation of a compound from its elements is usually an exothermic process. Furthermore, the lower the formation energy is, the stronger the alloying ability is, and the more stable the crystal structure is[23]. The calculated energies of Al, Cu and Zr in their respective crystals are –3.696 eV, –3.728 eV, –8.457 eV. The calculated results of these compounds are also listed in **Table 2**. It is clear that all

Table 1: Calculated and experimental lattice parameters a (nm), equilibrium volume V_0 (nm^3), bulk modulus B_0 (GPa) and the pressure derivation of the bulk modulus B'_0 for $AlCu_3$, $AlCu_2Zr$, $AlZr_3$

Tabela 1: Izračunani in eksperimentalno določeni mrežni parametri a (nm), ravnotežni volumen V_0 (nm^3), modul pri stiskanju B_0 (GPa) in izpeljava modula iz tlaka B'_0 za $AlCu_3$, $AlCu_2Zr$, $AlZr_3$

	$AlCu_3$		$AlCu_2Zr$		$AlZr_3$	
	Present.	Expt.	Present.	Expt.	Present.	Expt.
a/nm	0.3693	0.3607 [19]	0.6256	0.6216 [21]	0.4381	0.4392 [20]
V_0/nm^3	$50.358 \cdot 10^{-3}$	–	$244.805 \cdot 10^{-3}$	$240.210 \cdot 10^{-3}$ [21]	$84.110 \cdot 10^{-3}$	$84.700 \cdot 10^{-3}$ [20]
B_0/GPa	131.010	–	128.600	–	100.800	101.4 [7]
B'_0	4.47	–	4.280	–	3.48	3.33 [7]

the ΔH is negative, which means that the structure of these compounds can exist and be stable. A further comparison and analysis showed that the alloying abilities of $AlCu_2Zr$ were much stronger than $AlCu_3$ and $AlZr_3$. It should be noticed that the alloying ability of $AlZr_3$ was higher than that of the $AlCu_3$ alloy.

3.2 Elastic properties

The density-functional theory has become a powerful tool for investigating the elastic properties of materials (in the limit of zero temperature and in the absence of zero-point motion). For a given crystal it is possible to calculate the complete set of elastic constants by applying small strains to the equilibrium unit cell and determining the corresponding variations in the total energy. The necessary number of strains is imposed by the crystal symmetry[24]. For a material with cubic symmetry, there are only three independent elastic constants, C_{11}, C_{11} and C_{11}. The strain tensor is given by:

$$\delta = \begin{pmatrix} \delta_{11} & \delta_{12} & \delta_{13} \\ \delta_{21} & \delta_{22} & \delta_{23} \\ \delta_{31} & \delta_{32} & \delta_{33} \end{pmatrix} \tag{3}$$

In the present study we applied three kinds of strains $\delta^{(N)}$ (N = 1, 2, 3) so as to obtain the elastic constants, and they are listed in **Table 3**. The first strain is a volume-conserving tetragonal deformation along the z axis, the second refers to a uniform hydrostatic pressure, and the last one corresponds to a volume-conserving orthorhombic shear[24]. The elastic strain energy was given by:

$$U = \frac{\Delta E}{V_0} = \frac{1}{2} \sum_{i=1}^{6} \sum_{j=1}^{6} C_{ij} e_i e_j \tag{4}$$

where $\Delta E = E_{\text{total}}(V_0,\delta) - E_{\text{total}}(V_0,0)$ is the total energy variation between the deformed cell and the initial cell, V_0 is the equilibrium volume of the cell, C_{ij} is the elastic constant and δ is the deformation added to the equilibrium cell. The elastic strain energy is also listed in **Table 3**. For each kind of lattice deformation, the total energy has been calculated for different strains $\gamma = \pm 0.01n$ ($n = 0 \approx 2$). By means of a polynomial fit, we extracted three values of the second-order coefficients, corresponding to $3(C_{11} - C_{12})$, $3(C_{11} + 2C_{12})/2$ and $2C_{44}$, respectively, the elastic constants C_{11}, C_{12} and C_{44} were obtained[25], and the results are shown in **Table 4**. From **Table 4** we can see that our calculation results agree well with the experimental data or other first-principle calculations. These elastic constants satisfy the requirement of mechanical stability for cubic crystals[24]: $(C_{11} - C_{12}) > 0$, $C_{11} > 0$, $C_{44} > 0$, $(C_{11} + 2\ C_{12}) > 0$. This shows that $AlCu_3$, $AlCu_2Zr$ and $AlZr_3$ have a stable structure. The average bulk modulus is identical to the single-crystal bulk modulus, i.e., $B = (C_{11} + 2\ C_{12})/3$. Interestingly, we noted that the bulk modulus calculated from the values of the elastic constants is in good agreement with the one obtained through fitting to the Birch-Murnaghan equation of state (B_0), giving a consistent estimation of the compressibility for these compounds[26].

Table 3: The strains used to calculate the elastic constants of $AlCu_3$, $AlCu_2Zr$ and $AlZr_3$, with $\gamma = \pm 0.01n$ ($n = 0 \approx 2$)

Tabela 3: Napetosti, uporabljene za izračun konstant elastičnosti $AlCu_3$, $AlCu_2Zr$ in $AlZr_3$, z $\gamma = \pm 0.01n$ ($n = 0 \approx 2$)

Strain	Parameters (unlisted $\delta_{ij} = 0$)	$\Delta E/V_0$ to $0(\gamma^2)$
$\delta^{(1)}$	$\delta_{11} = \delta_{22} = \gamma$, $\delta_{33} = [(1+\gamma)^{-2} - 1]$	$3(C_{11} - C_{22})\gamma^2$
$\delta^{(2)}$	$\delta_{11} = \delta_{22} = \delta_{33} = \gamma$	$(3/2)(C_{11} + 2C_{12})\gamma^2$
$\delta^{(3)}$	$\delta_{12} = \delta_{21} = \gamma$, $\delta_{33} = [\gamma^2(1 - \gamma^2)^{-1}]$	$2C_{44}\gamma^2$

In order to further validate our results, the elastic modulus, such as the shear modulus G(GPa), Young's modulus E(GPa), Poisson's ratio v and anisotropy constant A for a polycrystalline material were also calculated with the single-crystal elastic constants C_{ij}, all of these elastic moduli are shown in **Table 4**. In the present study we adopted Hershey's averaging method[27], which has been known to give the most accurate relation between single-crystal and polycrystalline values for a cubic lattice[28]. According to this method, G is obtained by solving the following equation:

$$G^3 + \frac{5C_{11} + 4C_{12}}{8} G^2 - \frac{C_{44}(7C_{11} - 4C_{12})}{8} G - \frac{C_{44}(C_{11} - C_{12})(C_{11} + C_{12})}{8} = 0 \tag{5}$$

The calculated shear moduli G for $AlZr_3$ are the largest, while the quantities for $AlCu_2Zr$ are less than for $AlCu_3$.

Pugh[29] found that the ratio of the bulk modulus to the shear modulus (B/G) of polycrystalline phases can predict the brittle and ductile behavior of the materials. A high and low value of B/G are associated with ductility and brittleness, respectively. The critical value which separates ductility from brittleness is about 1.75. From B/G calculated in **Table 4** we can see that all the B/G ratios are larger than 1.75. Therefore, $AlCu_3$, $AlCu_2Zr$ and $AlZr_3$ have good ductility. In contrast, the biggest B/G ratio for $AlCu_2Zr$ indicates that $AlCu_2Zr$ is of very good ductility in these three Al-based alloys. $AlCu_3$ has an intermediate ductility, while $AlZr_3$ has the worst ductility.

Besides B/G, the Young's modulus E and the Poisson's ratio v are important for technological and engineering applications. The Young's modulus is used to provide a measure of the stiffness of the solid, i.e., the larger the value of E, the stiffer the material[24]. According to Hershey's averaging method, the Young's modulus is defined as: $E = 9GB/3(B+G)$. Based on the calculated results, we find that $AlZr_3$ has a Young's modulus that is 18.806 GPa and 24.663 GPa larger than $AlCu_3$ and $AlCu_2Zr$, respectively. This indicates that the $AlZr_3$ phase has the highest stiffness, followed by $AlCu_3$ and finally the $AlCu_2Zr$. In addition, the Poisson's ratio v has also

Table 4: Calculated elastic constants (GPa) and elastic modulus (bulk modulus *B* (GPa), shear modulus *G* (GPa), Young's modulus *E* (GPa), Poisson's ratio *v* and anisotropy constant *A*) of $AlCu_3$, $AlCu_2Zr$ and $AlZr_3$

Tabela 4: Izračunane konstante elastičnosti (GPa) in elastični moduli (modul pri stiskanju *B* (GPa), strižni moduli *G* (GPa), Youngovi moduli *E* (GPa), Poissonov količnik *v* in konstante anizotropije *A*) za $AlCu_3$, $AlCu_2Zr$ in $AlZr_3$

Compound	C_{11}	C_{12}	C_{44}	*B*	*G*	*B/G*	*E*	*v*	*A*	reference
$AlCu_3$	150.707	120.565	81.880	130.612	43.593	2.996	117.686	0.350	1.887	this study
	176.000	117.400	92.400	136.900	49.600		132.800	0.340		[5]
$AlCu_2Zr$	157.504	115.305	62.685	129.371	41.237	3.137	111.829	0.356	1.528	this study
$AlZr_3$	148.653	79.387	70.834	102.476	53.400	1.919	136.492	0.278	1.487	this study
	163.800	79.300	86.500	107.670						[6]

been used to measure the shear stability of the lattice, which usually ranges from –1 to 0.5. The greater the value of the Poisson's ratio *v*, the better the plasticity of the materials. So we can see that $AlCu_3$, $AlCu_2Zr$ and $AlZr_3$ have a better plasticity.

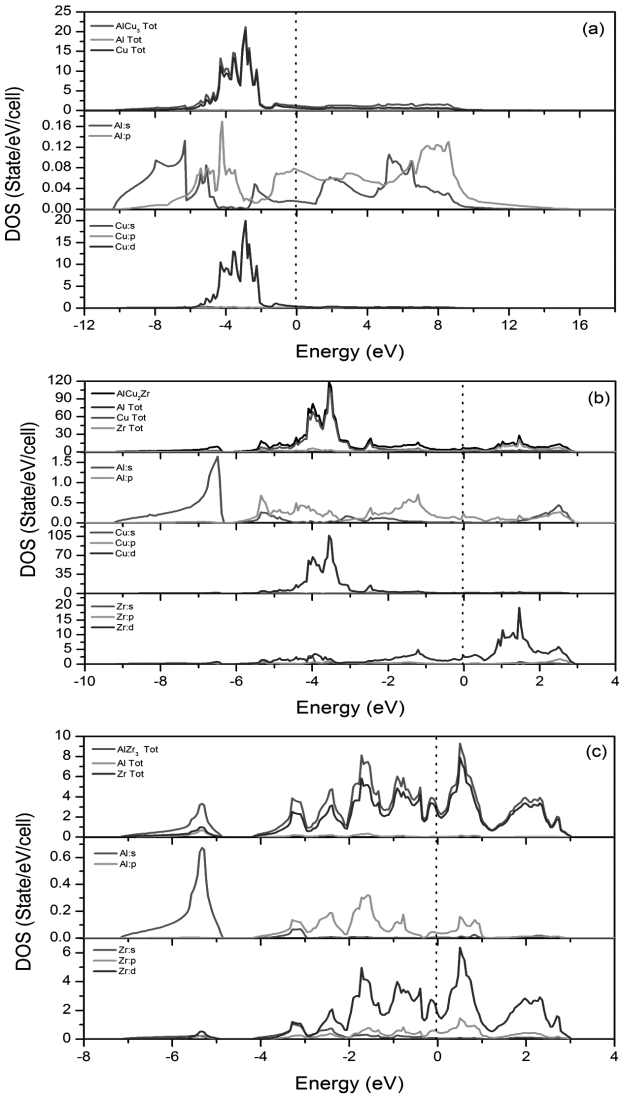

Figure 1: The total and partial density of states (DOS) of: a) $AlCu_3$ crystal cell, b) $AlCu_2Zr$ crystal cell, c) $AlZr_3$ crystal cell. The vertical dot line indicates the Fermi level.

Slika 1: Skupna in parcialna gostota stanj (DOS) za: a) kristalno celico $AlCu_3$, b) kristalno celico $AlCu_2Zr$, c) kristalno celico $AlZr_3$. Navpična pikčasta linija prikazuje Fermijev nivo.

The elastic anisotropy of the crystals has an important application in engineering materials since it is highly correlated with the possibility of inducing microcracks[24,30]. For cubic symmetric structures[31], the elastic anisotropy is defined as $A = (2C_{44} + C_{12})/C_{11}$. For a completely isotropic material the value of will be 1, while values smaller or bigger than 1 measuring the degree of elastic anisotropy[24]. Interestingly, we note that the values of *A* (**Table 4**) do not deviate far from unity, suggesting that the present cubic-structure alloys also do not deviate far from being isotropic. The calculated results also indicate that $AlCu_3$ is much more anisotropic than the other two alloys.

3.3 Density of states

For a beter understanding of the electronic characteristic and structural stability, the total density of states (DOS) for $AlCu_3$, $AlCu_2Zr$ and $AlZr_3$ were calculated, as shown in **Figure 1**, as well as the partial density of states (PDOS) of Al, Cu and Zr atoms in these Al-based intermetallic compounds. **Figure 1** has evidence for the metallic character of these considered $AlCu_3$, $AlCu_2Zr$ and $AlZr_3$ structures because of the finite DOS at the Fermi level. With regard to the total density of states curve of $AlCu_3$, it is clear from **Figure 1a** that the whole valence band of $AlCu_3$ is located between –7 eV and 9 eV, which is dominated by Cu 3d states and a small contribution from the 3s and 3p states of Al. The valence band of $AlZr_3$ (**Figure 1c**) can be divided into three areas. The first area is dominated by the valence electron numbers of Al 3s and Zr 4d states are mostly located between –7 eV and –5 eV, the second by the Zr 5s and 4d states located between –4 eV and –3 eV, and the third by Zr 4d states located between –2.8 eV and 3.0 eV. Both below and above the Fermi level, the hybridization between the Al-p states and Zr-d states is strong. Due to the strong hybridization (or covalent interaction) the entire DOS can be divided into bonding and anti-bonding regions, and that a pseudogap resides in between. The characteristic pseudogap around the Fermi level indicates the presence of the directional covalent bonding. The Fermi level located at a valley in the bonding region implies the system has a pronounced stability. It is

also generally considered that the formation of covalent bonding would enhance the strength of the material in comparison with the pure metallic bonding[32]. According to the covalent approach, the guiding principle is to maximize the bonding. Therefore, for a series of compounds having the same structure, the greater the occupancy in the bonding region the higher the stability[33]. It is indeed seen that the structural stability increases from $AlCu_3$ to $AlZr_3$. For $AlCu_2Zr$ (see **Figure 1b**) it is clear that the main bonding peaks between –6 eV and –2 eV are predominantly derived from the Cu 3d orbits, while the main bonding peaks between the Fermi level and 3 eV predominantly derived from the Zr 4d orbits. It should be noted that the phase stability of intermetallics depends on the location of the Fermi level and the value of the DOS at the Fermi level, i.e. $N(E_F)$ [34,35]. A lower $N(E_F)$ corresponds to a more stable structure. The value of the total DOS at the Fermi level is 3.64 states per eV for $AlZr_3$, and the value of the total DOS at the Fermi level is 5.74 states per eV for $AlCu_2Zr$. Therefore, $AlZr_3$ has a more stable structure in these three Al-based intermetallics. This is in accordance with the calculation of cohesive energy.

4 CONCLUSIONS

In summary, using the first-principles method we have calculated the alloying stability, the electronic structure, and the mechanical properties of $AlCu_3$, $AlCu_2Zr$ and $AlZr_3$. These intermetallics have a strong alloying ability and structural stability due to the negative formation energies and the cohesive energies. In particular, $AlCu_3$ is much more anisotropic than the other two intermetallics. The valence bonds of these intermetallics are attributed to the valence electrons of the Cu 3d states for $AlCu_3$, Cu 3d and Zr 4d states for $AlCu_2Zr$, and Al 3s, Zr 5s and 4d states for $AlZr_3$, respectively, and the electronic structure of the $AlZr_3$ shows the strongest hybridization, leading to the worst ductility.

Acknowledgements

This work was financially supported by the National Natural Science Foundation of China (No. 51175348). The authors are also grateful to colleagues for their important contribution to the work.

5 REFERENCES

[1] G. Sauthoff, In: J. H. Westbrook, R. L. Fleischer, editors, Intermetallic compounds, Wiley, New York 1994, 991
[2] R. W. Cahn, Intermetallics, 6 (**1998**), 563
[3] P. K. Rajagopalan, I. G. Sharma, T. S. Krishnan, J. Alloys Compd., 285 (**1999**), 212
[4] P. Wonwook, Mater Design, 17 (**1996**), 85
[5] W. Zhou, L. J. Liu, B. L. Li, Q. G. Song, P. Wu, J. Electron Mater., 38 (**2009**), 356
[6] E. Clouet, J. M. Sanchez, Phys. Rev. B, 65 (**2002**), 094105
[7] G. Ghosh, M. Asta, Acta Mater., 53 (**2005**), 3225
[8] G. Ghosh, Acta Mater., 55 (**2007**), 3347
[9] W. J. Ma, Y. R. Wang, B. C. Wei, Y. F. Sun, Trans Nonferrous Met. Soc. China, 17 (**2007**), 929
[10] S. Pauly, J. Das, N. Mattern, D. H. Kim, J. Eckert, Intermetallics, 17 (**2009**), 453
[11] H. Baltache, R. Khenata, M. Sahnoun, M. Driz, B. Abbar, B. Bouhafs, Physica B, 344 (**2004**), 334
[12] G. Kresse, J. Hafner, Phys. Rev. B, 49 (**1994**), 14251
[13] G. Kresse, J. Furthmüller, Phys. Rev. B, 54 (**1996**), 11169
[14] W. Kohn, L. J. Sham, Phys. Rev., 140 (**1965**), 1133
[15] J. P. Perdw, Y. Wang, Phys. Rev. B, 45 (**1992**), 13244
[16] P. E. Blöchl, Phys. Rev. B, 50 (**1994**), 17953
[17] H. J. Monkhorst, J. D. Pack, Phys. Rev. B, 13 (**1976**), 5188
[18] P. E. Blöchl, O. Jepsen, O. K. Andersen, Phys. Rev. B, 49 (**1994**), 16223
[19] M. Draissia, M. Y. Debili, N. Boukhris, M. Zadam, S. Lallouche, Copper, 10 (**2007**), 65
[20] W. J. Meng, J. Jr Faber, P. R. Okamoto, L. E. Rehn, B. J. Kestel, R. L. Hitterman, J. Appl. Phys., 67 (**1990**), 1312
[21] R. Meyer zu Reckendorf, P. C. Schmidt, A. Weiss, Z. Phys. Chem. N F, 163 (**1989**),103
[22] F. Birch, J. Geophys. Res., 83 (**1978**), 1257
[23] V. I. Zubov, N. P. Tretiakov, J. N. Teixeira Rabelo, Phys. Lett. A, 194 (**1994**), 223
[24] M. Mattesini, R. Ahuja, B. Johansson, Phys. Rev. B, 68 (**2003**), 184108
[25] W. Y. Yu, N. Wang, X. B. Xiao, B. Y. Tang, L. M. Peng, W. J. Ding, Solid State Sciences, 11 (**2009**), 1400
[26] B. Y. Tang, N. Wang, W. Y. Yu, X. Q. Zeng, W. J. Ding, Acta Mater., 56 (**2008**), 3353
[27] H. M. Ledbetter, J. Appl. Phys., 44 (**1973**), 1451
[28] A. Taga, L. Vitos, B. Johansson, Grimvall G., Phys. Rev. B, 71 (**2005**), 14201
[29] S. F. Pugh, Philos. Mag., 45 (**1954**), 823
[30] V. Tvergaard, J. W. Hutchinson, J. Am. Ceram. Soc., 71 (**1988**), 157
[31] B. B. Karki, L. Stixrude, S. J. Clark, M. C. Warren, G. J. Ackland, J. Crain, Am. Miner., 82 (**1997**), 51
[32] P. Chen, D. L. Li, J. X. Yi, W. Li, B. Y. Tang, L. M. Peng et al., Solid State Sciences, 11 (**2009**), 156
[33] J. H. Xu, W. Lin, A. J. Freeman, Phys. Rev. B, 48 (**1993**), 4276
[34] J. H. Xu, T. Oguchi, A. J. Freeman, Phys. Rev. B, 36 (**1987**), 4186
[35] T. Hong, T. J. Watson-Yang, A. J. Freeman, T. Oguchi, J. H. Xu, Phys. Rev. B, 41 (**1990**), 12462

UDK 537.622
Original scientific article/Izvirni znanstveni članek

ISSN 1580-2949
MTAEC9, 47(1)71(2013)

SYNTHESIS OF A Fe_3O_4/PAA-BASED MAGNETIC FLUID FOR FARADAY-ROTATION MEASUREMENTS

SINTEZA MAGNETNE TEKOČINE NA OSNOVI Fe_3O_4/PAA ZA MERITVE FARADAYEVE ROTACIJE

Serhat Küçükdermenci[1,3], Deniz Kutluay[1,2], İbrahim Avgın[1]

[1]Department of Electrical and Electronics Engineering, Ege University, Bornova 35100, Izmir, Turkey
[2] Departments of Electronics and Communications Engineering, Izmir University, Uckuyular 35290, Izmir, Turkey
[3]Department of Electrical and Electronics Engineering, Balikesir University, Campus of Cagis, 10145 Balikesir, Turkey
serhat.kucukdermenci@ege.edu.tr

Prejem rokopisa – received: 2012-07-24; sprejem za objavo – accepted for publication: 2012-08-27

Highly water-soluble Fe_3O_4/PAA (polyacrylic acid) nanoparticles (NPs) were synthesized with the high-temperature hydrolysis method. We report the first demonstration of Faraday rotation (FR) for a magnetic fluid (MF) synthesized with this novel method. The experiments were performed in the DC regime ($0–6 \cdot 10^{-2}$ T) at room temperature for 14 concentrations from 1.8 mg/ml to 5 mg/ml. The maximum rotation was recorded as 0.96° cm^{-1} for 3.33 mg/ml and this is called the critical concentration ($C_{CRITICAL}$). It was found that the rotation tends to decrease when the concentration is higher than $C_{CRITICAL}$. The MF behavior for FR is discussed with respect to substructure interactions (particle-particle, chain-chain). This work provides a new insight for the FR investigations of MFs including highly water-soluble magnetic NPs.

Keywords: magnetic fluids, Fe_3O_4 nanoparticles, magneto-optic response, Faraday rotation

V vodi dobro topni nanodelci Fe_3O_4/PAA (poly acrylic acid) so bili sintetizirani po metodi visokotemperaturne hidrolize. Poročamo o prvi demonstraciji Faradayeve rotacije (FR) za magnetno raztopino (MF), sintetizirano po tej novi metodi. Preizkusi so bili izvršeni v DC-režimu ($0–6 \cdot 10^{-2}$ T) pri sobni temperature za 14 različnih koncentracij od 1,8 mg/ml do 5 mg/ml. Največja rotacija je bila ugotovljena kot 0,96° cm^{-1} pri 3,33 mg/ml, kar smo imenovali kritična koncentracija ($C_{CRITICAL}$). Ugotovljeno je bilo, da se rotacija zmanjšuje, če je koncentracija višja od $C_{CRITICAL}$. Lastnost MF za FR je bila obravnavana z interakcijami podstrukture (delec-delec, veriga-veriga). To delo ponuja nov pogled v študij FR magnetnih raztopin (MFs), vključno z v vodi dobro topnimi nanodelci (NPs).

Ključne besede: magnetna tekočina, nanodelci Fe_3O_4, magnetnooptični odgovor, Faradeyeva rotacija

1 INTRODUCTION

Magnetic NPs have unique colloidal, magnetic and optical properties that differ from their bulk counterparts.[1–8] Core-shell NPs have been a topic of great interest due to their potential use in biology[9,10], imaging[11], medicine[12–14] and DNA separation.[15,16] Colloidal suspensions of magnetic NPs can self-assemble into ordered structures. The ability to manipulate this assembly with external tuning parameters such as the field, the temperature and the concentration is essential for developing new stimuli-responsive materials.

MFs, also named ferrofluids, are colloidal suspensions of magnetic NPs that have both characteristics – the fluidity of liquids and the magnetism of solid magnetic materials. Several applications of MFs have recently been introduced, such as a detection system design for glucose concentration in addition to optical-device applications.[17] It is suitable for fabricating optical devices such as optical attenuator, light modulator, optical switch, etc., by using the magneto-optic properties of MFs.[18–20]

In 2007, the Yin group synthesized novel superparamagnetic, magnetite colloidal NPs that can self-assemble into one-dimensional (1D) particle chains and exhibit excellent tunable photonic properties.[21] A suspension of these NPs displays tunable colors in the visible range of the electromagnetic spectrum. The freedom to tune a diffraction color not only depends on the particle size but also varies with the strength of an applied external magnetic field. Since then there has been a widespread interest in these NPs and their applications. Despite their tremendous potential in various applications, interesting fundamental questions referring to their colloidal crystallization with and without a magnetic field remain unanswered. Therefore, we report on the first demonstration of FR for MFs based on these NPs.

FR has been demonstrated in the visible[22,23] NIR[24,25] and MIR[26] regimes for different kinds of ferrofluids. Experimental investigation on γ-Fe_2O_3 NPs FR was done due to the particle-size dependence. Water-based ferrofluid samples are synthesized with the coprecipitation method followed by a size-sorting process[27]. The wavelength and concentration dependence of FR in MFs was studied by Yusuf et al.[28,29] Here we demonstrate that long-term, stable MFs including highly water-soluble NPs show FR in a DC regime ($0–6 \cdot 10^{-2}$ T) at room temperature. Water-based ferrofluid samples are synthesized with a novel high-temperature hydrolysis method.

2 MATERIALS AND METHODS

2.1 Materials

Diethylene glycol (DEG, 99.9 %), anhydrous ferric chloride ($FeCl_3$, 97 %), sodium hydroxide (NaOH, 96 %), and poly acrylic acid (PAA, M_w = 1800) were purchased from the Sigma-Aldrich company. Distilled water was used in all the experiments. All the chemicals were used as received without further treatment and/or purification.

2.2 Synthesis of water-dispersible Fe_3O_4/PAA NPs

The polyol method based on the theory that NPs will be yielded upon heating precursors in a high-boiling-point alcohol at elevated temperature. In this method, DEG is chosen as the solvent because it can easily dissolve a variety of polar inorganic materials due to its high permittivity (ε = 32) and high boiling point (246 °C). DEG is not only a solvent but also a reducing agent in an reaction. Hence, $FeCl_3$ can be used as the only precursor for synthesizing Fe_3O_4. PAA is used as the capping agent, on which the carboxylate groups show a strong coordination with Fe^{3+} on the Fe_3O_4 surface and the uncoordinated carboxylate groups extend into the water solution, rendering the particles with high water dispersibility. A strong coordination of carboxylate groups with the surface iron cations and the multiple anchor points for every single polymer chain is an important factor in creating a robust surface coating of PAA on magnetite NPs. Therefore, we used PAA as the capping agent in our synthesis to confer upon the particles high water dispersibility. A mixture of ethanol and water was used to wash the particles and remove the unwanted leftover material from the particles.

For the synthesis of Fe_3O_4 NPs, a NaOH/DEG solution was prepared by dissolving 100 mmol of NaOH in 40 ml of DEG at 120 °C under nitrogen for 1h. Then the light-yellow solution was cooled to 70 °C (the stock solution A). In a 100-ml, three-necked flask equipped with a nitrogen inlet, a stirrer and a condenser, 10 mmol of $FeCl_3$ and 20 mmol of PAA were dissolved in 41 ml of DEG under vigorous stirring. The solution was purged with bubbling nitrogen for 1 h and then heated to 220 °C for 50 min (the stock solution B). Subsequently, 20 ml of the NaOH/DEG solution was injected rapidly into the above solution. The reaction was allowed to proceed for 2 h. The black color of the solution confirms the formation of magnetite NPs. The resultant black product was repetitively washed with a mixture of ethanol and water and collected with the help of a magnet. The cycle of washing and magnetic separation was performed five times. A one-pot synthesis was done with the Fe_3O_4/PAA particles, so no extra process was needed for the surface modification. A flow chart of the synthesis is shown in **Figure 1**.

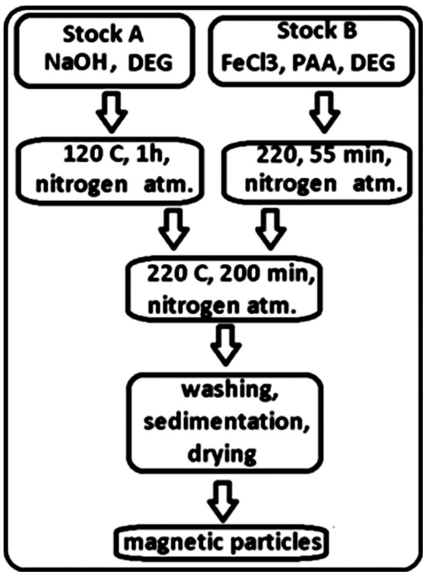

Figure 1: Flow chart of the synthesis
Slika 1: Potek sinteze

3 CHARACTERIZATION

3.1 Structural and magnetic characterization of Fe_3O_4/PAA NPs

A powder X-ray diffraction (XRD) analysis was performed on a Phillips EXPERT 1830 diffractometer with Cu K_α radiation. The XRD data were collected over the range of 10–80° (2 θ) with a step interval of 0.02° and a preset time of 1.6 s per step at room temperature. Magnetic measurements were carried out using a Lake-Shore 7400 (Lakeshore Cryotronic) vibration sample magnetometer (VSM) at 300 K. Particle sizes of NPs were measured using a Zetasizer 4 Nano S, dynamic light scattering instrument (Malvern, Worcestershire, UK). Light-scattering measurements were carried out with a laser of the wavelength of 633 nm at the 90° scattering angle. FTIR spectra were recorded on a KBr disc on a Perkin Elmer 100 spectrometer.

For the FR experiments we used a Thorlabs model HGR20 2.0 mW/nm laser source, a GMW Electro-magnet-Systems model 5403 electromagnet, a Kepco power-supply model BOP 20-5M, a LakeShore model 455 DSP Gaussmeter, a Stanford research systems model SR830 DSP lock-in amplifier, a new focus model 2051 photo detector, an ILX Lightwave model OMM – 6810B optical multimeter and an OMH – 6703B model silicon power head.

3.2 Experimental setup for a magneto-optical characterization

The magneto-optical-measurement setup is shown in **Figure 2**. The measurements of FR were made using an optical arrangement consisting of a He-Ne laser, a polarizer, MR3-2 magneto-optical glass (from Xi'an Aofa Optoelectronics Technology Inc., China) placed in the gap between the two poles of the electromagnet for the

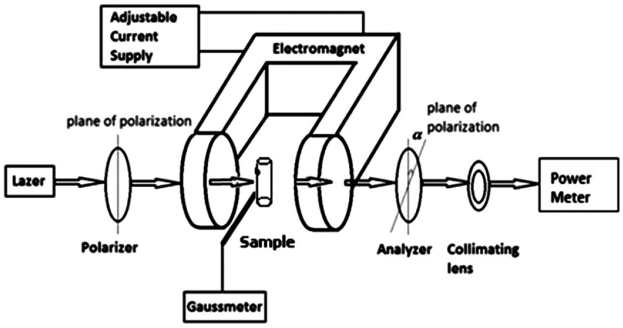

Figure 2: Magneto-optic-measurement setup
Slika 2: Magnetooptični merilni sestav

calibration process, an analyzer, collimating lens and a power meter. The electromagnet generates a uniform magnetic field in the sample region. The strength of the magnetic field can be adjusted by tuning the magnitude of the supply current and is monitored by a gauss meter.

According to Malus' law, as the polarized light I_0 passes through the transparent magneto-optical material, the light intensity I can be expressed as:

$$l = l_0 \cos^2 \theta = l_0 \cos^2(\alpha - \phi) \quad (1)$$

where α is the angle of the polarization axes of the polarizer and analyzer and ϕ is the rotation angle of the polarized plane of the transmitted light. With respect to MFs, this can be expressed as:

$$\phi(B) = C \frac{M(B)}{M_S} VBl(B) \quad (2)$$

where l is the chain length at the magnetic field B in an MF sample, C is a constant that can be found at a high field assuming that the saturated chain length has no change, M is the magnetization of the sample at the magnetic field B, M_S is the saturation magnetization of the sample and V is the Verdet constant varying with the wavelength and temperature. Generally, a positive Verdet constant corresponds to the L-rotation (anti-clockwise) when the direction of propagation is parallel to the magnetic field and to the R-rotation (clockwise) when the propagation direction is anti-parallel. To obtain the maximum sensitivity of the transmitted power, especially under very small magnetic fields, the FR angle ϕ can be identified as zero and the initial polarization angle of the analyzer is set, with α = 45°, according to equation (1). It can be described as:

$$\frac{d(\cos^2(\theta))}{d(\theta)} = 2 \sin\theta \cos\theta = \sin 2\theta \quad (3)$$

With respect to the FR experiments, the sensitivity is maximum when θ is 45° and dI/dΘ = 1 from equation (3). Therefore, the optical axis of the analyzer is aligned at an angle of 45° to the optical axis of the polarizer.

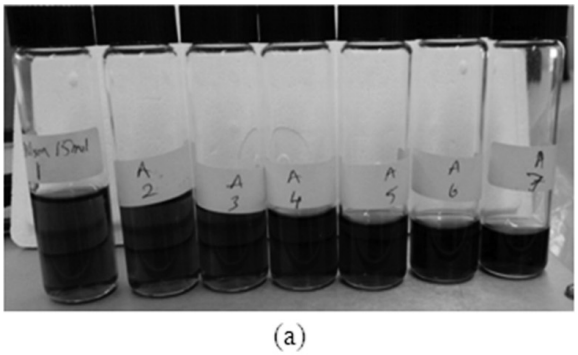

(a)

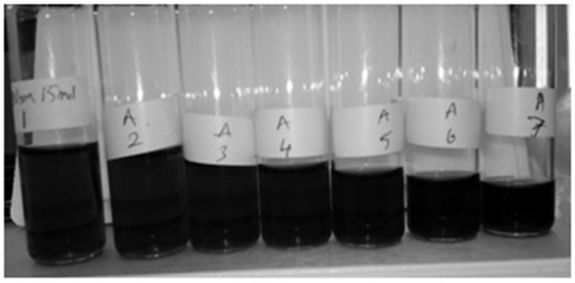

(b)

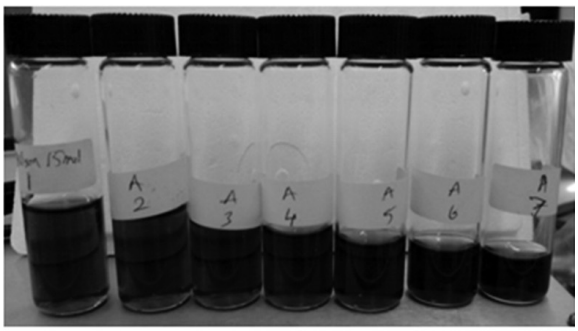

(c)

Figure 3: Pictures of the nanofluids containing Fe_3O_4/PAA NPs with various concentrations kept for different times: a) 1 h, b) 2 weeks, c) 4 weeks
Slika 3: Posnetki nanotekočin z Fe_3O_4/PAA-nanodelci z različno koncentracijo po zadržanju: a) 1 h, b) 2 tedna, c) 4 tedne

4 RESULTS

4.1 Stability of Fe_3O_4 /PAA-based ferrofluids

NPs in MFs are usually coated with a surfactant material to prevent agglomeration and provide stability.[30–33] The size of a magnetic NP, the material concentration, the carrier liquid and the surfactant are the main variations for MFs.

PAA was selected as a surfactant because of its strong coordination of carboxylate groups with iron cations on a magnetite surface. An additional advantage of PAA is that an extension of the uncoordinated carboxylate groups on polymer chains into an aqueous solution confers on the particles a high degree of dispersibility in water.

A well-dispersed nanofluid was prepared as shown in **Figure 3**. The particle content is 20 mg for various concentrations with an addition of distilled water from 4 ml to 17 ml. NPs can still be dispersing well after the

nanofluid has been kept standing still for more than 4 weeks and no sedimentation is observed for any of the samples. Due to its long-term stability, this kind of MFs is an ideal candidate for optical devices.

4.2 Physical and magnetic properties of Fe_3O_4/PAA NPs analyzed with XRD, DLS, TEM and FTIR

The crystal structure of the sample was confirmed with an X-ray diffraction (XRD) analysis as shown in **Figure 4**. The (220), (311), (400), (422), (511), and (440) diffraction peaks observed on the curves can be indexed to the cubic spinel structure, and all the peaks were in good agreement with the Fe_3O_4 phase (JCPDS card 19-0629).

The average diameter of the particles obtained with a dynamic light scattering (DLS) analysis is ~10 nm (**Figure 5**). As seen in the typical transmission electron microscopy (TEM) images of Fe_3O_4/PAA in **Figure 6a-b**, the average diameter of Fe_3O_4/PAA was about 8.16 nm **Figure 6c**. The average diameter was obtained by measuring about 100 particles.

The magnetic properties of NPs are shown in **Figure 7** as measured at 300 K with a vibrating sample mag-

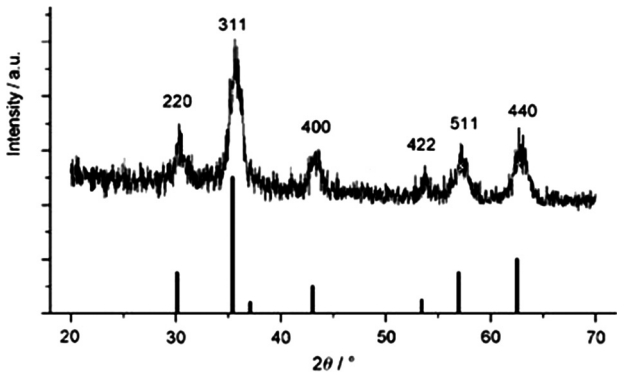

Figure 4: X-ray powder-diffraction pattern for PAA-coated Fe_3O_4 NPs. The peak positions and relative intensities recorded in the literature for bulk Fe_3O_4 samples are indicated by vertical bars.

Slika 4: Rentgenska difrakcija prahu za s PAA pokritimi Fe_3O_4-nanodelci. Pozicija vrhov in v literaturi zapisane relativne intenzitete za osnovne Fe_3O_4-delce so prikazane z navpičnimi črtami.

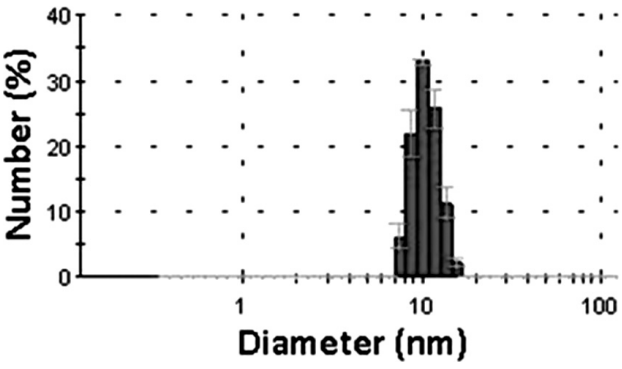

Figure 5: Size distributions of magnetic NPs obtained with DLS

Slika 5: Razporeditev velikosti magnetnih delcev (NPs), vzeto iz DLS

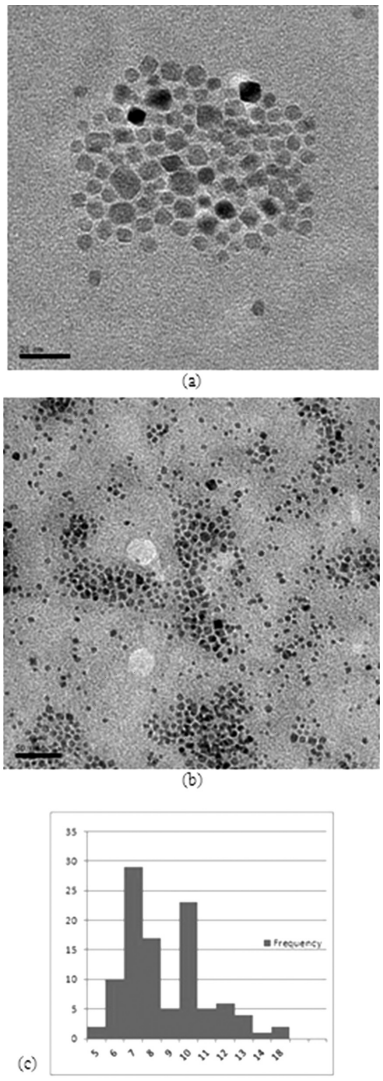

Figure 6: Representative TEM images of magnetite CNCs with: a) 20-nm scale bar, b) 50-nm scale bar, c) the average diameter of Fe_3O_4/PAA

Slika 6: Reprezentativni TEM-posnetki magnetitnih CNCs: a) merilo 20 nm, b) merilo 50 nm, c) povprečni premer Fe_3O_4/PAA

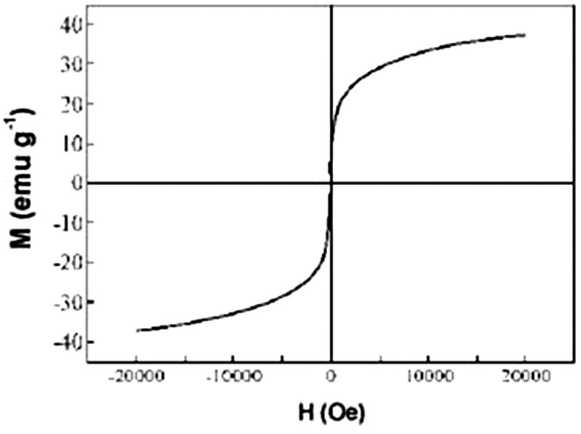

Figure 7: Hysteresis loop of superparamagnetic particles at room temperature

Slika 7: Histerezna zanka superparamagnetnih delcev pri sobni temperaturi

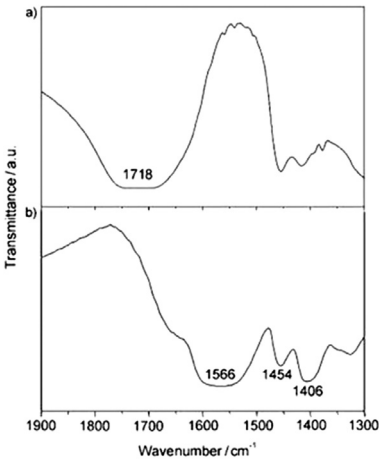

Figure 8: FTIR spectrum of: a) pure PAA, b) PAA with carboxylate-capped Fe_3O_4 NPs
Slika 8: FTIR-spekter: a) čisti PAA, b) PAA s karboksilatom omejeni Fe_3O_4-nanodelci

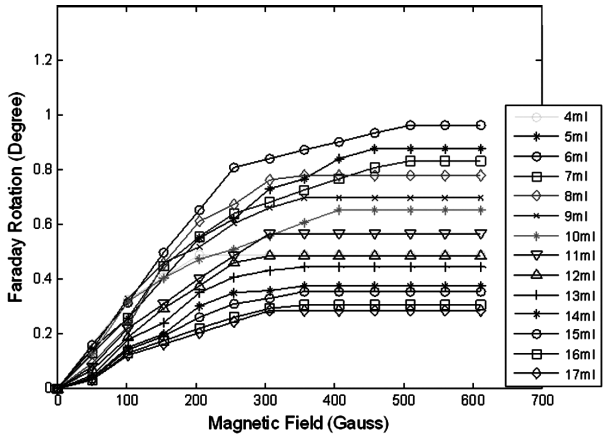

Figure 9: Applied magnetic-field dependence and concentration dependence of FR
Slika 9: Odvisnost FR od uporabljenega magnetnega polja in koncentracije

netometer (VSM). The saturation magnetization was determined as 38.8 emu/g. The particles showed no remanence or coercivity at 300 K, that is, superparamagnetic behavior.

The stability of PAA capped on Fe_3O_4 was confirmed by measuring the Fourier transform infrared spectroscopy (FTIR) spectrum on the sample as shown in **Figure 8a**. There is a very strong band at around 1718 cm^{-1} of pure PAA, which is characteristic of the C=O stretching mode for protonated carboxylate groups. The three peaks shown in **Figure 8b** and located at (1566, 1454 and 1406) cm^{-1} can be assigned to the characteristic bands of the carboxylate (COO^-) groups, corresponding to the CH_2 bending mode, asymmetric and symmetric C–O stretching modes of the COO^- group, respectively.

4.3 Magneto-optic properties of the Fe3O4/PAA-based magnetic fluid

Figure 9 shows FR versus the magnetic field and **Table 1** indicates the maximum rotations of MFs with different concentrations. The field and concentration dependence of FR in MFs was investigated. A 10-mm-thick cuvette was filled with the liquid of 14 various concentrations from 1.8 mg/ml to 5 mg/ml. It can be seen that the rotation increases rapidly with the field at low fields.

The initial susceptibility χ is determined by a linear magnetic response $M = \chi \cdot H$ at the field strength $H \rightarrow 0$ and it depends on the particle concentration of fluids. At low fields in **Figure 9** the initial slope is:

$$m_i = \frac{C}{B}\frac{M(B)}{M_S} + Vl(B) \quad (4)$$

As long as the concentration is decreased, fewer NPs are found in the medium and this situation causes a lower magnetization and a shorter chain length at a particular field. In other words, the volume fraction of MF and the initial slope are decreased. Black curves relate to samples 8–14 (**Table 1**) and their slopes are less steep than the ones of the first seven samples, because their magnetizations are lower and the chain lengths are shorter than those of the first seven samples. It needs to be pointed out that though the maximum FR of sample 1 (indicated as the yellow curve) is relatively low, its initial susceptibility is the highest value due to the volume fraction.

Table 1: Maximum FRs of the samples with different concentrations
Tabela 1: Maksimalna Faradayeva rotacija (FR) pri vzorcih z različnimi koncentracijami

Sample	Particle	Water	Concentration	Faraday rot.
no	mg	ml	mg/ml	Max. degree
1	20	4	5.00	0.49
2	20	5	4.00	0.87
3	20	6	3.33 ($C_{CRITICAL}$)	0.96
4	20	7	2.86	0.83
5	20	8	2.50	0.78
6	20	9	2.22	0.70
7	20	10	2.00	0.65
8	20	11	1.82	0.56
9	20	12	1.67	0.48
10	20	13	1.54	0.44
11	20	14	1.43	0.37
12	20	15	1.33	0.35
13	20	16	1.25	0.30
14	20	17	1.18	0.28

As the volume fraction of NPs increases, dipole interactions between the particles overcome the thermal forces more easily. A graphical representation of the maximum FR can be seen in **Figure 10**. It is important to mention that most experimental investigations, based on optical observations, of the chain formation in MFs are usually carried out on the samples in the low concentration regime, where the chain-chain interaction is weak.

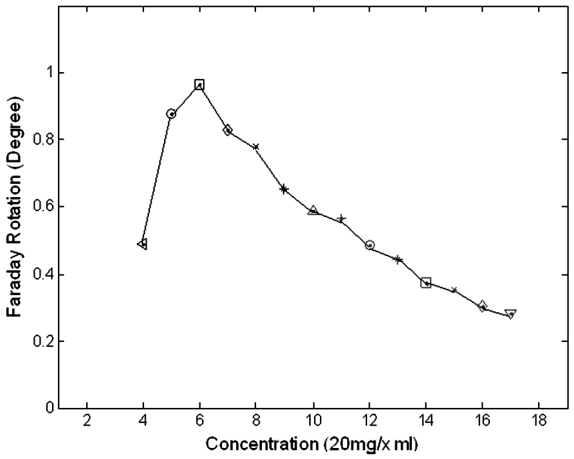

Figure 10: Graph of the maximum FR of the samples
Slika 10: Graf maksimalne Faradayeve rotacije (FR) vzorcev

However, we tried many samples with variable concentrations to see the effect of higher concentrations. When we analyze **Figure 10**, it can be seen that FR increases with higher concentrations (from 1.18 mg/ml to 2.26 mg/ml) up to $C_{CRITICAL}$ (3.33 mg/ml). But after the $C_{CRITICAL}$ (sample 3) value, FR tends to decrease with higher concentrations (4 mg/ml and 5 mg/ml). According to Stokes' law, there is a friction between the moving particles and the carrier fluids, which depends on the viscosity of the fluids.[34] Thus, the viscosity of MF and the friction in the medium were high for highly concentrated MFs and they affected the activity of the magnetic particles. It is also important to point out that the chain-chain interaction becomes much stronger once the concentration of a sample is increased and may lead to the closure of some chains or even the curling.[35,36] Therefore, it can be said that FR tends to decrease after $C_{CRITICAL}$ due to the substructure (particle-particle, chain-chain) interactions.

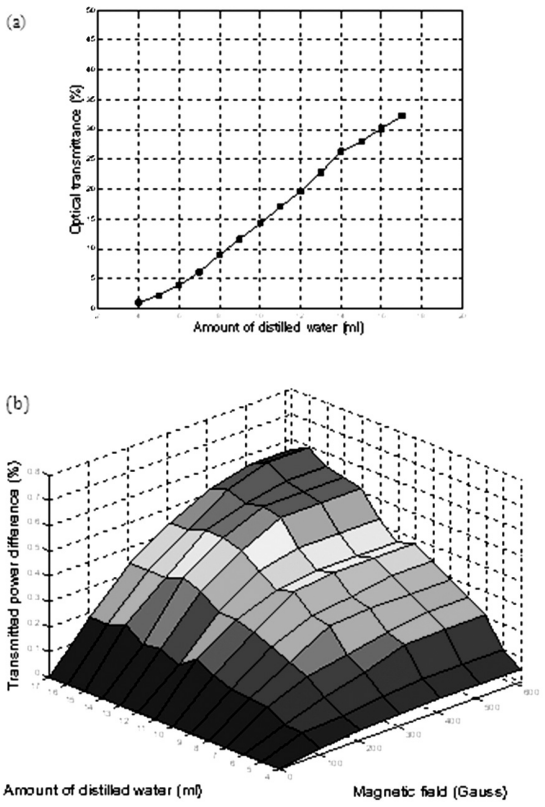

Figure 11: a) Transmissivity of Fe_3O_4 NPs, B = 0 T, b) transmitted power difference of Fe_3O_4 NPs at particular fields and with different concentrations
Slika 11: a) Transmisivnost Fe_3O_4-nanodelcev, B = 0 T, b) posredovana razlika v moči Fe_3O_4-nano delcev pri določenem polju z različno koncentracijo

Figure 11a shows the transmission of unpolarized light as percentage and **Figure 11b** shows the transmission difference of unpolarized light under magnetic fields for each concentration in the $1–6 \cdot 10^{-2}$ T region. The transmitted light difference as percentage in **Figure 12b** is calculated from the difference between the intensity of the light transmitted in a particular ($1–6 \cdot 10^{-2}$ T) magnetic field and the intensity in the zero field for the samples with different concentrations.

Low transmission responses to magnetic fields were observed for samples 1 and 2. Except for these samples, remarkable changes were observed for all the other samples because of the weakening of the viscosity effect. It can be said that samples 1 and 2 have a blocking property and other samples have a channeling property due to their concentrations. A decreasing percentage of NPs in a unit volume indicates a lower magnetization and a smaller chain length, which play important roles in the Faraday effect.[37]

5 DISCUSSION

5.1 Model for Explaining the Experimental Results

There are two physical phenomena for the magneto-optical effect in MFs in the presence of an external magnetic field. One is the orientation theory (magnetic orientation or physical orientation) based on the optical anisotropy of magnetic particles or its aggregation, and the other is the formation theory based on the chain formation of the magnetic particles (**Figure 12**). In the zero magnetic field the particles are distributed randomly with

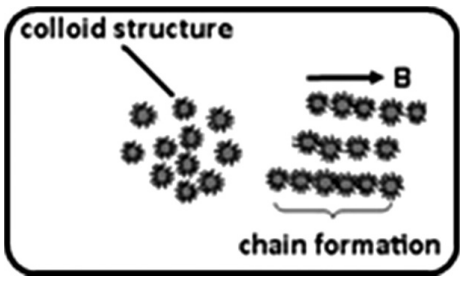

Figure 12: Magnetic NP alignment and the chain formation in the direction of the external magnetic field
Slika 12: Magnetna ureditev nanodelcev in nastajanje verig v smeri zunanjega magnetnega polja

no coercivity and remanence forming an isotropic material. Particles start to coagulate and form chain-like structures in the direction of the field with the help of an external magnetic field.[38,39]

Magnetic field induces NPs to line up or to behave asymmetrically, introducing anisotropy and resulting in birefringence. If lattice atoms of a crystal were not completely symmetrically arrayed, the binding forces on the electrons would be anisotropic, causing a material to be circularly birefringent with different indices of refraction.[40] When the applied magnetic field's direction is parallel to the light beam, the anisotropy is circular in a longitudinal configuration. However, the rotation of polarization does not seem to be linked to the particles' anisotropy-axis orientation but to the orientation of the magnetic moments of the particles in the applied field's (H) direction.[41]

When an external magnetic field is applied parallel to the plane of MF, magnetic particles in the fluid agglomerate to form chain-like structures. As the field strength is further increased, more particles contribute to agglomeration and the chains become longer under a higher field. It has been found that the chain length varies with the applied magnetic field and with the concentration of the MF.[42] In some experimental conditions, in which the wavelength of the electromagnetic waves passed through the sample is very small in comparison with the chain length, FR is not only governed by magnetization of the fluid but also affected by the chain formation.[43]

Additionally, MFs can be diluted magnetically by passive liquid carriers such as glycerol, ethylene glycol, diester, isopar M, ethanol or simply distilled water and it was seen that FR was affected by a change in the concentration. Different concentrations of MFs can help us describe various friction forces among the magnetic NPs. Carrier fluids significantly influence the response of the Faraday effect. Consequently, the chain formation is a crucial parameter of the optical properties of MFs. The chain lengths in MFs composed of magnetic NPs vary with respect to concentration.[44–46]

The positional and magnetic field dependence of the colloidal assembly of magnetite NPs arise from a sensitive interplay between the local concentrations of the particles, causing the effect of three types of forces between the colloidal NPs. These forces are (1) the hard-sphere repulsion between the particles in contact; (2) a combination of electrostatic repulsion due to the presence of the charges on the surface of NPs and Van-der-Waals attraction; (3) the magnetic dipolar attraction/repulsion due to the magnetite cores of the particles. The interaction potential of the third force is given by:

$$U_{ab}(r) = \frac{1}{r^2}(\vec{\mu}_a \cdot \vec{\mu}_b) \quad (5)$$

The dipolar interaction between two magnetic particles, a and b, depends on the magnitude and direction of their magnetic moments μ_i as well as on their relative position r_{ab}. Depending on the particles configuration, the dipolar energy may be repulsive or attractive. Heinrich and coworkers showed that these forces play a role in the assembly of magnetic nano-particles.[47] When a magnetic field is applied these particles initially form chain-like structures. These chains are then arranged into two-dimensional hexagonally packed sheets. This occurs by shifting a neighboring chain by a distance of r corresponding to the radius of NP. The chains are formed along the direction of an external magnetic field.

6 CONCLUSION

In conclusion, high-quality Fe_3O_4/PAA-based nanostructures for MF formation were synthesized successfully and FR investigations were made for many samples with variable concentrations. We report the first demonstration of FR for MF synthesized with this novel method. We have demonstrated the FR of a highly water-soluble MF that was measured to be in the $0–6 \cdot 10^{-2}$ T range in the DC regime. The effects of both viscosity and chain formation were observed on FR. We found the maximum FR to be 0.96°/(10 mm) at room temperature for 3.33 mg/ml. FR was on an increase with the higher concentrations up to C_{CRITICAL}. It was found that the rotation begins to decrease again when the concentration is higher than C_{CRITICAL}. The reason for this might be the blocking effect that arises from the particle-particle and chain-chain interactions. The experiment results shed some light on the role of agglomeration and chain formation in FR. Taking into account the flexibility of the liquid form (including the long-term stability and no-sedimentation property) in order to predict its optical behavior correctly, and the low-magnetic-field requirements, these fluids can be exploited for the fabrication of a wide range of applications in magneto-optics.

Acknowledgements

The authors wish to thank the Dokuz Eylul University, the Center for Fabrication and Application of Electronic Materials (EMUM) for providing technical support. We are grateful for the many helpful discussions with Dr. Erdal Çelik and Dr. Ömer Mermer.

7 REFERENCES

[1] J. Ge, Y. Hu, Y. Yin, Angew. Chem. Int. Ed., 46 (**2007**), 7428–7432
[2] P. H. C. Camargo, Z. Y. Li, Y. Xia, Soft Matter, 3 (**2007**), 1215–1222
[3] K. Butter, P. H. H. Bomans, P. M. Frederik, G. J. Vroege, A. P. Philipse, Nature Materials, 2 (**2003**), 88–91
[4] A. Yethiraj, A. van Blaaderen, Nature, 421 (**2003**), 513–517
[5] M. Klokkenburg, C. Vonk, E. M. Claesson, J. D. Meeldijk, B. H. Erne, A. P. Philipse, J. Am. Chem. Soc., 51 (**2004**), 16706–16707
[6] A. P. Hynninen, M. Dijkstra, Phys. Rev. Lett., 94 (**2005**), 138303

[7] M. Klokkenburg, B. H. Erne, J. D. Meeldijk, A. Widenmann, A. V. Petukhov, R. P. A. Dullens, A. P. Philipse, Phys. Rev. Lett., 9 (**2006**), 185702
[8] A. K. Agarwal, A. Yethiraj,. Phys. Rev. Lett., 102 (**2000**), 198301
[9] T. J. Yoon, K. N. Yu, E. Kim, J. S. Kim, B. G. Kim, S. H. Yun, B. H. Sohn, M. H. Cho, J. K. Lee, S. B. Park, Small 2 (**2006**) 2, 209–215
[10] J. Lee, Y. Lee, J. K. Youn, H. B. Na, T. Yu, H. Kim, S. M. Lee, Y. M. Koo, J. H. Kwak, H. G. Park, H. N. Chang, M. Hwang, J. G. Park, J. Kim, T. Hyeon, Small 4 (**2008**) 1, 143–152
[11] J. H. Lee, Y. M. Huh, Y. W. Jun, J. W. Seo, J. T. Jang, H. T. Song, S. Kim, E. J. Cho, H. G. Yoon, J. S. Suh, J. Cheon, Nature Medicine, 13 (**2007**) 1, 95–99
[12] J. H. Lee, K. Lee, S. H. Moon, Y. Lee, T. Gwan Park, J. Cheon, All-in-One Target-Cell-Specific, Angew. Chem. Int. Ed., 48 (**2009**), 4174–4179
[13] C. Xu, K. Xu, H. Gu, X. Zhong, Z. Guo, R. Zheng, X. Zhang, B. J. Xu, Am. Chem. Soc., 126 (**2004**), 3392–3393
[14] A. H. Lu, E. L. Salabas, F. Schuth, Angew. Chem. Int. Ed., 46 (**2007**), 1222–1244
[15] X. Zhao, R. Tapec-Dytioco, K. Wang, W. Tan, Anal. Chem., 75 (**2003**), 3476
[16] S. V. Sonti, A. Bose, Colloids and Surfaces B-Biointerfaces, 8 (**1997**) 4–5, 199–204
[17] S. Liu, E. Li, Q. Zhou, IEEE 3rd Int. Conf. on Bio. Eng. and Inf., (**2010**), 1532–1535
[18] S. Pu, M. Dai, G. Sun, Opt. Comm., 283 (**2010**), 4012–4016
[19] C. Y. Hong, J. Mag. Mag. Mat., 201 (**1999**), 178–181
[20] L. Martinez, F. Cecelja, R. Rakowski, Sens. Act. A, 123–124 (**2005**), 438–443
[21] J. Ge, Y. Hu, M. Biasini, W. P. Beyermann, Y. Yin, Angew. Chem. Int. Ed., 46 (**2007**) 23, 4342–4345
[22] N. A. Yusuf, J. Appl. Phys., 64 (**1988**), 5
[23] Z. D. Xianfeng, Appl. Phys. Lett., 89 (**2006**), 211106
[24] Y. T. Pan, J. Appl. Phys., 73 (**1993**), 10
[25] X. Fang, Nanoscale Research Letters, 6 (**2011**), 237
[26] M. M. Maiorov, J. Magnetism and Magnetic materials, 252 (**2002**), 111–113
[27] F. Royera, D. Jamona, J. J. Rousseaua, V. Cabuila, D. Zinsa, H. Rouxa, C. Boviera, The European Physical Journal Applied Physic, 22 (**2003**) 2, 83–87
[28] N. A. Yusuf, A. A. Rousan, H. M. El-Ghanem, J. Appl. Phys., 64 (**1988**), 2781
[29] N. A. Yusuf, I. Abu-Aljarayesh, A. A. Rousan, H. M. El-Ghanem, IEEE Trans. on Magn., 26 (**1990**), 5
[30] R. E. Rosensweig, Nature, 210 (**1966**), 613
[31] M. I. Shliomis, Zh. Eksp. Teor. Fiz., 61 (**1971**), 2411
[32] D. H. Lee, R. A. Condrate, J. S. Reed, J. Mater. Sci., 31 (**1996**), 471
[33] H. Li, C. P. Tripp, Langmuir, 21 (**2005**), 2585
[34] D. Lin, W. Shibin, L. Sen, IEEE Ann. Rep. Conf. on El. Ins. and Diel. Pheno., 2010
[35] P. C. Scholten, IEEE Trans. Magn., 16 (**1980**), 221
[36] P. G. De Gennes, P. A. Pincus, Phys. Condens. Matter, 11 (**1990**), 189
[37] R. E. Rosensweig, Magnetic Fluids, Annual Reviews
[38] M. Wu, Y. Xiong, Y. Jia, H. Niu, H. Qi, J. Ye, Q. Chen, Chem. Phy. Lett., 401 (**2005**), 374–379
[39] H. E. Horng, C. Y. Hong, S. Y. Yang, H. C. Yang, J. Phy. and Chem. of Sol., 62 (**2001**), 1749–1764
[40] E. Hecht, Optics, 4th ed., Addison Wesley
[41] F. Royer, D. Jamon, J. J. Rousseau, V. Cabuil, D. Zins, H. Roux, C. Bovier, Eur. Phys. J. AP, 22 (**2003**), 83–87
[42] N. A. Yusuf, J. Phys. D: Appl. Phys., 22 (**1989**), 1916–1919
[43] A. A. Rousan, H. M. El-Ghanem, N. A. Yusuf, IEEE Trans. on Mag., 25 (**1989**) 4, 3121–3124
[44] N. A. Yusuf, I. Abu-Aljarayesh, A. A. Rousan, H. M. El-Ghanem, IEEE Trans. on Mag., 26 (**1990**) 5, 2852–2855
[45] G. A. Jones, H. Niedoba, J. of Mag. and Mag. Mat., 73 (**1988**), 33
[46] W. Syed, D. A. Hammer, M. Lipson, Opt. Let., 34 (**2009**) 7, 1009–1011
[47] D. Heinrich, A. R. Goni, A. Smessaert, S. H. L. Klapp, L. M. C. Cerioni, T. M. Osan, D. J. Pusiol, C. Thomsen, Phys. Rev. Lett., 106 (**2011**), 208301

UDK 621.74.047:669.112.221
Original scientific article/Izvirni znanstveni članek

ISSN 1580-2949
MTAEC9, 47(1)79(2013)

A NEW APPROACH TO EVALUATING THE CHEMICAL MICRO-HETEROGENEITY OF A CONTINUOUSLY CAST STEEL SLAB

NOV NAČIN OCENJEVANJA KEMIJSKE MIKROHETEROGENOSTI KONTINUIRNO ULITIH SLABOV

Jana Dobrovská[1], František Kavička[2], Věra Dobrovská[1], Karel Stránský[2], Hana Francová[1]

[1]Faculty of Metallurgy and Materials Engineering, VSB-Technical University of Ostrava, 17. listopadu 15, 708 33 Ostrava, Czech Republic
[2]Faculty of Mechanical Engineering, Brno University of Technology, Technicka 2, Brno 616 69, Czech Republic
jana.dobrovska@vsb.cz

Prejem rokopisa – received: 2012-08-01; sprejem za objavo – accepted for publication: 2012-09-14

The paper deals with a new approach to measuring and evaluating the chemical micro-heterogeneity of the elements in solidified poly-component metallic systems. The original approach is based on experimental measurements made on the samples taken from characteristic places in a casting and the subsequent application of an original mathematical model for determining the element-distribution profile, characterizing the most probable distribution of an element concentration in the frame of a dendrite, and an original mathematical model for determining the effective partition coefficients of these elements in the structure of the analyzed alloy. The paper also describes an application of this method in the research of the chemical heterogeneity on a cross-section of a CC steel slab and presents the selected results (indices of the heterogeneity and effective partition coefficients of seven analyzed elements) characterizing the chemical micro-heterogeneity on one-half of the cross-section of this CC steel slab. The following main results were obtained: (*i*) the dendritic heterogeneity of the accompanying elements and impurities is comparatively high; (*ii*) all the analyzed elements segregate during the solidification into an inter-dendritic melt, and their partition coefficient is smaller than one; (*iii*) the effective partition coefficients calculated in this new way inherently include both the effect of segregation in the course of an alloy solidification, and the effect of the homogenization occurring during the solidification as well as during the cooling of an alloy.

Keywords: micro-segregation, effective partition coefficient, continuous casting, steel

Članek obravnava nov način merjenja in ocenjevanja kemijske mikroheterogenosti elementov v večkomponentnih kovinskih sistemih. Izviren način temelji na eksperimentalnih meritvah, narejenih na vzorcih, vzetih iz značilnih mest ulitka, in uporabi izvirnega matematičnega modela za določanje profila razporeditve elementov, kar omogoča oceno najbolj verjetne razporeditve koncentracije elementov v dendrite in določanje efektivnega koeficienta razporeditve teh elementov v strukturi analizirane zlitine. Članek opisuje tudi uporabo te metode pri raziskavi kemijske heterogenosti prečnega prereza kontinuirno ulitega slaba in predstavlja izbrane rezultate (indeks heterogenosti in koeficiente razporeditve sedmih analiziranih elementov) značilne kemijske mikroheterogenosti polovice prereza kontinuirno ulitega slaba. Glavni rezultati so: (*i*) heterogenost spremljajočih elementov in nečistoč je razmeroma velika; (*ii*) vsi analizirani elementi izcejajo med strjevanjem v meddendritno talino, njihov koeficient razporeditve je manjši od ena; (*iii*) na nov način izračunani koeficienti razporeditve vključujejo v sebi oba učinka, to je učinek izcejanja med potekom strjevanja in učinek homogenizacije, ki se pojavi med strjevanjem, in nadaljnjim ohlajanjem zlitine.

Ključne besede: mikroizcejanje, koeficient porazdelitve, kontinuirno ulivanje, jeklo

1 INTRODUCTION

The structure of metallic alloys is one of the factors, which significantly influence their physical and mechanical properties. The formation of a structure is strongly affected by production technology, casting and solidification of these alloys. Chemical heterogeneities are a common problem in castings and solidification processes. A solute segregation either on the macro- or micro-scale is sometimes the cause of unacceptable products due to poor mechanical properties of the resulting non-equilibrium phases.

Micro-segregation refers to a composition variation within a dendritic solidification structure, which has a length scale of the order of only a few micrometers. It is usual to characterize the extent of micro-segregation using a ranking scheme of randomly sampled electron micro-analysis data.[1–4] Thermodynamic quantities are often calculated from the measurements of an as-cast segregation profile, in particular, the partition coefficient. A well-founded technique is thus imperative for evaluating the compositional data from an X-ray microanalysis.[5,6]

Micro-segregation is caused by the redistribution of a solute during the solidification, as a solute is generally injected into the liquid. Its fundamental cause is the difference between the thermodynamic equilibrium solubility of the alloy elements in different phases that coexist in the mushy region during the solidification. This is combined with the inability of the solid-state diffusion to fully return the composition to its equilibrium constant level after the solidification is complete, due to the short times and small diffusion coefficients involved.[7]

A micro-structure prediction is a very difficult task requiring computationally intensive modeling methods, such as the phase field[8] and cellular automata.[9]

The presented paper describes a simple methodology for determining the chemical heterogeneity in metallic poly-component systems, which was developed on the basis of a long-term investigation and mathematical modeling of the segregation processes during the crystallization of metallic alloys at the authors' workplaces.

An original approach to determining the chemical heterogeneity in the structure of a poly-component system is based on the experimental measurements made on the samples taken from characteristic places of the casting. In the selected sections of these samples the concentration of solutes is determined in regular steps. The length of a measured line depends on the dendrite-arm spacing. The line segment, along which the concentration of the elements is measured, should appropriately intersect a number of these dendritic arms (at least five and even more). Depending on the chemical heterogeneity and the structure of the casting the selected sections usually have the lengths of 500 μm to 1000 μm, and the total number of steps, in which the concentration is determined, is set to 101. The method of the quantitative-energy dispersion (ED) or wave dispersion (WD) X-ray spectral micro-analysis is used for determining the concentration of the elements.

After the termination correspondence of the measured concentrations of the elements and the structure of the given alloy is documented, the average dendrite-arm spacing is metallographically determined within the frame of the measured section.

Further procedure is based on statistical processing of the concentration-data sets and the application of the original mathematical model for determining distribution curves of the dendritic segregation of the elements, characterizing the most probable element-concentration distribution in the frame of a dendrite,[10] and the original mathematical model for determining the effective partition coefficients of these elements in the analyzed alloy.

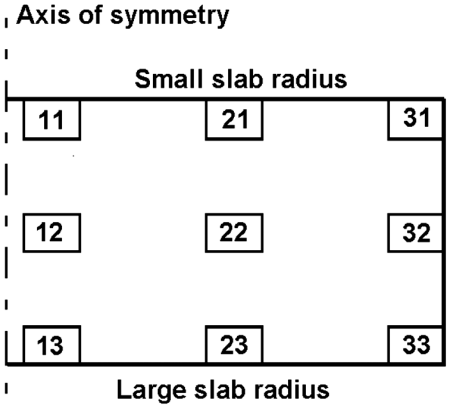

Figure 1: Scheme of a sampling from a slab and marking of the samples
Slika 1: Načrt vzorčenja in oznake vzorcev iz slaba

2 EXPERIMENTAL WORK

A continuously cast steel slab (CC steel slab) with the cross-section dimensions of 1530 mm × 250 mm was chosen for the presentation of the results. The chemical composition of the steel (in mass fractions, *w*/%) was the following: 0.14C; 0.75Mn; 0.23Si; 0.016P; 0.010S; 0.10Cr; 0.050Cu; 0.033Al_{total}.

After the solidification and cooling of the cast slab, a transversal band was cut out, which was then axially divided into halves. Nine samples were taken from one half for determining the chemical heterogeneity as seen on **Figure 1**. The samples had a form of a cube with an edge of about 20 mm, with recorded orientation of its original position in the CC slab.

All samples were prepared with the standard metallographic techniques. On each sample a concentration of seven elements (Al, Si, P, S, Ti, Cr and Mn) were measured along the line of 1000 μm. The distance between the measured points was 10 μm. An analytical, complex JEOL JXA 8600/KEVEX Delta V Sesame and an ED micro-analysis were used for determining the concentration distribution of the elements. As an example, **Figure 2** presents the basic concentration spectra of Mn and Si.

3 RESULTS AND DISCUSSION

The chemical micro-heterogeneity, i.e., the segregation of individual elements at the distances, the order of which is comparable to the dendrite-arm spacing, can be quantitatively evaluated from the basic statistical parameters of the measured concentrations of the elements in individual samples: C_{av} average concentration of an element in the measured section, σ_C standard deviation of the measured concentration of the element, C_{min} minimum and C_{max} maximum concentrations of the element in the same measured section of the sample.

Moreover, it is possible to calculate, from these data, the indices of dendritic heterogeneity I_H of the elements in the measured section as the ratio between the standard

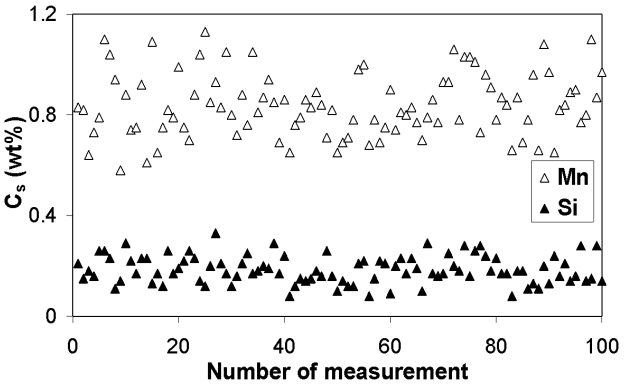

Figure 2: Basic concentration spectra of Mn and Si (sample 21)
Slika 2: Spekter osnovnih koncentracij Mn in Si (vzorec 21)

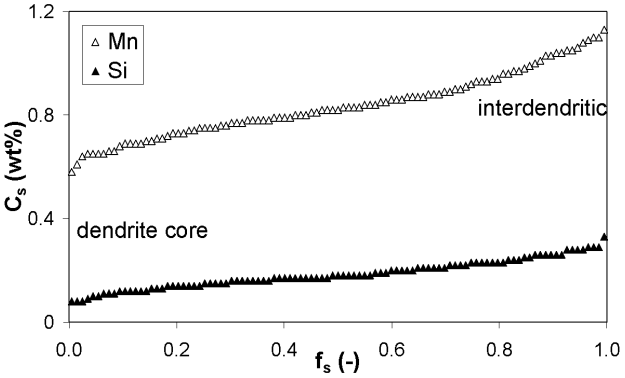

Figure 3: Distribution profiles of Mn and Si constructed from the experimentally obtained data according to the Gungor's method[11] (sample 21)

Slika 3: Profil razporeditve Mn in Si, dobljen iz eksperimentalno izmerjenih podatkov skladno z Gungorjevo metodo[11] (vzorec 21)

deviation σ_C and the average concentration C_{av} of an element.

Then the element-distribution profiles can be plotted according to the Gungor's method[11] from the concentration-data sets measured along the line segment with the length of 1000 μm. The data plotted as the measured weight-percent composition versus the number of data (**Figure 2**) were put in an ascending or descending order and the *x*-axis was converted to the fraction solid (f_S) by dividing each measured data number by the total measured data number. The element composition versus the fraction solid, i.e., the element-distribution profile (the distribution curve of a dendritic segregation) was then plotted; **Figure 3** represents such dependences for manganese and silicon. The slope of such a curve (ascending or descending) depended on whether the element in question enriched the dendrite core or the inter-dendritic area in the course of the solidification.

From these statistical data it is also possible to determine the values of effective partition coefficients k_{ef} for each element analyzed on each sample. The original mathematical model for an effective-partition-coefficient calculation will be outlined here as follows:

The sequence of the arranged concentrations (**Figure 3**) was seen as a distribution of concentrations of a measured element in the direction from the axis ($f_S = 0$) to the boundary ($f_S = 1$) of an average dendrite. The effective partition coefficient k_{ef} was, in this case, defined with the relation:

$$k_{ef}\,(f_S) = C_S\,(f_S)/C_L\,(f_S) \qquad (1)$$

where C_S is the solute concentration in the solid and C_L is its concentration in the melt and the argument (f_S) expresses the dependence of both concentrations on the fraction solid.

A perfect mixing of an element in an interdendritic melt was then assumed (this assumption is the same as, e.g., in the Scheil[12] and Brody-Flemings[1] model of solidification). It was therefore possible to substitute the equation (1) with the following formula:

$$k_{ef}\,(i) = C_i/C_R\,(i) \qquad (2)$$

where C_i is the concentration in the *i*-th point of a sequence (i.e., in the *i*-th point of the curve in **Figure 3**) and $C_R(i)$ is the average concentration of the element *i* in the residual part of the curve (i.e., for $f_S \in \langle i, 1\rangle$), expressed by the relation:

$$C_R(i) = \left(\frac{1}{n-i+1}\right)\cdot\sum_{j=i}^{n} C_j \qquad (3)$$

where *n* was the number of the measured points. In this way it was possible to determine the values of effective partition coefficients for all $i \in \langle 1, n\rangle$, i.e., for the entire curve characterizing the segregation during the solidification. The effective partition coefficients of all the analyzed elements were calculated with this original method. The average values for the determined effective partition coefficients are listed in **Table 1**. No segregation occurs when $k_{ef} = 1$; the higher the deviation from the number 1 is, the higher is the segregation ability.

The data presented in **Tables 1** and **2** make it possible to evaluate the dendritic heterogeneity (micro-heterogeneity) of the elements in individual samples, and also in the frame of the whole analyzed half of the slab's cross-section. It is obvious that the dendritic heterogeneity of the elements is comparatively high. This is demonstrated with the index of dendritic heterogeneity I_H. It follows from Table 1 that distinct differences exist between micro-heterogeneities of individual elements. The average value of this coefficient for all the analyzed elements and the whole set of nine samples is given in

Table 1: Average values of the heterogeneity index I_H and the effective partition coefficient k_{ef} of the elements in individual samples

Tabela 1: Povprečna vrednost indeksa heterogenosti I_H in koeficienta porazdelitve k_{ef} elementov v posameznem vzorcu

Sample		Element						
		Al	Si	P	S	Ti	Cr	Mn
11	I_H	1.24	0.28	1.22	1.45	0.30	0.22	0.14
	k_{ef}	0.32	0.78	0.33	0.26	0.76	0.83	0.88
12	I_H	1.54	0.30	1.12	1.74	0.29	0.27	0.15
	k_{ef}	0.24	0.77	0.36	0.20	0.78	0.79	0.88
13	I_H	1.44	0.30	1.25	1.48	0.30	0.29	0.15
	k_{ef}	0.27	0.78	0.32	0.26	0.77	0.78	0.88
21	I_H	1.33	0.29	1.58	1.49	0.31	0.24	0.13
	k_{ef}	0.29	0.78	0.24	0.25	0.76	0.81	0.89
22	I_H	1.14	0.28	1.31	1.41	0.30	0.26	0.14
	k_{ef}	0.35	0.78	0.30	0.27	0.77	0.80	0.88
23	I_H	1.56	0.29	1.34	1.86	0.26	0.28	0.13
	k_{ef}	0.24	0.78	0.29	0.18	0.80	0.78	0.89
31	I_H	1.11	0.28	1.22	2.34	0.31	0.23	0.16
	k_{ef}	0.37	0.78	0.33	0.18	0.76	0.82	0.87
32	I_H	1.44	0.27	1.16	1.49	0.34	0.25	0.14
	k_{ef}	0.27	0.79	0.34	0.25	0.74	0.80	0.88
33	I_H	1.32	0.29	1.24	1.64	0.35	0.26	0.13
	k_{ef}	0.30	0.78	0.32	0.22	0.74	0.80	0.89

Table 2: Average values of the measured and calculated quantities in the set of all the samples
Tabela 2: Povprečne vrednosti izmerjenih in izračunanih količin za sklop vseh vzorcev

	$C_{av} \pm \sigma_C$	$I_H \pm \sigma_I$	$k_{ef} \pm \sigma_k$	$k^{(ref)}$ 13–15
Al	0.0136 0.0029	1.352 0.162	0.294 0.046	0.12–0.92
Si	0.1910 0.0068	0.285 0.011	0.781 0.005	0.66–0.91
P	0.0141 0.0023	1.270 0.133	0.314 0.035	0.06–0.50
S	0.0136 0.0030	1.657 0.297	0.232 0.035	0.02–0.10
Ti	0.0951 0.0032	0.306 0.027	0.765 0.019	0.05–0.60
Cr	0.1758 0.0076	0.255 0.023	0.799 0.017	0.30–0.97
Mn	0.8232 0.0169	0.143 0.009	0.873 0.033	0.72–0.90

Table 2. It follows from this table that the dendritic heterogeneity of the slab decreases in this order of elements: sulphur, aluminium, phosphor, titanium, silicon, chromium and manganese, which has the lowest index of heterogeneity.

The dendritic heterogeneities of the analyzed elements are also expressed with the values of their effective partition coefficients for the individual samples as listed in **Table 1** and for the set of samples in **Table 2**. It is obvious that pair values of the index of dendritic heterogeneity and the effective distribution coefficient for the same element do mutually correspond. The fact is that the higher the value of a heterogeneity index, the lower the value of an effective partition coefficient and vice versa. The lowest value of the effective partition coefficient is found in sulphur and the highest value is found in manganese. It follows from **Table 2** that an effective distribution coefficient increases in this order of elements: S, Al, P, Ti, Si, Cr and Mn. All the analyzed elements segregate during the solidification into an inter-dendritic melt, and their partition coefficient is smaller than one.

For comparison, **Table 2** contains also the values of the partition coefficients found in literature.[13–15] It is obvious that our values of the effective partition coefficients, calculated according to the original model, are in good agreement with the data from the literature, with the exception of sulphur (and titanium). The reason for this difference is probably the method of calculating an effective partition coefficient – the value of this parameter is calculated from the concentration-data set measured on a solidified and cooled casting. Consequently, the effective partition coefficients calculated in this way inherently include both the effect of segregation in the course of alloy solidification and the effect of homogenization, occurring during the solidification as well as during the cooling of an alloy.

The presented methodology of an investigation into the chemical micro-heterogeneity makes it possible to study and to describe the micro-segregation behavior of the selected elements in the representative areas of a steel slab. Since a microprobe was used for the experimental investigation, the results have a high accuracy (even though an assessment with a microprobe is time-intensive and costly). The results, acquired in this way, can also provide the standards for another, faster and cheaper method for investigating the (micro)heterogeneity of a CC steel slab.[16]

4 CONCLUSIONS

The following main findings and results were obtained during an investigation into the chemical micro-heterogeneity of a CC steel slab:

- the dendritic heterogeneity of the accompanying elements and impurities is comparatively high;
- all the analyzed elements segregate during the solidification into an inter-dendritic melt, and their partition coefficient is smaller than one (concrete values of the partition coefficients for the analyzed elements and individual samples are given in **Table 1**, the average values for all the samples are given in **Table 2**);
- the dendritic heterogeneity decreases in the following order of elements: S, Al, P, Ti, Si, Cr and Mn;
- the effective partition coefficients calculated in this new way inherently include both the effect of segregation in the course of an alloy's solidification, and the effect of homogenization, occurring during the solidification, as well as during the cooling of an alloy.

Acknowledgements

The authors acknowledge the support of the Czech Science Foundation, projects No. P107/11/1566.

5 REFERENCES

[1] M. C. Flemings, D. R. Poirier, R. V. Barone, H. D. Brody, Microsegregation in iron-base alloys, J. Iron Steel Int., 208 (**1970**), 371–81
[2] S. Tin, T. M. Pollock, Phase instabilities and carbon additions in single-crystal nickel-base superalloys, Mater. Sci. Eng. A, 348 (**2003**), 111–21
[3] M. Ganesan, D. Dye, P. D. Lee, A technique for characterizing microsegregation in multicomponent alloys and its application to single-crystal superalloy castings, Met. Mat. Trans A, 36 A (**2005**), 2191–2204
[4] K. Stransky, F. Kavicka, B. Sekanina, J. Dobrovska, V. Gontarev, Numerical and experimental analyses of the chemical heterogeneity of a solidifying heavy ductile-cast-iron roller, Mater. Tehnol, 46 (**2012**) 4, 389–392
[5] A. Howe, J. Lacaze, P. Benigni, Some issues concerning experiments and models for alloy microsegregation, Adv. Eng. Mater., 5 (**2003**), 37–46
[6] F. Xie, X. Yan, L. Ding, F. Zhang, S. Chen, M. G. Chu, Y. A. Chang, A study of microstructure and microsegregation of aluminum 7050 alloy, Mater. Sci. Eng. A, 355A (**2003**), 144–53

[7] Y. M. Won, B. G. Thomas, Simple Model of Microsegregation During Solidification of Steels, Met. Mat. Trans A, 32A (**2001**), 1755–1761

[8] J. Rappaz, J. F. Scheid, Existence of solutions to a phase-field model for the isothermal solidification process of a binary alloy, Math. Methods Appl. Sci., 23 (**2000**), 491–513

[9] Y. M. Won, K. H. Kim, T. Yeo, K. H. Oh, Effect of Cooling Rate on ZST, LIT and ZDT of Carbon Steels Near Melting Point, Iron Steel Inst. Jpn. Int., 38 (**1998**), 1093–99

[10] J. Dobrovská, V. Dobrovská, A. Rek, K. Stránský, Possible ways of prediction of the distribution curves of dendritic segregation of alloying elements in steels, Scripta Mat., 38 (**1998**), 1583–1588

[11] M. N. Gungor, A statistically significant experimental technique for investigating micro-segregation in cast alloys, Metall. Trans. A, 20A (**1989**), 2529–2538

[12] E. Scheil, Uber die eutektische kristallisation, Z. Metallkd., 34 (**1942**), 70–80

[13] L. Šmrha, Solidification and crystallisation of steel ingots, SNTL, Praha 1983 (in Czech)

[14] P. Levíček, K. Stránský, Metallurgical defects of steel castings (causes and their elimination), SNTL, Praha 1984, 257 (in Czech)

[15] H. J. Eckstein, Wärmebehandlung von Stahl, VEB, DVG, Leipzig 1971, 139

[16] H. Presslinger, S. Illie, A. Pissenberger, E. Parteder, C. Bernhard, Methods for assessment of slab centre segregation as a tool to control slab continuous casting with soft reduction, ISIJ Int., 46 (**2006**), 1845–1851

UDK 621.77.014.2
Original scientific article/Izvirni znanstveni članek

ISSN 1580-2949
MTAEC9, 47(1)85(2013)

HEAT-FLUX COMPUTATION FROM MEASURED-TEMPERATURE HISTORIES DURING HOT ROLLING

RAČUNANJE TOPLOTNEGA TOKA NA OSNOVI PRETEKLIH MERITEV TEMPERATURE MED VROČIM VALJANJEM

Jana Ondrouskova[1], Michal Pohanka[1], Bart Vervaet[2]

[1]Heat Transfer and Fluid Flow Laboratory, Faculty of Mechanical Engineering, Brno University of Technology, Technická 2, 616 69 Brno, Czech Republic
[2]Centre for Research in Metallurgy, Technologiepark 903c, 9052 Zwijnaarde, Belgium
ondrouskova@lptap.fme.vutbr.cz

Prejem rokopisa – received: 2012-08-31; sprejem za objavo – accepted for publication: 2012-09-18

Due to the long service life of work rolls it is very important to follow the thermal load, but it is very difficult to measure it. One option for computing this thermal load is to measure the temperature and to study the thermal load through the heat flux. A unique work roll was made for testing different process conditions, such as rolling velocity, roll cooling, skin cooling and reduction. This work roll was tested on a real, hot-rolling, continuous pilot line. Two types of temperature sensors were embedded in the work roll in order to measure the temperature and these gave very detailed information about the development of the temperature inside the work roll. A time-dependent heat flux was computed using an inverse heat-conduction task with a detailed numerical model. The surface-temperature history was also obtained from this computational model. These boundary conditions give detailed information about the influence of different process conditions and allow a computation of the temperature field in the work roll. The paper describes the measuring equipment, details of the used temperature sensors, the inverse heat-conduction task for computing the thermal-surface boundary conditions and the results obtained from hot-rolling conditions.

Keywords: heat flux, hot rolling, roll cooling, inverse heat-conduction problem, surface temperature

Zaradi dolge dobe trajanja delovnih valjev je pomembno sledenje njihovih toplotnih obremenitev, ki jih je težko izmeriti. Ena od opcij izračuna termičnih obremenitev je merjenje temperature in študij toplotne obremenitve s toplotnim tokom. Izdelan je bil valj za preizkušanje različnih procesnih pogojev, kot so hitrost valja, ohlajanje valja, ohlajanje skorje valja in odvzem. Ta delovni valj je bil preizkušen na realni kontinuirni vroči valjarniški pilotni liniji. V delovni valj sta bili vgrajeni dve vrsti temperaturnih senzorjev, da bi izmerili temperature, in obe sta dali zelo podrobno informacijo o poteku temperature v njem. Izračunana je bila časovna odvisnost toplotnega toka z natančnim matematičnim modelom inverznega toka toplote. Iz tega računskega modela je bila dobljena tudi zgodovina temperature površine. Ti mejni pogoji so dali natančno informacijo o učinku različnih parametrov procesa in omogočili izračun temperaturnega polja v delovnem valju. V članku je predstavljena merilna oprema, detajli uporabljenih senzorjev temperature, inverzno prevajanje toplote za izračun mejnih termičnih razmer na površini in rezultati, dobljeni pri valjanju.

Ključne besede: toplotni tok, vroče valjanje, hlajenje valja, problem inverznega prevajanja toplote, temperatura površine

1 INTRODUCTION

The work roll is repeatedly heated and cooled during the hot-rolling process. A good knowledge of the temperature field of the work roll and a stress-strain analysis help us improve the cooling of the work roll and, thus, to extend its service life. The measurement of temperature histories inside the work roll during a hot-rolling trial was reported by Raudensky et al.[1] This article describes the results of the measurements in the pilot mill of CRM, Gent. The temperature sensors were embedded into the roll using inserts (as seen on the top of **Figure 1**). There were five thermocouples in each roll. An example of the data from the real measurement is on the bottom of **Figure 1**. The thermocouples were placed at two different depths. Two thermocouples were soldered at a depth of 0.4 mm (**Figure 1**) and three were drilled at a depth of 0.8 mm. A detailed description of the plug with a drilled shielded thermocouple and the discretization used for the computational model is given in[2].

2 INVERSE HEAT-CONDUCTION PROBLEM

A complex 2D-axis symmetric model was used for the numerical computation. The model includes the shielded thermocouple with all its parts and the used solder. The thermocouple must be taken into account because the homogeneity of the material is disturbed by the inserted thermocouple, and, thus, the temperature profile is also disturbed. One-dimensional sequential Beck's approach[3] is used for the computing of the heat fluxes and the surface temperatures. The main feature of this method is the sequential estimation of the time-varying heat fluxes and surface temperatures using the future time-step data to stabilize an ill-posed problem. The measured temperature history is used as input T^* to minimize the equation:

$$SSE = \sum_{i=m+1}^{m+f} (T_i^* - T_i)^2 \quad (1)$$

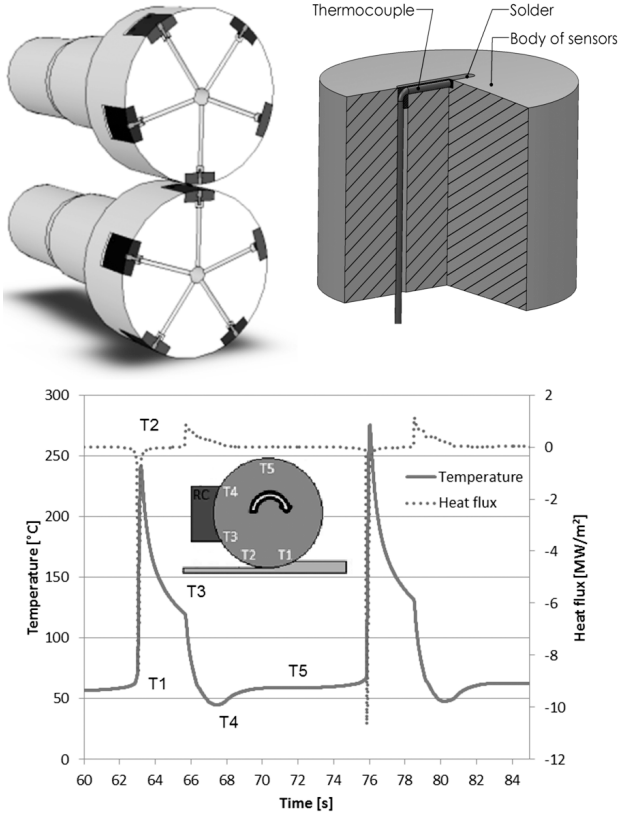

Figure 1: Cross-section of the rolls with the inserts from HiCr and HSS materials and the holes for the thermocouple wires; a detail of the plug with a soldered shielded thermocouple; temperature data of the two roll cycles (depth of 0.4 mm, speed of 0.1 m/s, reduction of 10 %)

Slika 1: Prečni prerez valja z vložki iz materialov HiCr in HSS in luknje za žico termoelementov; detajl čepa s prispajkanim termoelementom; podatki o temperaturah pri dveh ciklih valjanja (globina 0,4 mm, hitrost 0,1 m/s, odvzem 10-odstoten)

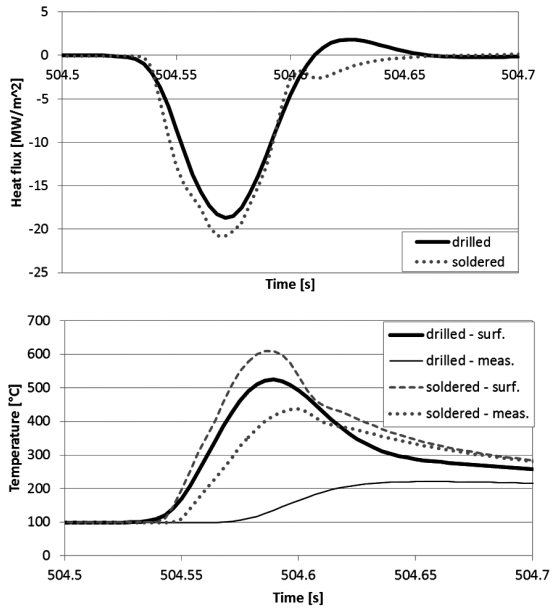

Figure 2: Comparison of the results obtained from the drilled and soldered thermocouple

Slika 2: Primerjava rezultatov, dobljenih iz izvrtanega oziroma prispajkanega termoelementa

where m is the current time, f is the number of future time steps and T_i indicates the computed temperatures from the forward solver[4]. *SSE* denotes the sum of square errors. The value of surface heat flux q at time m is:

$$q^m = \frac{\sum_{i=m+1}^{m+f} (T_i^* - T_i\big|_{q^m=0})\zeta_i}{\sum_{i=m+1}^{m+f} (\zeta_i)^2}; \zeta_i = \frac{\partial T_i}{\partial q_m} \qquad (2)$$

where ζ_i is a sensitivity coefficient of the temperature sensor at the time index i to the heat-flux pulse at time m. The temperatures $T_i\big|_{q^m=0}$ at the sensor location, computed from the forward solver, use all the previously computed heat fluxes without the current one, q^m. When the heat flux is found for time m, the corresponding surface temperature T_m^{surf} is computed from the forward solver. Using this procedure, the whole heat-flux history and surface-temperature history are computed.

3 RESULTS

The heat fluxes and surface temperatures computed using an inverse heat-conduction problem are presented here. The measured data were used for computing. **Figure 2** shows a comparison of the results obtained from the soldered and drilled sensor. It is obvious that faster changes can be studied with a thermocouple being implemented closer to the surface. During the measurements various parameters such as reductions (10 %, 30 % and 50 %, **Figure 3**), velocities (0.1 m/s, 0.3 m/s and 0.5 m/s), and roll cooling (on/off) were tested.

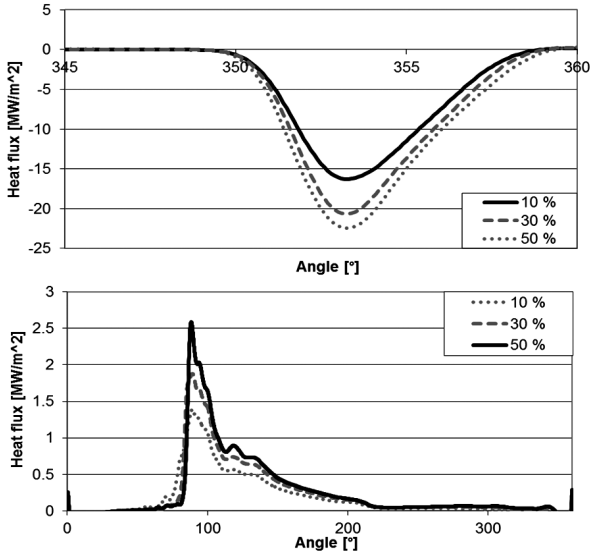

Figure 3: Influence of the slab reductions on the heat flux computed from the thermocouple situated 0.8 mm under the roll surface. The contact with the hot strip is on the top and the cooling of the roll is on the bottom.

Slika 3: Vpliv redukcije slaba na izračunan tok toplote, izračunan z uporabo termoelementa, nameščenega 0,8 mm pod površino valja. Zgoraj je prikazan na stiku z vročim trakom, spodaj pa ohlajanje valja.

4 CONCLUSION

An implementation of shielded thermocouples in a work roll used in a pilot mill of CRM, Ghent, was presented. Two types of plugs were used. One type had a soldered thermocouple very close to the surface and the other type had a thermocouple placed in a drilled hole that was 0.8 mm under the surface. An inverse algorithm, which enables a computation of the surface heat fluxes and surface temperatures from the measured temperature history inside a roll, was described. The presented results show the influence of the distance of the thermocouple from the investigated surface on the calculated surface-temperature and heat-flux accuracy. The closer the thermocouple is to the surface the faster changes can be investigated. The sensor with a soldered thermocouple gives a more accurate result as it is closer to the surface; however, the durability of this sensor is very low and it is destroyed after several contacts with the hot strip. On the other hand, the durability of a sensor with a drilled hole is much longer, but its results are not so accurate because the distance of the thermocouple from the surface is longer.

Acknowledgement

The research has been supported within the project No. CZ.1.07/2.3.00/20.0188, HEATEAM–Multidisciplinary Team for Research and Development of Heat Processes, and partially investigated within the RFCS project CHILLUB, Advanced method to improve work-roll life time and surface quality of hot rolled strip by new coupled oil-free lubrication and chilling, No. RFSR-CT-2008-00012.

5 REFERENCES

[1] M. Raudenský, J. Horsky, A. A. Tseng, J. Weng, Heat Transfer Evaluation of impingement cooling in hot rolling of shaped steels, Steel Research, 65 (**1994**) 9, 375–381

[2] M. Pohanka, M. Raudenský, Determination of heat resistances between installed thermocouple and body used for computing heat transfer coefficients. In: Engineering mechanics, Svratka, Czech Republic, 2002, 227–228

[3] J. Beck, B. Blackwell, C. R. Clair, Inverse heat conduction: ill-posed problems, Wiley, New York 1985, 308

[4] W. J. Minkowycz, E. M. Sparrow, J. Y. Murthy, Handbook of Numerical Heat Transfer, 2nd edition, John Willey & Sons, New Jersey 2006, 968

UDK 533.9:678.7
Original scientific article/Izvirni znanstveni članek

ISSN 1580-2949
MTAEC9, 47(1)89(2013)

THERMAL DEFUNCTIONALIZATION OF AN OXYGEN-PLASMA-TREATED POLYETHERSULFONE

TERMIČNA DEFUNKCIONALIZACIJA POLIMERA POLIETERSULFONA, OBDELANEGA V KISIKOVI PLAZMI

Miran Mozetič, Alenka Vesel

Jožef Stefan Institute, Jamova cesta 39, 1000 Ljubljana, Slovenia
miran.mozetic@ijs.si

Prejem rokopisa – received: 2012-09-03; sprejem za objavo – accepted for publication: 2012-09-14

The phenomenon of spontaneous decay of oxygen-rich functional groups on the surface of a polymer was studied with high-resolution X-ray photoelectron spectroscopy (XPS). Samples of smooth poly(ether-sulfone) PES foils were exposed to a highly non-equilibrium oxygen plasma created in an electrodeless RF discharge. After receiving a dose of about 1×10^{24} m^{-2} oxygen atoms the surface of the polymer became saturated with oxygen-rich functional groups such as C–O, C=O, COO^-. The XPS survey spectra showed an increase in the oxygen concentration from the original mole fractions 21 % to more than 42 %, while the high-resolution C1s spectra showed that the carboxyl group prevailed. The samples were heated in the XPS chamber for different periods and characterized in-situ right after the heat treatment. It is shown that the functional groups decay spontaneously with time and their concentration decreases below the detection limit after annealing at 200 °C for 8 min.

Keywords: oxygen plasma, polymer, functionalization, defunctionalization, thermal stability, activation, deactivation

Z metodo rentgenske fotoelektronske spektroskopije (XPS) smo raziskovali proces spontanega razpada kisikovih funkcionalnih skupin na površini polimera. Vzorce folije PES smo izpostavili visoko neravnovesni kisikovi plazmi, ustvarjeni v brezelektrodni radiofrekvenčni razelektritvi. Po izpostavitvi vzorcev kisikovi plazmi, kjer je bila prejeta doza kisikovih atomov okoli 1×10^{24} m^{-2}, se je površina vzorca nasitila z različnimi funkcionalnimi skupinami, kot so C–O, C=O, COO^-. Iz preglednih XPS-spektrov smo ugotovili, da je koncentracija kisika na površini narasla iz prvotnih molskih deležev 21 % na 42 %, medtem ko smo iz visokoločljivih spektrov ogljika ugotovili, da prevladuje karboksilna skupina. Plazemsko obdelane vzorce smo nato po kemijski analizi v posodi XPS in-situ segrevali različno dolgo, jih ohladili in še enkrat pomerili površinsko sestavo. Ugotovili smo, da funkcionalne skupine s časom spontano razpadajo. Po 8 min gretja pri 200 °C pade njihova koncentracija pod detekcijsko mejo.

Ključne besede: kisikova plazma, polimer, funkcionalizacija, defunkcionalizacija, termična stabilnost, aktivacija, deaktivacija

1 INTRODUCTION

Polymer materials are nowadays widely used in practical life and science. The surface properties of selected polymers are often not adequate so they should be modified prior to specific applications. The basic property of a polymer is its hydrophilicity. Most polymers are moderately hydrophobic. If it is necessary to make them more hydrophobic, the surface is functionalized with nonpolar functional groups, typically fluorine-rich functional groups.[1–4] Together with the high surface roughness, the polymers can be made superhydrophobic which means that the contact angle of a water drop approaches 180°. On the other hand, it is sometimes necessary to make polymers more hydrophilic. A standard procedure is the functionalization of a surface with polar functional groups – usually oxygen-rich functional groups such as carboxyl, carbonyl, hydroxyl, etc. Surprisingly enough, a combination of a high concentration of these functional groups and a very rough surface, which is due to an intense etching of a polymer surface,[5–8] often leads to a superhydrophilic character of the polymer.[9] Namely, the contact angle of the water drop becomes immeasurably low. In practice it means that the contact angle is below a few degrees.

There are many methods for the surface functionalization, but it seems that the nowadays treatment with non-equilibrium gaseous plasma prevails. Plasma treatment often assures for rapid functionalization.[10] While atmospheric plasmas are increasingly popular, low-pressure plasmas are still more applicable because they assure for a rather uniform treatment of the arbitrary samples with a complex shape. Plasma treatment is nowadays widely used also on the industrial scale. A phenomenon that is known to many researchers, but often neglected in relevant literature, is a slow loss of hydrophilicity.[11–13]

Highly hydrophilic properties of polymer materials are usually obtained by applying weakly ionized, highly reactive oxygen plasma. There are numerous reports on the functionalization of different materials with an oxygen-plasma treatment, including polyethylene terephthalate[9,14,15], polyethersulphone[16], polystyrene[17], polyvinylchloride[18], polymethyl methacrylate[19], cellulose[20,21], etc. While many authors use plasma as a black box (i.e., they do not measure the plasma parameters but present the results on the functionalization as a function of discharge parameters), there are also reports in the literature about a precise determination of both plasma parameters and the surfaces of plasma-treated

materials.[22,23] A decent scientific paper would typically include a flux of positively charged oxygen as well as neutral oxygen atoms on the surface of a polymer, and a characterization with XPS and/or SIMS and AFM and/or SEM. In fact, quite a few scientific papers include all these data. There are many papers studying the ageing effects (especially with the water-contact-angle measurements)[9] but, on the other hand, very few papers address the ageing phenomenon, i.e., a spontaneous decrease in the concentration of functional groups induced with thermal effects. In the present paper we address these phenomena. The decay of the functional groups was studied in-situ in the XPS chamber in order to minimize the number of possible effects.

2 EXPERIMENTAL WORK

Samples of the commercially available PES foils with pretty smooth surfaces were prepared as follows. The freshly packed foils were unpacked, cut into small pieces and mounted to a plasma system to be functionalized. The plasma system has been described to details elsewhere.[9] For the sake of the completeness of the paper let us just summarize the properties. Plasma is excited with an electrodeless RF discharge at variable power and oxygen pressure. In the case of our latest experiment we used a rather low RF power of about 100 W. At the pressure of 75 Pa the density of the charged particles was about 8×10^{15} m^{-3}, while the density of the neutral oxygen atoms was orders of magnitude larger at a value of about 4×10^{21} m^{-3}. The samples of PES foil were exposed to the plasma with such parameters for 3 s. The resultant flux of the neutral oxygen atoms was about 6×10^{23} m^{-2} s^{-1} and the received dose of the atoms in 3 s was close to 2×10^{24} m^{-2}. Such a large dose of the neutral oxygen atoms assures for a saturation of the polymer surface with the oxygen-rich functional groups as has been already shown in another paper[9].

The plasma-treated samples were exposed to air for a short time and mounted into the XPS instrument (TFA XPS Physical Electronics). The XPS (X-ray photoelectron spectroscopy) measurement was performed as follows: a plasma-treated sample was first analyzed to see its chemical composition after the plasma treatment. Then the sample holder in the XPS chamber was heated, in a short time, to 200 °C to study the thermal stability of the functional groups formed during the plasma treatment. The sample was kept at this temperature for a certain time (1 min and 8 min) and the holder was cooled down to room temperature before the XPS characterization of the treated sample.

During the XPS measurement the sample was excited with the X-rays with a monochromatic Al $K_{\alpha 1,2}$ radiation at 1486.6 eV. The photoelectrons were detected with a hemispherical analyzer positioned at an angle of 45° with respect to the normal to the sample surface. The survey-scan spectra were made at a pass energy of 187.85 eV and with a 0.4 eV energy step. The high-resolution spectra of C1s were made at a pass energy of 23.5 eV and with a 0.1 eV energy step. The concentration of the elements was determined using MultiPak v7.3.1 software from Physical Electronics, which was supplied together with the spectrometer. The high-resolution spectra were fitted using the same software. The curves were fitted with the symmetrical Gauss-Lorentz functions. A Shirley-type background subtraction was used. Both the relative peak positions and the relative peak widths (FWHM) were fixed in the curve-fitting process.

3 RESULTS

Small pieces of foils were treated with the oxygen plasma in order to get the surface saturated with the oxygen-rich functional groups. Several samples were tested, but the differences between particular samples treated under the same conditions were minimal. The XPS survey spectra of the selected samples are shown in **Figure 1**. The lowest curve refers to the untreated sample and the other curves refer to the sample treated by plasma, the sample treated by plasma and heated at 200 °C for 1 min and the sample treated by plasma and heated for 8 min at the same temperature. From **Figure 1** it can be estimated that the plasma treatment caused an increase in the oxygen concentration, while the thermal treatment caused a decrease in the oxygen concentration on the plasma-treated samples. The quantitative values of the surface composition for all four cases are presented in **Table 1**. As expected, the concentration of oxygen on the plasma-treated sample is much larger than on the original sample. The O/C ratio is increased by almost a factor of 3. The values of the oxygen concentration on the samples treated by plasma and then heated in the

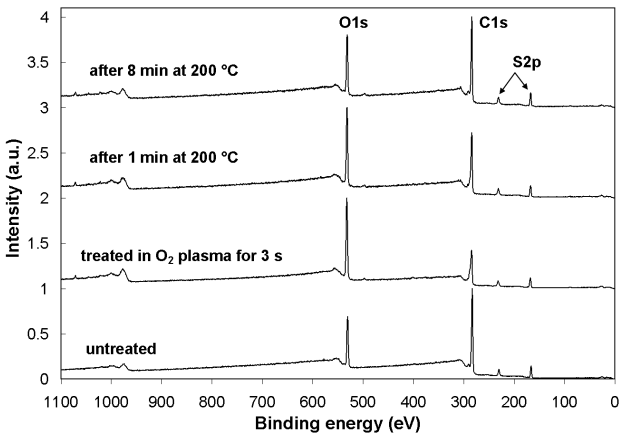

Figure 1: Comparison of the XPS survey spectra of an untreated polymer, a polymer treated in oxygen plasma for 3 s, a polymer treated in plasma and heated at 200 °C for 1 min and the one heated at 200 °C for 8 min

Slika 1: Primerjava preglednih spektrov XPS neobdelanega polimera, polimera obdelanega v plazmi 3 s in plazemsko obdelanega polimera, ki je bil za 1 min ter 8 min segret na 200 °C

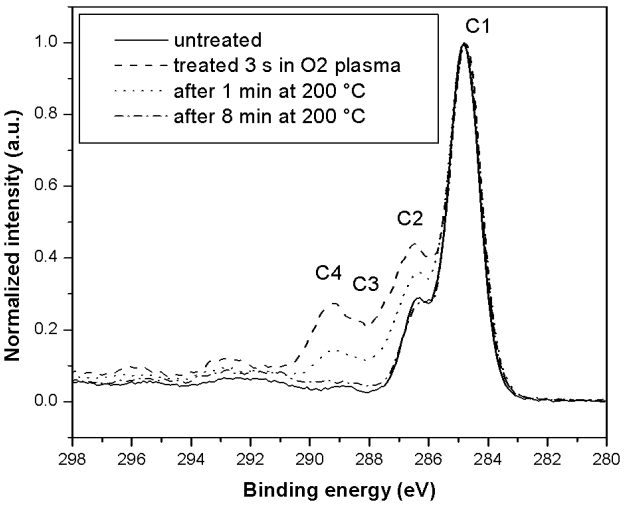

Figure 2: Comparison of the high-resolution C1s spectra of the untreated and treated PES polymers
Slika 2: Primerjava visokoločljivih spektrov ogljika C1s neobdelanega in obdelanega polimera PES

Table 1: Surface compositions of the untreated and treated PES polymers
Tabela 1: Površinska sestava neobdelanega in obdelanega polimera PES

Sample	C	O	S	O/C
untreated	73.8	21.1	5.1	0.29
treated for 3 s in O_2	52.0	42.3	5.7	0.81
after 1 min at 200 °C	61.3	33.4	5.4	0.54
after 8 min at 200 °C	69.8	24.6	5.6	0.35

Table 2: Concentrations of different chemical states of carbon atoms on the untreated and treated PES polymers
Tabela 2: Deleži različnih kemijskih stanj atomov ogljika na neobdelanem in obdelanem polimeru PES

Sample	C1 C-C C-S	C2 C-O	C3 C=O	C4 COO^-
untreated	82.7	17.3		
treated for 3 s in O_2	55.5	24.5	7.3	12.7
after 1 min at 200 °C	71.1	21.3	2.1	5.5
after 8 min at 200 °C	84.2	15.8		

XPS chamber are more interesting. Table 1 shows that the oxygen concentration drops substantially even after 1 min of heat treatment. After 8 min of heat treatment the oxygen concentration becomes so low that any speculation about the ratio between O and C for these samples and the untreated sample would not be fair.

Figure 2 represents the high-resolution C1s peaks for the selected samples. From this figure one can conclude that any difference between the untreated sample and the sample treated with oxygen plasma and heated for 8 min is below the detection limit of our device. On the other hand, the high-resolution C1s peak for the sample treated in the oxygen plasma for 3 s is completely different. The quantification of these results is summarized in **Table 2**. From this table we can see that the majority of the oxygen is incorporated into the surface layer of PES in the form of carboxyl groups. It is interesting that the decay of a particular functional group during the heat treatment is not very selective. Within the experimental error one cannot conclude weather any of the newly formed functional groups decays faster than the other groups. It is only possible to conclude that the thermal decay is pretty effective.

Finally, it is worth mentioning that the original concentration of sulphur is preserved after the oxygen-plasma treatment and also after the heating experiments. This is an indication that the original structure of the polymer is preserved and oxygen is bonded practically only on the carbon atoms of the phenyl ring.

4 CONCLUSIONS

The experiments on the ageing of a plasma-functionalized PES showed a spontaneous decrease in the functional groups during the heat treatment. The temperature of 200 °C was found suitable for the effective decay of the functional groups. Since the experiments were performed in an ultra-high vacuum in the XPS chamber the decay of the groups cannot be explained with the environmental effects. The two possible explanations (either a diffusion of oxygen inside the polymer or a thermal desorption from the surface) should be taken into account. However, it is not possible to draw the final conclusion from the experimental results presented in this paper.

Acknowledgements

The work was financially supported by the Slovenian Research Agency within the research project L7-4009 "Functionalization of biomedical samples with thermodynamical non-equilibrium gaseous plasma".

5 REFERENCES

[1] N. Vandencasteele, H. Fairbrother, F. Reniers, Plasma Process. Polym., 2 (**2005**), 493–500
[2] R. di Mundo, F. Palumbo, R. d'Agostino, Langmuir, 24 (**2008**), 5044–5051
[3] S. Marais, Y. Hirata, C. Cabot, S. Morin - Grognet, M. R. Garda, H. Atmani, F. Poncin - Epaillard, Surf. Coat. Technol., 201 (**2006**), 868–879
[4] F. Poncin - Epaillard, D. Debarnot, Inform. Midem, 38 (**2008**), 252–256
[5] T. Belmonte, C. D. Pintassilgo, T. Czerwiec, G. Henrion, V. Hody, J. M. Thiebaut, J. Loureiro, Surf. Coat. Technol., 200 (**2005**), 26–30
[6] M. Mafra, T. Belmonte, F. Poncin - Epaillard, A. S. D. S. Sobrinho, A. Maliska, Plasma Chem. Plasma Process., 28 (**2008**), 495–509
[7] T. Belmonte, T. Czerwiec, H. Michel, Surf. Coat. Technol., 142 (**2001**), 306–313
[8] V. Hody, T. Belmonte, T. Czerwiec, G. Henrion, J. M. Thiebaut, Thin Solid Films, 506–507 (**2006**), 212–216
[9] A. Vesel, I. Junkar, U. Cvelbar, J. Kovac, M. Mozetic, Surf. Interface Anal., 40 (**2008**), 1444–1453
[10] A. Vesel, Inform. Midem, 38 (**2008**), 257–265

[11] P. Jannasch, Macromolecules, 31 (**1998**) 4, 1341–1347
[12] J. Larrieu, B. Held, H. Martinez, Y. Tison, Surf. Coat. Technol., 200 (**2005**), 2310–2316
[13] R. Morent, N. De Geyter, C. Leys, L. Gengembre, E. Payen, Surf. Coat. Technol., 201 (**2007**), 7847–7854
[14] C. Riccardi, R. Barni, E. Selli, G. Mazzone, M. R. Massafra, B. Marcandalli, G. Poletti, Appl. Surf. Sci., 211 (**2003**), 386–397
[15] R. Zaplotnik, M. Kolar, A. Doliska, K. Stana - Kleinschek, Mater. Tehnol., 45 (**2011**) 3, 195–200
[16] J. Feng, G. Wen, W. Huang, E. Kang, K. G. Neoh, Polym. Degrad. Stabil., 91 (**2005**), 12–20
[17] M. J. Wang, Y. I. Chang, F. Poncin - Epaillard, Surf. Interface Anal., 37 (**2005**), 348–353
[18] M. Sowe, I. Novak, A. Vesel, I. Junkar, M. Lehocky, P. Saha, I. Chodak, Int. J. Polym. Anal. Ch., 14 (**2009**), 641–651
[19] B. Tomcik, D. R. Popovic, I. V. Jovanovic, Z. L. J. Petrovic, J. Polym. Res. – Taiwan, 8 (**2001**), 259–266
[20] N. Puač, Z. Lj. Petrović, M. Radetić, A. Djordjević, Mat. Sci. Forum, 494 (**2005**), 291–296
[21] P. Jovancic, D. Jocic, M. Radetic, T. Topalovic, Z. L. Petrovic, Curr. Res. Adv. Mater. Process, 494 (**2005**), 283–290
[22] A. Drenik, A. Tomeljak, M. Mozetic, A. Vesel, D. Babic, M. Balat - Pichelin, Vacuum, 84 (**2010**), 90–93
[23] G. Primc, R. Zaplotnik, A. Vesel, M. Mozetic, AIP Advances, 1 (**2011**), 022129-1–022129-11

UDK 669.14:621.78
Original scientific article/Izvirni znanstveni članek

ISSN 1580-2949
MTAEC9, 47(1)93(2013)

DIAGNOSTICS OF THE MICROSTRUCTURAL CHANGES IN SUB-ZERO-PROCESSED VANADIS 6 P/M LEDEBURITIC TOOL STEEL

DIAGNOSTIKA SPREMEMB MIKROSTRUKTURE PRI KRIOGENI OBDELAVI P/M LEDEBURITNEGA ORODNEGA JEKLA VANADIS 6

Jana Sobotová[1], Peter Jurči[2], Jan Adámek[3], Petra Salabová[4], Otakar Prikner[4], Borivoj Šuštaršič[5], Darja Jenko[5]

[1]Czech Technical University in Prague, Faculty of Mechanical Engineering, Karlovo nám. 13, 121 35 Prague 2, Czech Republic
[2]Faculty of Material Sciences and Technology in Trnava, Paulínská 16, 917 24 Trnava, Slovakia
[3]Czech Technical University in Prague, Faculty of Nuclear Sciences and Physical Engineering, Břehová 7, 115 19 Prague 1, Czech Republic
[4]Prikner - tepelné zpracování kovů, Martínkovice 279, 550 01, Czech Republic
[5]Institute of Metals and Technology, Lepi pot 11, 1000 Ljubljana, Slovenia
jana.sobotova@fs.cvut.cz

Prejem rokopisa – received: 2012-09-11; sprejem za objavo – accepted for publication: 2012-09-19

Specimens made from P/M Vanadis 6 cold-work steel were austenitized, quenched and tempered for various combinations of the parameters. The selected sets of samples, also in the sub-zero range, were treated at a temperature of –196 °C after quenching. The microstructure was investigated as a function of the austenitizing temperature and the parameters of the sub-zero processing using transmission electron microscopy (TEM), high-resolution transmission electron microscopy (HRTEM) and X-ray diffraction. It was found that the as-quenched microstructure is composed of martensite, retained austenite and carbides. The sub-zero processing reduced the amount of retained austenite and led to an increase in the tetragonality of the martensitic lattice. As a result, the hardness of the material was higher by 2 HRc before the tempering of the samples after the sub-zero processing, but the hardness of the sub-zero-processed material after tempering is about 2.5 HRc lower than that of the non-sub-zero-processed steel. Based on the facts that the sub-zero-processed steel contained less retained austenite and an unknown amount of the expected nano-precipitates, we expected it to have a lower capability to manifest the secondary-hardening effect.

Keywords: P/M cold-work steel, heat treatment, sub-zero treatment, precipitates

Vzorci, izdelani iz jekla za delo v hladnem P/M Vanadis 6, so bili avstenitizirani, kaljeni in popuščani pri različnih kombinacijah parametrov. Izbrana skupina vzorcev je bila obdelana v kriogenem področju pri temperaturi –196 °C po kaljenju. Preiskana je bila mikrostruktura v odvisnosti od temperature avstenitizacije in parametrov kriogene obdelave, s presevno elektronsko mikroskopijo (TEM), visoko ločljivo presevno elektronsko mikroskopijo (HRTEM) in z rentgensko difrakcijo. Ugotovljeno je, da kaljeno mikrostrukturo sestavljajo martenzit, zaostali avstenit in karbidi. Kriogena obdelava zmanjša delež zaostalega avstenita in povzroči povečano tetragonalnost martenzitne rešetke. Posledica je povečanje trdote za 2 HRc pred popuščanjem kriogeno obdelanega materiala, po popuščanju tega materiala pa je bila trdota za okrog 2,5 HRc nižja v primerjavi z jeklom brez kriogene obdelave. Na osnovi dejstva, da kriogeno obdelano jeklo vsebuje manj zaostalega avstenita in nepoznano količino nanoizločkov, pričakujemo njegovo manjšo zmožnost za pojav sekundarnega utrjevanja.

Ključne besede: P/M jeklo za delo v hladnem, toplotna obdelava, kriogena obdelava, izločki

1 INTRODUCTION

Vanadis 6 is a powder-metallurgy cold-work ledeburitic tool steel. It is well known that the materials manufactured with powder metallurgy exhibit an extremely refined and homogenous microstructure compared with that of the conventionally produced steels. According to these facts and, also due to its nominal chemical composition, Vanadis 6 has a very high wear resistance, good toughness and high compressive strength. Based on these characteristics, Vanadis 6 is suitable for cutting blades, rolling planes or tools for forming operations.

The structure and properties of ledeburitic steels are determined by the character of the matrix and the type, quantity, size and distribution of carbides and, therefore, the demanded tool life is determined by the conditions of heat treatment. During austenitizing the eutectoid and a part of the secondary carbides are dissolved in austenite, which results in a high hardness of the material after quenching. Other carbides, which are not subjected to dissolution, inhibit the coarsening of the austenite grains and make the steel wear resistant. Bílek et al.[1] reported that there are two types of carbides in Vanadis 6 after austenitizing. The first phase of M_7C_3 carbides underwent the dissolution in the austenite to a greater extent than the second phase of MC carbides, which is stable up to the temperature of 1150 °C. A previous publication[2] states that a higher austenitizing temperature results in an increase in the hardness of Vanadis 6 and a reduction of the three-point bending strength, since the increased austenitizing temperature results in a grain coarsening. After quenching, Cr-V ledeburitic steels contain martensite, retained austenite and undissolved carbides. For a more complete martensitic transformation,

sub-zero treatment can be inserted between quenching and tempering.

Recent investigations[3–5] have established that sub-zero treatment does not only substantially reduce the content of retained austenite but also significantly modifies the precipitation behaviour of the carbides in the processed materials. These changes are expected to have a considerable influence on the mechanical properties and, subsequently, on the wear resistance of tool steels. Opinions on the effect of sub-zero processing on the properties of ledeburitic steels differ. Debdulal et al.[3] reported that sub-zero treatment reduces the fracture toughness of the cold-work tool steel AISI D2 that is lower than that of the conventionally heat-treated ones. However, the degree of reduction in fracture toughness varies with the types of sub-zero treatment; it is the lowest for deep, cryogenically treated DCT (–196 °C to –160 °C) specimens and the highest for shallow, cryogenically treated (–160 °C to –80 °C) ones. Fracture-toughness values decrease, expectedly, with an increase in the hardness, a reduction of the retained-austenite content, an increase in the amount of secondary carbides and their size refinement. According to Oppenkowski[4], further investigations on D2 cold-work tool steel show that η-carbides can be observed at higher tempering temperatures, but in some investigations it was impossible to detect any η-carbides. Opposing results have also been obtained with respect to the precipitation of η-carbides. Some investigations found that carbides precipitated after DCT during tempering, others report about the precipitation during the DCT process. Shaohong[5] reported that DCT decreases the retained austenite and increases the hardness and wear resistance of cold-work die steel. Carbon atoms were segregated close to dislocations in the DCT process, ε-carbides precipitated in the twinned martensite during the process of tempering.

The aim of this research is to assess the microstructural changes during the DCT process made to powder-metallurgical tool steel Vanadis 6.

2 EXPERIMENTAL WORK

The nominal chemical composition of the experimental material Vanadis 6, manufactured with P/M is shown in **Table 1**. Details of the experimental heat-treatment program were published elsewhere[6]. Two types of the heat-treatment process were performed. The conventional heat treatment involved the following steps: vacuum austenitizing up to a temperature of 1000 °C or 1075 °C, respectively, and nitrogen gas quenching at a pressure of 5 bar. For the novel heat-treatment process, a sub-zero period at a soaking temperature of –196 °C lasting for 4 h was inserted after quenching and tempering. No tempering was carried out in order to highlight the possible changes in the microstructure of the processed material due to the sub-zero period. A microstructural analysis was performed using a transmission electron microscope TEM JEOL 200CX at an acceleration voltage of 200 kV. Thin foils for the TEM were prepared with an electrolytic jet-polisher (Tenupol) or with an ion slicer. The content of the retained austenite was measured with X-ray diffraction. X-ray patterns were recorded using a Phillips PW 1710 device with Fe-filtered $Co_{\alpha 1,2}$ characteristic radiation. The detector arm was equipped with a monochromator. The data were recorded in the range of 20–144° of the two-theta angle with a 0.05° step and a counting time per step of 5 s.

Table 1: Chemical composition of the investigated steel in mass fractions (*w*/%)
Tabela 1: Kemijska sestava preiskovanega jekla v masni deležih (*w*/%)

Steel	C	Si	Mn	Cr	Mo	V	Fe
Vanadis 6	2.1	1.0	0.4	6.8	1.5	5.4	balance

3 RESULTS AND DISCUSSION

The mechanical properties obtained after different steps of the heat treatment are summarized in **Table 2** [2,6]. Although the hardness is approximately the same after quenching and after quenching and sub-zero processing at both austenitizing temperatures, the hardness of the sub-zero-processed material after tempering is by about 2.5 HRc lower than that of the non-sub-zero-processed steel.

The tempering of the material induced different behaviours of the non-sub-zero- and sub-zero-processed steels. Generally, the non-sub-zero-processed steel had a higher hardness than the sub-zero-processed one. We assume that, firstly, the occurrence of a high number of nano-particles and, secondly, a lower share of the retained austenite are responsible for the deterioration of the secondary hardenability of the material. This seems to be logical because the secondary hardenability can be considered as a comprehensive effect of the tempering of martensite (hardness decrease), transformation of the retained austenite to martensite (hardness increase) and precipitation of carbides (hardness increase). Based on the facts that the sub-zero-processed steel contained a lower share of the retained austenite and an expected large number of nano-precipitates, we anticipated its capability to manifest the secondary-hardening effect to be lower.

Figure 1 shows a bright-field image of the microstructure of the specimen quenched from 1000 °C without DCT and tempering. The matrix of the material apparently has a two-phase structure. The main structural constituent is the twinned martensite, which is typical for high-carbon steels. The second structural feature of the matrix is the retained austenite as shown in the dark-field image of the area, **Figure 2**. The fact that the material after quenching, without DCT, contains a large amount

Table 2: Hardness and bending strength of differently heat-treated specimens[2,6]
Tabela 2: Trdota in upogibna trdnost različno toplotno obdelanih vzorcev[2,6]

Austenitizing temperature	Hardness A HRc	Sub-zero processing	Hardness B HRc	Hardness C HRc	Bending strenght MPa
1000 °C	66.0	no		59.0	3564
1075 °C	66.0	no		63.0	2768
1000 °C	65.0	–196 °C/4 h	66.0	56.5	3272
1075 °C	65.5	–196 °C/4 h	67.0	60.5	3087
Hardness A	hardness after quenching				
Hardness B	hardness after quenching and sub-zero processing				
Hardness C	hardness after complete heat treatment with a double tempering at 530 °C/2 h				

of retained austenite could have been expected. During austenitizing some of the carbides are dissolved and the austenite becomes saturated with carbon and alloying elements. This induces a lowering of both the M_s and M_f temperatures of Cr-V ledeburitic steels, whereas M_f lies well below the freezing point. As a result, the martensitic transformation is not fully completed. The diffraction patterns from both structural constituents are shown in **Figures 3** and **4**.

After quenching from the austenitizing temperature of 1000 °C and DCT at –196°C/4 h, the matrix again has a two-phase structure as seen in **Figures 5** and **6**. This means that even the sub-zero processing does not completely remove the retained austenite from the structure. This could be evidently expected. From the physical-

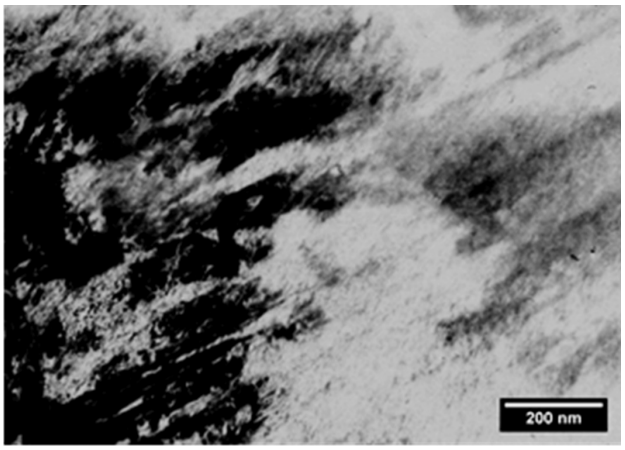

Figure 1: Microstructure of Vanadis 6 after quenching from 1000 °C without DCT and tempering – TEM bright-field image
Slika 1: Mikrostruktura Vanadis 6 po kaljenju iz 1000 °C, brez DTC in popuščanja (TEM – svetlo polje)

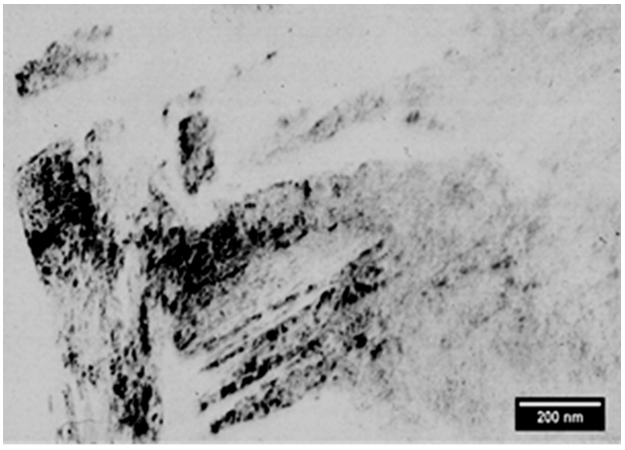

Figure 2: Microstructure of Vanadis 6 after quenching from 1000 °C without DCT and tempering – TEM dark-field image
Slika 2: Mikrostruktura Vanadis 6 po kaljenju iz 1000 °C, brez DCT in popuščanja (TEM – temno polje)

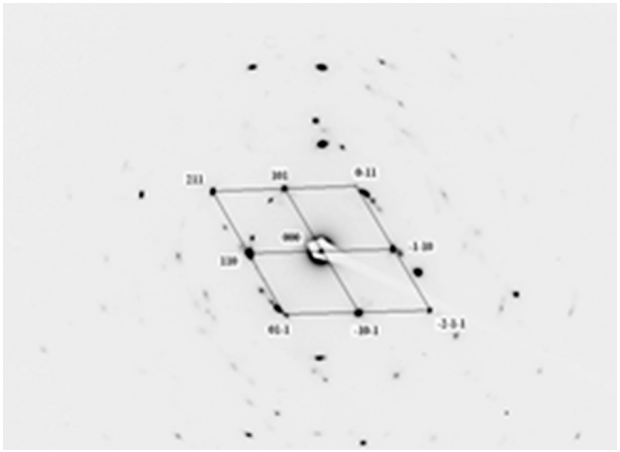

Figure 3: Electron-diffraction patterns from martensite
Slika 3: Uklonska slika martenzita

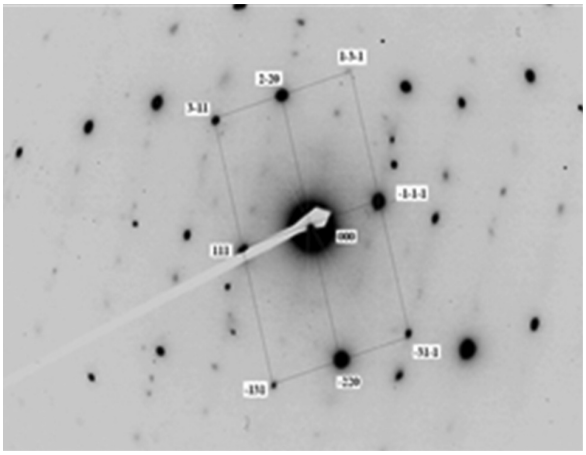

Figure 4: Electron-diffraction patterns from retained austenite
Slika 4: Uklonska slika zaostalega avstenita

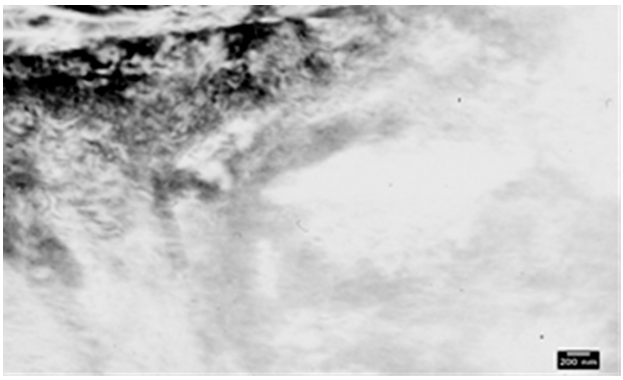

Figure 5: Microstructure of Vanadis 6 after quenching from 1000 °C and DCT without tempering – TEM bright-field image
Slika 5: Mikrostruktura Vanadis 6 po kaljenju iz 1000 °C in DCT, brez popuščanja (TEM – svetlo polje)

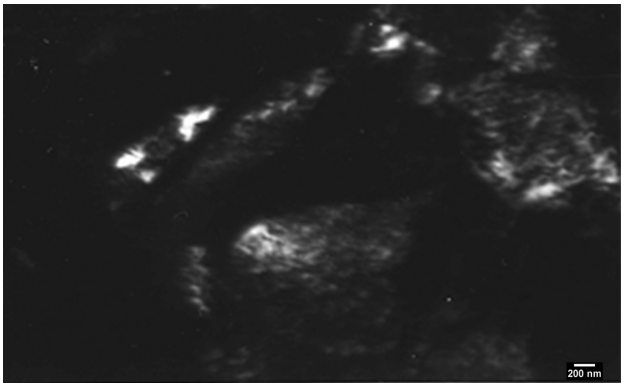

Figure 6: Microstructure of Vanadis 6 after quenching from 1000 °C and DCT without tempering – TEM dark-field image
Slika 6: Mikrostruktura Vanadis 6 po kaljenju iz 1000 °C in DCT, brez popuščanja (TEM – temno polje)

metallurgy viewpoint the martensitic transformation cannot be fully completed and after quenching a certain share of the retained austenite will always remain in the structure. The problem is how to minimize the content of the retained austenite. Transmission microscopy, however, will never precisely quantify the content of the retained austenite.

A quantification of the amount of the retained austenite was performed with an X-ray diffraction analysis, the results are in **Table 3**.

Besides the martensite and the retained austenite, MC (or M_4C_3) and also M_7C_3 carbides were found in the structure. The contents of these carbides were found to be independent of the use (or no use) of DCT in the heat-treatment cycle. This is logical since it is the austenitizing temperature that plays a substantial role in the changes in the volume fraction of these carbides. On the contrary, a large difference was found in the contents of the retained austenite and martensite. The content of the retained austenite was almost three times lower for the DCT material than for the non-DCT material. It is thus evident that DCT really contributes to a marked decrease in the amount of the retained austenite in the structure of the material after the heat treatment with DCT. At the same time, a higher supersaturation of the martensite occurred due to DCT – the degree of tetragonality c/a was found to be much higher for the DCT material.

Besides deformation twins, a dense dislocation network can also be found in the martensite needles. This was well apparent at high magnification in **Figures 7** and **8**. The dislocation network prevents the identification of the potential minority phases, so that, at this stage of the research, the assumed precipitation of carbide nanoparticles during the DCT, often published in literature, could not be confirmed. On the other hand, the presence of such a high number of dislocations is a sign of a high plastic deformation and an apparently high stress in the crystal lattice. Plastic deformation can induce various processes, e.g., self-tempering of martensite accompanied by a formation of carbide nanoparticles.

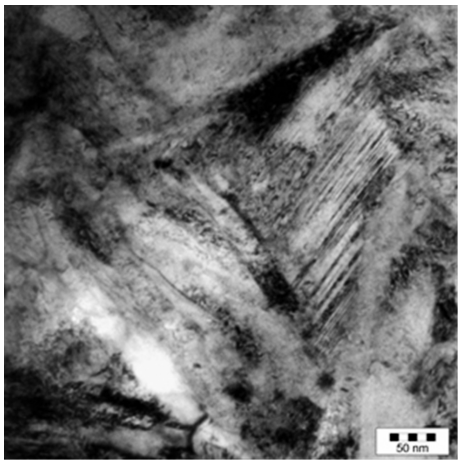

Figure 7: Microstructure of Vanadis 6 after quenching from 1000 °C and DCT without tempering – TEM bright-field image – a detail
Slika 7: Detajl mikrostrukture Vanadis 6 po kaljenju iz 1000 °C in DCT, brez popuščanja (TEM – svetlo polje)

Table 3: Results of an X-ray diffraction of Vanadis 6 after quenching from the temperature of 1075 °C and sub-zero processing at –196 °C/4 h
Tabela 3: Rezultati rentgenske difrakcije Vanadis 6 po kaljenju iz temperature 1075 °C in kriogeni obdelavi pri –196 °C/4 h

Heat treatment	Content of martensite, *w*/%	Content of retained austenite, *w*/%	Lattice parameter of martensite (nm) degree of tetragonality *c/a*	Other phases
Quenching	49.45	17.76	a = 0.28623, c = 0.29154 c/a = 0.101186	MC (M_4C_3) M_7C_3
Quenching + DCT	63.1	6.1	a = 0.28596, c = 0.29234 c/a = 0.10223	MC (M_4C_3) M_7C_3

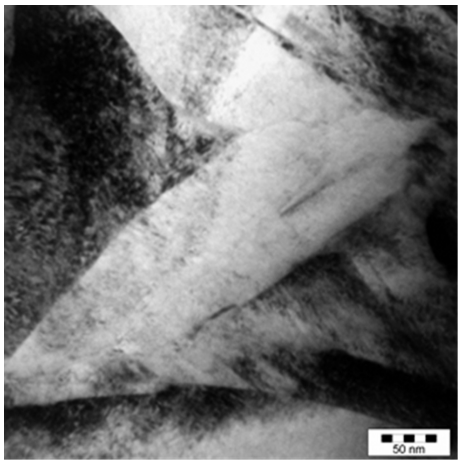

Figure 8: Microstructure of Vanadis 6 after quenching from 1000 °C and DCT without tempering – TEM dark-field image – a detail
Slika 8: Detajl mikrostrukture Vanadis 6 po kaljenju iz 1000 °C in DCT, brez popuščanja (TEM – temno polje)

This could explain the assumed higher stresses in the lattice and the similarly high dislocation density in the martensite obtained with DCT, **Figures 7** and **8**.

It was shown that the magnification of a standard TEM is not sufficient for the identification of the assumed precipitation of carbide nanoparticles. According to this, we tried to investigate the assumed precipitation of carbides, often recorded in literature, with HRTEM, **Figures 9** and **10**.

On the left-hand side of **Figure 9** there is a typical contrast between an amorphous layer and some faint underlying fringes of the crystal planes. To the right the contrast passes to Moire fringes due to the superimposed, twisted crystal lattices. A Moire pattern is also in the bottom right-hand corner of the micrograph. In the central part of the lattice the fringes are not clear, perhaps due to some internal strains. Their clearest contrast is in the top right-hand corner. However, the

Figure 9: Microstructure of Vanadis 6 after quenching from 1000 °C and DCT without tempering – HRTEM
Slika 9: Mikrostruktura Vanadis 6 po kaljenju iz 1000 °C in DCT, brez popuščanja (HRTEM)

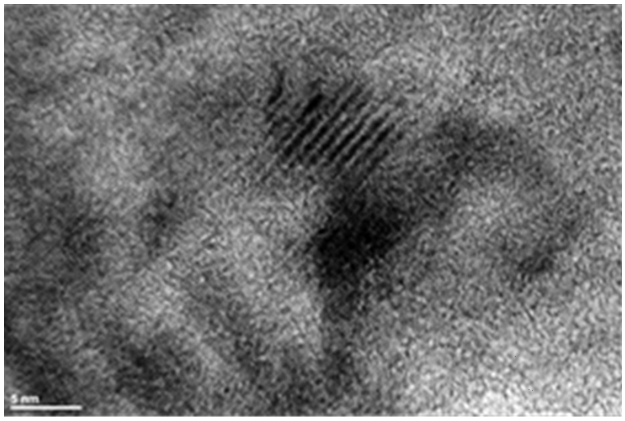

Figure 10: Microstructure of Vanadis 6 after quenching from 1075 °C and DCT without tempering – HRTEM
Slika 10: Mikrostruktura Vanadis 6 po kaljenju iz 1075 °C in DCT, brez popuščanja (HRTEM)

atomic columns are not parallel to the electron beam and so no dots, but only fringes, are visible.

In the central part of **Figure 10** there is a dot contrast between the atomic columns, probably in the 111-Fe projection. The regular pattern in the upper central part could be a nanotwinned region or a Moire pattern caused due to the superimposed, twisted crystal lattices or a faulted nanoparticle. However, the contrast is not clear enough to allow an unambiguous interpretation.

The expected nano-precipitates could not even be confirmed by using HRTEM. Neither did the results of EDS analyses show the differences between the materials after quenching and after quenching and DCT.

In the next investigation we will turn our attention to the assessment of microstructural changes after tempering the sub-zero-processed cold-work tool steel Vanadis 6. Such a research might answer the question as to whether it is possible to identify the nanoparticles in the structure after a complete heat treatment including DCT, often addressed in literature.

4 CONCLUSIONS

- The content of the retained austenite was almost three times lower for the DCT Vanadis 6 than that without DCT.
- At the same time, a higher supersaturation of martensite occurred due to DCT – the degree of tetragonality c/a was found to be much higher for the DCT material.
- Using TEM it was proved that the dislocation network prevents the identification of potential minority phases in the microstructure of the DCT material.
- The expected nano-precipitates in the microstructure of the DCT material could not be confirmed, even by using HRTEM.
- For the next investigation we recommend an assessment of the microstructural changes after tempering the DCT cold-work tool steel Vanadis 6.

Acknowledgements

The authors wish to thank the Ministry of Industry and Trade of the Czech Republic for the financial support given to the Project TIP FR-TI1/003. The paper was created within the research MSM6840770021 "Diagnostic of materials" and project OPPA CZ.2.17/1.1.00/32213 "Qualifications of the academic workers from CTU in Prague in science and research".

5 REFERENCES

[1] P. Bílek, J. Sobotová, P. Jurči, Evaulation of Structural changes in Cr-V Ledeburitic Tool Steels Depending on Temperature Austenitization, Mater. Tehnol., 44 (**2011**) 4, 33–37

[2] P. Jurči et al., Effect of Sub-zero Treatment on Mechanical Properties of Vanadis 6 PM Ledeburitic Tool Steel, in Metal 2010: 19th International Conference on Metalurgy and Materiále, Roznov pod Radhostem

[3] D. Debdulal et al., Influence of sub-zero treatments on fracture toughness of AISI D2 steel, Materials Science and Engineering A, 528 (**2010**), 589–603

[4] A. Oppenkowski, S. Weber, W. Theisen, Evaluation of factors influencing deep cryogenic treatment that affect the properties of tool steels, Journal of Materials Processing Technology, 210 (**2010**), 1949–1955

[5] L. Shaohong et al., Influence of deep cryogenic treatment on microstructure on microstructure and evaluation by internal friction of tool steel, Cryogenics, 50 (**2010**), 754–758

[6] J. Sobotova et al., Structure and properties of sub-zero processed Vanadis P/M ledeburitic tool steel, in Metal 2011: 20th Anniversary International Conference on Metalurgy and Materilas, Brno

UDK 66.095.26:691:539.411
Professional article/Strokovni članek

ISSN 1580-2949
MTAEC9, 47(1)99(2013)

UTILIZATION OF GEOPOLYMERIZATION FOR OBTAINING CONSTRUCTION MATERIALS BASED ON RED MUD

UPORABA GEOPOLIMERIZACIJE ZA PRIDOBIVANJE GRADBENEGA MATERIALA NA OSNOVI RDEČEGA BLATA

Mira Vukčević[1], Danka Urović[1], Milun Krgović[1], Ivana Bošković[1], Mileta Ivanović[1], Radomir Zejak[2]

[1]University of Montenegro, Faculty of Metallurgy and Technology, 81000 Podgorica, Montenegro
[2]University of Montenegro, Faculty of Civil Engineering, Džordža Vašingtona bb, 81000 Podgorica, Montenegro
mirav@ac.me

Prejem rokopisa – received: 2012-05-08; sprejem za objavo – accepted for publication: 2012-08-29

In this study the geopolymerization process for obtaining construction materials based on red mud was used. The aim of this study was to define the most favorable conditions enabling the utilization of the geopolymerization process in the production of construction materials based on red mud as a by-product of alumina production. For this purpose, the physicochemical and mechanical properties of the obtained construction (geopolymers) materials were tested. On the basis of the results the optimal conditions for geopolymerization and the effect of the main synthesis parameters were determined with repect to the satisfactory mechanical and other properties of the obtained materials. The inorganic polymeric materials produced by the geopolymerization of red mud developed satisfactory compressive strength, which leads to the conclusion that these materials may be used in the sector of construction materials.

Keywords: geopolymerization, red mud, compressive strength, metakaolin

V tej študiji je bil uporabljen postopek geopolimerizacije za pridobivanje gradbenega materiala na osnovi rdečega blata. Namen študije je bil opredeliti najugodnejše razmere, ki bi omogočile uporabo geopolimerizacijskega postopka za pridobivanje gradbenega materiala na osnovi rdečega blata, ki je stranski proizvod pri proizvodnji aluminija. Za ta namen so bile preizkušene fizikalno-kemijske in mehanske lastnosti materiala (geopolimera). Na osnovi dobljenih rezultatov so bile določene optimalne razmere za geopolimerizacijo in učinki glavnih parametrov sinteze s stališča zadovoljivih mehanskih in drugih lastnosti. Anorganski polimerni material, izdelan z geopolimerizacijo rdečega blata, je imel zadovoljivo tlačno trdnost, kar omogoča sklep, da bi bil ta material uporaben kot gradbeni material.

Ključne besede: geopolimerizacija, rdeče blato, tlačna trdnost, metakaolin

1 INTRODUCTION

The present work investigates the possibility of using the red mud from the Bayer process for the production of construction elements made with the process of geopolymerization. The geopolymerization process is based on the heterogeneous chemical reaction that occurs between the solid, aluminosilicate-rich materials, and the highly alkaline silicate solution. The basic part of this process is the hardening of geopolymers which is based on the polycondensation reactions of the alkali precursors formed from a dissolution of active silicates and aluminosilicate solid materials in an alkali-hydroxide solution. The polymeric network as a result of the polycondensation process hardens rapidly acting as a gluing component[1]. The geopolymerization is an exothermic reaction that takes place at an atmospheric pressure and a temperature bellow 100 °C leading to a formation of compact, solid materials, typical for their three-dimensional polymer structure. Such materials are called geopolymers[2–4]. The first stage in this reaction is the formation of hydroxyl complexes of silicon and aluminum with the polymer-bond types of Si-O-Si and Si-O-Al, followed by the formation of three-dimensional aluminosilicate networks containing SiO_4 and/or AlO_4 tetrahedral, alternatively linked through a common oxygen ion. The last stage in the process is the wrapping of the insoluble solid particles in the geopolymer[5–10].

The aim of this investigation is to define the optimal combination of the relevant parameters that would enable the use of red mud from the alumina-production process to be the dominant raw material in combination with the activator and the binder for the production of geopolymers. Geopolymerization creates favorable conditions in promoting red mud as the basis for the development of a new class of construction materials, inorganic polymers – geopolymers. The most important expectations regarding the construction materials are good physicochemical and mechanical characteristics, dimensional stability, a good fire resistance and an aggressive-environment resistance. However, the presence of hydroxyl Fe oxides in bauxite (goethite) compromises their use in the conventional construction materials because of their dehydroxylation-hydroxylation activities generating a dimensional instability. Geopolymerization lowers the level of water absorption because of the amorphous or semi-crystal structure,

lowers the micro porosity, enables higher values of the specific mass, compressive strength, etc. The final objective of this investigation was to define the influence of the relevant parameters affecting the geopolymerization. The compressive strength, the apparent density and the microstructure of polymeric materials were investigated to define the optimal conditions for a polymeric-material synthesis.

2 EXPERIMENTAL WORK

2.1 Materials

For the production of construction materials the following raw materials were used:

- red mud obtained as a byproduct of the Bayer process of obtaining alumina (Podgorica Aluminum Factory),
- sodium hydroxide of analytical grade (Merck, anhydrous pellets),
- metakaolin, which initially provides a geopolymeric system with soluble silicon and aluminum that are essential for an aluminosilicate-oligomer formation and the progress of geopolymeriztion,
- sodium-silicate solution (Merck: $m(Na_2O)$: $m(SiO_2)$ = 3.4, $w(Na_2O)$ = 7.5–8.5 %, $w(SiO_2)$ = 25.5–28.5 % and d = 1,347 g cm^{-3}),
- deionized water for the synthesis of the polymeric material.

Red mud originated from the aluminum metallurgical plant in Podgorica, Montenegro, as a by-product of the alumina production known for the presence of hydroxylation Fe oxides, dried to a constant mass at a temperature of 105 °C, and then sifted through a sieve with a hole diameter of φ = 1 mm.

Metakaolin is a dehydroxylation product of the industrial mineral kaolin in the temperature range between 650 °C and 850 °C. The thermal dehydroxylation of kaolin increases its solubility in an alkaline media and it was performed at 750 °C. The basic material was mineral kaolin from the Bijele Poljane site in Montenegro. Metakaolin is a predominantly amorphous material with minor crystalline constitutes.

As an alkaline activator of the process of geopolymerization, a combination of sodium water glass and sodium hydroxide was used. The activator solution was prepared by mixing the previously mentioned components 48 h before the geopolymer production. Different concentrations of NaOH (C_{NaOH} = (3, 7 and 10) mol dm^{-3}) and a concentration of Si in Na-silica (1, 1.5 and 3.5) mol dm^{-3} were used. The levels of substitution of red mud with metakaolin in the solid phase were in mass fractions w = (4, 8 and 15) %.

2.2 Experimental procedure

The process of the sample production was performed as follows:

- mixing the solid and liquid phases (the solid-to-liquid-phase ratio was 2.5 g cm^{-3}) until a fine, thick pulp was obtained,
- mass transfer to a rectangular mould with a cover,
- setting the mould to the shaking mode for 10 min to displace the residual air,
- keeping the samples at the room temperature for 48 h and
- keeping the samples in a dryer at the temperature of 100 °C for 72 h,
- aging the samples for 14 d.

3 RESULTS AND DISCUSSION

The chemical content of red mud is shown in **Table 1**, while the chemical content of metakaolin is shown in **Table 2**. The proportion of SiO_2 in kaolin was 59.87 %, the proportion of Fe_2O_3 was 3.12 %, the proportion of Al_2O_3 was 19.45 % and the rest was water.

Table 1: Chemical content of the red mud from the Podgorica Aluminum Factory in mass fractions
Tabela 1: Kemijska sestava rdečega blata iz Tovarne aluminija Podgorica v masnih deležih

oxide	*w*/%
Fe_2O_3	40.78
Al_2O_3	17.91
SiO_2	11.28
TiO_2	10.20
Na_2O	6.9

Table 2: Chemical content of metakaolin in mass fractions
Tabela 2: Kemijska sestava metakaolina v masnih deležih

oxide	*w*/%
SiO_2	52.26
Al_2O_3	42.83
Fe_2O_3	1.01
CaO	0.02
MgO	0.09
Na_2O	0.02
K_2O	1.56
TiO_2	0.13
ZnO	<0.01

The XRD analysis of red mud (**Figure 1**) shows the presence of hematite Fe_2O_3, gibbsite $Al(OH)_3$, akdalaite $4Al_2O_3 \cdot H_2O$, lapidocrocte FeO(OH) and calcite $CaCO_3$.

The value of the specific mass of red mud was ρ_{CM} = 2.7773 g cm^{-3}, and for metakaolin this value was ρ_{MK} = 2.4738 g cm^{-3}.

The investigation of the chemical composition, mineralogical content and thermal characteristics was performed on several geopolymeric samples obtained under different synthesis conditions (**Table 3**).

According to the X-ray diffraction analysis, the geopolymer samples (specimens under numbers 1 and 8 from **Table 3**) showed that the dominating minerals are

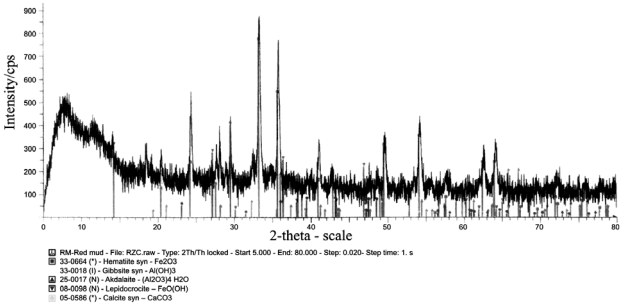

Figure 1: X-ray diffractogram of red mud
Slika 1: Rentgenski difraktogram rdečega blata

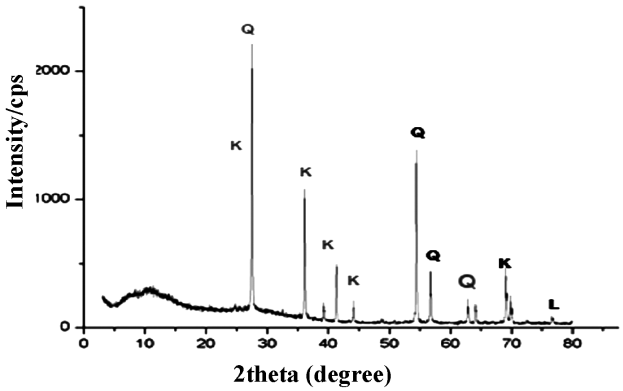

Figure 2: X-ray diffractogram of sample 1
Slika 2: Rentgenski difraktogram vzorca 1

Table 3: Geopolymer samples under different synthesis conditions
Tabela 3: Vzorci geopolimerov iz različnih razmer pri sintezi

Number of sample	C_{NaOH}/ (mol dm^{-3})	C_{Si}/ (mol dm^{-3})	Content of metakaolin (w/%)
1	3	1	2
2	7	1	2
3	10	1	2
4	3	1.5	2
5	7	1.5	2
6	10	1.5	2
7	3	3.5	2
8	7	3.5	2
9	10	3.5	2
10	3	1	8
11	7	1	8
12	10	1	8
13	3	1.5	8
14	7	1.5	8
15	10	1.5	8
16	3	3.5	8
17	3	3.5	8
18	10	3.5	8
19	3	1	15
20	7	1	15
21	10	1	15
22	3	1.5	15
23	7	1.5	15
24	10	1.5	15
25	3	3.5	15
26	7	3.5	15
27	10	3.5	15

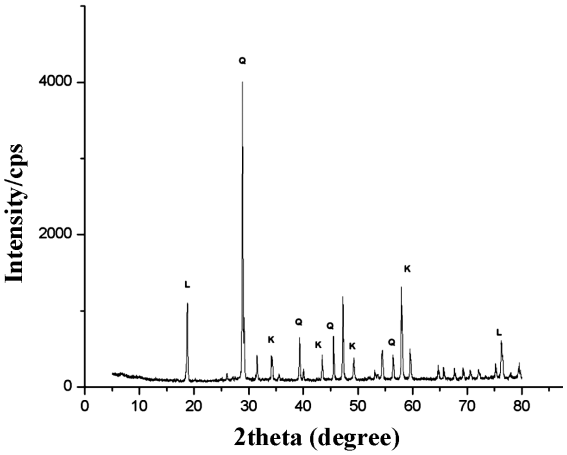

Figure 3: X-ray diffractogram of sample 8
Slika 3: Rentgenski difraktogram vzorca 8

quartz (Q) and kaolinite (K) as shown in **Figures 2** and **3**. The feldspar appears in trace amounts. The X-ray diagrams indicate that the treatment is characterized by dissolution of the starting material and a formation of amorphous and crystalline aluminosilicate phases as well as the stable phases of leucite and kalsilite. The existence of non-dissolved solid particles of red mud is also indicated. The unidentified peaks in XRD diagrams represent the residual unreacted kaolinite or sodium-aluminosilicate phase. The selected diagrams show the existence of an amorphous phase in the system (baseline noise) of the aluminosilicate material. It is also clear that

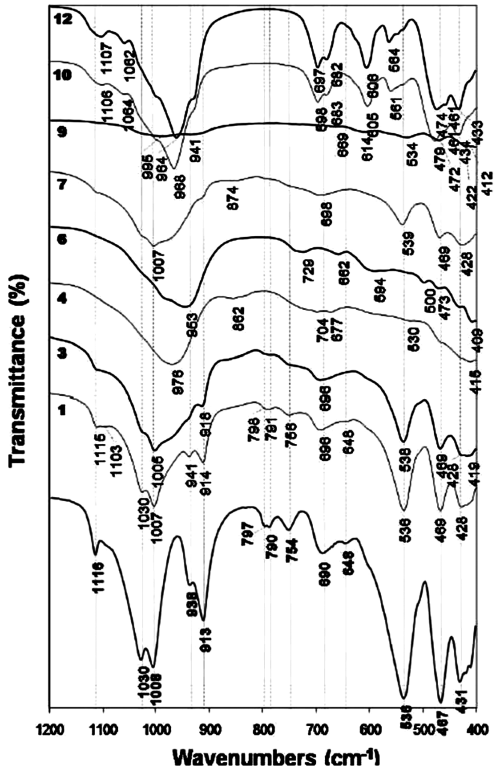

Figure 4: Infrared spectroscopy of geopolymer samples
Slika 4: Infrardeča spektroskopija vzorca geopolimera

increasing concentrations of NaOH as well as an increasing participation of the binder in the solid phase lead to a formation of a more pronounced peak of the new phase, i.e., sodium aluminosilicate.

The FTIR spectroscopy was used to determine the changes in the structure during the treatment of the starting material using the concentrated solution of NaOH and Na-silica (**Figure 4**).

The characteristic wavenumbers for kaolinite are:

OH- at (3700, 3650, 3620) cm^{-1};

Al–OH at 913 cm^{-1};

Si–O at (1032, 1008, 469) cm^{-1};

Si–O–Al at 538 cm^{-1}.

The absence of the Al-O-H bands at 913 cm^{-1} as well as the band duplication at 3700 cm^{-1} and 3620 cm^{-1} are evident. The absence of the bands at 539 cm^{-1} and 913 cm^{-1} and the presence of the new bands at 800 cm^{-1} can be explained with the transformation of the octahedral structure of Al^{3+} into a tetrahedral one under the influence of the agents. The bands at 1100 cm^{-1} and 1200 cm^{-1} are related to the amorphous SiO_2. The characteristic peaks of metakaolin were reduced under the influence of the agents, but they did not disappear after introducing 1 mol dm^{-3} NaOH solution. When using 7 mol dm^{-3} NaOH solution, these peaks almost disappear and create a new band within the wavenumber range of 1200–850 cm^{-1}.

The TG-analysis was performed within the temperature range of 20–1200 °C.

The TGA results (**Figures 5** and **6** refer to the specimens under the numbers 1 and 8 in **Table 3**, respectively) show that the mass loss occurs in two steps. In the first step, at a temperature below 150 °C, the absorbed water is released into the pores and on the surface. In the temperature range of 150–600 °C, the weight loss is associated with the pre-dehydration process, where there is a reorganization of the octahedral lattice. In the second step, the dehydroxylation of the starting material occurs within the temperature range of 350–800 °C.

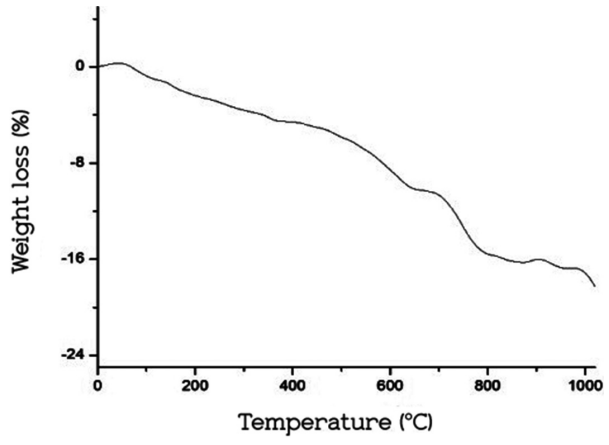

Figure 5: TG analysis of geopolymer, sample 1
Slika 5: TG-analiza geopolimera, vzorec 1

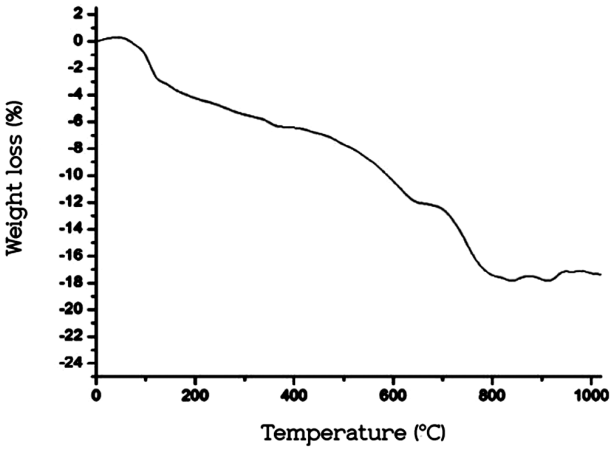

Figure 6: TG analysis of geopolymer, sample 8
Slika 6: TG-analiza geopolimera, vzorec 8

Table 4: Values of the sample density
Tabela 4: Gostota vzorcev

Number of sample	C_{NaOH}/ (mol dm^{-3})	C_{Si}/ (mol dm^{-3})	Content of metakaolin (*w*/%)	Density (g cm^{-3})
1	3	1	2	2.2743
2	7	1	2	2.2760
3	10	1	2	2.2750
4	3	1.5	2	2.2791
5	7	1.5	2	2.2808
6	10	1.5	2	2.2820
7	3	3.5	2	2.2747
8	7	3.5	2	2.2806
9	10	3.5	2	2.2816
10	3	1	8	2.2673
11	7	1	8	2.2705
12	10	1	8	2.2710
13	3	1.5	8	2.2650
14	7	1.5	8	2.2670
15	10	1.5	8	2.2690
16	3	3.5	8	2.2655
17	3	3.5	8	2.2659
18	10	3.5	8	2.2690
19	3	1	15	2.2520
20	7	1	15	2.2530
21	10	1	15	2.2550
22	3	1.5	15	2.2443
23	7	1.5	15	2.2480
24	10	1.5	15	2.2550
25	3	3.5	15	2.2510
26	7	3.5	15	2.2520
27	10	3.5	15	2.2540

The density values of the obtained samples are shown in **Table 4**. The density values for the geopolymer samples are in the range between 2.2443 g cm^{-3} and 2.2816 g cm^{-3}.The highest density values were obtained with the lowest percentage of metakaolin as a binder in the raw mixture. The explanation for this can be found in the fact that the participation of red mud as a very dense component in the raw mixture is the highest in the samples with the lowest percentage of the added binder. The results also show that an important parameter is the

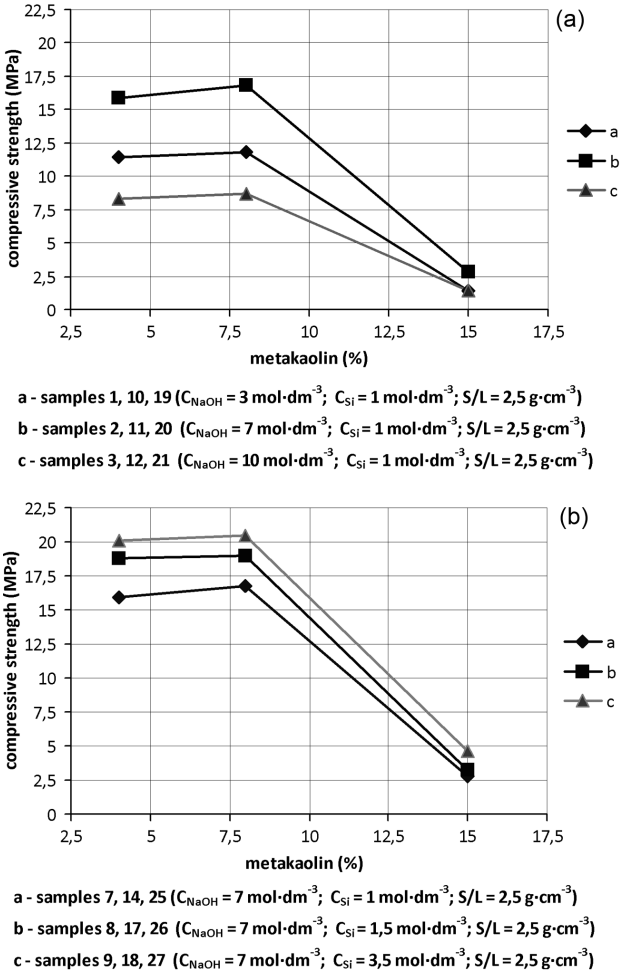

Figure 7: Values of compressive strength of geopolymer samples: a) influence of NaOH concentration on compressive strength as a function of binder percentage; b) influence of Si concentration on compressive strength as a function of binder percentage

Slika 7: Vrednosti tlačne trdnosti vzorcev geopolimera: a) vpliv koncentracije NaOH na tlačno trdnost v odvisnosti od deleža veziva; b) vpliv koncentracije Si na tlačno trdnost v odvisnosti od deleža veziva

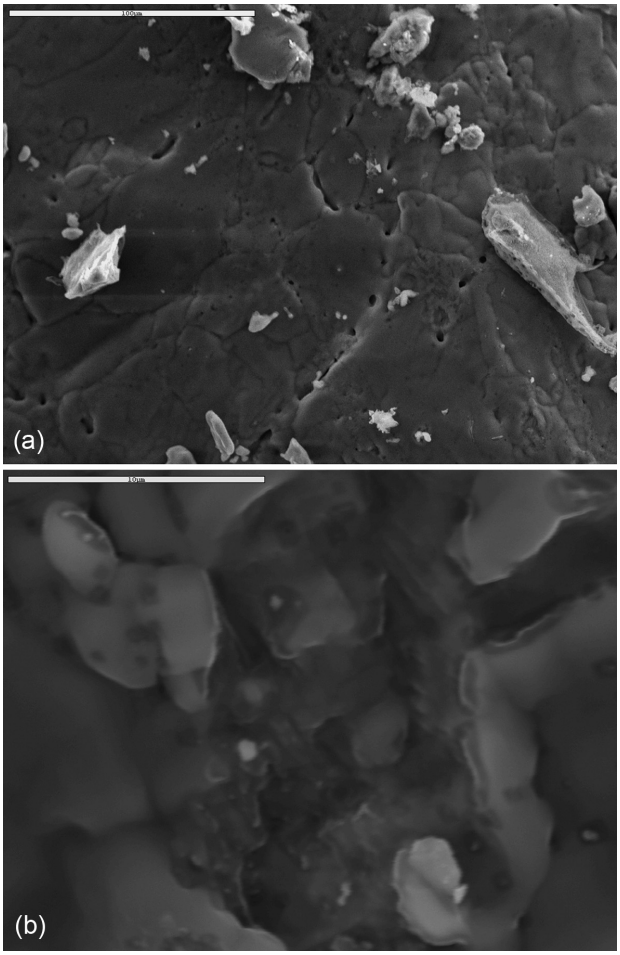

Figure 8: SEM microphotographs of inorganic polymer materials: a) sample (C_{NaOH} = 7 mol dm^{-3}; C_{Si} = 1.5 mol dm^{-3}; *S/L* = 2.5 g cm^{-3}), magnification 500-times; b) sample (C_{NaOH} = 7 mol dm^{-3}; C_{Si} = 1.5 mol dm^{-3}; *S/L* = 2.5 g cm^{-3}), magnification 5000-times

Slika 8: SEM-posnetek anorganskega polimera: a) vzorec (C_{NaOH} = 7 mol dm^{-3}; C_{Si} = 1,5 mol dm^{-3}; *S/L* = 2,5 g cm^{-3}), povečava 500-kratna; b) vzorec (C_{NaOH} = 7 mol dm^{-3}; C_{Si} = 1,5 mol dm^{-3}; *S/L* = 2,5 g cm^{-3}), povečava 5000-kratna

ratio of the components in an alkaline activator, so the combination of a high hydroxide concentration and a low silicate concentration generates lower density values. The explanation can be found in the fact that a high NaOH concentration influences the deficit of the silicon needed for the reaction of geopolymerization.[2,4]

The values of compressive strength of geopolymer in dependence of the concentration of the activator (NaOH -Na-silicate) and the presence of a binder are shown in **Figures 7a** and **b**, respectively.

The factors affecting an increase in compressive strength are different concentrations of alkaline activators. The results show that with the increasing concentrations of NaOH (3, 7, 10) mol dm^{-3} the compressive strength increases up to a NaOH concentration of 7 mol dm^{-3}. Higher NaOH concentrations (10 mol dm^{-3}) cause a reduction in the compressive-strength value. The explanation for this lies in the fact that the initial increase in the NaOH concentration leads to an increase in the silicon and aluminum dissolution from the solid phase[2]. The increased Si and Al contents in the aqueous phase are essential for initiating the oligomer formation and polycondensation. The decrease in the values that occurs under higher NaOH concentrations is the consequence of the fact that dissolved silicon and aluminum remain almost constant while the free NaOH increases, resulting in a lower SiO_2/Na_2O ratio in the aqueous phase. Therefore, the monosilicates and oligomeric species are predominantly in favor of polymer and consequently the polycondensation is slower[2].

Change in the silicon concentration in Na-silicate (1, 1.5, 3.5) mol dm^{-3} causes an increase in the compressive strength of the geopolymer samples. With the increasing concentration of the alkaline activator, the amount of dissolved silicon in the reaction mixture increases as well. Silica originating from sodium silicate has an

important role because it starts the reaction of geopolymerization by allowing a faster and more complete dissolution from the raw material[2]. A higher silicon concentration leads to the formation of silicate species with a complex polymeric structure, thus allowing the three-dimensional polymeric framework to rise. Soluble silica fosters the polycondensation. Under the higher initial silica concentrations, the surface cracks were noticed. This might be because of the entrapped free water of the aqueous phase (the water for the Na-silicate dissolution).

The level of substitution of red mud with metakaolin w = (4, 8 and 15) % causes an increase in the compressive-strength value up to w = 15 %. The lower level of the compressive strength with 15 % of metakaolin, or higher, can be explained with a lack of NaOH for dissolving such a quantity of metakaolin, or with the fact that a high level of polycondensation (because of an excessive amount of metakaolin) can create a surface non-permeable membrane entrapping water from the liquid phase (water for the dissolution of Na-silicate)[4].

The microstructure of the synthesized inorganic polymer material was investigated by scanning electron microscopy and it is shown in **Figure 8**.

SEM microphotographs show that the obtained materials are compact, with no discontinuity, which is confirmed by the mechanical properties. The isolated pores noticed inside the material are in the range of up to 200 μm. The presence of a new amorphous phase can be seen in **Figure 8a**. In **Figure 8b** a gelatinous phase around the particles of the starting material is identified under high magnification.

4 CONCLUSION

This investigation shows that the red mud obtained as a by-product of the Bayer process for obtaining aluminum in the Podgorica Aluminum Factory is, according to its physicochemical and mechanical properties, a good-quality aluminum-silicate material appropriate for geopolymer formation. Under the optimum synthesis conditions (the S/L ratio of 2.5 g cm^{-3}, the NaOH concentration of 7 mol dm^{-3}, the metakaolin percentage of 10 %), the red-mud/metakaolin-based polymeric materials develop satisfactory compressive strength. These mechanical properties were attributed to the formation of the amorphous phase that bonded the non-dissolved particles of the raw solid materials in a good manner. The presence of this phase was also revealed by the XRD, TG and FTIR analyses as well as SEM analysis.

The results of the investigations of the basic properties of the developed geopolymer show that it can be used in civil engineering (as a substitute for brick products and road foundations). Depending on the purpose of a product, an additional research is required (resistance to different external effects, durability in exploitation conditions, etc.) as well as an analysis of the economic feasibility.

Apart from that, the described process of geopolymerization can contribute significantly to environmental preservation, since there is a possibility of conserving large quantities of industrial waste.

5 REFERENCES

[1] J. Davidovits, Geopolymer, green chemistry and sustainable development: The poly (sialate) terminology: a very usefull and simple model for the promotion and understanding of green chemistry, Proceedings of the world congress Geopolymer 2005; Ed.: J. Davidovits, Published by Institut Geopolymer, 2005, 9–17

[2] I. Giannopoulou, D. Dimas, I. Maragkos, D.Panias, Utilization of Metallurgical solid by-products for the development of inorganic polymeric construction materials, Global NEST Journal, 11 (**2009**), 127–136

[3] J. C. Swanepoel, C. A. Strydom, Utilization of fly ash in a geopolymeric material, Applied Geochemistry, 17 (**2002**) 8, 1143–1148

[4] D. Dimas, I. Giannopolu, D. Panias, Utilization of aluminia red mud for synthesys of inorganic polymeric materials, Mineral processing and extractive metallurgy review, 30 (**2009**) 3, 211–239

[5] M. Izquierdo, X. Querol, C. Phillipart, D. Antenucci, World of coal ash (WOAC) Conference, Lexington, KY, USA, 2008

[6] B. V. Rangan, Fly ash-based geopolymer concrete, Research report GC 4, Engineering Faculty, Curtin University of Technology, Perth, Australia, 2008

[7] P. De Silva, K. Sagoe-Crenstil, V. Sirivivatnanon, Kinetics of geopolymerisation: Role of Al_2O_3 and SiO_2, Cement and Concrete Research, 37 (**2007**), 512–518

[8] K. Sagoe-Crenstil, L. Wang, Dissolution processes, hydrolysis and condensation reaction during geopolymer synthesis: Part 2. High Si/Al ratio systems, Journal of Materials Science, 42 (**2007**), 3007–3014

[9] J. S. J. van Deventer, J. L. Provis, P. Duxon, G. C. Lukey, Reaction mechanisms in the geopolymeric conversion of inorganic waste to usefull products, Journal of hazardous materials, A139 (**2007**), 506–513

[10] J. L. Provis, J. S. J. van Deventer, Geopolimerysation kinetics. 2. Reaction kinetic modelling, Chemical Engineering Science, 62 (**2007**), 2318–2329

UDK 621.923:620.179.11:519.233.4
Professional article/Strokovni članek

ISSN 1580-2949
MTAEC9, 47(1)105(2013)

ANALYSIS OF PROCESS PARAMETERS FOR A SURFACE-GRINDING PROCESS BASED ON THE TAGUCHI METHOD

ANALIZA PROCESNIH PARAMETROV POSTOPKA BRUŠENJA POVRŠINE S TAGUCHIJEVO METODO

Mustafa Kemal Külekcı

Mersin University, Tarsus Technical Education Faculty, Department of Mechanical Education, 33140, Tarsus-Mersin, Turkey
mkkulekci@gmail.com

Prejem rokopisa – received: 2012-06-18; sprejem za objavo – accepted for publication: 2012-08-27

In this study, the Taguchi method that is a powerful tool to design optimization for quality is used to find the optimum surface roughness in grinding operations. An orthogonal array, a signal-to-noise (S/N) ratio, and an analysis of variance (ANOVA) are employed to investigate the surface-roughness characteristics of AISI 1040 steel plates using EKR46K grinding wheels. Through this study, not only can the optimum surface roughness for grinding operations be obtained, but the main grinding parameters affecting the performance of grinding operations can also be found. Experimental results are provided to confirm the effectiveness of this approach. The results of this study showed that the depth of cut and the wheel speed have significant effects on the surface roughness, while the rate of feed has a lower effect on it.

Keywords: grinding, surface integrity, surface topography, surface roughness

V tej študiji je bila uporabljena Taguchijeva metoda kot močno orodje za določanje pogojev za doseganje optimalne hrapavosti pri brušenju. Za preiskavo značilnosti hrapavosti površine plošč iz jekla AISI 1040 pri uporabi brusnih kolutov EKR46K so bile uporabljene ortogonalna matrika, signal hrupa (S/N) in analiza variance (ANOVA). S to študijo je bilo mogoče dobiti optimalno hrapavost površine ter glavne parametre brušenja, ki vplivajo na zmogljivost brušenja. Na voljo so eksperimentalni rezultati, ki potrjujejo ta način. Rezultati študije kažejo, da imata globina brušenja in hitrost vrtenja brusnega koluta pomemben učinek na hrapavost površine. Hitrost podajanja pa ima manjši vpliv na hrapavost površine.

Ključne besede: brušenje, površinska integriteta, topografija površine, hrapavost površine

1 INTRODUCTION

Grinding is a manufacturing process with an unsteady process behavior, whose complex characteristics determine the technological output and the quality. An assessment of the grinding-process quality usually includes the micro-geometric quantities of the component. In order to predict the component behavior during the use or to control the grinding process, it is necessary to quantify surface roughness, which is one of the most critical quality constraints for the selection of grinding factors in a process planning. The process set-up often depends on the operator competence[1].

The quality of a surface generated by grinding determines many workpiece characteristics such as the minimum tolerances, the lubrication effectiveness and the component life, among others. A typical surface is characterized by clean cutting paths and plowed material to the sideway of some grooves. However, many other marks can be found, such as cracks produced by the thermal impact, back-transferred material and craters produced by a grain fracture[2,3].

The surface quality produced in surface grinding is influenced by various parameters such as[4,5]: *i.* wheel parameters – abrasives, grain size, grade, structure, binder, shape and dimension; *ii.* workpiece parameters – fracture mode, mechanical properties and chemical composition; *iii.* process parameters – wheel speed, depth of cut, table speed and dressing condition; *iv.* machine parameters – static and dynamic characteristics, spindle system, and table system.

Kwak[4] evaluated the effect of grinding parameters on the geometric error and optimum grinding conditions. Krajinik et al.[1] developed a second-order surface-roughness model using the central composite design technique. Hecker et al.[2] presented a prediction of the arithmetic mean surface roughness based on a probabilistic, undeformed, chip-thickness model for surface roughness in a grinding process. Gupta et al.[6] optimized grinding-process parameters using a numerical method. Tawakoli et al.[7] investigated the effects of a workpiece and grinding parameters on minimum quantity lubrication (MQL) and they compared the results with dry lubrication. Silva et al.[7–9] investigated the effects of grinding parameters on the ABNT 4340 steel using the MQL technique. Shaji et al.[5] analyzed the effects of process parameters and the mode of dressing on the force components and surface using the Taguchi experimental design method. Taguchi is the developer of the Taguchi method. He proposed that an engineering optimization of a process or product should be carried out with a three-step approach: i. system design, ii. parameter design, and iii. tolerance design[10,11].

In this study the wheel speed (V), the rate of feed (F) and the depth of cut (D) were selected as variable parameters. Other process parameters were fixed. The above parameters of grinding were analyzed and optimized with the Taguchi method using the experimentally obtained surface-roughness (Ra) results. Confirmation experiments were conducted at the optimum level to verify the effectiveness of the Taguchi approach.

2 EXPERIMENTAL STUDIES

Commercial AISI 1040 steel plates with the dimensions of 10 mm × 60 mm × 100 mm were used as the workpiece material. The grinding experiments were carried out on a grinding machine as shown in **Figure 1** using EKR46K grinding wheels.

The intense heat generated during the grinding due to a relatively high friction impairs the workpiece quality by inducing thermal damage. Therefore, the cooling and lubrication play a decisive role in grinding. In this study, a cutting fluid was used as a coolant in order to cool the workpiece and, hence, to prevent the thermal damage of the workpiece.

The initial grinding parameters were selected as follows: the wheel speed (V) of 1000 r/min; the feed rate (F) of 25 m/min and the depth of cut (D) of 0.10 mm. A feasible space for the grinding parameters was defined on the basis of the reference[12]. These parameters were further defined as follows: the wheel speed in the range of 1000–2 000 r/min, the feed rate in the range of 20–30 m/min, and the depth of cut in the range of 0.05–0.15 mm. Also, during the grinding operation the workpieces were cooled using cutting fluids. In the grinding parameter design, three levels of grinding parameters were selected as shown in **Table 1**. The surface roughness of grinded workpices was recorded as the R_a value with the ISO class-3-type, surface-roughness tester.

Figure 1: Experimental grinding machine
Slika 1: Eksperimentalni brusilni stroj

Table 1: Grinding parameters and their levels
Tabela 1: Parametri pri brušenju in njihove ravni

Symbol	Grinding parameter	Unit	*Level 1*	*Level 2*	*Level 3*
V	Wheel speed	r/min	1000	1500[a]	2000
F	Rate of feed	m/min	20	25[a]	30
D	Depth of cut	mm	0.05	0.10[a]	0.15

a: initial grinding parameters

3 RESULTS AND DISCUSSION

To select an appropriate orthogonal array for the experiments, the total degrees of freedom need to be computed. The degrees of freedom are defined as the number of comparisons between the design parameters that need to be made to determine which level is better and, specifically, how much better it is. For example, a four-level design parameter counts for three degrees of freedom[11]. The degrees of freedom (V_f) associated with the interaction between two design parameters are given by the product of the degrees of freedom for the two design parameters. In this study, the interaction between the grinding parameters is neglected. Therefore, there are eight degrees of freedom (V_f = 9 –1= 8) owing to there being three grinding parameters (such as the wheel speed, the rate of feed and the depth of cut) of the grinding operations. Once the required degrees of freedom are known, the next step is to select an appropriate orthogonal array to fit the specific task. Basically, the degrees of freedom for the orthogonal array should be greater than, or at least equal to, those for the design parameters. In this study, an L_9 orthogonal array with four columns and nine rows was used. This array has eight degrees of freedom and it can handle three-level design parameters. Each grinding parameter is assigned to a column, having nine grinding-parameter combinations available. Therefore, only nine experiments are required to study the entire parameter space using the L_9 orthogonal array. The experimental layout for the three grinding parameters using the L_9 orthogonal array is shown in **Table 2**. Since the L_9 orthogonal array has four columns, one column of the array is left empty for the error of the experiments; orthogonality is not lost by keeping one column of the array empty[11]. To increase the sensitivity of the results

Table 2: Experimental layout of the L_9 orthogonal array
Tabela 2: Eksperimentalna postavitev ortogonalne matrike L_9

Experiment number	Grinding parameter level		
	V/(r/min) Wheel speed	*F*/(m/min) Rate of feed	*D*/mm Depth of cut
1	1	1	1
2	1	2	2
3	1	3	3
4	2	1	2
5	2	2	3
6	2	3	1
7	3	1	3
8	3	2	1
9	3	3	2

each experiment in the L_9 orthogonal array was repeated three times.

Experimental results were transformed into a signal-to-noise (S/N) ratio. There are three categories of quality characteristics, i.e., the-lower-the-better, the higher-the-better, and the-nominal-the-better. In the present study the-lower-the-better quality characteristic was selected for the surface roughness. The loss function of the-lower-the-better quality characteristics can be expressed as[13]:

$$L_j = \frac{1}{n}\sum_{k=1}^{n} y_i^2 \quad (1)$$

$$\eta_j = -10 \lg L_j \quad (2)$$

where n is the number of tests, y_i is the experimental value of the i^{th} quality characteristic, L_j is the overall loss function and η_j is the S/N ratio. **Table 3** shows the average experimental results for the surface roughness and the corresponding S/N ratio using equations (1) and (2).

Table 3: Experimental results for the surface roughness and S/N ratio
Tabela 3: Eksperimentalno izmerjena hrapavost površine in razmerje S/N

Experiment number	Process parameters			R_a (μm)	S/N ratio (dB)
	V (r/min)	F (m/min)	D (mm)		
1	1000	20	0.05	0.22	13.15
2	1000	25	0.10	0.32	9.90
3	1000	30	0.15	0.56	5.04
4	1500	20	0.10	0.28	11.06
5	1500	25	0.15	0.30	10.46
6	1500	30	0.05	0.20	13.98
7	2000	20	0.15	0.48	6.38
8	2000	25	0.05	0.38	8.40
9	2000	30	0.10	0.40	7.96

Since the experimental design is orthogonal, it is then possible to separate out the effect of each grinding parameter at different levels[11,13]. The mean S/N ratio for each level of the grinding parameters is summarized in an S/N response table for the surface roughness. In addition, the total mean S/N ratio for the nine experiments is also calculated and listed in **Table 4**.

As shown in equations (1) and (2), from the view point of the-lower-the-better quality characteristic, a greater S/N ratio corresponds to a smaller variance of the output characteristic around the desired value. As indicated in **Figure 2**, the optimum parameters for the

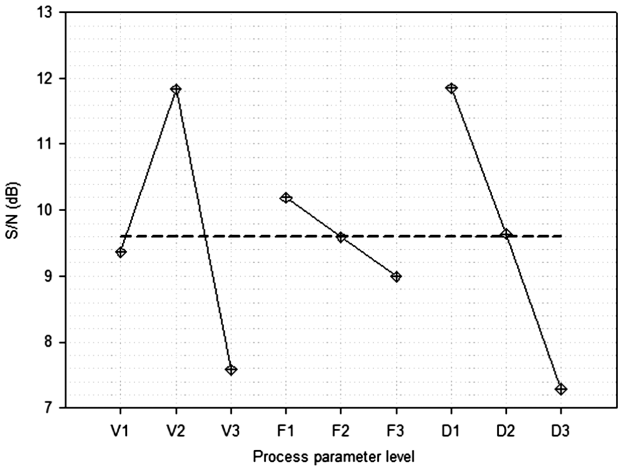

Figure 2: S/N graph for the surface roughness
Slika 2: S/N-graf za hrapavost površine

grinding of the AISI 1040 steel become the wheel speed at level 2, the feed rate at level 1 and the depth of cut at level 1 and therefore the combination of parameters is $V_2F_1D_1$.

The purpose of the analysis of variance (ANOVA) is to investigate which design parameters significantly affect the quality characteristic. This is accomplished by separating the total variability of the S/N ratios, which is measured with the sum of the squared deviations from the total mean S/N ratio, into contributions by each design parameter and the error. First, the total sum of squared deviations SS_{Total} from the total mean S/N ratio η_m can be calculated as[11,13]:

$$SS_{Total} = \sum_{i=1}^{n} (\eta_i - \eta_m)^2 \quad (3)$$

where η_i is the mean S/N ratio for the i^{th} experiment. Statistically, there is a tool called an F test named after Fisher[14] enabling us to see which design parameters have a significant effect on the quality characteristic. Normally, the change of the grinding parameter has a significant effect on the surface roughness when the F value is large. In performing the F test, the mean of squared deviations for each design parameter needs to be calculated. The mean of squared deviations is equal to the sum of squared deviations divided by the number of degrees of freedom associated with the design parameter. Then the F value for each design parameter is simply the ratio of the mean of squared deviations to

Table 4: S/N response table for grinding parameters
Tabela 4: Tabela odzivov S/N za različne parametre brušenja

Symbol	Grinding parameters	Mean S/N ratio (dB)			Total mean S/N (dB)	Maximum-Minimum
		Level 1	*Level 2*	*Level 3*		
V/(r/min)	Wheel speed	9.36	11.83	7.58	9.60	4.25
F/(m/min)	Rate of feed	10.19	9.59	8.99		1.20
D/mm	Depth of cut	11.85	9.64	7.29		4.56

Table 5: Results of ANOVA for the grinding parameters
Tabel 5: Rezultati za parametre brušenja ANOVA

Symbol	Grinding parameters	Degree of freedom	Sum of square	Mean square	*F*	Contribution (%)
V	Wheel speed	2	0.040	0.020	2.48	40
F	Rate of feed	2	0.009	0.003	0.40	9
D	Depth of cut	2	0.050	0.025	3.09	50
Error		2	0.001	0.003		1
Total		8	0.1			100

Table 6: Results of the confirmation experiment
Tabela 6: Rezultati potrditvenih preizkusov

	Initial grinding parameters	Optimum grinding parameters		Improvement of the S/N ratio (dB)
		Prediction	*Experiment*	
Level	$V_1F_1D_1$	$V_2F_1D_1$	$V_2F_1D_1$	0.68
R_a/μm	0.22	0.19	0.20	
S/N (dB)	13.15	14.69	13.83	

the mean of the squared error. **Table 5** shows the results of ANOVA for the grinding parameters.

It can be found that the depth of cut and the wheel speed have significant effects on the surface roughness. Increasing wheel speed and depth of cut increase the surface roughness. However, the change in the rate of feed has a lower effect on the surface roughness. In the present study, the contribution order of the studied grinding parameters for the surface roughness of the AISI 1040 steel is found to be as follows: the depth of cut (50 %), the wheel speed (40 %) and the rate of feed (9 %).

Once the optimum level of design parameters has been selected, the final step is to predict and verify the improvement of the quality characteristic using the optimum level of design parameters. The estimated S/N ratio $\hat{\eta}$ using the optimum level of design parameters can be calculated as:

$$\hat{\eta} = \eta_m + \sum_{i=1}^{j} (\eta_i^- - \eta_m)^2 \quad (4)$$

where η_m is the total mean S/N ratio, η_i^- is the mean S/N ratio at the optimum level, and *j* is the number of the main design parameters that affect the quality characteristic. The estimated S/N ratio using the optimum grinding parameters for surface roughness can then be obtained and the corresponding surface roughness can also be calculated by using equations (1) and (2). **Table 6** shows a comparison of the predicted surface roughness with the actual surface roughness using the optimum grinding parameters. A close agreement between the predicted and actual surface roughness is observed.

The increase in the S/N ratios from the initial surface roughness to the optimum surface roughness is calculated as 0.68 dB.

The values given in **Table 6** were calculated with the Taghuchi method and experimentally verified.

4 CONCLUSIONS

In this study, an application and adaptation of the Taguchi optimization and quality-control method were established for the optimization of the surface roughness in a grinding process. The Taguchi method provides a systematic and efficient methodology with fewer experiments and trials. The experimental results obtained in this study showed that the depth of cut and the wheel speed have significant effects on the surface roughness. The rate of feed has a lower effect on the surface roughness. The contribution order of the grinding parameters including the depth of cut, the wheel speed and the rate of feed is 50 %, 40 % and 10 %, respectively. A change made to all the grinding parameters significantly changes the surface roughness. The optimum grinding-parameter combination for the AISI 1040 steel includes the wheel speed (*V*) of 1 500 r/min and the depth of cut (*D*) of 0.05mm.

5 REFERENCES

[1] P. Krajnik, J. Kopac, A. Sluga, Design of grinding factors based on response surface methodology, Journal of Materials Processing Technology, 162 (**2005**), 629–636

[2] L. R. Hecker, Y. L. Steven, Predictive modeling of surface roughness in grinding, International Journal of Machine Tools & Manufacture, 43 (**2003**), 755–761

[3] C. P. Bhateja, Grinding: theory, techniques and troubleshooting, Society of Manufacturing Engineers Society of Manufacturing Engineers (SME), Dearborn, 1982

[4] J. Kwak, Application of Taguchi and response surface methodologies for geometric error in surface grinding process, International Journal of Machine Tools & Manufacture, 45 (**2005**), 327–334

[5] S. Shaji, V. Radhakrishnan, Analysis of process parameters in surface grinding with graphite as lubricant based on the Taguchi method, Journal of Materials Processing Technology 141 (**2003**) 1, 51–59

[6] R. Gupta, K. S. Shishodia, G. S. Sekhon, Optimization of grinding process parameters using enumeration method, Journal of Materials Processing Technology, 112 (**2001**), 63–67

[7] T. Tawakoli, M. J. Hadad, M. H. Sadeghi, A. Daneshi, S. Stockert, A. Rasifard, An experimental investigation of the effects of workpiece and grinding parameters on minimum quantity lubrication-MQL grinding, International Journal of Machine Tools & Manufacture, 49 (**2009**), 924–932

[8] L. R. Silva, E. C. Bianchi, R. E. Catai, R. Y. Fusse, T. V. França, P. R. Aguiar, Study on the behavior of the minimum quantity lubricant-MQL technique under different lubrication and cooling conditions when grinding ABNT 4340 steel, J. Braz. Soc. Mech. Sci. Eng., 27 (**2005**) 2, 192–199

[9] L. R. Silva, E. C. Bianchi, R. Y. Fusse, R. E. Catai, T. V. França, P. R. Aguiar, Analysis of surface integrity for minimum quantity lubricant-MQL in grinding, Int. J. Mach. Tools Manuf., 47 (**2007**) 2, 412–418

[10] G. Taguchi, Introduction to Quality Engineering, Asian Productivity Organization, Tokyo 1990

[11] W. H. Yang, Y. S. Tarng, Design Optimization of cutting parameters for turning operations based on the Taguchi method, Journal of Materials Processing Technology, 84 (**1998**), 122–129

[12] M. P. Groover, Fundamentals of Modern Manufacturing, John Wiley & Sons, Inc., Danvers 2010

[13] D. C. Montgomery, Design and Analysis of Experiments, Wiley, Singapore 1991

[14] R. A. Fisher, Statistical Methods for Research Workers, Oliver and Boyd, London 1925

UDK 621.762:621.762.5:621.785.797
Professional article/Strokovni članek

ISSN 1580-2949
MTAEC9, 47(1)111(2013)

CHARACTERIZATION OF AN Cu-Cr-Zr ALLOY SYNTHESIZED WITH THE POWDER-METALLURGY TECHNIQUE

KARAKTERIZACIJA ZLITINE Cu-Cr-Zr, SINTETIZIRANE S TEHNIKO PRAŠNE METALURGIJE

Mediha Ipek

Sakarya University, Engineering Faculty, Department of Metallurgy and Materials Engineering, Esentepe Campus, 54187 Sakarya-Turkey
mipek@sakarya.edu.tr

Prejem rokopisa – received: 2012-08-16; sprejem za objavo – accepted for publication: 2012-09-14

A Cu-1.5 % Cr-0.5 % Zr alloy was prepared with the powder-metallurgy (PM) method. Cu-Cr-Zr powders were pressed under 390 MPa of uniaxial compression and sintered at 1000 °C for 2 h. After the holding time, the samples were immediately taken out of the furnace and pressed at 850 MPa. The sintered samples were solution-treated at 1000 °C for 15 min and water quenched. Then they were deformed by 20 % at room temperature and aged at 470 °C for (2, 4, 6 and 8) h. A SEM investigation revealed that the Cr and Zr particles having a limited solubility in Cu distributed homogeneously in the copper matrix. An XRD analysis showed that each sample (sintered and aged at 470 °C for different times) has the same phases: copper and trace Cr_2O_3. The relative density of the sinter-pressed sample increased from 92 % to 96 % due to cold deformation. The microhardness of the samples ranged from 77 HV for the solution-treated and water-quenched sample to 116 HV for the aged sample, and the electrical conductivity of the samples increased from 76 % IACS for the sinter-pressed sample to 87 % IACS for the sample aged for 8 h.

Keywords: Cu-Cr-Zr, powder metallurgy, age hardenable, electrical conductivity, hardness

Zlitina Cu- 1,5 % Cr- 0,5 % Zr je bila izdelana po metodi prašne metalurgije (PM). Prahovi Cu-Cr-Zr so bili enoosno stisnjeni s 390 MPa in 2 h sintrani na temperaturi 1000 °C. Potem so bili vzorci vzeti iz peči in stisnjeni z 850 MPa. Sintrani vzorci so bili raztopno žarjeni 15 min na temperaturi 1000 °C in ohlajeni v vodi. Nato so bili deformirani za 20 % pri sobni temperaturi in starani (2, 4, 6 in 8) h na temperaturi 470 °C. Preiskava s SEM je odkrila, da imajo delci Cr in Zr omejeno topnost v Cu in da so enakomerno razporejeni v osnovi iz bakra. Rentgenska analiza (XRD) je pokazala, da ima vsak vzorec (sintran in različno dolgo staran na 470 °C) enake faze: baker in sledove Cr_2O_3. Relativna gostota sintranega in stisnjenega vzorca je s hladno deformacijo narasla iz 92 % na 96 %. Mikrotrdota vzorcev je bila v območju od 77 HV za raztopno žarjen in v vodi ohlajen vzorec ter do 116 HV za staran vzorec. Električna prevodnost sintranega in stisnjenega vzorca je bila 76 % IACS in je narasla na 87 % IACS pri vzorcu, staranem 8 h.

Ključne besede: Cu-Cr-Zr, prašna metalurgija, utrjevanje s staranjem, električna prevodnost, trdota

1 INTRODUCTION

Age hardenable Cu-Cr-Zr alloys are widely used for many applications such as trolley wires, electrodes for resistance welding and lead-frame materials due to their high strength, high electrical and thermal conductivities[1–3]. Thermal aging is used to obtain high strength and, simultaneously, high electrical conductivity of the Cu–Cr–Zr alloys. The high electrical conductivity of an alloy is due to a very low solubility of Cr and Zr in the Cu matrix, whereas the excellent strength is attributed to the combined effect of precipitation hardening, work hardening, texture strengthening and alloy strengthening[1,3–6]. In order to control the microstructure and improve the properties of a Cu–Cr–Zr alloy, it is of great importance to optimize the aging process and identify the composition of the precipitates. There has been no unanimous agreement on the precipitation phase of the alloy[1,7]. In general, the manufacturing processing of Cu-Cr-Zr alloys includes casting, hot rolling, solution treatment, water quenching, cold deformation and aging steps[1,2]. In the present study, we characterized the age-hardenable Cu-Cr-Zr alloys produced in the open atmosphere with the powder-metallurgy technique. There is little information about this method in the available literature.

2 EXPERIMENTAL DETAILS

In this study, an Cu-1.5 % Cr-0.5 % Zr alloy was prepared with the powder-metallurgy (PM) method. For this purpose, the Cu-Cr-Zr powders obtained from Alpha Aesar with the average grain sizes of (10, <10, 2–3) μm, respectively, were mixed mechanically for 2 h, pressed under 390 MPa of uniaxial compression and sintered at 1000 °C for 2 h in an open-atmospheric, electric-resistance furnace. After the holding time, the samples were immediately taken out of the furnace and pressed at 850 MPa. The sinter-pressed samples were solution-treated at 1000 °C for 15 min and water-quenched. Then they were mechanically deformed by 20 % at room temperature and aged at 470 °C for (2, 4, 6 and 8) h. A phase analysis of the sinter-pressed, solution-treated, water-quenched and aged samples was performed with the XRD-analysis

technique using the Cu Kα radiation with a wave length of 15.418 nm over a 2θ range of 10° ≤20° ≤90°. The microstructures of the products were examined by means of scanning electron microscopy, energy dispersive spectroscopy (SEM-EDS). Relative densities of the sintered samples were determined with the Archimedes' method. The microhardness of the polished specimens was measured with a load of 50 g.

3 RESULTS AND DISCUSSION

Figure 1 shows the SEM micrographs of a sinter-pressed sample and a sintered, solution-treated, water-quenched sample aged for 8 h. The microstructures in **Figure 1** generally include homogenously distributed dark-grey particles in the light-grey matrix. The light-grey areas show the copper matrix, while the dark-grey particles mainly include chromium and small amounts of copper and zirconium (**Figure 2a**, Mark 4 and **Figure 2b**, Marks 3, 4, 10). In addition, the lighter-grey particles in the copper matrix are rich in zirconium which was confirmed by EDS analyses. As in the chromium-rich regions, the zirconium-rich regions include small

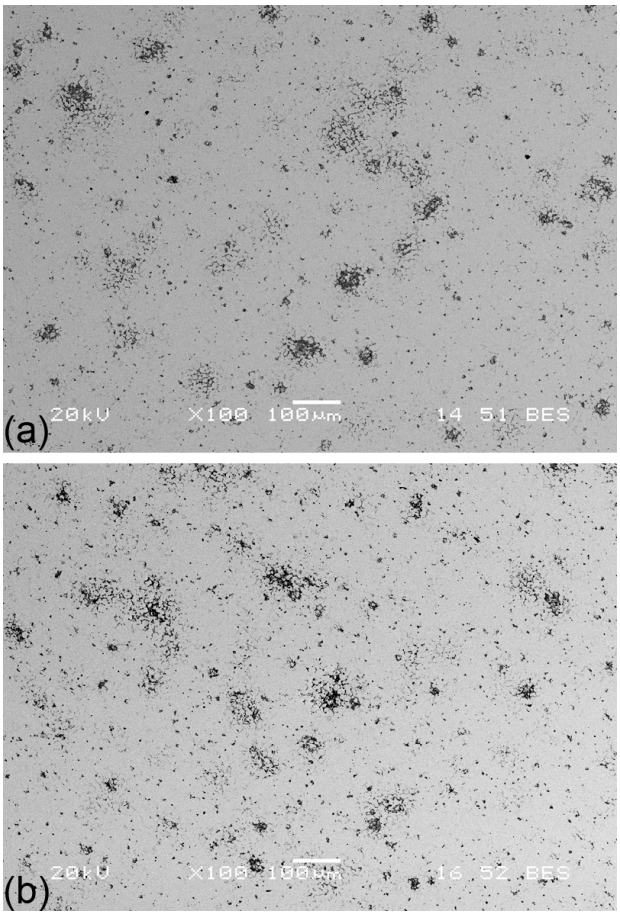

Figure 1: SEM micrographs of the samples: a) sinter-pressed, b) sintered, solution-treated, quenched and aged for 8 h

Slika 1: SEM-posnetka vzorcev: a) sintrano-stisnjeno, b) sintrano in raztopno žarjeno, hitro ohlajeno, starano 8 h

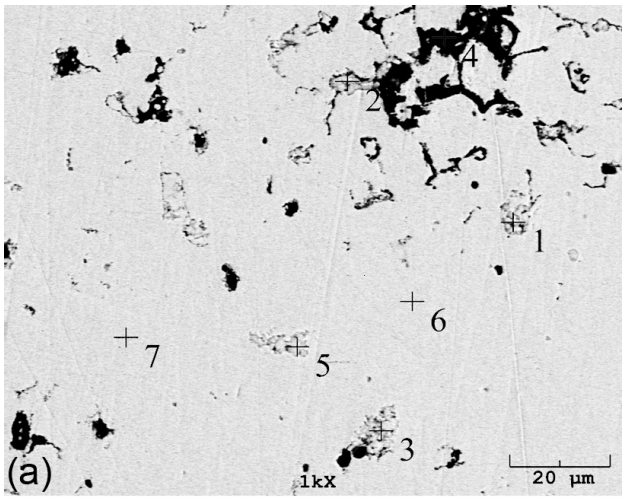

Mark	Mass fractions, *w*/%			
	O	Cr	Cu	Zr
1	10.1	0.4	56.1	33.4
2	17.0	4.4	31.0	46.6
3	18.8	0.1	11.9	69.2
4	28.5	65.2	5.8	0.5
5	13.4	0.3	45.7	40.6
6			100.0	
7			100.0	

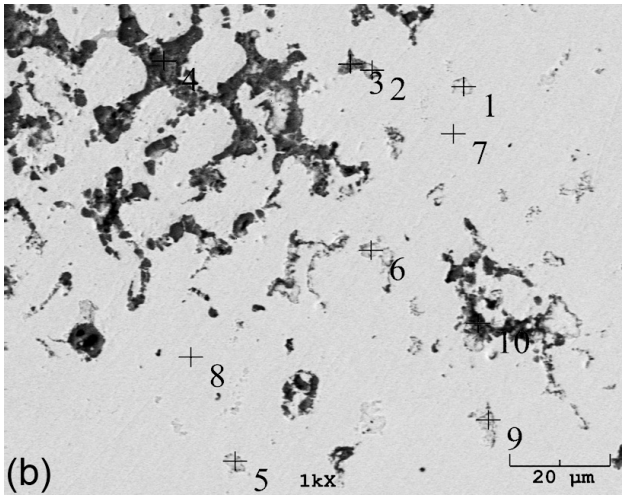

Mark	Mass fractions, *w*/%			
	O	Cr	Cu	Zr
1	2.6	1.3	95.4	0.7
2	29.6	8.6	8.3	53.5
3	27.1	35.3	37.4	0.2
4	39.5	49.2	11.0	0.3
5	16.3	4.2	20.6	58.9
6	19.5	0.7	11,0	68.8
7	0.0	0.2	99.6	0.2
8	0.6	0.2	99.0	0.2
9	10.9	9.8	78.7	0.6
10	37.4	52.4	10,0	0.2

Figure 2: SEM micrographs and EDS point analyses of the samples: a) sinter-pressed, b) sintered, solution-treated and quenched

Slika 2: SEM-posnetka in EDS točkaste analize vzorcev: a) sintrano-stisnjeno, b) sintrano-raztopno žarjeno-hitro ohlajeno

Table 1: Variation of the relative density, hardness and electrical conductivity of the test materials as a function of process
Tabela 1: Spreminjanje relativne gostote, trdote in električne prevodnosti preizkušanih materialov v odvisnosti od postopka

Sample	Process		Relative density, %	Hardness, HV	Electrical conductivity, % IACS
Cu-Cr-Zr	Sintered and hot-pressed		91.9	123	76
	Solution-treated and water-quenched		92.2	77	77
	Cold pressed and aged (470 °C)	Time, *t*/h			
		2	94.5	86	85
		4	95.5	96	85
		6	95.3	98	86
		8	96.2	116	87

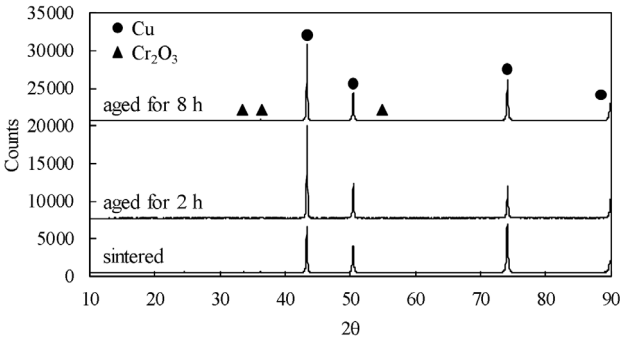

Figure 3: XRD patterns of the sinter-pressed sample and the sintered, solution-treated, quenched and aged samples
Slika 3: Rentgenski posnetek vzorcev sintrano-stisnjeno in sintrano-raztopno žarjeno-hitro ohlajeno-starano

amounts of copper and chromium (**Figure 2a**, Marks 1, 2, 5 and **Figure 2b**, Marks 2, 5, 6). In addition, oxygen was detected in the chromium- and zirconium-rich regions. SEM-EDS analyses revealed that the solution heat treatment increases the solubility of Cr and Zr in the copper matrix, but this solubility is still low. XRD patterns of the sinter-pressed samples and the sintered, solution-treated, water-quenched, 20 % cold-pressed and aged samples are similar to each other and have predominantly copper and trace Cr_2O_3 phases (**Figure 3**). In the present study, EDS analyses also revealed that chromium oxidized and this shows that the heat treatments of this alloys must be done in a controlled atmospheric medium. Relative density, hardness and electrical conductivity of the samples are given in **Table 1** as a function of process steps. While the relative densities of the sinter-pressed and sintered, solution-treated samples are approximately 92 %, the cold-deformed and aged samples have relative densities of over 94 %. It is obvious that cold deformation increases relative densities. The hardness values were determined by taking the average of the five different measurements made on each sample.

The hardness values for the sinter-pressed samples and the solution-treated, water-quenched samples are 123 HV and 77 HV, respectively. It was found that the hardness of a sample decreased after the processes of solution treatment and water quenching. The plastic deformation after the sintering may have caused the deformation hardening and the hardness therefore increased. After the aging the hardness value amounted to 116 HV for the sample aged for 8 h. A large number of dislocations and vacancies, introduced into the alloy by cold deformation, provide the nucleation sites for the formation of the Cr- and Zr-rich clusters and Guinier-Preston zones during the aging treatment, resulting in the acceleration of the precipitation process of the solute atoms[8]. These hardness values are lower than those from the other reports on the Cu-Cr-Zr alloys, which have 150–200 HV deformed by approximately 70 %.[6,9] Electrical-conductivity values for casting and hot rolling the Cu-Cr-Zr alloys given in the literature are 70–80 % IACS[10,11] and in the present study, an electrical conductivity of 87 % IACS was obtained for the sample aged for 8 h. A remarkable improvement in the mechanical and electrical properties of the Cu–Cr–Zr alloy during the aging treatment is due to the precipitation which hardens the copper matrix with the high density of the nano-scale particles and, simultaneously, depletes the solute concentration in the copper matrix. In addition, cold-deformation characteristics, such as dislocations and vacancies, provide nucleation sites for the precipitation[8].

4 CONCLUSION

The following results can be drawn from the present study: cold deformation enhances the relative density of the sinter-pressed samples; cold deformation and aging increase the hardness and electrical conductivity from 77 HV to 116 HV, and from 76 % IACS to 87 % IACS, respectively.

5 REFERENCES

[1] H. Li, S. Xie, X. Mi, P. Wu, J. Materials Science Technology, 23 (**2007**) 6, 795–800
[2] H. Fuxiang, M. Jusheng, N. Honglong, Geng Zhiting, L. Chao, G. Shumei, Y. Xuetao, W. Tao, L. Hong, L. Huafen, Scripta Materialia, 48 (**2003**), 97–102
[3] M. Hatakeyama, T. Toyama, Y. Nagai, M. Hasegawa, M. Eldrup, B. N. Singh, Materials Transactions, 49 (**2008**) 3, 518–521
[4] C. A. Poblano-Salasa, J. D. O. Barceinas-Sanchez, J. Alloys and Compounds, 485 (**2009**), 340–345

[5] J. Su, P. Liu, H. Li, F. Ren, Q. Dong, Materials Letters, 61 (**2007**), 4963–4966
[6] J. P. Tu, W. X. Qi, Y. Z. Yang, F. Liu, J. T. Zhang, G. Y. Gan, N. Y. Wang, X. B. Zhang, M. S. Liu, Wear, 249 (**2002**), 1021–1027
[7] J. Su, Q. Dong, P. Liu, H. Li, B. Kang, Materials Science and Engineering A, 392 (**2005**), 422–426
[8] C. Xia, Y. Jia, W. Zhang, K. Zhang, Q. Dong, G. Xu, M. Wang, Materials and Design, 39 (**2012**), 404–409
[9] Z. Wang, Y. Zhong, X. Rao, C. Wang, J. Wang, Z. Zhang, W. Ren, Z. Ren, Transactions of Nonferrous Metals Society of China, 22 (**2012**), 1106–1111
[10] Z. Wang, Y. Zhong, Z. Lei, W. Ren, Z. Ren, K. Deng, J. Alloys and Compounds, 471 (**2009**), 172–175
[11] http://www.albaksan.com/fr_CuCrZr.htm

UDK 621.9.02:628:477.6
Professional article/Strokovni članek

ISSN 1580-2949
MTAEC9, 47(1)115(2013)

CUTTING-TOOL RECYCLING PROCESS WITH THE ZINC-MELT METHOD FOR OBTAINING THERMAL-SPRAY FEEDSTOCK POWDER (WC-Co)

POSTOPEK RECIKLIRANJA ORODIJ ZA REZANJE Z METODO TALJENJA V Zn ZA PRIDOBIVANJE PRAHU WC-Co ZA TERMIČNO NABRIZGAVANJE

Ekrem Altuncu[1], Fatih Ustel[2], Ahmet Turk[3], Savas Ozturk[4], Garip Erdogan[2]

[1]Sakarya University, Tech. Fac., Dept. Metallurgical and Materials Eng. Sakarya, Turkey
[2]Sakarya University, Eng. Fac., Dept. Metallurgical and Materials Eng. Sakarya, Turkey
[3]Celalbayar University, Eng Fac., Dept. Metallurgical and Materials Eng. Manisa, Turkey
[4]İzmir K. Çelebi University, Eng Fac., Dept. Metallurgical and Materials Eng. İzmir, Turkey
altuncu@kocaeli.edu.tr

Prejem rokopisa – received: 2012-08-16; sprejem za objavo – accepted for publication: 2012-09-19

Various recycling processes for WC-Co cermets from cutting tools, such as chemical modification, thermal modification, the cold-stream method and the electrochemical method have been investigated and some of them are actually employed in industry. However, these conventional methods have many problems to be solved and they are not always established technologies. Therefore, a more economical and high-efficiency recycling procedure needs to be developed. In this study we investigated the applicability of the zinc-melt method (ZMM) for recycling WC-Co as a powder from cutting-tool scraps. It was proven that ZMM is an available technique for recovering the WC powder from the cutting tools. WC-Co powders are recovered and then spray dried, sintered and obtained as a feedstock material for thermal-spray coating processes.

Keywords: cutting tool, WC-Co, recycling, zinc-melt method, spray dryer

Preiskovane so bile različne metode za recikliranje cermetov WC-Co iz orodij za rezanje, kot so kemijska modifikacija, termična modifikacija, metoda s hladnim tokom in elektrokemijska metoda, nekatere od njih pa se že uporabljajo v industriji. Vendar pa imajo te konvencionalne metode veliko problemov, ki jih je treba rešiti in nimajo vedno ustaljene tehnologije. Zato je treba razviti bolj ekonomične in visoko zmogljive postopke recikliranja. V tej študiji je bila preučevana uporabnost metode s taljenjem odpadkov rezilnih orodij v cinku (ZMM) za recikliranje WC-Co v obliki prahu. Dokazano je bilo, da je ZMM uporabna tehnika za pridobivanje WC-prahu iz orodij za odrezavanje. WC-Co-prahovi so bili najprej pridobljeni, nato posušeni z razprševanjem ter sintrani v obliko, primerno za termično nabrizgavanje prevlek.

Ključne besede: orodje za rezanje, WC-Co, recikliranje, metoda s taljenjem cinka, sušenje z razprševanjem

1 INTRODUCTION

The $2-billion, worldwide tungsten-carbide industry generates large quantities of scrap due to the parts rejected at various stages of the production and the worn-out cutting tools. The most basic recycling approach would be to break down the scrap pieces into powders and then fabricate more WC-based cutting tools. This approach would cause a severe equipment wear due to the abrasive nature of the cutting-tool materials and is, therefore, not feasible. As a result, the recycling is done by chemical means, such as the zinc-recovery process, electrolytic recovery, and extraction by oxidation. The conventional recycling processes for cutting tools have many problems to be solved, so they are not efficient technologies. One of them takes a very long processing time and the other requires high-scale equipment. Another process leads to decomposition and an undesirable phase occurrence. The recycling rate of WC-Co is only about under 20 % and the rates are still low[1–5]. Nowadays, the approaches to recovering WC and Co materials are not only economically important but also, due to the environmental factors, ecologically significant. Globally, one third of the consumption of WC for the cutting tools is being produced from their scrap. In recent years, a new technique for recovering WC and Co from the hard cutting-tool scraps using a molten-zinc (Zn) bath has been studied. Due to its efficiency and applicability, the zinc-melt process is considered to have a higher potential for recycling the cutting tools[3]. In this study, the zinc-melt-method parameters, such as temperature and time were optimized. A biscuit-structured WC-Co bulk was ground to obtain fine powders and then mixed with a Co powder by ball milling. These powders were produced with a spray dryer, having a spherical form and utilizing the thermal-spray process (**Figure 1**). The microstructure and chemical properties of these powders were studied with SEM and XRD.

2 EXPERIMENTAL WORK

The powder microstructures and surface morphologies were examined with the scanning electron microscopy (SEM). An elemental distribution analysis of the recovered powder was conducted with the energy-

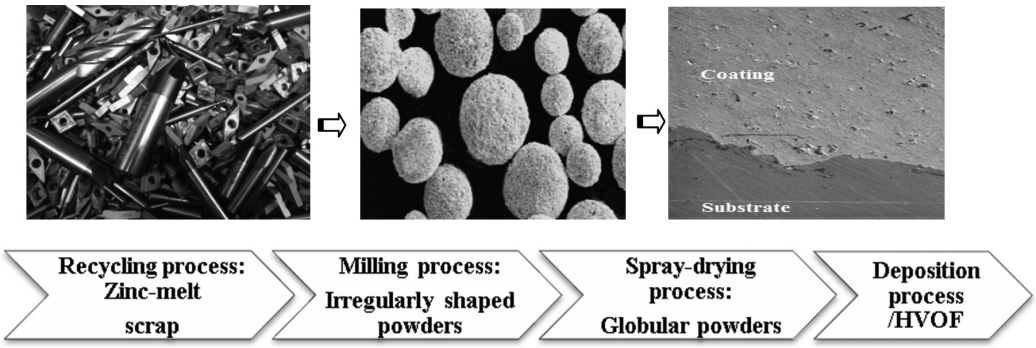

Figure 1: Experimental route of recycling scrap cutting tools
Slika 1: Eksperimentalna pot recikliranja odpadkov rezilnih orodij

dispersive X-ray spectroscopy (EDS). The crystalline phases were identified with the X-ray diffractometry (XRD). The density of the sintered body was measured in water using the Archimedes method. The flowability was measured with a Hall flowmeter. The particle-size distribution was measured with a laser particle sizer.

3 ZINC-MELT-METHOD (ZMM) RECYCLING PROCESS

In a zinc-recovery process, cemented carbide scraps are immersed in molten zinc in an electrical furnace at 1 atmosphere of inert gas at 650–800 °C. The zinc is subsequently distilled at 700–950 °C.[6,7] The optimum conditions depend on the Co content and the zinc-to-cobalt ratio. The properties of the reclaimed powders are the same as the virgin powders. Scrap cemented carbides can be sorted into medium (1.2–2 mm), coarse (≈4 mm), and mixed grain sizes with optical microscopy and by composition with x-ray spectroscopy before the zinc-recovery process. When the WC-Co scraps are dipped in a molten-zinc bath, the molten zinc starts to penetrate the WC particles and the dissolving Co binder, i.e., the Co film between the WC particles. The dissolution of the Co film results in a separation of the WC particles and independent particles float in the molten Zn-Co alloy. Since zinc has a high vapor pressure, it is easily removed in vacuum condition after the separation of WC particles. As zinc evaporates under vacuum, the Co content gradually increases and the Co metal has to precipitate on the WC surface from the molten alloy. When zinc evaporates completely, all Co precipitates on the WC particle surface resulting in the WC-Co powders with the same chemistry as found in the original powder before

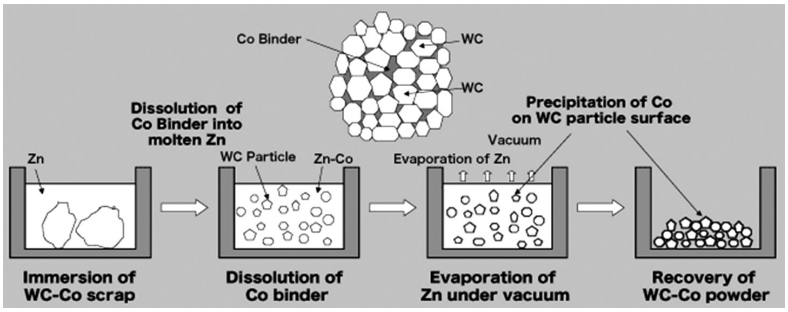

Figure 2: Zinc-melt process[8]
Slika 2: Postopek s taljenjem v cinku[8]

Figure 3: Recycling process of WC-Co
Slika 3: Postopek recikliranja WC-Co

Table 1: Biscuit structures after different thermal treatments
Tabela 1: Kolači, dobljeni po različnih termičnih obdelavah

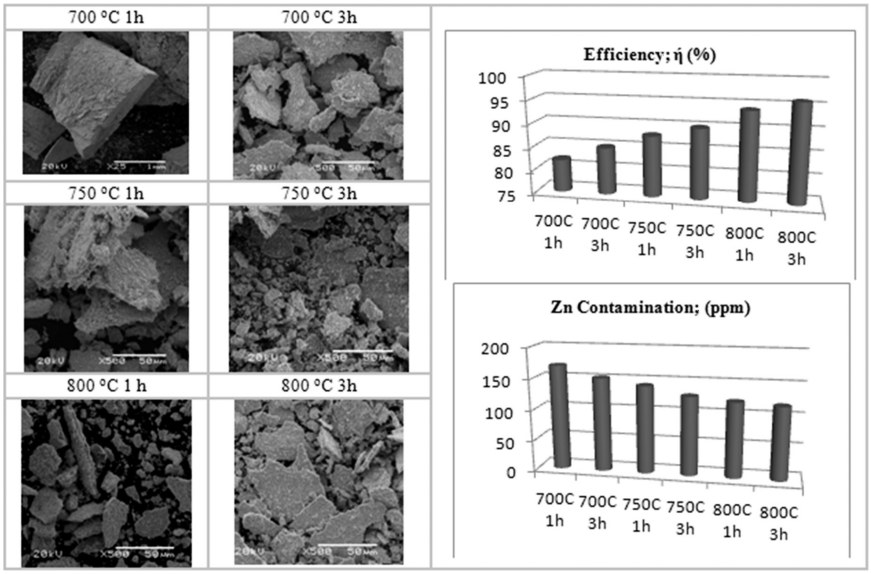

the sintering[8] (**Figures 2** and **3**). By increasing the process temperature and time, the recycling efficiency was improved. The zinc contamination was reduced (**Table 1**).

Process specifications: Process temperature: 700–900 °C under $Ar+N_2$ atmosphere, Melting time: 1–10 h, Charge: 14–22 kg (Scrap/Zn:1/ 1.3), Efficiency: 82–97 %.

4 SPRAY DRY PROCESS

Spray drying which is the most versatile powder-processing method consists of spraying a water-based suspension (called slurry) of the materials to agglomerate into a stream of heated air. The rapid heat and mass transfer which occurs during the drying combined with the presence of various slurry compounds result in dried granules having a large variety of shapes – from the uniform solid spheres, which are regarded as ideal granules for most ceramic systems, to elongated, pancake, donut-shaped, needle-like or hollow granules[9–11]. The spray-drying process transforms a solution with a certain solid content into a powder of the solid in one step. In this study we used volume fractions 25 % WC-Co + water solution (slurry). The solid aggregates are collected at the bottom of the chamber and separated from the gas in cyclone collectors. The main controlled operating parameters are the air temperature at the entry (185–210 °C), at the exit (100–140 °C) and inside the chamber (165–180 °C), the atomizing nozzle design and the air- and slurry-flow rates. The flowability of thermal spraying is good. The mean particle size is $D_{50} \approx 48$ μm. According to the X-ray diffraction (XRD) investigations

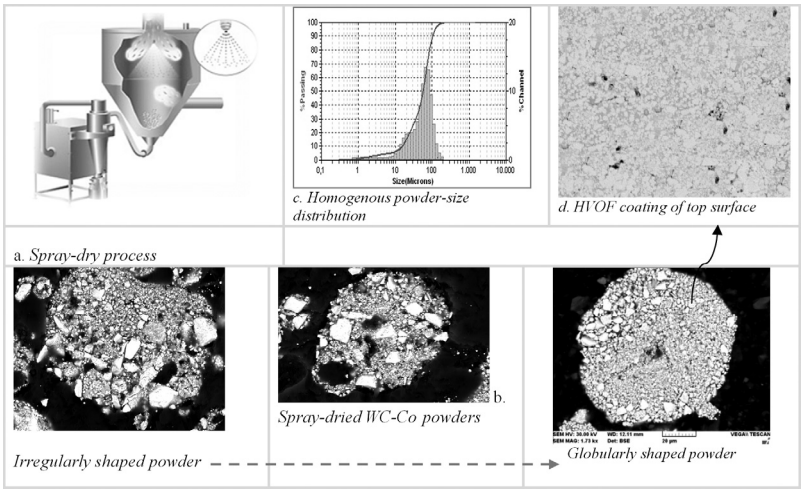

Figure 4: Spray-dried powders and deposition
Slika 4: Prah, osušen z razprševanjem in po depoziciji

of the spray-dried feedstock presented earlier, WC, WC_2, WO_3, $CoWO_4$ and metallic Co were present. The feedstock powder consisted of a-few-micrometers-sized agglomerates where the WC particles of 1–5 μm were finely distributed in the Co matrix.

Figure 4 shows the variety of shapes: from uniform solid spheres to elongated, pancake, donut-shaped, needle-like or hollow granules. It was found that the higher the inlet temperature, the faster is the moisture evaporation. A higher outlet temperature leads to a larger size of the powder. And the outlet temperature also controls the final moisture content of the powder. As the viscosity is lowered, less energy or pressure is required to form a particular spray pattern. Care must be taken with high solid loadings to maintain proper atomization ensuring a correct droplet formation. Then the spray-dried WC-Co feedstock powder was sintered at 1100 °C for 8 h to attain a sufficient granule strength, and then classified to a diameter of <30 μm. As the sintering temperature increased, the peak intensity of eta-carbide increased as well, while, simultaneously, the peak intensity of the WC and W_2C phases decreased. Depending upon the particle size and the shape of the tungsten-carbide-cobalt, spray-dried powder, the flowability can be under control. The highest flowability is obtained with the optimum spray-drying parameters. The measured Hall-flow rate of the reprocessed powder is approximately 160 g/min.

5 DEPOSITION PROCESS

Using the thermal-spray processing to deposit a coating of powders provides for a high-rate deposition method allowing an effective pressure and the temperature required for sintering high-density powders. High-velocity, oxy-fuel (HVOF), thermal-spray WC/Co coatings have been used widely in many fields such as metallurgy, energy sources and construction industry where they can be subjected to severe abrasive wear due to their excellent abrasive-wear resistance[12–16]. Spraying was performed at Sulzer Metco Robot Controlled Coating System during an HVOF process using a hydrogen-fuelled gun (DJ2600). The coating was free of any macroscopic porosities or cracks exhibiting excellent bonding to the substrate and a dense structure. The optimum spray parameters were determined from the preliminary experiments in order to minimize the coating porosity and WC decomposition (**Figure 4d**).

6 CONCLUSION

Our recycling and modification of the powder processes have been successful. The obtained granulated powders can be used for the thermal-spray feedstock materials. With respect to the zinc-melt process, the bonding metal (cobalt) reacts with the high-purity zinc during the cemented-carbide-recovery operation. The zinc contamination is low. The zinc-melt process shows a higher efficiency than the other process. The process parameters were optimized according to the shape, crystallinity and flowability properties. These powders can be easily used in the HVOF process. However, prior to starting further production of the recycled WC/Co powders, it will have to be demonstrated that this is a cost-effective production.

Acknowlodgements

The author is thankful to the members of the Sakarya University Thermal Spray Laboratory.

7 REFERENCES

[1] T. Kojima, T. Shimizu, R. Sasai, H. Itoh, Recycling process of WC-Co cermets by hydrothermal treatment, J. of Materials Sci., 40 (**2005**), 5167–5172

[2] J. C. Lee, E. Y. Kim, J. H. Kim, W. Kim, B. S. Kim, D. P. Banshi, Recycling of WC-Co hardmetal sludge by a new hydrometallurgical route, Int. J. of Refractory Metals and Hard Materials, 29 (**2011**) 3, 365

[3] W. D. Venkateswaran, B. Schubert, M. Lux, B. D. Ostermann, W. Kieffe, Scrap recycling by the melt bath technique, Int. J. of Ref. Metals and Hard Materials, 14 (**1996**) 4, 263–270

[4] C. Edtmaier, R. Schiesser, C. Megssl, W. D. Schubert, A. Bockb, A. Schoen, B. Zegler, Selective removal of the cobalt binder in WC/Co based hardmetal scraps by acetic acid leaching, Hydrometallurgy, 76 (**2005**), 63–71

[5] R. Sasai, F. Inagak, H. Itoh, Resource Recovery from Cemented Carbide by Subcritical Hydrothermal Treament, J. of the Soc. of. Mat. Sci., Japan, 55 (**2006**) 3, 254–257

[6] K. Hirose, I. Aoki, Recycling Cemented carbides without Pollut ion – Sorting Charging Material for Zinc Process, Int. Conf. Process. Mater. Prop., 1st 1993, 845–848 (English). Edited by Henein, Hani; Oki, Takeo. Miner. Met. Mater. Soc: Warrendale, PA

[7] A. K. Maiti, N. Mukhopadhyay, R. Raman, Effect of adding WC powder to the feedstock of WC–Co–Cr based HVOF coating and its impact on erosion and abrasion resistance, Surface and Coatings Technology, 201 (**2007**), 7781–7788

[8] Kohsei Co., Kitakyushu plant, http://www.kohsei.co.jp, 21. 05. 2012

[9] W. J. Walker Jr., J. S. Reed, S. K. Verma, Influence of Slurry Parameters on the Characteristics of Spray-Dried Granules, J. of the American Ceramic Society, 82 (**1999**) 7, 1711–1719

[10] D. E. Walton, C. J. Mumford, Spray dried products—characterization of particle morphology, Transactions of the Institution of Chemical Engineers, 77 (**1999**), 21–38

[11] Y. Wang, S. Jiang, M. Wang, S. Wang, T. D. Xiao, P. R. Strutt, Abrasive wear characteristics of plasma sprayed nanostructured alumina/titania coatings, Wear, 237 (**2000**), 176–185

[12] M. C. Nyongesa, Preparation, Characterisation And Testing Of Wc-Vc-Co Hp/Hvof Thermal Spray Coatings, School of Process and Materials Engineering – Faculty of Engineering and the Built Environment, WITS library, PHd thesis, 2006

[13] D. A. Stewart, P. H. Shipway, D. G. McCartney, Abrasive wear behaviour of conventional and nanocomposite HVOF-sprayed WC–Co coatings, Wear, 225–229 (**1999**), 789–798

[14] R. Joost, J. Pirso, M. Viljus, S. Letunovitš, K. Juhani, Recycling of WC-Co hardmetals by oxidation and carbothermal reduction in combination with reactive sintering, Estonian J. of Eng., 18 (**2012**) 2, 127–139

[15] M. G. Park, J. K. Han, Processing of Reclaimed Tungsten Carbide/Cobalt Powders with Virgin Properties, Taehan Kumsok Hakhoechi, 30 (**1992**) 8, 996–1004 (Korean)

[16] E. Altuncu, S. Ozturk, F. Ustel, Recycling of WC-Co from cutting tools by zinc melt method, 16th International Metallurgy & Materials Congress, TÜYAP Fair, İstanbul 2012

UDK 66.017:620.168
Professional article/Strokovni članek

ISSN 1580-2949
MTAEC9, 47(1)119(2013)

PERFORMANCE TESTING OF AN OPTICAL GROUND WIRE COMPOSITE

PREIZKUŠANJE ZMOGLJIVOSTI KOMPOZITNEGA PODZEMNEGA OPTIČNEGA KABLA

Sedat Karabay, Ersin Asim Güven, Alpay Tamer Ertürk

Kocaeli University, Mechanical Engineering Department, Kocaeli, Turkey
sedatkarabay58@gmail.com

Prejem rokopisa – received: 2012-08-27; sprejem za objavo – accepted for publication: 2012-09-26

An optical ground wire (OPGW) composed of different materials was presented in detail before delivering the product to the communication and electrical-energy markets. The performance level of its composite structure differs from the performance of the original material. Therefore, to measure whether the OPGW had reached the required quality, it was exposed to several tests simulating the real working conditions to detect the behavior of the composite structure. These included the stress-strain/fibre-strain and tensile tests, aeolian vibration, galloping, creep, short circuit, temperature cycling and lightning tests. Thus, the technical story of OPGW designed to serve the environment was explained in details and the test results were interpreted. The required material improvements to the master alloys made due to the failures of the composite conductor (OPGW) under heavy test conditions were also explained so that approval could be obtained.

Keywords: OPGW, lightning strike, creep, aeolian, composite structure, fiber failure

Optični podzemni kabel (OPGW), sestavljen iz različnih materialov, je bil predstavljen do podrobnosti, preden je bil proizvod poslan na trg komunikacij in energije. Zmogljivost kompozitne strukture se razlikuje od osnovnega materiala. Da bi preizkusili zmogljivost kompozitnega materiala in izmerili, ali OPGW doseže sprejemljivo kvaliteto, je bil kabel izpostavljen različnim preizkusom, ki so simulirali realne razmere. To so natezna napetost – raztezek vlakna, eolianske vibracije, galopiranje, lezenje, kratek stik, spreminjanje temperature in preizkus z bliskanjem. Podrobno je predstavljena celotna zgodba razvoja OPGW in vpliva okolja, razloženi pa so tudi rezultati preizkusov. Razložene so izboljšave osnovnih zlitin, potrebne zaradi napak v kompozitnem prevodniku (OPGW), da bi se doseglo soglasje za uporabo.

Ključne besede: OPGW, udar strele, lezenje, eolianske vibracije, kompozitna struktura, porušitev vlaken

1 INTRODUCTION

The OPGW cable today forms an integral part of any power company's transmission network and is utilized for the mission-critical circuit control ensuring the optimum operational efficiency and protection. The OPGW cable is defined as a composite cable which serves as a conventional overhead ground wire with the added benefit of providing the optical-fiber communications. An optical communication carrier can be completely separated from the power-transmission line to form an additional revenue stream, whilst the cable serves the traditional purpose of conducting fault currents to the ground and protecting the power conductors against lightning strikes. With proper design considerations, the OPGW cable has proven its reliability in protecting the optical fibers from electrical, mechanical, and environmental stresses[1]. With an increasing demand for more information transmission, such as the widespread use of the internet in the recent years, a much higher fiber-count OPGW is needed. The previous study shows the structure and the main test result of a stainless-steel tube with optical fibers in the stainless-steel tubes used instead of the conventional aluminum pipes in an extra-high multi-core OPGW[2]. Thus, a technical story of OPGW designed for a long-term reliability in the real working conditions was explained and the test results interpreted. Remedies for the failures of the composite conductor (OPGW) under heavy test conditions required material improvements that were also explained to reach approval in field conditions.

The composite conductor used in the experiments is composed of one stainless-steel tube with fibers, six galvanized steel wires and 12 AA–6101 aluminum-alloy wires at the outer layer (**Figure 1**)[3].

2 CHARACTERISTICS OF OPGW IN A STAINLESS-STEEL TUBE

2.1 Stress-Strain/Fiber-Strain and Tensile Test

The objective of this test is to monitor the optical characteristics and verify the mechanical characteristics of OPGW under the test up to the breaking load. An OPGW sample was installed in a hydraulically activated, horizontal test machine[4–7]. A displacement transducer was fixed to the conductor to measure the cable elongation over the 8 m gage length. The gage length for attenuation measurements was taken for the length under tension. The conductor elongation, the output signal from the optical power meters and the conductor tension as measured by a load cell were monitored using a digital-data logging system. After completing the tests, if

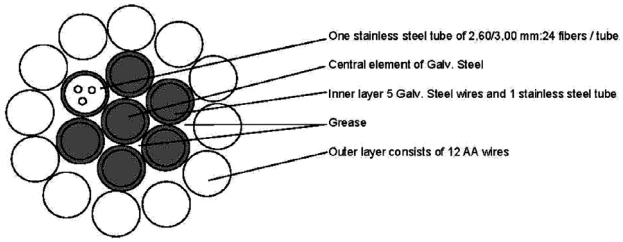

Figure 1: Design properties of OPGW
Slika 1: Sestav OPGW

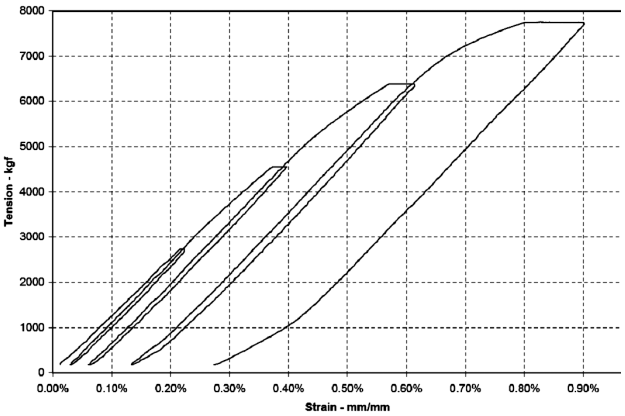

Figure 2: Load plotted against conductor strain
Slika 2: Obremenitev v odvisnosti od raztezka prevodnika

the fiber elongation at 0.45 % of conductor elongation is greater than 0.01 % and if at 72 % of RTS the temporary increase in the fiber attenuation is greater than 1 dB/km, as compared to the value measured before the test, and there is a measurable permanent increase in the fiber attenuation that is greater than 0.02 dB/km, the test shall be considered unsuccessful. Some results of the completed test are presented in **Figures 2** and **3**. **Figure 2** shows the data at the load (conductor tension) plotted against the conductor strain. On the other hand, **Figure 3** shows optical attenuation and the load/conductor tension plotted against time.

2.2 Creep Test

The objective of the creep test is to measure the room-temperature, long–term tensile-creep properties of the conductor. The data from this test are used to assist in the calculation of the sags and tensions. The test was performed according to IEC 61395. The length of the sample between the dead-end clamps was 15 m. The test was carried out in a temperature-controlled laboratory at 20 °C ± 2 °C. In line with the Aluminum Association's method, the long-term tensile creep of the cable under a constant tension is taken to be the permanent strain occurring between 1 h and the specified test time.

The last reading during this test was taken at 1000 h. A log-log plot of strain versus the elapsed time for LVDT (the linear variable differential transformer) is shown in **Figure 4**. On the completion of the test, the best-fit straight line was fitted to the LVDT data and extrapolated to 10 years (87000 h).

The equation of the line:

$$Strain = A^*(Hours)^B \rightarrow y = 8.5073E - 0.5\ X^{1.3965E-01}$$

2.3 Temperature-Cycle Test

The objective of this test was to verify the good performance of the fiber when the cable is subjected to extreme thermal cycles. The test was performed in accordance with EIA/TIA-455-3A. A reel with approximately 761 m of an OPGW cable was placed in a 5 m × 6 m × 4 m environmental chamber. Three thermocouples were placed in the environmental chamber to measure the temperature. Two were placed on separate 25 cm cable samples and located on either side of the cable reel. The third was located under the first layer of the cable reel. All twenty-four fibers were spliced to form one continuous loop. The total test-fiber length was approximately 18.3 km. The cable was subjected to two thermal cycles. Each thermal cycle started with the chamber temperature of 23 °C, which was then lowered to –40 °C and held at this level for a minimum of 16 h. The chamber temperature was then increased to 65 °C and held at this level for a minimum of 16 h. To com-

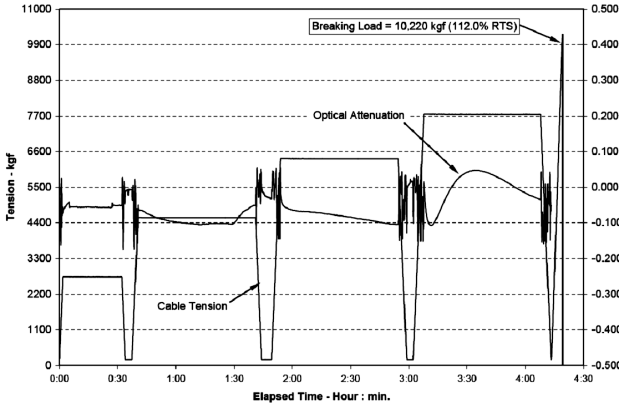

Figure 3: Optical attenuation plotted against time
Slika 3: Prikaz optičnega dušenja v odvisnosti od časa

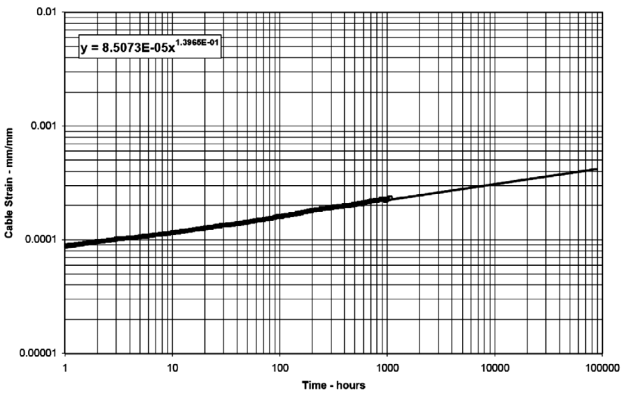

Figure 4: Cable strain versus time
Slika 4: Raztezanje kabla v odvisnosti od časa

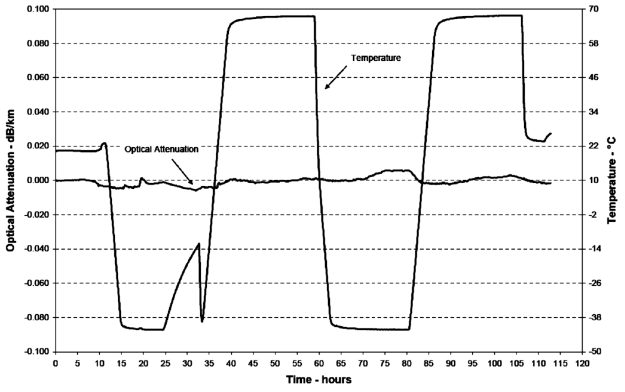

Figure 5: Records of the heat-cycle test of OPGW
Slika 5: Zapis iz preizkusa cikličnega segrevanja OPGW

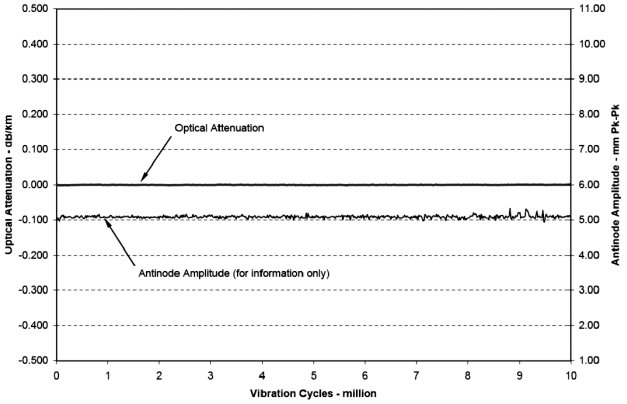

Figure 6: Aeolian-vibration test results
Slika 6: Rezultati preizkusa eolijskih vibracij

plete the cycle, the chamber temperature was returned to 23 °C. All the temperature transitions were conducted at a rate of less than 20 °C/h. The chamber temperature was based on one of the thermocouples on the 25 cm cable samples, located on one side of the cable reel. The cable-reel temperature and the optical data were recorded every five minutes throughout the test.

The optical attenuation and the chamber temperature versus time are shown in **Figure 5**. The variation in the optical attenuation due to the temperature was no greater than 0.006 dB/km. The maximum allowable change in the attenuation, between the extreme temperature limits, is 0.05 dB/km.

2.4 Aeolian-Vibration Test

The objective of the aeolian-vibration test is to assess the fatigue performance of OPGW and the optical characteristics of the fibers under typical aeolian vibrations. The tests were performed according to IEC 60794-1-2, Method E19 and IEC 60794-4-1. Thus, OPGW was pre-tensioned to 1795 N and an initial optical measurement was taken. OPGW was then tensioned to 17 903 N or 20 % of the RTS cable and the exit angles of the cable from the suspension clamp were measured. The initial target vibration frequency was 54.4 s^{-1}, which is the frequency produced by a 4.5 m/s wind (i.e., frequency = 830 ÷ diameter of OPGW in mm). The actual vibration frequency was the system resonance that was nearest to the target frequency and provided a better system stability, while the target free-loop peak-to-peak antinode amplitude was 5.08 mm or one third of the OPGW diameter. This amplitude was maintained at this level in the first free loop from the suspension assembly towards the shaker. The amplitudes in the passive span and the section between the shaker and the dead end in the active span were maintained at the levels no greater than one third of the cable diameter. OPGW was subjected to 10-million vibration cycles. Optical measurements were taken for 2 h after the completion of the vibration cycles.

All twenty-four fibers were spliced to make the total fiber length of 720 m (24 × 30 m). The test sample was terminated beyond both dead ends so that the optical fibers could not move relative to OPGW.

Dissection: After the completion of 10 million cycles, the cable was dissected down to the stainless-steel tube and visually examined. Active dead end: There were no visible signs of breaks, cracks, failure or discoloration of any of the dissected components of OPGW (**Figure 6**). Passive dead end: There were no visible signs of breaks, cracks, failure or discoloration of any of the dissected components of OPGW. Suspension: There were no visible signs of breaks, cracks, failure or discoloration of any of the dissected components of OPGW.

2.5 Galloping Test

The objective of the galloping test is to assess the fatigue performance of the fiber optical ground wire and the optical characteristics of the fibers under typical galloping conditions. The test was performed according to IEC 60794-4-1. For that aim, an initial optical measurement was taken one hour prior to the test. The difference between the reference and test signals for the initial measurement provided an initial base reading. The change in this difference during the test indicated the change in the attenuation of the test fiber. The cable was subjected to 100 000 galloping cycles in the single-loop mode. The free-loop peak-to-peak antinode amplitude was maintained at the minimum of about 0.8 m or 1/25th of the distance from the dead end to the suspension-clamp length (i.e., 20 m). Optical measurements were taken for two hours after the completion of the galloping test. The galloping frequency at the start and during the test was 1 s^{-1} without any variations. The free-loop antinode amplitude in the active (driven) span was maintained at approximately 0.9 m. The free-loop antinode amplitude in the passive span varied between 0.3 m to 0.4 m during the test. The tension in the cable fluctuated between 529 N to 1432 N during the galloping. After the completion of 100 000 cycles, the cable was dissected

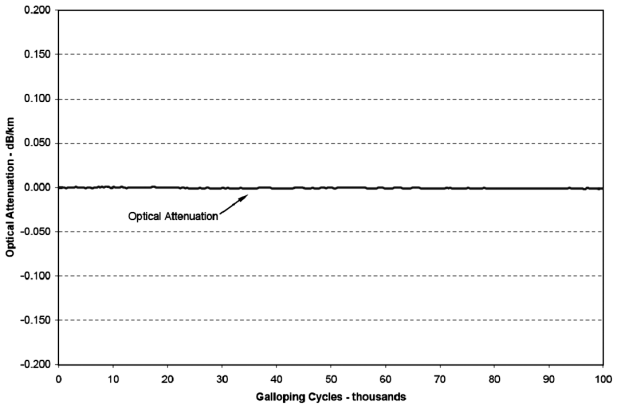

Figure 7: Galloping-test records of OPGW and attenuation of fibers
Slika 7: Zapis preizkusa galopiranja OPGW in optično slabljenje vlaken

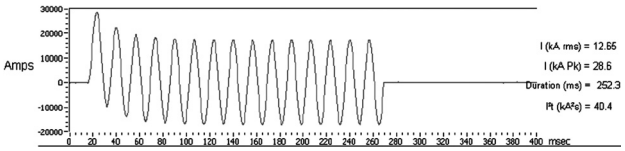

Figure 8: Applied short-circuit arc current and its time
Slika 8: Uporabljeni tok kratkega stika in njegovo trajanje

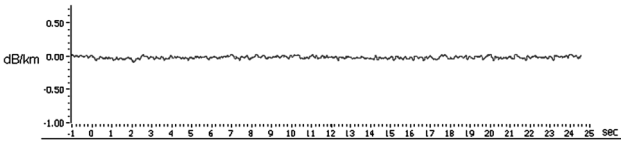

Figure 9: Attenuation range for OPGW when a lightning strike is applied
Slika 9: Področje optičnega slabljenja vlaken OPGW pri uporabi udarca strele

down to the stainless-steel tube and visually examined. Active dead end: There were no visible signs of breaks, cracks, failure or discoloration of any of the dissected components of OPGW. Passive dead end: There were no visible signs of breaks, cracks, failure or discoloration of any of the dissected components of OPGW (**Figure 7**). Suspension: There were no visible signs of breaks, cracks, failure or discoloration of any of the dissected components of OPGW.

2.6 Short-Circuit Test

The objective of the short-circuit test is to verify if OPGW can withstand repeated short-circuit applications without exceeding optical, physical or thermal requirements. The test was performed in accordance with the TEIAS Specification and IEC 60794-1-2, Method H1.

The cable was first subjected to two low-level calibration shots and then ten "official" shots. The purpose of the calibration shots was to ensure that the current level was correct. For the "official" shots, the target values for the electrical parameters were: the parameter target energy value of 109.5, the minimum kA^2s^{-1} fault current of 14.8 kA, the duration of 0.5 s, the maximum possible asymmetric waveform to be symmetrical after the 3rd cycle for each shot, the fault current and the duration may vary slightly from the target values. The objective was to achieve the minimum energy level for each shot. To ensure that optical signals were stable, the power meters were powered on and operating for at least one hour before the first shot. The optical measurement was normalized to zero before the first official shot. The cables were visually inspected for birdcaging or other damage during the test. The optical and temperature data were being acquired for one hour after the tenth shot. The cable was maintained at the temperature of 40 °C during this period.

As specified by IEC 60794-1-2, Method H1, the acceptance criteria of the product are summarized below:

a) The temperature immediately after the current pulse shall be less than 180 °C inside the optical unit. The temperature inside the optical unit is measured by thermocouple.
b) The attenuation increase during the tests shall be less than 1.0 dB/km. There shall be no change in the attenuation after the cable has cooled down to 40 °C.
c) There shall be no irreversible birdcaging. The cable and hardware shall be dissected after the test and visually examined for damage at each dead-end assembly and at the midpoint of the span. Each separable component of the cable shall be inspected. There shall be no signs of birdcaging, excessive wear, discoloration, deformation or other signs of a breakdown (**Figures 8** and **9**).

2.7 Lightning Tests

The essential function of OPGW in transmission lines is to guard the aerial conductor from the lightning strikes and its secondary job is to transmit the signals of data and communications. The excessive lightning energy generally flows through the outer layer of the OPGW conductor. However, when this energy jumps from the clouds to an OPGW conductor, a small region on the outer layer is liable to overheating. Therefore, the conductivity of the material used in an OPGW conductor, including both electrical and heat transfer, should be as high as possible. If not, regional melting occurs as seen in **Figures 10 a, b** and finally the wires are broken. These **Figures 10 a, b** refer to the first trial of the lightning test. In this test, 2 × 10 m OPGW samples, connected in parallel to measure the attenuation of the fibers and the effects of the overcurrent, failed due to a lightning strike.

The test was realized under an amplitude of 200 A, with a charge of 100 C and within the time of 500 ms. The main acceptance restriction is to keep the resistance increase below a 20 % change. This corresponds to three wires breaking at the outer layer. However, at first the trial 9–10 wires were broken.

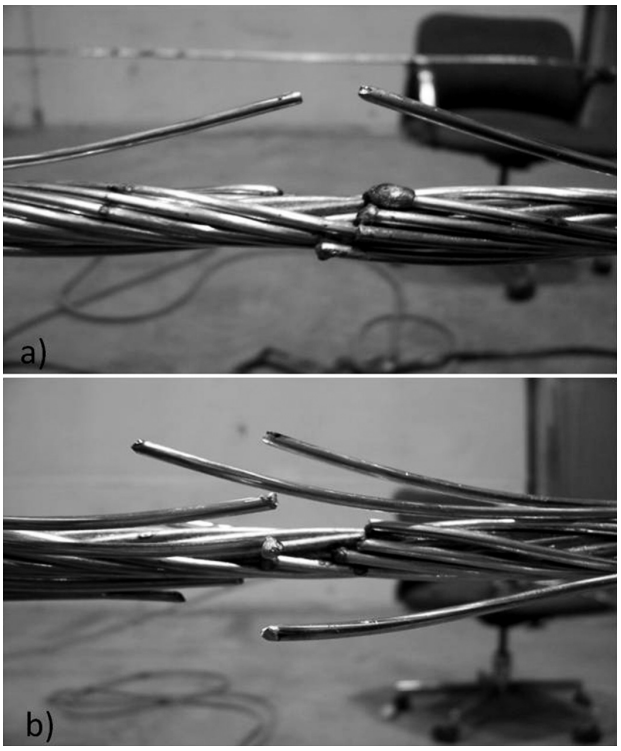

Figure 10: a, b) Spot melting of AA-6101 aluminum-alloy wires due to an application of lightning strike
Slika 10: a, b) Točkasto taljenje aluminijeve žice AA-6101 zaradi udarca strele

Therefore, the AA–6101 aluminum alloy was modified with AlB_2 (**Figure 11**) at the casting stage and then the conductivity of the wires increased from 52.5 % IACS to 57–58 % IACS.[3] The second test was thus performed with modified wires and stranded with a short lay length to obviate the arc between the wires. The second trial met all the requirements perfectly (**Figures 12 a, b**).

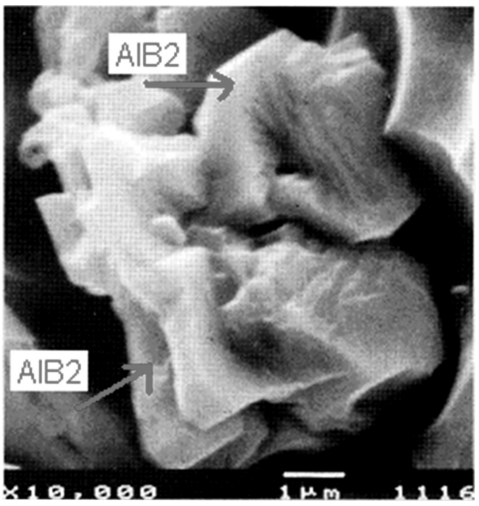

Figure 11: AlB_2 master alloy used to increase the conductivity of the AA–6101 aluminum alloy by inoculating it in the casting stage in a foundry tandish[3]
Slika 11: Osnovna zlitina AlB_2, uporabljena za povečanje prevodnosti aluminijeve zlitine AA-6101 z inokulacijo med ulivanjem v livarski vmesni posodi[3]

3 RESULTS

Before a new OPGW product, prepared with a combination of different materials, is introduced to the market, it should be exposed to several tests to determine its mechanical and electrical behaviors under simulated working conditions. Here, the required important tests were applied to the OPGW composite structure. The tested product passed most of them perfectly, but the lightning test destroyed it completely. Therefore, the designed and constructed composite structure should be changed or the conductive material must be modified.

4 DISCUSSION

The initially designed and constructed OPGW conductor successfully passed most of the tests defined previously, except for the lightning test. As a remedy, AlB with AlB_2 phases of the master alloy was fed into the molten AA–6101 alloy as 3 kg per ton. Then conductivity of the AA–6101 wires increased from 52 % IACS to 57–58 % IACS. An increase in electrical conductivity also causes an increase in heat conductivity. When the above modification is applied other properties such as tensile strength, elongation, 1 % elongation strength, etc. remain constant.

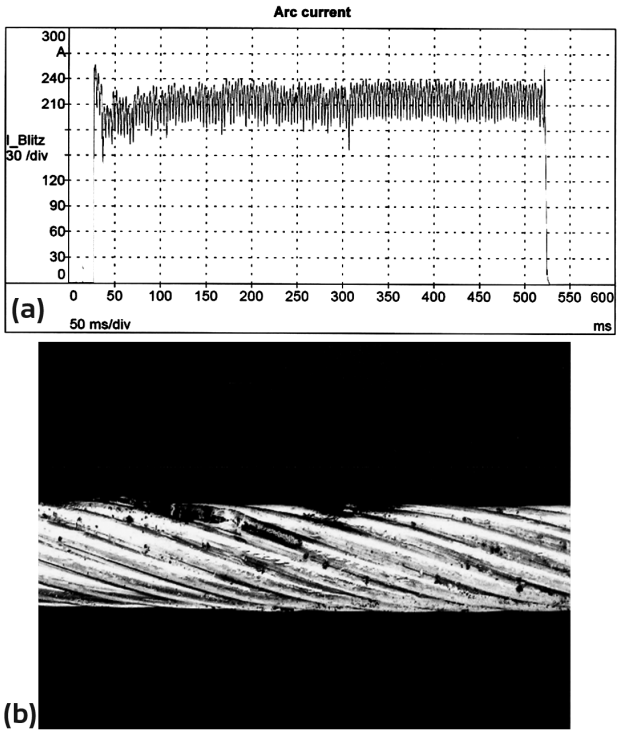

Figure 12: a) Lightning arc, b) view after a strike to the OPGW conductor without broken wires on the outer layer
Slika 12: a) Oblok bliska, b) po udaru v OPGW prevodnik brez porušenih žic na zunanji strani

By modifying the wires and reducing the lay length of the conductor, a new test sample was manufactured. Then a lightning strike was applied again. Now the results met the requirements and the standard used in the test and the product passed perfectly all the required tests.

5 CONCLUSION

The design, construction and modification of an OPGW aerial conductor using a combination of different materials is presented by explaining its behavior under type tests before introducing it into the communication and energy markets. This research also shows that a lightning strike is the hardest test applied to the conductor. OPGW can resist the lightning strike when we strand the wires tightly, decrease the lay length and increase electrical conductivity by inoculating it with AlB_2 in a tundish at 750 °C. The short-circuit test applied to OPGW is not the only way of determining its performance in the event of lightning.

6 REFERENCES

[1] M. Yokoya, Y. Katsuragi, Y. Goda, Y. Nagata, Y. Asano, IEEE Transaction on Power Delivery, 9 (**1994**), 1517–1523
[2] F. Jakl, IEEE Transaction on Power Delivery, 15 (**2000**), 1524–1529
[3] S. Karabay, Y. Tayşı, Materials and Manufacturing Process, 19 (**2004**), 1–13
[4] T. Torvath, Journal of Electrostatics, 60 (**2004**), 265–275
[5] S. J. Guavac, M. D. Nimrihter, L. R. Geric, Electrical Power System Research, 78 (**2007**), 556–583
[6] D. Ruiz, C. Torraba, Journal of Electrostatics, 67 (**2009**), 496–500
[7] Y. Goda, Y. Shigenu, S. Watanabe, IEEE Transaction on Power Delivery, 19 (**2004**), 1734–1739

UDK 621.78.084:620.3
Professional article/Strokovni članek

ISSN 1580-2949
MTAEC9, 47(1)125(2013)

INVESTIGATION OF THE COOLING PROCESS WITH NANOFLUIDS ACCORDING TO ISO 9950 AND ASTM D 6482 STANDARDS

PREISKAVA POSTOPKA OHLAJANJA V NANOTEKOČINI PO STANDARDIH ISO 9950 IN ASTM D 6482

Josip Župan, Darko Landek, Tomislav Filetin

University of Zagreb, Faculty of Mechanical Engineering and Naval Architecture,
Quenching Research Centre (QRC), I. Lucica 5, 10000 Zagreb, Croatia
josip.zupan@fsb.hr

Prejem rokopisa – received: 2012-09-01; sprejem za objavo – accepted for publication: 2012-09-19

Introducing nanofluids as liquid quenchants in order to improve the heat-transfer characteristics is a novel approach in heat treatment. These new liquid quenchants are called nanoquenchants and are colloid suspensions of nanoparticles in the base fluid (BF). For the purpose of this research standard liquid quenchants, such as water and polymer solution, were used as base fluids. Nanoparticles were added to the base fluid in order to increase its thermal properties without a significant effect on the viscosity of the fluid. The added nanoparticles cause an enhancement of the heat-transfer characteristics of the liquid quenchants. In this research TiO_2 nanoparticles, with the average size of 50 nm, were added to the base fluid. The cooling curves for every tested quenchant were recorded using the IVF SmartQuench system and the quenching process parameters were determined and compared. The tested quenchants were deionised water and polyalkylene-glycol (PAG) water solutions of (5, 10 and 20) % in volume fractions of polymer concentrations. Quenching experiments were first conducted in pure BFs without the addition of nanoparticles and without agitation according to the ISO 9950 standard. The experiments were then repeated with an addition of 0.2 g/l TiO_2 nanoparticles. The second series of experiments was conducted in a quenching bath with agitation according to the ASTM D 6482 standard. All of the recorded cooling curves were compared and the effects of the nanoparticle addition and agitation were investigated. The addition of the nanoparticles and quenching with agitation caused an increase in the maximum cooling rate and a shorter full-film stage.

Keywords: quenching, nanofluids, agitation, TiO_2 nanoparticles

Uvajanje nanotekočin za kaljenje za izboljšanje lastnosti prenosa toplote je nov način toplotne obdelave. Te nove tekočine za kaljenje se imenujejo nanokalilne tekočine, ki so koloidna suspenzija nanodelcev v osnovni tekočini (BF). Za preiskavo je bila kot standardna tekočina za kaljenje uporabljena mešanica vode in raztopine polimera. Nanodelci so bili dodani osnovni tekočini za povečanje termičnih lastnosti brez velikega učinka na viskoznost tekočine. Dodani nanodelci so povečali toplotno prevodnost tekočine za kaljenje. V tej raziskavi so bili dodani osnovni tekočini nanodelci TiO_2 povprečne velikosti 50 nm. Krivulje ohlajanja za vsako preizkušeno kalilno tekočino so bile posnete s sistemom IVF SmartQuench in procesni parametri kaljenja so bili določeni in primerjani. Preizkušene kalilne tekočine so bile deionizirana voda, vodna raztopina polialkilen glikola (PAG) z volumenskim deležem (5, 10 in 20) % polimera. Preizkusi kaljenja so bili najprej izvršeni v osnovni tekočini (BF) brez dodatka nanodelcev in brez premešavanja, skladno s standardom ISO 9950. Eksperimenti so bili nato ponovljeni z dodatkom nanodelecev 0,2 g/l TiO_2. Druga serija preizkusov je bila izvršena v kalilni kopeli s premešavanjem, kot določa standard ASTM D 6482. Vse posnete krivulje so bile primerjane in preiskovan je bil tudi učinek dodatka nanodelcev in premešavanja. Dodatek nanodelcev in kaljenje s premešavanjem sta povzročila povečanje maksimalne hitrosti hlajenja in krajše stanje popolnega prekritja s paro.

Ključne besede: kaljenje, nanotekočine, mešanje, nanodelci TiO_2

1 INTRODUCTION

Nanofluids (NFs) are colloidal suspensions of a base fluid (BF) and particles that are usually less than 100 nm in diameter[1]. The particles are added with the aim of improving the thermal properties of the pure base fluids, which primarily refers to the significant increase in the heat-transfer dynamics of the cooling process. It is important that the rheological properties of NFs do not change much[2–4]. Base fluids can be water, ethylene glycol, polyalkylene glycol (PAG) or quenching oil, while metal nanopowders (Cu, Au, Ag), oxide-ceramic particles (Al_2O_3, SiO_2, TiO_2), carbon powders and nanotubes are added to a base fluid. This is the reason why nanofluids are interesting as liquid quenchants. Physical properties of a quench-hardened work piece highly depend on the cooling rate during the quenching process. In order to achieve specific properties, different cooling rates have to be applied[5]. So far, several studies were conducted to demonstrate the efficiency of nanofluids as liquid quenchants[6–9]. The experiments showed that nanofluids exhibit a higher heat-transfer coefficient (HTC) and a better thermal conductivity than base fluids, but also a shorter full-film boiling phase. Further analysis of the cooling curves showed an increase in the critical heat flux (CHF) caused by an addition of nanoparticles to BF.

So far, all of the experiments were conducted according to the ISO 9950 standard. There are no published results regarding the quenching in nanofluids with mechanical agitation. For this reason a series of experiments according to the ASTM D 6482 standard were

conducted to compare the cooling curves of BFs and NFs, but also to see the effect of agitation.

2 EXPERIMENTS

A standard test probe used in this set of experiments is in compliance with the international standards and is a part of the IVF SmartQuench system consisting of a data-acquisition unit, a certified standard test probe, a furnace and software. The data acquisition unit and software have the capacity of gathering 100 samples per second, which is considered to be high enough for registering all the rapid changes that occur during the quenching process. The experiments with still fluids were conducted in a one-litre beaker, and a two-litre quenching bath was constructed for the experiments with agitation. The electric-motor rotational speed is set to 1000 r/min and agitation is induced with a three-blade propeller. For the preparation of NFs, the titanium-oxide (TiO_2) particles produced by Degussa, Germany, were used. The average size of the nanoparticles was 50 nm, and they come in the form of a white powder. No dispersants, surfactants or activating agents were used. Pure TiO_2 nanoparticles were added to BFs and homogenized. The method of homogenization consisted of adding 0.2 g/l of TiO_2 nanoparticles to deionised (DI) water and then sonified for 60 min. This was the nanoparticle concentration for all of the tested nanoquenchants. This was followed by mixing the nanoparticles with a defined volume of PAG. The fluid was then sonified for additional 30 min and mechanically stirred from time to time. The ultrasonic bath, type BRANSONIC 220, with the frequency of 50 kHz and power of 120 W, was used to homogenize the nanofluids. With respect to the water-based polymer solution, polyalkylene glycol, known as Ucon Quenchant E, was added to water. Its tested concentrations were volume fractions (5, 10 and 20) % of PAG, while the concentration of nanoparticles was 0.2 g/l. The bath temperature of all liquid quenchants was 44 °C ± 1 °C.

3 RESULTS

A set of quenching experiments was conducted with and without agitation in order to determine the cooling characteristics of the liquid quenchants. First, the base fluids were tested. To see the effect of a nanoparticle addition, nanofluids were used as liquid quenchants in both still and agitated conditions. All of the recorded cooling curves are shown in **Figure 1**. Water and water-based nanofluids show very small differences in the cooling characteristics. The maximum cooling rate is within 10 % but the most significant influence is observed during the full-film phase. The transition temperature from the full-film phase to the nucleate boiling phase (T_{vp}) is much higher for NFs and for both

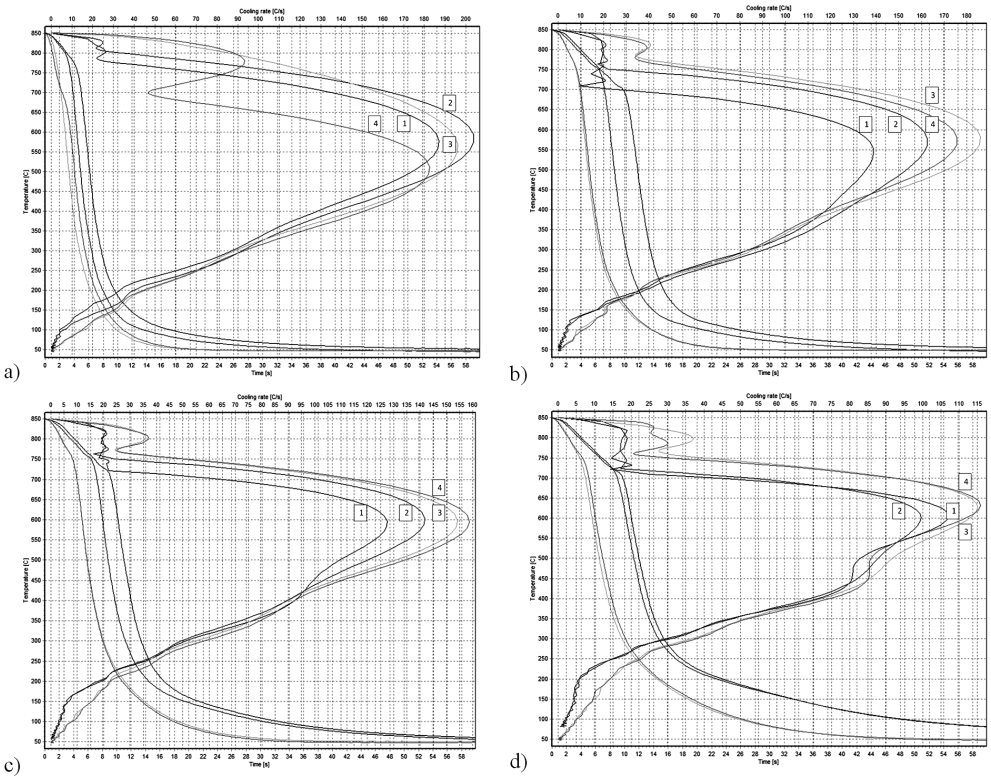

Figure 1: Cooling-curve diagrams for: a) water, b) 5 %, c) 10 % and d) 20 % volume fractions of PAG with the curves for BF 1 and NF 2 in still conditions and the cooling curves for BF 3 and NF 4 with agitation

Slika 1: Diagrami ohlajevalnih krivulj za: a) vodo, b) 5 %, c) 10 % in d) 20 % volumenskih deležev PAG s krivuljami za BF 1 in NF 2 v mirovanju in ohlajevalne krivulje za BF 3 in NF 4 s premešavanjem

Table 1: Resulted characteristics derived from the cooling curves
Tabela 1: Značilnosti, ki izhajajo iz ohlajevalnih krivulj

Quenchant	CR_{max}/(°C/s)	$T(CR_{max})$/°C	$t(CR_{max})$/s	T_{cp}/°C	T_{vp}/°C
Water	187.1	577.8	6.7	127.0	786.5
Water + 0.2 g TiO_2	209.5	584.0	4.9	152.6	843.4
Water with agitation	196.1	556.5	3.9	87.4	850.1
Water + 0.2 g TiO_2 with agitation	182.1	496.4	5.1	72.8	849.4
Water + 5 % PAG	138.8	535.7	12.5	134.5	707.8
Water + 0.2 g TiO_2 + 5 % PAG	162.5	564.7	9.2	127.5	757.1
Water + 5 % PAG with agitation	185.8	566.2	5.6	151.5	786.1
Water + 0.2 g TiO_2 + 5 % PAG with agitation	175.6	579.4	5.7	154.6	780.3
Water + 10 % PAG	127.5	585.9	11.3	181.8	727.6
Water + 0.2 g TiO_2 + 10 %PAG	141.8	596.2	9.1	164.3	757.8
Water + 10 %PAG with agitation	154.2	597.7	6.2	163.8	772.3
Water + 0.2 g TiO_2 + 10 %PAG with agitation	158.7	595.0	6.2	162.7	772.2
Water + 20 % PAG	107.1	604.2	11.9	241.0	717.0
Water + 0.2 g TiO_2 + 20 % PAG	99.6	605.0	11.2	206.9	728.2
Water + 20 % PAG with agitation	115.0	622.4	5.3	224.4	767.0
Water + 0.2 g TiO_2 + 20 % PAG with agitation	115.8	631.6	6.7	482.1	761.0

cases of quenching with agitation. All the specific values of the cooling curves for each quenching case are given in **Table 1**. The polymer solution with 5 % PAG shows that, in still conditions, an addition of nanoparticles shortens the full-film stage and causes a 17 % increase in the maximum cooling rate (CR_{max}).

When quenching with agitation, the cooling curves for BFs and NFs are almost identical. The full-film phase is more than 6 s shorter than BF and the increase in CR_{max} is 34 %. Note that the CR_{max} of BF is higher than in the case of NF. As the polymer concentration is increased, the difference between the cooling rates is getting smaller. All of the cooling curves with agitation show that an addition of nanoparticles does not cause better cooling characteristics. This means that agitation is the main cause of a shorter full-film phase and a higher CR_{max}. During the research it has been noted that the effect of the deposition of nanoparticles on the surface probe was more evident after the quenching in still conditions.

4 CONCLUSION

The research results led to the following conclusions:

- Quenching with agitation caused a shorter full-film phase and a higher CR_{max}.
- Nanofluids provided an enhancement of the heat-transfer characteristics in still conditions for all the cases except for the high polymer concentration.
- There is almost no difference between the cooling curves for BFs and NFs with agitation.
- Agitation, not an addition of nanoparticles, is the main cause for a shorter full-film phase and higher $CR_{max.}$
- The effect of an addition of nanoparticles becomes lower as the polymer concentration increases.

Acknowledgments

The presented investigations were achieved within the project No. 120-1201780-1779 – Modelling of Material Properties and Process Parameters supported by the Ministry of Science, Education and Sports of the Republic of Croatia.

5 REFERENCES

[1] S. K. Das, S. U. S. Choi, W. Yu, T. Pradeep, Nanofluids – science and technology, John Wiley & Sons, Inc., Hoboken, New Jersey 2008, 397

[2] W. Duangthongsuk, S. Wongwises, Measurement of temperature-dependent thermal conductivity and viscosity of TiO2-water nanofluids, Experimental Thermal and Fluid Science, 33 (**2009**) 4, 706–714

[3] J. Buongiorno et al., A benchmark study on the thermal conductivity of nanofluids, Journal of Applied Physics, 106 (**2009**) 9, 094312

[4] S. W. Lee, S. D. Park, S. Kang, I. C. Bang, J. H. Kim, Investigation of viscosity and thermal conductivity of SiC nanofluids for heat transfer applications, International Journal of Heat and Mass Transfer, 54 (**2011**), 433–438

[5] B. Liščić, H. M. Tensi, L. C. F. Canale, G. E. Totten, Quenching Theory and Technology – Second Edition, CRC Press, Taylor & Francis Group, Boca Raton 2010, 709

[6] K. Babu and T. S. Prasanna Kumar, Effect of CNT concentration and agitation on surface heat flux during quenching in CNT nanofluids, International Journal of Heat and Mass Transfer, 54 (**2011**) 1–3, 106–117

[7] A. Bolukbasi, Pool boiling heat transfer characteristics of vertical cylinder quenched by SiO2–water nanofluids, International Journal of Thermal Sciences, 50 (**2011**) 6, 1013–1021

[8] H. Kim, G. DeWitt, T. McKrell, J. Buongiorno, L. Hu, On the quenching of steel and zircaloy spheres in water-based nanofluids with alumina, silica and diamond nanoparticles, International Journal of Multiphase Flow, 35 (**2009**) 5, 427–438

[9] J. Župan, T. Filetin, D. Landek, The effect of TiO2 nanoparticles on fluid quenching characteristics, International Heat Treatment and Surface Engineering, 6 (**2012**) 2, 56–60

UDK 621.37
Professional article/Strokovni članek

ISSN 1580-2949
MTAEC9, 47(1)129(2013)

ANALYSIS OF THE EFFECTS OF METAMATERIALS ON THE RADIO-FREQUENCY ELECTROMAGNETIC FIELDS IN THE HUMAN HEAD AND HAND

ANALIZA UČINKOV METAMATERIALOV NA RADIOFREKVENČNO ELEKTROMAGNETNO POLJE V ČLOVEŠKI GLAVI IN ROKI

Mohammad Rashed Iqbal Faruque[1,2], Mohammad Tariqul Islam[1], Nik Abdullah Nik Mohamed[1], Baharudin Yatim[1], Mohd. Alauddin Mohd. Ali[1]

[1]Institute of Space Science (Angkasa), Faculty of Engineering and Built Environment Building, Universiti Kebangsaan Malaysia, 43600 UKM, Bangi, Selangor, Malaysia
[2]Dept. of Electrical, Electronic and Systems Engineering, Faculty of Engineering and Built Environment, Universiti Kebangsaan Malaysia, 43600 UKM, Bangi, Selangor, Malaysia
rashedgen@yahoo.com

Prejem rokopisa – received: 2012-09-02; sprejem za objavo – accepted for publication: 2012-09-19

The development of split-ring resonators (SRRs) consisting of two concentric square rings of a conductive material exhibiting a resounding electric response at a microwave frequency is described in this paper. Each square ring has a gap and is oppositely placed in the gap of the other ring. A size reduction is always possible in this kind of structure, but one should be careful about the set frequency. The described square type of metamaterial design is completely novel in the context of the head and hand with respect to the specific absorption-reduction rate (SAR). This design was used because more arrays can be placed within a given area. Mobile phones are relatively small, requiring small metamaterial designs. The finite-difference time-domain method with the lossy-Drude model is adopted in this analysis by using CST Microwave Studio®. The technique of a SAR reduction is discussed, and the effects of the relating position, distance, and size of the square metamaterials on the SAR reduction were investigated. Using the square-type metamaterials, we have achieved a 53.03 % reduction of the initial SAR value for the case of 1 g SAR and a 68.08 % reduction for the case of 10 g SAR.

Keywords: antenna, head model, SRRs, SAR

V članku je prikazan razvoj resonatorja iz deljivih obročev (SRR), ki so sestavljeni iz dveh koncentričnih obročev kvadratnega prereza iz prevodnega materiala, ki kaže pomemben električni odziv pri mikrovalovni frekvenci. Oba kvadratna obroča imata režo in vsak obroč je nasprotno nameščen v reži drugega obroča. Zmanjšanje velikosti teh struktur je vedno mogoče, vendar pa je treba biti pozoren na načrtovano frekvenco. Trdimo, da je kvadratna oblika metamateriala popolnoma nov dizajn v okviru glave in roke za zmanjšanje stopnje absorpcije (SAR). Eden od pomembnih razlogov, zakaj je bila ta oblika uporabljena, je možnost več postavitev v danem področju. Mobilni telefoni so razmeroma majhni in zahtevajo majhne naprave iz metamaterialov. Domena končnih časovnih razlik z uporabo modela lossy-Drude je bila uporabljena v tej študiji uporabljajoč CST Microwave Studia®. Prikazana je tehnika zmanjšanja SAR ter preiskovanih učinkov priloženih pozicij, razdalje in velikosti kvadratnega metamateriala na zmanjšanje SAR. S kvadratno obliko metamateriala je bilo doseženo 53,03-odstotno zmanjšanje začetne vrednosti SAR pri 1 g SAR in 68,08-odstotno zmanjšanje pri 10 g SAR.

Ključne besede: antena, model glave, SRR, SAR

1 INTRODUCTION

Recently, there has been an increasing public concern about the health risk caused by electromagnetic (EM) waves emitted from cellular phones. These phones send their signals using very small surges of high-frequency EM waves, or microwaves, favored over most over-the-air telecommunication systems. The fundamental safety limits for the radio-frequency (RF) revelation are defined in terms of the immersed power per unit mass, which is expressed by the specific absorption rate (SAR) in watts per kilogram (W/kg). These protection guidelines are set in terms of the utmost mass-normalized rates of the electromagnetic energy deposition (SARs) for 1 g or 10 g of tissue. The two most generally used SAR limits today are IEEE, 1.6 W/kg for 1 g of tissue, and ICNIRP [1–8], 2 W/kg for 10 g of tissue, disregarding the extremities such as ankles, hands, and feet, where higher SARs, up to 4 W/kg for any 10 g of tissue, are allowed in both of these standards. Therefore, SAR becomes an important performance parameter for the marketing of mobile phones and underlines the interest in low-SAR mobile phones by both consumers and mobile-phone manufactures.

SAR is the parameter employed to properly quantify the response of the biological structure in terms of incident and induced field of the energy absorbed and maintained inside the human body. It is the time derivative (rate) of the incremental energy (dW) absorbed by or dissipated in an incremental mass (dm) contained in a volume element (dV) of a given density (ρ), as seen in (1):[4]

$$SAR = \frac{\mathrm{d}}{\mathrm{d}t}\left(\frac{\mathrm{d}W}{\mathrm{d}m}\right) = \frac{\mathrm{d}}{\mathrm{d}t}\left(\frac{\mathrm{d}W}{\rho \mathrm{d}m}\right) \quad (1)$$

The SAR is expressed in units of watts per kilogram (W/kg) or, equivalently, in milliwatts per gram (mW/g). It can also be related to the induced electrical field using (2):

$$SAR = \sigma E^2/\rho \quad (2)$$

where E is the electric field's root mean square (V/m), σ is the biological tissue's electrical conductivity (S/m) and ρ is the biological tissue's density (kg/m^3).

The demand on the portable mobile devices is increasing progressively with the development of novel wireless communication techniques. In this respect, compact size, light weight, low profile and low cost are now quite important challenges to be accomplished by the designers of any wireless mobile component. One of the most important components of any wireless system is its radiating element. In addition to the physical requirements, the emerging requirements of wireless systems are a high directivity, a large gain, and an efficient and broadband operability of the antennas. Many broadband techniques have been investigated to overcome the trade-off between the antenna size and the minimum achievable quality factor, which is dictated by Chu formulations[9]. These techniques are mainly increasing the thickness of the substrate, using differently shaped slots or radiating patches[10–14], stacking different radiating elements or loading the antenna laterally or vertically[12–17], utilizing magneto-dielectric substrates[18] and engineering the ground plane as in the case of EBG metamaterials[9].

Metamaterials are artificially structured materials providing electromagnetic properties not encountered in nature. A left-handed material was first implemented in a two-dimensional periodic array of split-ring resonators and long wire strips by Smith[19]. The logical approach was to excite the split-ring resonators and wire strips in order to force the structure to behave like magnetic and electric dipoles, respectively[12].

In references[20,21] it was found that the SAR value is affected by various parameters, such as the attachment position of conductive materials, the sizes and configurations of the antenna ground plane. In the reference[22] studies, a reflector used for a SAR reduction was inserted between the radiator and the head. Other studies applied ferrite sheets[2], shielding materials[23,24], resistive sheets[9], and artificial magnetic conductors[13] to reduce the EM field around the antenna.

Recently, metamaterials, including electromagnetic band-gap (EBG) structures, have been proposed for handset antennas with low SAR characteristics.

Metamaterials combining a negative permittivity and permeability, i.e., negative index materials (NIMs), can be obtained by using tiny electrical circuits called split-ring resonators and continuous wires as the metamaterial constituent units.

The specific absorption rate (SAR) in the head can be reduced by placing the metamaterials between the antenna and the head. In the case of studying the SAR reduction of an antenna operating at the GSM 900 band, the metamaterial parameter (i.e., the permittivity is $\varepsilon < 0$, hence, the refractive index is $n < 0$) and the effective medium would be set negative. Hence, the effectiveness of different positions, sizes, and metamaterials with various parameters are also analysed for SAR reduction.

2 MATERIALS AND METHODS

CST MWS is a device used as a major simulation instrument based on the finite-integral time-domain technique (FITD). An unvarying meshing scheme was chosen to make the major computation devoted to inhomogeneous mark boundaries and aimed at the fastest and faultless results. Two-cut schemes are needed for a complete model to show the region with the closely com-

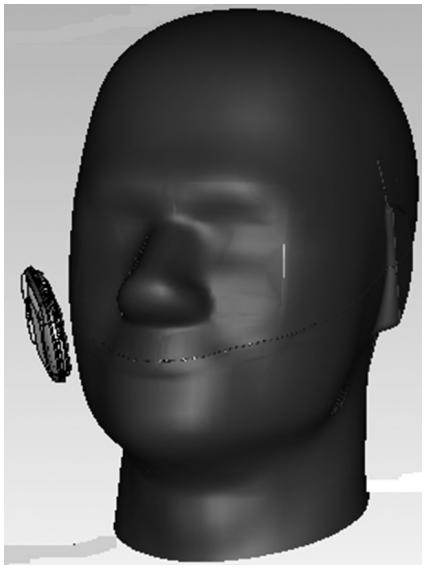

Figure 1: Head model with a handset antenna
Slika 1: Model glave z ročno anteno

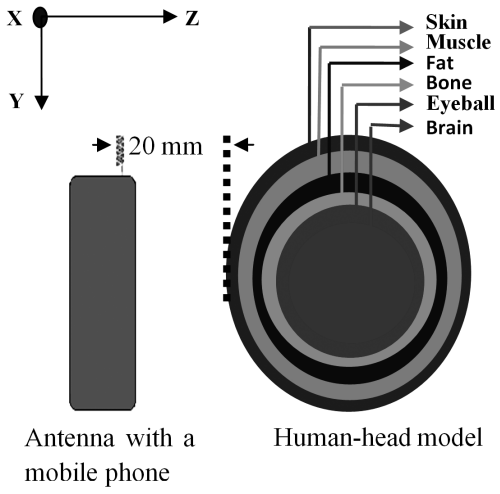

Figure 2: Head model with a mobile phone for a SAR calculation
Slika 2: Model glave z mobilnim telefonom za izračun SAR

pacted meshing onward to inhomogeneous boundaries. Here the lowest and highest mesh sizes were 0.3 mm and 1.0 mm, respectively. As a result, a total of 2 122 164 mesh cells were generated and the simulation time was 1208 s, including the mesh generation for each effort on an Intel Core ™ 2 Duo E 8400 3.0 GHz CPU with a 4 GB RAM system, for a complete model. It is noted here that at first the materials are placed between the antenna and the human head, and then all of these are replaced by a metamaterial.

For this research, the SAM head model was considered. It consists of about 2 097 152 cubical cells at a 1 mm resolution. **Figure 1** represents a portable telephone model with a handset antenna considered in the SAR calculation.

The head models used in this study were obtained from an MRI-based head model through the whole-brain Atlas website. Six types of tissues, i.e., bone, brain, muscle, eye ball, fat, and skin were involved in this model[9,19]. A space domain enclosing the human head and the phone model is also shown in **Figure 2**. **Tables 1** and **2** show their dielectric properties for 900 & 1800 MHz. Numerical simulations of the SAR value were performed by the FDTD method. The parameters for the FDTD computation were as follows. The simulation domain was 128 × 128 × 128 cells. The cell sizes were set as $\Delta x = \Delta y = \Delta z = 1$ mm. The computational domain was terminated with 8 cells of a perfectly matched layer (PML). A PIFA antenna was modeled with a thin-wire approximation.

Table 1: Dielectric tissue properties at 900 MHz
Tabela 1: Dielektrične lastnosti tkiva pri 900 MHz

Material	Density ρ/(kg m^{-3})	Conductivity σ/(S m^{-1})	Relative permittivity, ε_r
Fat, bone	1130	0.12	4.83
Muscle, skin	1020	1.5	50.5
Brain	1050	1.11	41.7
Eye ball	1000	2.03	68.6

Table 2: Dielectric tissue properties at 1800 MHz
Tabela 2: Dielektrične lastnosti tkiva pri 1800 MHz

Material	Density ρ/(kg m^{-3})	Conductivity σ/(S m^{-1})	Relative permittivity, ε_r
Fat, bone	1130	0.11	4.48
Muscle, skin	1020	1.35	47.80
Brain	1050	1.09	39.50
Eye ball	1000	1.99	65.3

3 SRRS STRUCTURE AND DESIGN

With this work we established that, using the FDTD analysis, square metamaterials (SMMs) can reduce the peak SAR for 1 g and SAR for 10 g in the head. In this section, the SMMs are evaluated in a cellular phone with the 900 MHz and 1800 MHz bands. Periodically arranged square split-ring resonators (SSRRs) can work

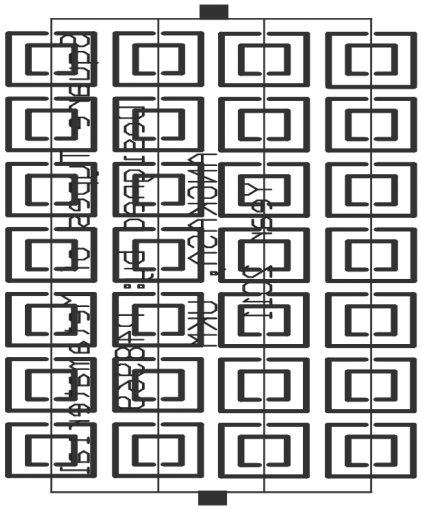

Figure 3: Square Metamaterial arrays used in this calculation
Slika 3: Kvadratna razporeditev metamateriala, uporabljena pri izračunu

as SMMs. The SSRR structure involves two conductive-material, concentric square rings. Both square rings have a gap, and each ring is placed in the gap of the other ring. The schematic of the SSRR structure used in this study is shown in **Figure 3**.

To construct the SMMs for a SAR reduction, SSRRs were used as the resonator model, as shown in **Figure 3**. The resonators operated in the 900 MHz bands. The SSRRs contain two square rings, each with a gap on the opposite side[5]. The SSRRs were introduced by Pendry et al.[11] (1999), and subsequently used by Smith et al. (2000) to synthesize the first left-handed artificial medium[19].

Figure 4 shows the fabricated SMM arrays used in this measurement. The metamaterials in this work were designed with periodic SSRR arrangements to reduce the

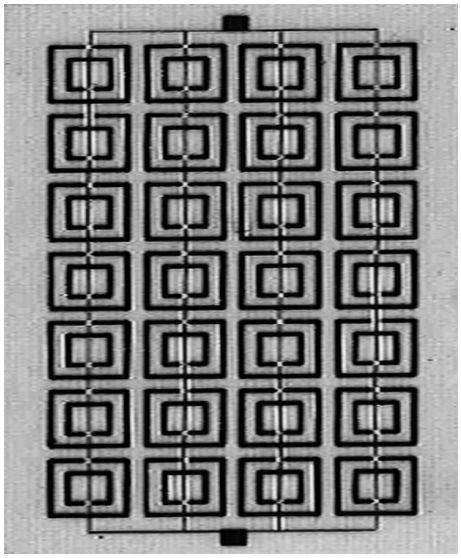

Figure 4: Fabricated square metamaterial arrays used in this research
Slika 4: Izdelana kvadratna razporeditev metamateriala, uporabljena v tej raziskavi

SAR value. By properly designing the SSRR structure parameters, a negative effective medium parameter can be achieved for the 900 Hz and 1800 Hz bands.

4 NUMERICAL RESULTS AND DISCUSSION

The designed SSRRs were placed between the antenna and the human head, thus reducing the SAR value. To study the SAR reduction of the antenna, operating at the GSM 900 band, different positions, sizes, and metamaterials for the SAR-reduction effectiveness are also analyzed by using the FDTD method in conjunction with a detailed human-head model. The antenna was put equidistant to the head axis. The distances from 5 mm to 20 mm were checked and ultimately the distance of 20 mm was selected. Moreover, the maximum SAR reduction was achieved when the proposed structure was placed to the near side of the cellular phone. In the present paper, the power output of the mobile was considered to be 600 mW at the operational frequency of 900 MHz. In the case when the main network station is far from the mobile phone, the actual power is 1 W to 2 W. The highest values were 2.002 W/kg for SAR 1 g and 1.293 W/kg for SAR 10 g, calculated when the cellular phone model was at a distance of 20 mm from the human-head model and without any metamaterial attachment. Obviously, this SAR reduction is more desirable than the metamaterial free attachment. The results quoted in[12,7] are 2.28 W/kg and 2.17 W/kg for SAR 1 g. This is due to the use of different antennae placed in different locations relative to the head model. These SAR values agree with the compared result reported in[5], i.e., 2.43 W/kg for SAR 1 g. This was achieved using different radiating powers and different antenna.

To study the effect of a SAR reduction with the use of SMMs, the radiated power from the PIFA antenna with $\mu = 1$ and $\varepsilon = -3$ was fixed at 600 mW. Calculating SAR at 900 MHz, we obtained the value of 1.673 W/kg for SAR 10 g without a metamaterial; however, in the case of a metamaterial, the reduced SAR value for 10 g was 0.737 W/kg. Thus, a reduction of 55.95 % was achieved, whereas the sketch furnish design in[5] acquired a 32.03 % reduction. The reasons for this difference are different densities, antennae, sizes of the metamaterial and types of conductivity. The result implies that only suppressing the maximum current on the front side of the conducting box contributes significantly to the reduction of the spatial-peak SAR, as the decreased quantity of the power absorbed in the head is considerably larger than that dissipated in the metamaterials. It is clear from the simulation results that metamaterials can reduce the peak SAR successfully where the antenna reduction is merely pretended. So, both the inner capacitance and inductance of the metamaterials are reinforced. At this stage, the mediums will exhibit stop band walks with a single negative medium parameter.

5 EXPERIMENTAL EVALUATIONS

The SAR measurement was performed using the COMOSAR measurement system. The system uses a robot to position the SAR probe inside the head phantom. The head phantom is filled with a liquid that has dielectric properties selected on the basis of the IEEE standard 1528, which are $\varepsilon_r = 41.5$ and $\sigma = 0.97$ S/m for 900 MHz and $\varepsilon_r = 40$ and $\sigma = 1.4$ S/m for 1800 MHz. The measured and simulated SAR values without the inclusion of TMMs are shown in **Table 3**.

Table 3: SAR simulation and measurement results without the inclusion of TMMs (distance between the head and the phone model, d = 20 mm)

Tabela 3: Simulacije SAR in rezultati meritev brez upoštevanja TMMs (razdalja med glavo in modelom telefona, d = 20 mm)

	Value of SAR	
	SAR 1 g	SAR 10 g
Simulated	2.002	1.673
Measured	1.936	1.609

Table 3 shows that the simulated SAR value is greater than 3.29 % for SAR 1 g and 3.82 % for SAR 10 g due to the fact that the distance between the head and phone model was not correctly set at the measurement stage. In addition, the distance between the source and the internal surface of the phantom affects the SAR. For a 5-mm distance, a positioning uncertainty of ±0.5 mm would produce a SAR uncertainty of ±20 %. An accurate device positioning is therefore essential for accurate SAR measurements.

The simulated and measured SARs are obtained using the tilted position of the SMMs with the antenna revealing the simulated and measured SAR values of 1.1673 W/kg and 1.0623 W/kg for SAR 1 g, respectively. The simulated and measured SARs differed by 6.27% for SAR 1 g. Regarding the difference in the absolute values of the peak SAR, the phone-model casing for the simulation was different from the casing used for the measurement. In addition, Scotch tape was used to attach the SMMs and antenna at the measurement stages. The simulated and measured results also differ because the parameters for the measurement system change with water evaporation and temperature. Furthermore, the measurement system contains several parameters (source, network emulator, probe, electronic evaluation procedures) that affect the SAR calculation but are not included in the simulation.

6 CONCLUSION

The process of the EM absorption between an antenna and the human head, while using new SMMs, has been thoroughly and intensively experimented and presented in this paper. After examining the substance of the developed SMMs for the phone model, the SAR values were found to be about 0.639 W/kg for SAR 10 g

and 1.0623 W/kg for SAR 1 g. These results will be the core points when providing information in the field of designing communication equipment, safe from interruptions.

7 REFERENCES

[1] M. R. I. Faruque, M. T. Islam, N. Misran, Progress In Electromagnetics Research, PIER, 124 (**2012**), 119–135

[2] M. T. Islam, M. R. I. Faruque, N. Misran, Progress In Electromagnetics Research, PIER, 98 (**2009**), 191–205

[3] M. R. I. Faruque, M. T. Islam, N. Misran, Medical Engineering & Physics, 33 (**2011**), 646–652

[4] M. R. I. Faruque, M. T. Islam, N. Misran, Electromagnetics Journal, 31 (**2011**), 215–232

[5] J. N. Hawang, Fu-chiarng chen, IEEE Trans. on antenna and propagat., 54 (**2006**), 3763–3770

[6] M. T. Islam, M. R. I. Faruque, N. Misran, Informacije MIDEM, 40 (**2010**), 238–240

[7] C. M. Kuo, C. W. Kuo, in IEEE-APS Int. Symp. Dig., Columbus, OH, (**2003**), 1025–1028

[8] M. R. I. Faruque, M. T. Islam N. Misran, Applied Computational electromagnetic society Journal (ACES Journal), 25 (**2010**), 1097–1107

[9] H. H Chou, H. T. Hsu, H. T. Chou, K. H. Liu, F. Y Kuo, Progress in Electromagnetic Research, 94 (**2009**), 281–296

[10] M. R. I. Faruque, M. T. Islam, N. Misran, Frequenz Journal, 64 (**2010**), 144–149

[11] J. B. Pendry, A. J. Holen, D. J. Robbins, W. J. Stewart, IEEE Trans. Microwave Theory Tech., 47 (**1999**), 2075–2084

[12] J. Wang, O. Fujiwara, IEEE Trans. Microwave Theory Tech., 47 (**1999**), 1528–1534

[13] R. Y. S. Tay, Q. Balzano, N. Kuster, IEEE Trans. Antennas Propagat., 46 (**1998**), 798–806

[14] D. Sievenpiper, IEEE Trans. Microw. Theory Tech., 47 (**1999**), 2059–2074

[15] N. Kuster, Q. Balzano, IEEE Trans. Veh. Technol., 41 (**1992**), 17–23

[16] R. W. Ziolkowski, IEEE Trans. Antennas Propag., 51 (**2003**), 1516–1529

[17] M. Bayindir, K. Aydin, E. Ozbay, Appl. Phys. lett., 81 (**2002**), 120–122

[18] M. T. Islam, M. R. I. Faruque, N. Misran, IEICE Electronics Express, 7 (**2010**), 240–246

[19] D. R. Smith et al, Phys. Rev. Lett., 84 (**2000**), 4184–4187

[20] K. H. Chan, K. M. Chow, L. C. Fung, S. W. Leung, Microwave Optical Tech. Lett., 44 (**2005**), 140–144

[21] A. Hirata, T. Adachi, T. Shiozawa, Microwave Optical Tech. Lett., 40 (**2004**), 272–275

[22] L. C. Fung, S. W. Leung, K. H. Chan, Microwave Optical Tech. Lett., 36 (**2003**), 419–422

[23] S. Lee, N. Kim, 34th annual conference of the bioelectromagnetics society, 2012, 49–50

[24] M. R. I. Faruque, M. T. Islam, N. Misran, Frequenz Journal, 66 (**2012**), 79–83

UDK 669-982:669.15
Professional article/Strokovni članek

ISSN 1580-2949
MTAEC9, 47(1)135(2013)

POSSIBILITIES FOR DESULPHURIZATION OF AN ALLOY STEEL IN A VOD DEVICE WHILE USING CHEMICAL HEATING

MOŽNOST RAZŽVEPLJANJA LEGIRANEGA JEKLA V VOD-NAPRAVI Z IZKORIŠČANJEM KEMIJSKEGA OGREVANJA

Karel Michalek[1], Libor Čamek[1], Karel Gryc[1], Tomáš Huczala[2], Vladimír Troszok[2]

[1]VŠB-Technical University of Ostrava, FMME, Department of Metallurgy and Foundry, 17. listopadu 15/2172, 708 33 Ostrava, Czech Republic
[2]Třinecké železárny, a. s., Průmyslová 1000, 739 70 Třinec-Staré Město, Czech Republic
karel.michalek@vsb.cz

Prejem rokopisa – received: 2012-09-03; sprejem za objavo – accepted for publication: 2012-09-18

The paper describes the knowledge about and results of the experimental heats performed in an electric steel plant. The aim was to verify the possibilities of a controlled desulphurization of alloy steel in a VOD (Vacuum Oxygen Decarburization) device, particularly when using chemical heating through the OVD process (Oxygen Vacuum Deoxidation/Degassing), as well as the standard slag formers. Experimental procedures were used in the production of alloy tool steel. Both, the system of making the reducing slag and optimizing the composition of individual oxides in order to achieve the desired basicity, are complicated by the products of the chemical heating. Therefore, it was necessary to develop a new production technology that would eliminate such oxide products of chemical heating and, thus, the maximum degree of desulphurization could be achieved. The main principle of the technology is to create appropriate thermodynamic and kinetic conditions required for desulphurization. In particular, this concerns a low oxygen activity in the steel, the composition of refining slag, and an intense bath stirring with argon.

Keywords: steel desulphurization, VOD device, OVD process, slag, steel cleanliness

Članek opisuje znanje in rezultate raziskave eksperimentalnih talin, izdelanih v elektrojeklarni. Namen je bil preveriti možnost kontroliranega razžvepljanja legiranega jekla v VOD (Vacuum Oxygen Decarburization)-napravi, posebno med uporabo kemijskega ogrevanja med OVD (Oxygen Vacuum Deoxidation/Degassing)-postopkom, kot tudi standardnih gradnikov žlindre. Eksperimentalni postopki so bili uporabljeni pri proizvodnji legiranega orodnega jekla. Oboje, tvorba reduktivne žlindre in optimalna sestava posameznih vključkov, z namenom doseganja želene bazičnosti, ovirajo produkti kemijskega ogrevanja. Zato je bilo potrebno razviti novo tehnologijo proizvodnje, ki bi preprečila oksidne produkte kemijskega ogrevanja, kar bi omogočilo doseganje maksimalne stopnje razžvepljanja. Osnovni princip nove tehnologije je zagotoviti ustrezne termodinamične in kinetične pogoje, potrebne za razžvepljanje. To pomeni nizko aktivnost kisika v jeklu, sestavo rafinacijske žlindre in intenzivno mešanje kopeli z argonom.

Ključne besede: razžvepljanje jekla, VOD-naprava, OVD-postopek, žlindra, čistost jekla

1 INTRODUCTION

The technology of the production of alloy tool steels require a special preparation of the input materials, followed by a strict compliance with technological and metallurgical processes when producing steel in a 10-ton electric arc furnace (EAF), as well as the ladle's optimal preparation. The final steel processing in a VOD device requires a continuous and systematic management of individual production stages, in particular the chemical heating, creating a high vacuum, production of reduction and refining slag[1,2], additional steel alloying, and continuous, optimal purification with argon.

The required steel desulphurization in the VOD device can only be achieved by mastering the technology and metallurgy of the processes, especially by optimizing the slag regime and complying with the basic thermodynamic and kinetic conditions of a desulphurization reaction.

2 PRINCIPAL FACTORS AFFECTING THE REQUIRED DEGREE OF STEEL DESULPHURIZATION

In the paper formerly presented[3], the technology of the low-sulphur-content steel production (up to the mass fraction w = 0.002 %) in the conditions of EAF using CaO and Refraflux additives was described in detail. With regard to the product range of tool steels, desulphurization technology in the VOD device with an oxidation stage at the beginning of the process, used for the chemical heating of steel, has been assessed and gradually developed.

The desired degree of desulphurization in a vacuum station when applying chemical heating is largely limited by the output sulphur content from EAF. In the production of alloy steel grades in VOD, the chemical-heating method creates entirely different starting conditions for the formation of the reducing slag compared to the standard technological processes in EAF. Nevertheless,

the reduction conditions ensuring a successful desulphurization of steel can be created using special procedures in this relatively harsh environment.

Standard patterns of the desulphurisation of steel and their review are listed in our earlier works[3,4]. The principles that must be met in order to obtain low sulphur content in steel can be summarized into the following:

- A high level of activity of free-oxygen anions in the slag, i.e., a high basicity of the slag with a high proportion of alkaline oxides and a low proportion of acidic oxides.
- A low activity of oxygen a_o in steel, i.e., a low content of dissolved oxygen and a low value of the activity coefficient f_o.

A negative factor affecting the degree of steel desulphurization is the presence of the "easily reducible" oxides in the refining slag – besides FeO there are also MnO, P_2O_5 and Cr_2O_3. The sum percentage content of the aforementioned elements for a well-working refining slag is usually recommended to be up to the mass fraction $w = 3$ %.

From the kinetic point of view, an increased temperature positively affects steel desulphurization. An increase in the temperature helps us decrease the viscosity of the slag and metal, increase the sulphur diffusion coefficient, and allows a reduction in the surface tension, which results in the chemical reaction more quickly reaching the state of equilibrium. However, the effect of appropriate kinetics of the ongoing processes is closely connected with meeting the basic thermodynamic conditions.

Creating appropriate conditions for desulphurization in the steel processing in VOD upon the use of chemical heating requires a specific technology. A negative factor after the chemical heating in VOD is a gradual decrease in the temperature. In a formed temperature interval, and in a gradual cooling of the steel, it is necessary to carry out all the necessary technology operations to create suitable thermodynamic and kinetic conditions for the desired degree of desulphurization.

3 CURRENT TECHNOLOGICAL AND METALLURGICAL PROCEDURES OF FORMING A REDUCING SLAG

The original technology of the alloy-steel production with a low sulphur content that is below 0.005 % was based on the standard charge of recyclable waste. Thus, it was ensured that the critical sulphur content would not be exceeded during the processing in EAF, and that the desired sulphur content of below $w = 0.005$ % would be reached in the VOD device using the chemical heating (based on Al + O_2).

For the actual production process the calcium slag containing calcium fluorite (CaF_2) was used in the electric steel plant of TŘINECKÉ ŽELEZÁRNY, a. s. (TŽ, a. s.). The positive effect of CaF_2 supporting the thermodynamics and also the kinetics of the required processes is widely known and has already been discussed in our earlier work[3]. The disadvantages of using fluorite are the reduction of the lifetime of the lining of furnaces and ladles, and its adverse impact on the working environment (formation of fluorites).

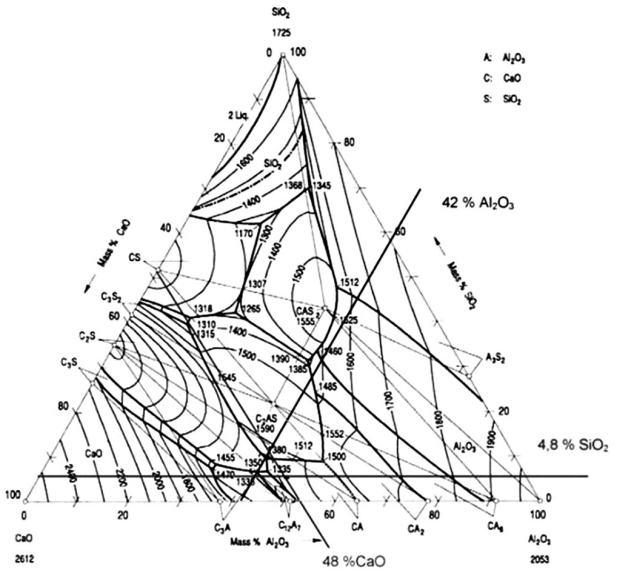

Figure 1: Area of the chemical composition of the tested synthetic slag REFRAFLUX 4842 S in the ternary diagram Al_2O_3-CaO-SiO_2[5]
Slika 1: Področje kemijske sestave preizkušene sintetične žlindre REFRAFLUX 4842 S v ternarnem diagramu Al_2O_3-CaO-SiO_2[5]

Currently, in the production of alloy steels in EAF the fluorite is being replaced with a high-quality, industrially produced synthetic slag. The chemical composition of the tested synthetic slag is shown in the ternary diagram[5] in **Figure 1**. The slag-formation reduction technology with a high refining effect is based on the application of a mixture of quicklime and synthetic slag Refraflux, where both components are transported using alternating dosing to the surface of the bath in EAF.

The original slag additive – fluorite – stays in use to create the reducing slag in the secondary-metallurgy processing VOD device. The main reason is the need for the use of chemical heating with aluminium, where the product of this chemical reaction – Al_2O_3 – negatively affects the system of chemical optimization of the reducing-slag composition, as well as the secondary products of oxidation of FeO, MnO and Cr_2O_3. The standard requirement for the range of chemical heating in the production of alloy-steel grades is 130–180 °C, which leads to a significant increase in the content of Al_2O_3 in the slag after oxidation.

4 PRODUCTION CONDITIONS AND PROCEDURES FOR EXPERIMENTAL HEATS

Production processes for desulphurization have been tested on VOD using the technology of chemical heating

(OVD) in the production of the alloy tool-steel grade 19569 (X63CrMoV5.1). **Table 1** shows the internal release chemical composition of the steel grade 19569.

Table 1: Internal release chemical composition of 19569 steel in mass fractions, *w*/%
Tabela 1: Interna kemijska sestava jekla 19569 v masnih deležih, *w*/%

Chemical composition	**19569** (X63CrMoV5.1) *w*/%
C	0.58–0.68
Si	0.7–1.1
Mn	0.25–0.55
P	max. 0.015
S	max. 0.010
Cr	4.5–5.5
Mo	0.8–1.2
V	0.2–0.4
W	max. 0.6

The output from EAF is the sulphur content of w = 0.005 % achieved as a standard, which can be, during the subsequent processing with the VOD technology using chemical heating, maintained at the achieved level or reduced below the given limit.

The technological process involved the following operations:

- Dislodging the reducing slag from the ladle after tapping EAF. This part of the technology is, from the perspective of preventing the reverse transition of sulphur from the slag into the metal and the possibility of creating a new reducing slag, very favourable. However, it also negatively affects the heat loss through the uncovered steel surface, which increases the need for the strength of the chemical heating.
- A creation of a new cover slag on the steel surface. This was carried out by applying the basic charge of 50 kg lime and by adding again the same charge of lime in addition to an approximately 20 kg of fluorite upon the installation of the casting ladle (CL) into the VOD device.
- An addition of aluminium and oxygen-blowing in one or two stages combined with chemical heating, in this way the temperature was increased by 150–200 °C above the liquidus temperature of the alloy steel grade produced.
- A gradual formation of a non-foaming reducing slag caused by the lime additive.
- Steel evacuation to perform a vacuum deoxidation and to create conditions for increasing the cleanliness of the steel including its precise additional alloying.
- Temperature and chemical homogenization with argon at atmospheric pressure, whose duration was set by the temperature margin of the gradual, controlled cooling, within which the treatment of the chemical composition of the reducing slag was carried out, or small corrections to the chemical composition of the alloy tool steel were made.
- After reaching the required steel temperature above the liquidus, the processing in VOD was completed and the casting into the moulds was done.

In the process of gradual cooling from the temperatures after the chemical heating, it was difficult to approach the optimum values of the chemical composition of the reducing slag, which should contain mass fractions from 45 % to 55 % CaO, 18 % to 25 % Al_2O_3, ≤ 10 % SiO_2. At the same time and in accordance with the theory of steel desulphurization, it was also very important to maintain a low oxygen activity in the metal. This requirement has been, in terms of the VOD device, met particularly by maintaining the maximum possible content of aluminium in the liquid metal. Suitable kinetic conditions were continuously provided with the optimum control – blowing argon through the bottom porous block with the volumetric flow rates of up to 20 l min^{-1}.

5 ACHIEVED RESULTS

The course of each experimental heat was, in the secondary metallurgy VOD with chemical heating, to some extent, unique. A total of 10 heats were produced. The aim was to verify the options of the controlled steel desulphurization in the VOD device using chemical heating (OVD) as well as the standard slag-forming additives. The comparison of the basic chemical analyses of the slag and steel of the selected 19569 heat grade tested is shown in **Table 2.**

The achieved results describing the composition of the final reducing slag after the steel processing show some differences, especially the differences for Al_2O_3 and SiO_2 oxides. These variations result from individual processing procedures in the VOD device in relation to the method of how to control chemical heating. In most of the heats the CaO/Al_2O_3 ratio ranged from 1.0 to 2.63, and the basicity (CaO/SiO_2) was in the range from 2.15 to 10.

Table 2: Selected chemical analyses of the final reducing slag and steel grade 19569 in mass fractions, *w*/%
Tabela 2: Izbrane kemijske analize končne redukcijske žlindre jekla 19569 v masnih deležih, *w*/%

Heat No.	CaO	Al_2O_3	MgO	SiO_2	FeO	Cr_2O_3	MnO	S_{steel}	Temperature before chemical heating	Temperature after chemical heating
4	35.49	35.82	2.74	13.22	0.35	0.19	0.17	0.0030	1559 °C	1682 °C
9	40.62	26.38	3.46	18.88	1.03	0.66	0.74	0.0030	1529 °C	1685 °C
6	41.00	31.70	5.20	13.90	0.19	0.32	0.45	0.0030	1544 °C	1723 °C
7	48.37	18.40	4.40	4.80	0.28	0.09	0.01	0.0020	1575 °C	1734 °C

In terms of a successful desulphurization it was very important to maintain the parameters of the input chemical analyses and to optimize the steel temperatures before and after the chemical heating in the VOD device so that the composition of the arising reducing slag was not subsequently tasked, in particular by a high content of aluminium oxide.

During the subsequent processing following the chemical heating it was necessary to continue the adding of lime and, based on the visual inspection results, to substitute the additive for its liquefaction. Based on the information obtained from the chemical analysis, it was recommended to only alloy the materials that do not allow batching the VOD device during the next phase of vacuuming.

The changes in the chemical compositions of the steel and the slag during the processing in the secondary-metallurgy VOD device are shown in **Figures 2** to **5**.

In terms of reducing the slag formation, any deviation from the recommended technology causes deflection from its optimum composition, which prevents the alloy steel from achieving the required degree of desulphurization.

The processing of the No. 4 heat can be shown as an example (**Figure 2**). A low content of CaO in the reducing slag did not ensure a further desulphurization of the steel, so that the resulting sulphur content was identical to the initial content (30 µg/g).

A similar course of processing can be noted in the cast No. 9 (**Figure 3**), which resulted in a relatively rapid drop in the temperature (due to the insufficient heat capacity of the ladle) following the completion of the vacuuming phase, leading to an unsatisfactory content of CaO in the reducing slag due to the worsened assimilation of lime. The final sulphur content of the heat was identical to the initial content (30 µg/g).

From the course of processing the heat No. 6 (**Figure 4**), where the input sulphur content was 40 µg/g – it is clear that after the completion of the vacuuming phase the sulphur content was increased to 70 µg/g. The result of the repeated measurement of the oxygen activity in the steel showed a higher value (7.3 µg/g), which was probably associated with a low total aluminium content in the steel (w = 0.001 %). The subsequent additional deoxidation by aluminium in the phase of the controlled additional cooling decreased this activity (to 1.7 µg/g), but, on the other hand, it shifted the optimum composition of the reducing slag (too high a content of Al_2O_3). Through specified treatments we managed to keep the resulting sulphur content at the value of 30 µg/g.

The process of operating the experimental heat No. 7, whose course is shown in **Figure 5**, has been found to be

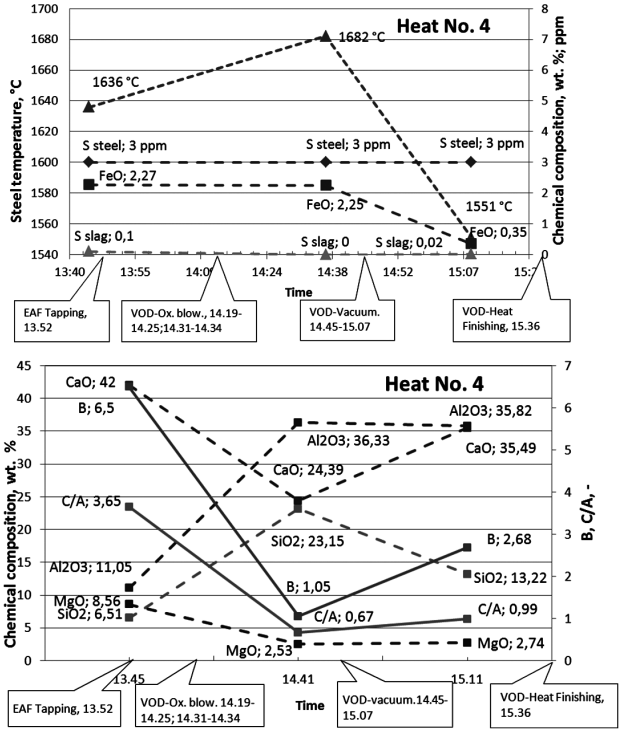

Figure 2: Development of the chemical composition of the steel and the slag during the secondary-metallurgy processing in the VOD device with chemical heating in the heat No. 4

Slika 2: Razvoj kemijske sestave jekla in žlindre med procesom sekundarne metalurgije v VOD-napravi s kemijskim segrevanjem taline št. 4

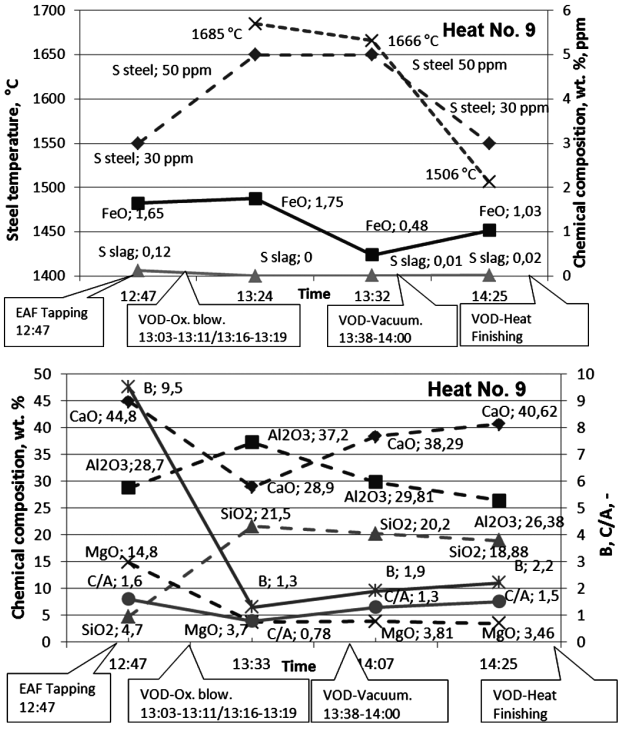

Figure 3: Development of the chemical composition of the steel and the slag during the processing in the secondary-metallurgy VOD device with chemical heating in the heat No. 9

Slika 3: Razvoj kemijske sestave jekla in žlindre med procesom sekundarne metalurgije v VOD-napravi s kemijskim segrevanjem taline št. 9

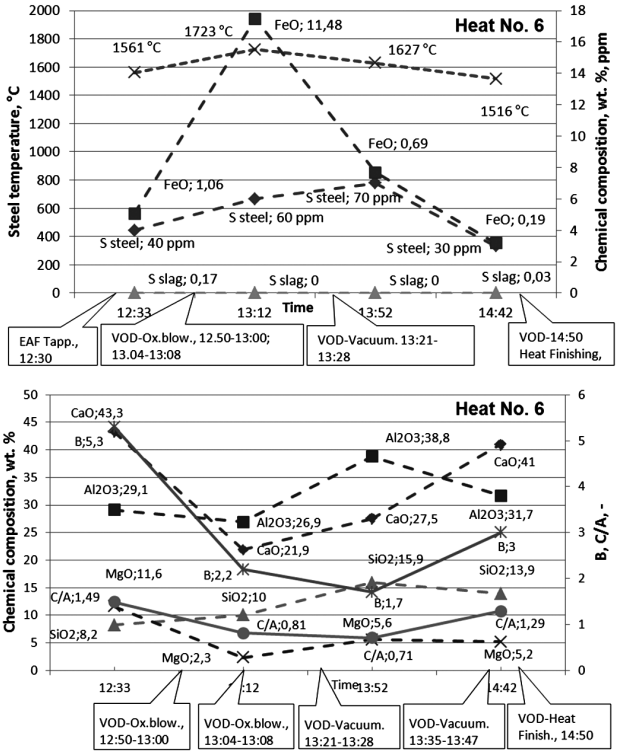

Figure 4: Development of the chemical composition of the steel and the slag during the processing in the secondary-metallurgy VOD device with chemical heating in the heat No. 6

Slika 4: Razvoj kemijske sestave jekla in žlindre med procesom sekundarne metalurgije v VOD-napravi s kemijskim segrevanjem taline št. 6

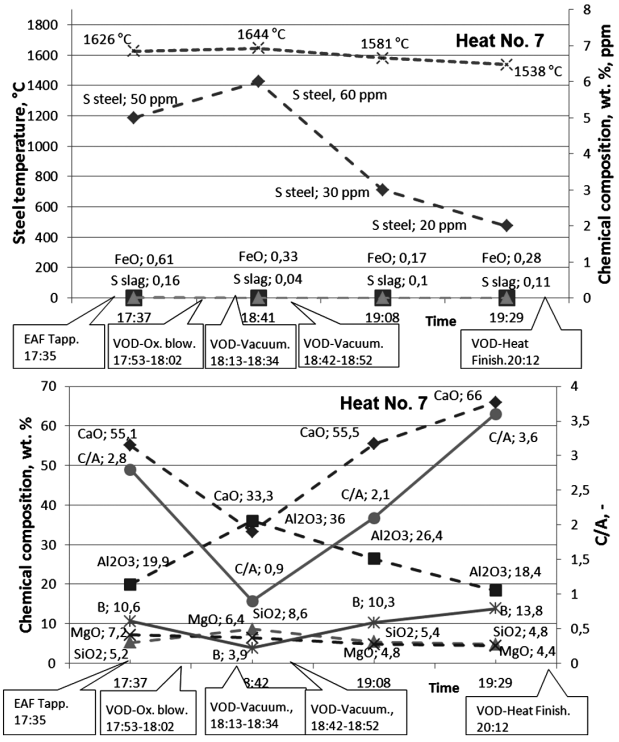

Figure 5: Development of the chemical composition of the steel and the slag processing in the secondary-metallurgy VOD-device with chemical heating in the heat No. 7

Slika 5: Razvoj kemijske sestave jekla in žlindre med procesom sekundarne metalurgije v VOD-napravi s kemijskim segrevanjem taline št. 7

the optimal course of the steel processing in the secondary-metallurgy VOD device with chemical heating. The initial sulphur content in the steel of 50 µg/g was, after meeting the recommended procedures for the steel-processing technology, reduced to the resulting content of 20 µg/g. What contributed to this result were not only a suitable composition of the reducing slag (CaO > 50 %, B > 5, CaO/Al_2O_3 > 2, FeO < 0.3 %), and a low oxygen activity in the steel (1.4 µg/g), but also the stirring of the steel.

6 IMPACT OF TECHNOLOGY ON CLEANLINESS OF STEEL

The carried-out experimental heats were assessed in terms of the achieved cleanliness of the steel. An electron microanalyzer Hitachi S-3500N was used for the evaluation, on the basis of which we determined the framework compositions of non-metallic inclusions, their numbers and geometrical proportions. The achieved results for the heats No. 6 and No. 7 are shown as the ternary diagrams in **Figure 6**. As for these heats, the lime additive was, in the final phase of the controlled additional cooling, added with no fluorite additive. This led to a cooling of the reducing slag, increasing its viscosity, and a worsening of the kinetic conditions for

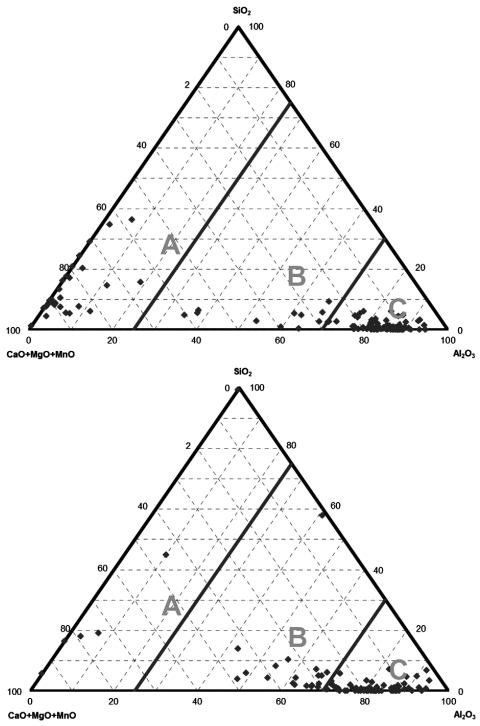

Figure 6: Ternary diagrams as a result of the chemical microanalysis of the inclusions from the heats No. 6 and No. 7

Slika 6: Ternarni diagrami kot rezultat kemijske mikroanalize vključkov iz talin št. 6 in št. 7

the absorption of non-metallic inclusions, which also led to a higher incidence of the inclusions based on $CaO\text{-}Al_2O_3$. The micro-purity results for the other experimental heats were standard.

7 CONCLUSION

The production technology of the controlled steel desulphurization with a requirement to keep the target sulphur content below 0.0050 % was optimized in the VOD device using chemical heating of the steel. Technologies have been applied in the production of the alloy tool-steel grade No. 19569 (X63CrMoV5.1). The main issue in the design of the technology was that the systems for the production of the reducing slag and optimized compositions of individual oxides have been disrupted by the chemical-heating products.

The essential problems are the amount of Al_2O_3, which is formed after the chemical heating during the oxidation of added aluminium by gaseous oxygen and, simultaneously, the formed quantity of the easily reducible oxides MnO, FeO and Cr_2O_3. With regard to this, it is necessary to add high quantities of CaO to achieve an appropriate content of free CaO and an increase in the CaO/Al_2O_3 ratio. However, this quantity results in a noticeable drop in the temperature during the heat completion. The reduction of oxides is completed after the vacuuming.

In accordance with the theory of steel desulphurization, the efficiency of maintaining a low oxygen activity in the metal where the FeO content in the slag is below 1 % was confirmed. This requirement has been ensured in the VOD device after the chemical heating primarily by maintaining the maximum possible aluminium content in the liquid metal. It is also necessary to maintain the appropriate slag basicity (over 5) and the CaO/Al_2O_3 ratio, which should be in the range of 1.8 to 2.2.

Results of the microanalysis of the inclusions showed that, to achieve the desired cleanliness of the tested steel grade, it is required, after the completed vacuuming, to run the final phase of processing the reducing slag only with the optimum steel temperature, weight and chemical composition of the slag. It was found that an increase in the CaO additive changes the chemical compositions of the inclusions, in particular causing an increase in the CaO content. The impact of the change in the chemical compositions of the inclusions on the beneficial properties of the steel will be monitored with a final customer.

Acknowledgements

This work was supported by the Ministry of Industry and Trade of the Czech Republic in the framework of the projects No. FR-TI3/374 and FR-TI3/373.

8 REFERENCES

[1] L. Socha, J. Bažan, K. Gryc et al., Assessment of influence of briquetting fluxing agents on refining slags at steel treatment by secondary metallurgy. In: 20th Anniversary International Conference on Metallurgy and Materials: METAL 2011, 2011, 163–169

[2] Z. Adolf, I. Husar, P. Suchánek, Investigation of the influence of the melt slag regime in a ladle furnace on the cleanliness of the steel, Mater. Tehnol., 41 (**2007**) 4, 185–188

[3] K. Michalek, L. Čamek, K. Gryc, M. Tkadlečková, T. Huczala, V. Troszok, Desulphurization of the high-alloy and middle-alloy steels under the conditions of an EAF by means of synthetic slag based on $CaO\text{-}Al_2O_3$, Mater. Tehnol., 46 (**2012**) 3, 297–303

[4] K. Michalek, L. Čamek, Z. Piegza, V. Pilka, J. Morávka, Use of Industrially Produced Synthetic Slag at Trinecke Zelezarny, a.s., Archives of Metallurgy and Materials, 55 (**2010**) 4, 1159–1165

[5] M. Allibert, H. Gaye, J. Geiseler et. al., Slag atlas, 1995

UDK 669:378(497.4)
Dogodki/Events

ISSN 1580-2949
MTAEC9, 47(1)141(2013)

PROMOCIJA ŠTUDIJA IN RAZISKAV MATERIALOV

Slovensko društvo za materiale, Lepi pot 11, 1000 Ljubljana, je 6. 12. 2012 že deseto leto zapored pripravilo sklop predavanj v okviru Promocije študija in raziskav materialov. Prireditev je bila v predavalnici P5 Naravoslovnotehniške fakultete, Oddelek za materiale in metalurgijo, Aškerčeva 12 v Ljubljani.

Na prireditvi je 7 predavateljev predstavilo dosežke s področja kovinskih in polimernih materialov ter trdih prevlek, prisotnih pa je bilo 122 dijakov in njihovih spremljevalcev. Ker je bil eden od dijakov gluh, ga je spremljal prevajalec za gluhoneme.

Najprej je predstavnica NTF OMM, dr. Maja Vončina, predstavila študij materialov in metalurgije na Univerzi v Ljubljani, Naravoslovnotehniški fakulteti, Oddelek za materiale in metalurgijo, ki je organiziran po bolonjskih načelih in obsega Univerzitetni študijski program 1. stopnje – Inženirstvo materialov ter Visokošolski študijski program 1. stopnje – Metalurške tehnologije. Nova oblika organiziranja študija omogoča tudi vključevanje študentov v raziskovalno delo že takoj na začetku študija.

V naslednjih predavanjih so bili predstavljeni rezultati raziskav in smeri razvoja na področju sodobnih kovinskih materialov, trdih prevlek in polimernih materialov.

Prisotni dijaki so menili, da je taka oblika predavanj koristna, saj se tako lahko seznanijo z možnostmi za študij materialov in bolje spoznajo raziskovalno dejavnost ter delo na področju materialov.

Dokaz, da obstaja med mladimi zanimanje za materiale, je letošnja prireditev, ki je bila že deseta zapovrstjo. Dijaki in njihovi spremljevalci so izrazili željo, da bi Slovensko društvo za materiale tako prireditev še naprej pripravilo vsako leto.

Promocija študija in raziskav materialov je namenjena dijakom, da pridobijo nekaj koristnih informacij s področja študija in raziskav materialov. Za mlajše predavatelje pa je prireditev priložnost, da si pridobijo potrebne izkušnje za nastopanje v javnosti.

doc. dr. Matjaž Torkar
tajnik SDM
Slovensko društvo za materiale
Lepi pot 11
1000 Ljubljana

Predstavnica NTF OMM, dr. Maja Vončina predstavlja možnosti študija materialov

Dijaki – udeleženci Promocije študija in raziskav materialov v predavalnici P5. Predavanja je prevajal tudi tolmač za gluhoneme.